

# **Computational Studies on Functionalized ZnO Surfaces and Nanostructures**

M. Sc. Ney Henrique Moreira

University of Bremen 2011



# Computational Studies on Functionalized ZnO Surfaces and Nanostructures

Vom Fachbereich für Physik und Elektrotechnik  
der Universität Bremen

zur Erlangung des akademischen Grades eines  
Doktor der Naturwissenschaften (Dr. rer. nat.)  
genehmigte Dissertation

von

M. Sc. Ney Henrique Moreira

- |               |                                       |
|---------------|---------------------------------------|
| 1. Gutachter: | Prof. Dr. rer. nat. E. Erstgutachter  |
| 2. Gutachter: | Prof. Dr. rer. nat. Z. Zweitgutachter |

Eingereicht am: 28.02.2011

Tag des Promotionskolloquiums: 11.04.2011



# Contents

<b>Summary</b>	<b>v</b>
<b>Preface</b>	<b>xii</b>
<b>1 – Introduction</b>	<b>1</b>
1.1 – Hybrid Materials	1
1.1.1 – First Class: Composites	2
1.1.2 – Second Class: Covalently Bonded Hybrids	3
1.1.3 – Third Class: Building Blocks Hybrids	4
1.1.3.1 – Nanocomposites	4
1.1.3.2 – Single Nano-elements	4
1.2 – Inorganic Building Blocks	6
1.2.1 – Nanoparticles	6
1.2.2 – One-dimensional Structures	6
1.2.2.1 – Carbon Nanotubes	8
1.2.2.2 – Silicon Nanowires	8
1.2.2.3 – Metal Oxide 1D Nanostructures	9
1.2.2.3.1 – ZnO 1D Nanostructures	10
1.2.3 – Two-Dimensional (2D) Nanostructures	11
1.3 – Computational Materials Science	11
1.3.1 – Continuous Media	13
1.3.2 – Coarse Grained Models	14
1.3.3 – Classic Atomistic Simulations	14
1.3.4 – Quantum Simulations	16
1.3.4.1 – Ab Initio Methods	16
1.3.4.2 – Density Functional Theory Methods	16
1.3.4.3 – Semi-Empirical Methods	17
1.4 – The Aim and Structure of this Work	18
<b>2 – Theoretical Background</b>	<b>21</b>

2.1 – The Time-Independent Schrödinger Equation	21
2.2 – The Born-Oppenheimer Approximation	23
2.3 – The Hartree-Fock Approximation	25
2.3.1 – The Form of the Wave-Function	25
2.3.2 – The Hartree-Fock Equations	26
2.3.3 – The Variation Theorem and the Roothaan Equation	28
2.3.4 – The Self-Consistent-Field Method	31
2.4 – Changing the Paradigm: Density Functional Theory	31
2.4.1 – The Hohenberg-Kohn Theorems	32
2.4.1.1 – The First Hohenberg-Kohn Theorem	32
2.4.1.2 – The Second Hohenberg-Kohn Theorem	33
2.4.2 – The Kohn-Sham Equations	35
2.4.2.1 – The Kohn-Sham Effective Potential	36
2.4.3 – Exchange Correlation Functionals	37
2.4.3.1 – Local Density Approximation	37
2.4.3.2 – The Generalized Gradient Approximation	38
2.4.3.3 – The Band Gap Problem	40
2.4.4 – The Pseudo Potential Method	41
2.5 – Equilibrium Configurations and Atomic Forces	43
2.6 – Modeling Crystalline Solids	44
2.6.1 – The Reciprocal Lattice	45
2.6.2 – The Wigner-Seitz Cell and The First Brillouin Zone	46
2.6.3 – The Bloch Theorem	47
2.6.3.1 – Energy Bands and Band Structures	48
2.6.3.2 – Integration over the First Brillouin Zone and $k$ -points Sampling	49
2.6.3.3 – Density of States (DOS)	50
2.6.4 – The Tight Binding Model	50
2.6.4.1 – General Tight Binding Formulation	50
2.6.4.2 – The SCC-DFTB Method	53
2.6.4.2.1 – Rearranging the Kohn-Sham Total Energy Formula	54
2.6.4.2.2 – The SCC-DFTB Approximations	56
2.7 – Notes and Remarks on Basis Sets	59
<b>3 – Bulk ZnO</b>	<b>63</b>
3.1 – Bulk ZnO	63
3.2 – Simulation Details	65
3.3 – Structural Properties and Compressibility	65

3.4 – Cohesive Properties	68
3.4 – Electronic Properties	70
<b>4 – Functionalized ZnO non-Polar Surfaces</b>	<b>75</b>
4.1 – Surface Functionalization and ZnO	75
4.2 – Simulation Details	77
4.3 – Thermodynamic Properties of the Functionalized Surfaces	77
4.3.1 – Ligand-Substrate Bond Strength and Adsorption Regimes	77
4.3.2 – Coverage Stability	79
4.3.2.1 – Does a Stronger $E_B$ Yield a More Stable Coverage?	79
4.3.2.2 – Coverage Stability under Ligand-rich Conditions	79
4.3.2.3 – Coverage Stability Under Ordinary Laboratory Conditions	80
4.3.2.4 – Coverage Stability in Aqueous Media	83
4.4 – Adduct Geometries and Electronic Structure Analysis	84
4.4.1 – Me-OH and Me-NH <sub>2</sub> on ZnO-(10 $\bar{1}$ 0)	85
4.4.2 – Me-SH and Me-COOH on ZnO-(10 $\bar{1}$ 0)	87
4.4.3 – Me-CN on ZnO-(10 $\bar{1}$ 0)	91
<b>5 – SCC-DFTB Model for ZnO plus Organics</b>	<b>95</b>
5.1 – Why do we need a SCC-DFTB model?	95
5.2 – The ZnO + Organics SCC-DFTB Parametrization	96
5.2.1 – Parametrization Details	96
5.2.1.1 – Reference DFT Calculations	97
5.2.2 – Validation of the Parameters	97
5.2.2.1 – SCC-DFTB Calculations: Simulation Details	97
5.2.2.2 – Zn-containing Bulk Solids	98
5.2.2.3 – Zn-containing Molecular Complexes	100
5.2.2.4 – Clean ZnO Surfaces	103
5.2.2.5 – ZnO 1D nanostructures	106
5.2.2.6 – Small Molecules on ZnO non-Polar Surfaces	107
5.2.2.6.1 – CO <sub>2</sub> and NH <sub>3</sub> on ZnO-(10 $\bar{1}$ 0)	107
5.2.2.6.2 – Organic Ligands on ZnO-(10 $\bar{1}$ 0)	110
<b>6 – Native Defects in ZnO Nanowires and Defect Healing with Organic Acids</b>	<b>117</b>
6.1 – Why Characterizing Native Defects in ZnO Nanowires?	117
6.2 – Simulation Details	118
6.3 – The Potential Alignment Procedure	120

6.4 – Defect Positions and Atomic Relaxations	122
6.5 – Healing Surface Oxygen Vacancies with Organic Acids	125
<b>7 – Concluding Remarks and Future Plans</b>	<b>131</b>
<b>Acknowledgments</b>	<b>135</b>
<b>References</b>	<b>139</b>
<b>Curriculum Vitae</b>	<b>155</b>
<b>List of Scientific Publications</b>	<b>157</b>



# Summary

Functionalization of nanostructures is a crucial step in many electronic, photonic, and sensing applications. Experimentally, nanodevices with a specific or multiple functionalities have been designed by capping semiconductor surfaces with organic molecules, polymers or biomolecules. In this scenario, ZnO shows a huge technologic potential, since its electric, magnetic and optoelectronic properties can be optimized via functionalization. In principle, molecular recognition properties can be also incorporated to ZnO nanostructures, by attaching biomolecules to their surfaces. For all this reasons, ZnO nanomaterials have been considered extremely promising for applications in nanotechnology; and understanding the influence of surface modification on their properties is a prerequisite for the development of new ZnO-based functional nanodevices.

In this work, we have used electronic structure simulations to investigate the role of organic functionalization on the electronic and structural properties of ZnO surfaces and nanostructures. *Density Functional Theory* (DFT) calculations have been employed to study the interactions of non-polar ZnO surfaces with different organic functional groups - i.e. -OH, -NH<sub>2</sub>, -SH, -COOH and -CN - showing the surface stabilization mechanisms involved in each case and identifying the most promising anchoring groups for ZnO functionalization in different chemical environments.

Aiming to large scale simulations on functionalized ZnO, we have developed a *Self-Consistent-Charge Density Functional based Tight Binding* (SCC-DFTB) model for ZnO plus organics. The model has been validated by comparison against standard DFT calculations, achieving good performances in simulating Zn-containing bulk solids and molecular complexes, ZnO surfaces and nanostructures, and the adsorption of organic acids on (10 $\bar{1}$ 0)-ZnO surfaces. We have also employed this SCC-DFTB model in order to characterize native defects in ZnO hexagonal nanowires, finding that surface defects are expected to be dominant. Besides, oxygen vacancies and Zn interstitials are favored under Zn-rich conditions, while zinc vacancies and oxygen interstitials are the most stable defects at O-rich environments. Finally, we have studied the interaction of surface oxygen vacancies with organic acids, finding that an oxidation-reduction reaction promotes a defect healing process, which allowed us to propose a mechanism to explain the suppression of photoluminescence anomalies observed for polymer coated ZnO nanowires.



# Preface

This text is the result of my work as *Doktorand* – i.e. doctoral candidate – in the *Bremen Center for Computational Materials Science (BCCMS)*, *University of Bremen*.

Along the last 3 and  $\frac{1}{2}$  years, I have dedicated all my efforts to understand – via electronic structure simulations – the influence of organic functionalization on the structural and electronic properties of ZnO surfaces and nanostructures. That is indeed a very up-to-date and exciting topic: The technological potential of ZnO based materials is huge – especially for applications in sensing and optoelectronics. Additionally, the knowledge on the ZnO surface chemistry is still in its infancy in comparison with other commonly employed nanomaterials – such as carbon or silicon. Currently there are still several open questions and much research space for those interested in ZnO based hybrid materials.

Of course, here we cover just a small part of this formidable challenge; but a necessary one. Although from the very beginning our target has been simulating materials with possible applications in real life, it is important to keep in mind that mastering technologies is hardly possible without understanding the basic science behind them – and that is particularly true in nanotechnology. Therefore, we have focused on fundamental aspects of functionalized ZnO – i.e. ligand-substrate interactions, defect spatial distributions, electronic structure effects, etc. By reporting our research here – in chapters 3, 4, 5 and 6, and in all scientific publications derived from this work – I hope I am giving my humble contribution to the scientific discussion on hybrid ZnO materials and on materials science in general.

However, this work has also another important aspect for me: It is an opportunity to reach other students and share my experience with them. During my scientific training here in Bremen I have got to know several people interested on *Computational Materials Science (CMS)*, including my fellow students here at the BCCMS and those from other universities – who came to visit us for a while. From the contact with these students, I have learned that most of us share a particular basic difficulty: *Computational Materials Science* is a broad interdisciplinary research field, where concepts from physics, chemistry, biology and engineering meet. Of course, that is one of the reasons why *CMS* is so exciting; but on the other hand, students coming to this field usually have a hard beginning while they must learn topics far beyond their original background disciplines. In fact, it still surprises me how often the same questions I had are brought back to me by some of my fellow students.

After us, there will be other students coming to the BCCMS and to other *CMS* research groups. Thinking about these students – or about leaving something helpful for them – I have organized the first chapter of this dissertation as a small literature review, not only on hybrid ZnO but on hybrid and nanomaterials in general. With this approach, I intend to: *i)* contextualize my own work on a wider perspective, and *ii)* introduce some general ideas on hybrid materials, referring to both basic texts and advanced research papers where the reader can find a more detailed information. Accordingly, I've included also a brief overview on

computational materials science, commenting on the different approximation levels available to simulate materials in different size and time scales.

Following the same philosophy, in Chapter 2 I have tried to present the theoretical background of this work by extending it a little beyond the limits of the *Kohn-Sham Density Functional Theory* (DFT). I have incorporated some general concepts of quantum mechanics – like the Born-Oppenheimer approximation – and also a brief discussion on the *Hartree-Fock* method, from where some important concepts in DFT came originally. There is also an entire section dedicated to basic *solid-state theory* and *periodic quantum calculations*, which may be helpful for those readers with less background in physics. In the same section, an introduction is given to both the *Tight Binding* model – a very useful theoretical tool in solid state physics – and to the *Self Consistent Charge Density Functional Tight Binding* method, which will be widely employed along this thesis. The idea was constructing bridges between the different theoretical concepts applied along this work. Accordingly, in Chapter 2 I have tried to present the demonstration of the most important equations in a step-by-step fashion, so that the text becomes more comprehensive for those less familiar with quantum mechanical formalisms.

Finally, it is necessary to point out that neither the literature review on Chapter 1 nor the theoretical discussion on Chapter 2 are original research material. Instead, their contents are based on several sources cited along the text, from which I have been learning in the last few years. By sharing my understanding on these works, I hope I am not only providing a comprehensive basis for my research work presented in Chapters 3,4,5 and 6, but also that I will help some of the students who are going to simulate hybrid materials in the near future.





# Chapter 1

---

## Introduction

*"Dante can be understood only within the context of Italian thought, and Faust would be unthinkable if divorced from its German background; but both are part of our common cultural heritage."*

*Gustav Stresemann – German Statesman.*

In this chapter, the scientific context of this work is overviewed. Starting from a broad and general perspective, we will present different classes of materials which are related to functionalized ZnO surfaces and nanostructures – the object of this study. A brief discussion on relevant technological examples will be given in each case, intending to demonstrate the main motivations of this project. Besides, a brief introduction on computational materials science is given. At the end of the chapter, we will outline the structure of this work.

### 1.1 – Hybrid Materials

As the name already suggests, *hybrid materials* are complex systems formed by different chemical species. They are present in several daily life situations, such as when we brush our teeth or paint our living rooms with a white paint. Hybrid materials are also present in our own bodies, constituting the complex structures of our bones, cartilages and teeth. The greatest advantage of hybrid materials is joining the functionalities of different constituents into a single improved element, like in ordinary white paints for example, where the optical properties of a white pigment – usually  $\text{TiO}_2$  – are combined with the viscoelastic and adhesive properties of a latex rubber, producing a coating material.

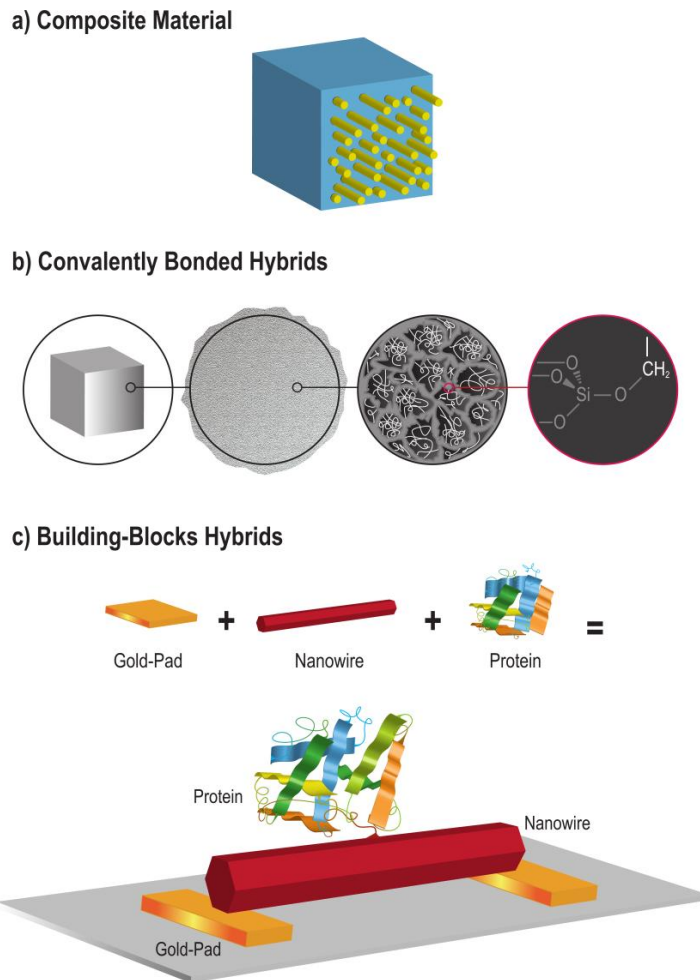


**Figure 1.1** – Different classes of hybrid materials: a) Composites, b) Covalently bonded hybrids and c) Building blocks hybrids (schematic biosensor).

### 1.1.1 – First Class: Composites

The simplest class of hybrid materials is where a structural inorganic material – in the form of solid particles, fibers, lamellae or meshes – is embedded into a second substance – a matrix – resulting in a compound with improved mechanical properties. From the technological point of view, the most relevant examples of such materials are perhaps those applied to the engineering of macro-structures, like the reinforced concretes employed in the construction industry or *Glass Reinforced Plastics* (GRP) common in the automotive and equipments industry. Despite their importance, such materials are nothing else than a simple mixture of their macroscopic components – from a chemical perspective – being intrinsically heterogeneous in their physicochemical constitutions. One clear disadvantage of this kind of materials is related to their processabilities, which are severely limited by the rigidity of their structural components. Such drawback can be partially overcome by reducing the size of the rigid bodies incorporated into the matrixes, which also enhances homogeneity [1] and may result in some mechanical performance gains. For example, polymers reinforced with carbon fibers may be more than 200% more resistant to tensile stress than their analogous with commercial E-glass fibers [2].



Nevertheless, significant improvements in this direction usually must be credited to the quality of the structural material itself, and not to its size.

### 1.1.2 – Second Class: Covalently Bonded Hybrids

A second class of hybrid materials is where different components are formed in the same reaction media – i.e. *in situ* – or merged into one through a chemical reaction. In both cases, organic and inorganic components are intimately connected via strong chemical interactions in the final product. The most representative examples of such materials are the organo-silica compounds prepared through the so called *sol-gel process* [3].

In the conventional sol-gel process, metal alkoxides react in presence of water to form a colloidal suspension of amorphous oxide particles (i.e. a sol). If properly aged, the colloidal particles start to interconnect with each other and form a tridimensional structure with large solvent quantities incorporated (i.e. a gel). Once dried, the gel gives origin to an amorphous solid body. Since C-Si bonds are extremely resistant to hydrolysis, organosilanes can be introduced in the alkoxides mixture (i.e. the precursor) in order to be incorporated in the material[1]. If the silane's carbon chain is connecting two or more silyl groups, the silane is incorporated into the solid network, producing an alternating chain containing both organic and inorganic units. If it is connected only with one silyl group, the molecule acts as chain-terminator, letting its organic part covering the solid's surface. In both cases, organic and inorganic components are connected via strong covalent bonds.

As mentioned above, hybrid silica surfaces can also be modified through an additional synthetic step; namely via a surface silylation reaction, where –OH surface groups react with silyl silane molecules to yield a permanent organic coating. Such materials also have a remarkable technologic importance. Among other applications, hybrid silica particles and porous matrix are extensively used in *Reverse Phase Chromatography*\* [4]. Before its development, the performance of chromatographic methods on separating complex non-polar mixtures – like crude oil samples – was rather limited; mainly because of the strongly hydrophilic character of the conventional stationary phases (e.g. silica or alumina). With the advent of modified silica, it became possible using hydrophobic stationary phases [5], which allowed new efficiency levels to the separation of organic mixtures [6]. Today, the quality of virtually every product of the modern oil and pharma industries relies, at some stage, on reverse phase chromatographic analyses. With the increasing importance of reverse phase chromatography, also other hydrophobic stationary phases have been developed – mainly composed of block copolymer particles – but modified silica materials are still the most used.

---

\*The basic idea of all chromatographic methods is separating the components of complex chemical mixtures according to their chemical polarities. The mixture is applied to one end of a *stationary phase* and eluted through it by a carrying media – i.e. a *mobile phase*. The mixture components with less affinity for the stationary phase will elute faster, whereas those with more affinity will stay adsorbed on the stationary phase for longer times. The stationary phase can assume several different forms – such as a plate covered by alumina powder, a column filled with silica particles or a silica thin-film on the inner surface of a capillary tube – while the mobile phase can be either a liquid or a gas.

### 1.1.3 – Third Class: Building Blocks Hybrids

A third class of hybrid materials can be identified somewhere between the first two classes sketched above. It comprehends the materials formed by joining well defined “building blocks”, which in this context means pre-existing functional chemical units – such as nanostructures, isolated molecules or polymeric matrices. One particularly exciting aspect in this approach is the possibility of creating multi-functional architectures simply by assembling diverse building blocks. In principle, each block should add its original functionalities to the final material, but completely new capabilities can eventually emerge in the final material. That is a consequence of using nano/molecular size building blocks, whose properties may be quite susceptible to changes in their chemical environment. Nevertheless, there is a clear separation among different components in such materials, although the interface between them may be mediated by strong chemical interactions.

#### 1.1.3.1 - Nanocomposites

Among these third class hybrid materials, it is still possible to identify at least two distinct groups. The first results from the combination of distinct building blocks in a composite. Often called nanocomposites, such materials have been studied at least since the 60’s, when the interactions of organophilic clay minerals with polymeric matrixes have been originally observed [7]. However, the recent advent of synthetic nanostructures – in special the large-scale production of carbon nanotubes [8] and synthetic inorganic nanoparticles [9] – gave a new impulse to the field. Currently, there are more than 100.000 scientific publications dedicated to the study of nanocomposites. Two decades ago this number was still smaller than 10.000. A prominent example of such materials is represented by carbon nanotubes composites [10]. From a pragmatic point of view, many hopes deposited on nanocomposites along the last decades are still to be confirmed<sup>†</sup>, but on the other hand, several relevant findings came from the research of nanoscale composite materials. The so called “quantum dots”, for example, have been firstly observed dispersed into glass matrices [11].

#### 1.1.3.2 – Single Nano-elements

The second type of building blocks-based hybrid materials consists on single nanostructures – like carbon nanotubes or silicon nanowires – functionalized with organic molecules. Sensing devices are perhaps the most straightforward applications for such materials, since functionalizing a material with biomolecules can confer molecular recognition properties to it [12]. A more visionary perspective on the subject, however, is using such molecular recognition properties to induce and control self-assembling processes involving well-defined nanostructures. According to this view, individual functionalized nanostructures could be employed as active elements in complex electric devices, like field-effect transistors (FET) or nano switches. It is important to remember that FETs based on single nanostructures have been demonstrated almost 10 years ago [13], but interfacing different elements in nanodevices is still very challenging today. In this sense, using self-assembly phenomena for organizing

---

<sup>†</sup> For example, polymers reinforced with *Carbon Nanotubes* have fairly worse mechanical performances than carbon fiber reinforced polymers.

the elements of a device or controlling its functionalities would represent a huge step towards overcoming the traditional “top-down” lithographic technologies for electronics – which are already reaching their ultimate limits.

Another important potential application of building blocks-based hybrid materials is in energy production. A *Dye-Sensitized Solar Cell* (DSSC) employing functionalized  $\text{TiO}_2$  thin-films has been demonstrated almost 20 years ago by *Grätzel et al* [14], immediately achieving energy conversion efficiencies of  $\sim 12\%$  under diffuse sun radiation. This excellent beginning has created a huge expectation on the potential of DSSC, but in reality the efficiency of such devices has not improved much since that pioneer work. Along the last decade, the major bottlenecks in the general performance of DSSCs have been identified as the stability of their commonly employed  $\text{I}^-/\text{I}_3^-$  redox-couple and the light adsorption capacity of the  $\text{TiO}_2$  thin films [15], but attempts to overcome these difficulties have mostly lead to performance losses [16-20]. Today, it is consensual that the efficiency of DSSCs relies on a delicate equilibrium among electronic transport through the cathode, excitonic recombinations on its surface and the redox step involving the immobilized dye and the redox-couple. Apparently, the original DSSC design has already reached a considerable success in balancing these three phenomena, achieving conversion performances already close to the current limits – 20 years later.

A promising alternative to increase the efficiency of DSSC is substituting the thin-film cathodes traditionally employed by arrays of monolithic nanowires. By packing dense arrays of nanowires, it is possible to expose larger surfaces to the sun radiation, so maximizing the light adsorption process. Furthermore, monolithic nanowires are expected to improve the electronic transport on the cell's cathode, since they are not affected by electron percolation problems like metal oxide thin-films are. In fact, DSSC have been already fabricated with ZnO nanowires [21], although showing fairly low conversion efficiencies –  $\sim 2\%$ . Some efficiency improvement has been recently achieved by covering ZnO nanowires with a  $\text{TiO}_2$  thin film [15], but the mechanisms leading to such improvements are still not fully understood.

Obviously, at this nano-scale, the properties of the inorganic building blocks are mostly dominated by surface effects. Consequently, they may be very susceptible to the interactions with the soft matter. DSSCs are again a good illustrative example of that. In their case, the devices' functionality consists exactly on exciting electrons in the organic dye – via sun light – in order to inject them into the cathode's solid material. Similarly, the interaction with the cathode's surface is also expected to influence the excitation energies of the dye. In fact, the essential idea behind any hybrid material is joining parts to produce an effect which could not be achieved by the isolated components. But the interesting point in nano-scale hybrids is: the desired effects often come from the interactions among the materials, and not from the materials themselves. Synergy is an important word in nanotechnology.

Of course, mastering such delicate and interconnected effects requires a deep understanding on the physico-chemical interactions involved. Therefore, the surface chemistry of nanomaterials is a topic of major relevance today; although still in its infancy in most cases.

## 1.2 – Inorganic Building Blocks

The natural candidates for inorganic building blocks in nano-hybrid materials are, of course, inorganic nanostructures. From a pure scientific perspective, such materials are very interesting, because they simply do not behave like their macroscopic analogs. Their sizes and forms usually have a determining influence on their properties, enabling fine-tuning to the exigencies of specific applications. That is an incredible technological advantage, but exploring it almost always requires uniform samples and a formidable level of control on the material's synthesis. Nevertheless, there is already a broad range of widely available nanostructures applied in several different technologies; from clinical imaging techniques to nanoelectronics. In most of them, the form of the nanostructures is almost as relevant as its chemical compositions.

### 1.2.1 – Nanoparticles

Although most people think that nanotechnology is a creation of modern science, synthetic nanoparticles have been finding technological applications for centuries already. In the ancient world, artisans synthesized copper, silver and gold nanoparticles by reducing metal-salt precursors and used them as coloring agent in art forms which last until our times, such as glass windows in European cathedrals and Chinese porcelain pieces. But in fact, the science of nanoparticles has sharply risen in the end of the 80's, benefited by the advent of new physicochemical characterization techniques. Since then, several modern approaches – such as sol-gel processes, reaction into inversed micelles, pyrolysis and vapor deposition [22] – have been employed to synthesize several metal and semi-conducting nanoparticles.

In the actual research stage, different nanoparticles are already being combined with organic molecules in order to design functional hybrid architectures, especially for medical applications. In a recent work [23], solid silica/iron-oxide composite nanoparticles have been designed for simultaneously imaging and treating cancerous tissues. The iron oxide crystallites act as magnetic active (contrasting) component for magnetic resonance imaging, while the silica – functionalized with both targeting agents and anti-tumor drugs – is responsible for driving the particles to the target tissues and delivering the therapeutic molecules. Note that such formidable functional nanoarchitectures strongly rely on the stable junction of their organic/inorganic components, which is achievable in this case just because the hydroxyl surface chemistry of silica is extremely well-known.

### 1.2.2 – One-dimensional (1D) Structures

In the beginning of the 21<sup>th</sup> century there was a *boom* in the number of articles reporting the synthesis of one-dimensional (1D) nanostructures, inclusive in large quantities and yielding high-quality single crystalline materials. According to *Yang et al* [24], now it seems inevitable that most solid-state lattices will be grown in a nanowire form.

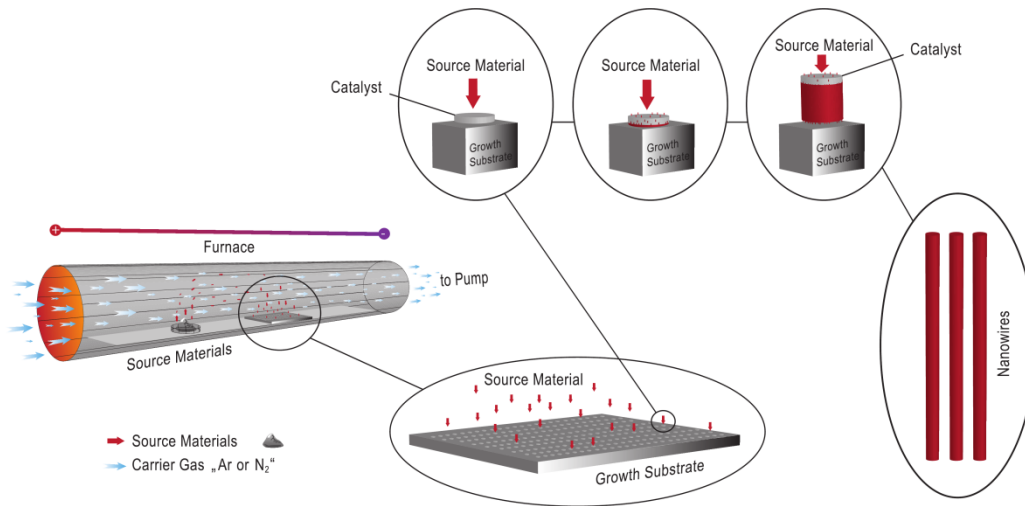


**Figure 1.2** – Vapor-liquid-solid synthesis of 1D-nanostructures.

One-dimensional nanostructures are formed by growing a given crystalline material preferentially along one of its crystallographic directions. Among the methods available for this purpose, the most popular are probably those based on metal catalyzed vapor-solid synthesis (Figure 1.2). The vapor-liquid-solid growth mechanism basically consists in using a liquid metal catalyst in order to catch gas-phase precursors through the formation of an eutectic alloy and consequently accelerate their deposition rates on a certain substrate. Perpendicular to the growth direction, the nanostructure's form is in general determined by the metal catalyst. For example, it has been demonstrated that Si and GaP nanowires of any specific diameter can be obtained by controlling the size of the colloidal gold catalysts employed [25,26]. Along the growth direction, the size of the nanostructures can be simply controlled by the reaction time. There are also several reports on catalyst-free synthesis of one-dimensional nanostructures – whose more important examples are the metal oxide nanobelts/nanoribbons synthesized by *Wang et al.* [27] – but the growth mechanisms involved are still poorly understood.

One of the drawbacks related to vapor-phase synthesis methods is their high energy demand. The formation of the gas-precursors into high temperature furnaces – by evaporating solid materials samples – is a very energy consuming procedure, which cannot be easily improved by scaling the process up. Therefore, there is also a great interest in developing mild wet chemical routes for synthesizing one-dimensional nanostructures. Actually, a broad range of metallic and semiconducting nanostructures has been already synthesized in solution, even in large (gram) scales [28]. In such wet syntheses, it is believed that molecular capping agents – i.e. molecules which adsorb preferentially to specific facets of a solid – have a fundamental role on controlling the growth kinetics and the shape of the structures. Nevertheless, the accumulated knowledge on the surface chemistry of most nanomaterials is still very limited (except for carbon and silicon) and choosing appropriate capping agents is still a rather empirical process consequently [24].

### 1.2.2.1 – Carbon Nanotubes

*Carbon Nanotubes* (CNT) were the first known and are still the most investigated kind of one-dimensional materials. They were first observed already in the 70's, in experiments on the vapor-synthesis of carbon fibers via thermal decomposition of hydrocarbons in the presence of metal catalysts [29]. Nevertheless, the official milestone of the CNT research dates back to the beginning of the 90's, when a Japanese [30] and a Russian groups [31] have independently reported the discovery of these interesting materials. Since then, CNT have been considered one of the greatest technological promises of our time. In fact, several CNT-based technologies have been already demonstrated along the last two decades, including FETs [13], logical circuits [32], switches [33], and interconnects [34]. In all these applications, CNT-based materials have shown performances either comparable to or better than their best commercial analogs. Furthermore, there is at least one kind of CNT-based devices about to be commercialized in the electronics market – the CNT-based displays recently demonstrated by Samsung and Motorola.

Despite the importance of the examples above, the technological applications of CNT are not restricted to electronic devices only. In the energy sector, for example, CNT are employed as fillers in lithium batteries and in polymer based solar cells, where they improve the electrical conductivity of the solid electrolytes [35,36]. Because of the extraordinary mechanical properties of single CNT, such materials have been also often suggested for reinforced polymer composites. However, despite the intense research activity, there has not been much progress in this direction. Up till now polymers reinforced with CNT still do not outperform their counterparts filled with carbon fibers [37].

CNT also have been demonstrated to be useful in gas and bio sensing applications [37]. In the last case, the sensor's functionality depends on nanotubes modified with biological molecules – i.e. proteins, enzymes, DNA fragments, etc. Indeed, in comparison with other nanomaterials, carbon has a natural advantage in applications where surface functionalization is required, since its chemistry is the best known among all existing chemical elements.

### 1.2.2.2 – Silicon Nanowires

Among all existing 1D semiconductor nanostructures, *Silicon Nanowires* (SiNW) have been considered the most promising alternative to substitute the traditional silicon electronic devices. According to *Fargas et al.* [38], "*SiNW offer an alternative route for the fabrication of 'end-of-roadmap' transistor technologies*". In fact, there are several good reasons for such confidence in the technological potential of SiNW, since they have been already employed in many functional nanodevices such as FETs [39-41], single-electron transistor geometries [42] and biosensors [43,44]. The electronic and photonic properties of SiNW can be controlled by doping [45-47] and, moreover, SiNW as thin as 1nm have been synthesized in a reproducible way [48-50]. Such dimensions are more than 10 times smaller than the smallest conceivable silicon transistor based on lithographic processes [37].

As a raw material for nanostructures, silicon shows numerous advantages in comparison with its competitors, like the fact that its production is already

completely integrated in the electronics industry. Besides, because of its technological importance, silicon has been widely investigated for decades, which ensures a large amount of knowledge accumulated on it. Concerning the chemical interface with soft matter, silicon also shows an additional advantage: its chemistry is closely related to the chemistry of carbon. Hence, the functionalization of silicon surfaces can be achieved by adapting very well-established protocols of organic chemistry, as already demonstrated in several opportunities [51-58]. Not surprisingly, SiNW have been extensively investigated for biosensing applications [59].

### 1.2.2.3 – Metal Oxide 1D Nanostructures

Despite their importance and multiple advantages, CNT and SiNW have at least one serious drawback: Their chemical compositions are fixed, and the possibilities of tuning their properties are rather limited. Of course, doping is always an option, but there are certain limits imposed to the efficiency of such a strategy.

In this sense, *Metal Oxides* (MO) represent a much wider platform for the development of functional nano building blocks. In the words of *Schmidt et al.* [60], “*The range of physical and chemical properties of oxide materials is overwhelming. Among metal oxides are superconductors and the best insulators; some oxides are inert enough to act as corrosion protection layers, whereas others are chemically active as catalysts. Some of the most interesting magnetic, optical and electronic properties are found within this class of materials*”. MOs are also usually sensitive to changes in their chemical environments, which has made them the heart of most commercial sensing technologies available [61]. Still, MO-based sensing devices can achieve new efficiency levels if constructed with 1D nanostructures. Gas sensors based on individual  $\text{In}_2\text{O}_3$  nanowires – for example – show sensitivities up to  $10^5$  times larger than their solid-films analogs [62].

1D nanostructures have been already synthesized from a range of MOs, including CdO, CuO, MgO, ZnO, CeO<sub>2</sub>, PbO<sub>2</sub>, TiO<sub>2</sub>, SnO<sub>2</sub>, Fe<sub>2</sub>O<sub>3</sub>, Ga<sub>2</sub>O<sub>3</sub> and In<sub>2</sub>O<sub>3</sub> [63,64]; most of them in a monocrystalline form. As mentioned before, such materials have been often appointed as promising alternatives for applications in electronics, optics, sensing and catalysis. At least in these last two cases, understanding the surface chemistry of such materials is a fundamental step towards developing nano-MO based technologies. That is perhaps the most serious drawback of MOs 1D nanostructures in comparison with their CNT or SiNW competitors – especially concerning sensing applications – since the surface chemistry of MO is still poorly understood in most cases. In fact, the appliance of surface science techniques to study MOs is a relatively new research field [60], where the electric characteristics of many oxides – i.e. the insulator ones – still hampers the use of most surface characterization techniques.

Providing an overview – even a brief one – on the applicability of each specific kind of MOs nanostructures would required a huge effort and is out of the scope of this thesis. Thus, from now we will focus only on ZnO 1D nanostructures, the most relevant species among all MO nanomaterials [65].

### 1.2.2.3.1 – ZnO 1D Nanostructures

Among all MOs employed in synthesizing 1D nanostructures, ZnO is by far the most important one. In order to confirm this fact, it is enough to remember that ZnO nanowires are the third most investigated nanostructures, closely behind CNT and SiNW in number of published articles in indexed journals [65]. That is actually not surprising given the unique characteristics of ZnO. Being naturally a multifunctional material, ZnO simultaneously shows semiconducting and piezoelectric properties, which makes it an ideal candidate for energy harvesting devices [66]. ZnO also is a wide band-gap semiconductor ( $E_g \sim 3.3$  eV), with a huge potential for applications in optoelectronics, lasers and photonics in the UV region [67-69]. Moreover, ZnO gives origin to the richest family of nanostructures among all known materials; comprising nanowires, nanobelts, nanotubes, nanohelices, nanopillars, nanobows, nanorings and nanocages [69]; most of them synthesized with purities of 100%.

ZnO nanowires are usually synthesized via the vapor-liquid-solid growth mechanism, which has been proven to yield large quantities of highly ordered arrays of nanowires [70,71]. Typically, Au or Sn nanoparticles are employed as catalysts in the growth of ZnO nanowires [69, 72], where they have a strong influence on the product's final morphology [73]. For example, it has been demonstrated that the density of a nanowires array can be controlled by using lithographically patterned Au seed-layers as catalyst [74]. Additionally, the pressure inside the reaction chamber – especially the oxygen partial pressure – is also considered an important parameter for controlling the growth kinetics and the products morphology consequently [75,76].

Aside from nanowires, most ZnO 1D nanostructures have been synthesized through a direct vapor-solid approach, where the material grows in the absence of a metal catalyst [64, 69, 72]. As mentioned above, such vapor-solid synthesis can be already extremely well-controlled and yield very pure final products [69]. Nevertheless the chemical kinetics behind vapor-solid syntheses is still not well understood. Several growth mechanisms have been proposed in the literature; but according to *Yang et al.* [24] most of them “*lack compelling thermodynamic and kinetic justification of one-dimensional growth*” and much fundamental research is still necessary to understand the vapor-solid synthesis of nanostructures.

Note that understanding the mechanisms of vapor-solid syntheses would be a big achievement not only from a fundamental perspective, but also in order to guide new research on mimicking them in solution. As discussed before, vapor-liquid-solid and vapor-solid syntheses are extremely energy consuming and therefore unviable for large-scale production. In fact, there is already a large amount of reports on wet-synthesis of ZnO nanostructures, but in most cases the results are hardly more than less symmetrical variations of nanowires or hierarchical structures based on them. Indeed, the outstanding structural variety of the ZnO 1D-materials synthesized via vapor-solid methods is still far from being achieved via solution synthesis. Despite that, it is important to keep in mind that such structural diversity is one of the biggest advantages of ZnO in comparison with other nano materials. From the lessons of molecular biology, scientists have learned that form and function are intimately related at nano/molecular scale. Thus, mastering the form of ZnO 1D nanostructures – or of



any other material – means opening perspectives of new functionalities and applications.

### 1.2.3 – Two-dimensional (2D) Nanostructures

As already mentioned in section 1.1.3.1, the first polymer nanocomposites were observed in the 60's, resulting from the combination of water soluble polymers with natural lamellar organophilic clays [7]. Today it is well-known that such clays show a lamellar structure, which can accommodate the polymeric material into the interstices between adjacent inorganic layers. Thereby, the resultant material also assumes a layered form, consisting of alternating organic and inorganic layers. Because of this alternating structure, such composites are called also intercalation compounds<sup>‡</sup>. The inorganic layers in such composites are typically ~ 1nm thick, whereas their areas can reach  $\mu\text{m}^2$  scales [77].

Such intercalation nanocomposites have several technological applications. One important example came in the first half of the 90's, when a group from the Toyota Research Center (Japan) demonstrated that charges as small as 2% vol. of layered silicates could increase the deformation temperature of polyamides – like Nylon<sup>®</sup> – by up to 100°C [78-80], extending their applicability to high temperature components in automobiles[81]. In a more recent work, organometallic complexes have been intercalated into layered double hydroxides, resulting in a precursor for metal oxide mixtures with improved catalytic properties [82].

Much attention has been also given to MO thin-films during the last two decades – i.e. since the advent of DSSCs – especially TiO<sub>2</sub> and ZnO. Such materials can be fabricated either by vapor deposition techniques or by electrochemical deposition [83]. Nevertheless, the films usually consist of a network of interconnected nanoparticles, which strictly cannot be considered as a 2D building block.

## 1.3 – Computational Materials Science

From a general perspective, there are two ways of tackling a particular problem. One way is performing experiments, i.e. inducing an event, observing it and then constructing empirical correlations between controllable conditions and observable properties. The second way is developing a theory, i.e. – with help of some basic assumptions – constructing a logical framework which permits predicting or explaining some event. Of course, such dichotomy is always arbitrary to some extent. Experimentalists often construct a theoretical model in order to explain their observations, while theoreticians are always either trying to explaining experiments or eager to have their models experimentally confirmed. Without experiments, a theory is hardly more than an elegant

---

<sup>‡</sup> An intercalation compound is defined as a material where a filling agent is introduced between the sheets of a host layered matrix. As a matter of fact, this definition is not restricted to organic-inorganic materials; the lithium-graphite anode used in batteries, for example, is a typical inorganic-inorganic intercalation compound. Nevertheless, layered polymer nanocomposites can be considered an important sub-class of intercalation compounds.

possibility<sup>§</sup>, while experiments without a guiding theory behind them are hardly more than scattered data.

Certainly, theory and experiment walk together in science, but the distinction between them is usually very clear. In physics and physical-chemistry, developing a theory generally requires very simple and well-defined objects of study – many times even idealized ones – whose properties can be reasonably described by a tractable set of mathematical equations. Unfortunately, that is not the case in most real materials. Real materials have an essentially complex nature and therefore it has been very difficult addressing them directly by theory. Thus, the study of materials properties has been dominated by empiric approaches since its early origins. However, with the advents of hybrid materials and nanotechnology, a better comprehension of molecular scale phenomena is becoming crucial in order to design new materials and optimize their functionalities. Understanding materials from a microscopic perspective is quickly turning from “just” an exciting scientific subject into a real necessity in our pursuit of new and more efficient technologies.

The problem at this point is that extracting molecular-scale information directly from experiments is also a complicated task. Although the last decades have witnessed the birth of several new characterization techniques – some of those already reaching atomic/molecular resolutions, like in the *Scanning-Tunneling Microscopy* (STM) and the *Atomic Force Microscopy* (AFM) cases – the truth of the matter is that their outputs are generally intricate and hard to analyze if supplementary information is not given. Even with such high-resolution characterization methods, it is always necessary to rationalize experiments in terms of a comprehensible model.

But how to proceed with that if the object of study is complex and intractable theoretically? Indeed, one of the most effective approaches to overcome such a situation is using computational simulations. In natural sciences, performing a simulation normally means breaking a complex problem into smaller and manageable pieces and after that solving them independently. The resulting set of equations is generally huge, but manageable with the help of computers. Note that in order to expand the problem in small tractable parts it is always necessary to assume some reasonable approximations. So, instead of pursuing an elegant analytical solution for the problem, a simulation basically consists in defining an approximated physics to a model system and observing how it behaves. It is like performing a virtual experiment, whose outcome can be compared with those of real experiments. If the comparison is reasonable, the approximations employed suit the problem; the bridge between experiments and theory is built and some physical insight can be extracted from that.

An important part of the art of computational simulations consists in choosing appropriate approximations for each object of study. Instead of using very elaborate and complete models in any case, the best solution ideally consists of a model capturing the essentials for the studied system and neglecting all unimportant effects. In practice it is not always easy to determine what is essential and what is not. On one hand, strong approximations may lead to unrealistic results, whereas some level of redundancy just increases the time necessary to perform the simulation. In this sense, it is always better to be

---

<sup>§</sup> This statement is obviously invalid if considering fields out the limits of natural sciences, such as pure mathematics for example.

conservative while choosing models. On the other hand, the more complicated your model is, the larger are the computing resources you need to solve it. So, being too conservative while choosing your approximations restricts the size of the system you are able to simulate, thereby also hampering the construction of realistic models.

There are diverse levels of approximation which are relevant for materials simulations (Figure 1.3). Given their particularities, each of these levels can be considered as a science itself. Indeed, making a detailed survey on them is out of scope here. Nevertheless, the next sub-sections provide a very brief overview on the main levels of approximation used in computational materials science. The reader can find more detailed information in the references indicated along the text.

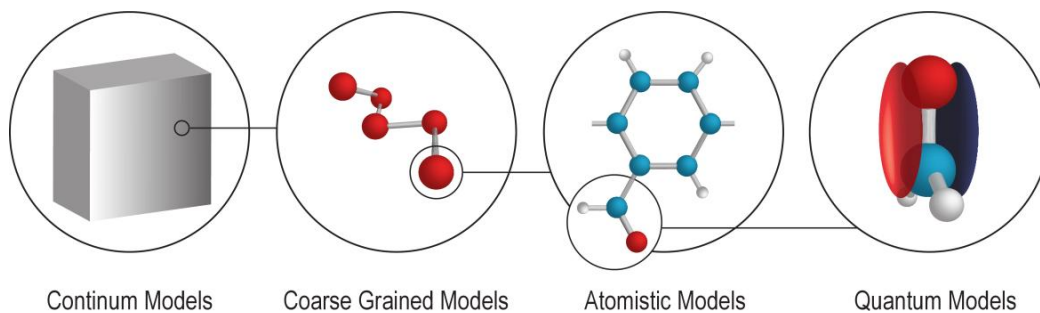


**Figure 1.3** – Different levels of approximation commonly employed in computational materials science.

### 1.3.1 – Continuous Media

The first important level of approximation in computational materials science is considering the materials as a continuous media. This approximation is widely applied in analysis of macro structures or in mechanics of fluids, where the studied phenomena can be satisfactorily described without considering nano/molecular scale interactions. At this level, the materials are simply characterized by macroscopic properties like compressibility or mass densities. In the case of heterogeneous materials, such properties change numerically from one phase domain to another, but all domains within the model are still treated as a continuous media. In the limit where the phase domains are much smaller than the entire model, the material can be simply represented by a homogeneous phase with average “effective” properties [84].

One important analytical tool employing this level of approximation is the so-called finite-element method [85], where a macroscopic material is discretized in smaller units (called elements) interconnected through their corners (called nodes). The physical properties within each element – e.g. its compressibility – are in general kept constant, while their shapes are determined by the movement of their nodes – according to pre-established physical rules. Each element can eventually have intermediate nodes between their ends in order to represent internal degrees of freedom. By imposing a load to the system it is possible to observe how it relaxes, by minimizing its potential energy for example [85]. The method allows mapping the stress along the system by analyzing the distribution

of forces among the nodes. So, finite elements analysis has straightforward applications in stress-analysis, but it has been also extended to other fields of materials engineering, such as heat and mass transport.

### 1.3.2 – Coarse Grained Models

*Coarse Grained* (CG) methods can be considered as an intermediate stage between macro and micro-scale simulation techniques, where groups of atoms are represented together in a particle-based mapping scheme (Figure 1.4). CG models are well suited for simulating macromolecular phenomena, e.g. protein folding [86], biomembranes organization [87,88] and melting of polymers [89], where a good description of polymers' thermodynamic properties and/or secondary and tertiary structures is more important than an accurate representation of atomistic primary structures. The derivation of coarse grained interaction potentials\*\* may be either target to reproduce well-known thermodynamic properties of a prototype system – such as energies or free energies – or pre-defined structures from atomistic simulations [90]. At the current development stage, however, it is still not clear if energy-based potentials are suitable to reproduce atomistic structures and vice-versa [91,92].

As a consequence of their simplified nature, CG models are computationally much less demanding than their atomistic counterparts, since representing groups of atoms by pseudo-atomic species reduces drastically the size of the mathematical problem to be solved. Furthermore, the *inertia* associated with the CG pseudo-atoms is always bigger than those with atomistic models; thus CG-based *Molecular Dynamics* (MD) simulations can use larger simulation time-steps (ca. 30 fs) than those allowed for traditional all-atoms MD (ca. 1fs) without producing simulation artifacts [93]. It is important to remark that not only MD algorithms are employed in CG simulations, but also the *Monte Carlo* (MC) stochastic technique [94].

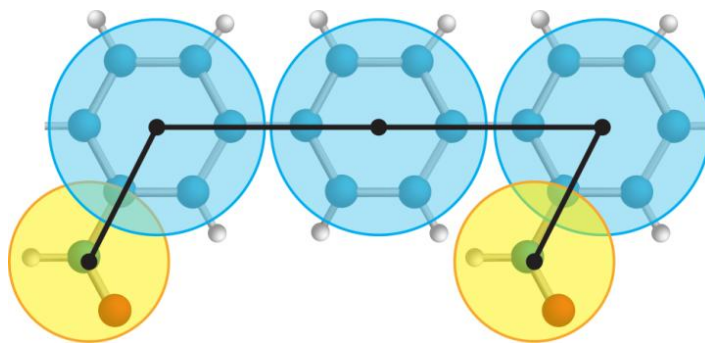


**Figure 1.4** – Schematic representation of a *Coarse Grained* (CG) model.

---

\*\* The CG pseudo-atomic interaction potentials – as the interatomic potentials in traditional atomistic simulations – are divided in bonded and non-bonded interactions. The bonded interactions consist of the stretching of consecutive covalent bonds, bending and dihedral bond angles, while the non-bonded interactions consist of pairwise additive potentials – like the Lennard-Jones potential for example – among all pseudo-atoms in the system.

### 1.3.3 – Classic Atomistic Simulations

As the name already suggests, classic atomistic simulations are performed by considering atomic species as basic simulation units. They are the “*high-resolution*” version of the CG techniques discussed in the last section<sup>††</sup>; so it is natural that the scopes of these two frameworks overlap. Atomistic simulations have also been widely used to study proteins [95], membranes [96] and polymers [90]; the difference is that atomistic simulations have enough size and time resolution to investigate environments dominated by local intermolecular interactions, such as hydrogen bonding media for example. In such simulations, the *meso* and *macroscopic* phenomena appear naturally as a consequence of the molecular-scale interactions. The drawback is that atomistic models are much more expensive than the CG ones, but the advantage on the other hand, is that sophisticated micro-scale phenomena – such as local stabilization mechanisms in biomolecular complexes [97] or dielectric relaxation effects [98] – become accessible.

In atomistic simulations – as in coarse grained ones – the bridge between the microphysics and the macroscopic world is done via *Statistical Mechanics*. The basic idea is that a given *Macrostate* – characterized by thermodynamic properties such as temperature, pressure and etc. – emerges as a weighted average over the mechanical *Microstates* of a considered system<sup>‡‡</sup>. Such weighted averages can be calculated by sampling the system’s configurational space either via randomly generated *Ensembles* (MC approach) or via time-resolved mechanical trajectories (MD approach)<sup>§§</sup>. Nevertheless, it is important to remark that the *Statistical Mechanics*’ framework is neither restricted to atomistic simulations nor even to strictly mechanical systems [101,102]. Instead, it is a broad theoretical platform, which among other things ensures that the microscopic and macroscopic worlds are interchangeable.

The quality of statistics-based simulations strongly depends on an appropriate sampling of the system’s configurational space. In the context of atomistic simulations, that means employing a reasonable physical model to describe all involved interatomic interactions. In both MD and MC approaches, such interatomic interactions are represented by a set of classical potentials, separated in a bonded and a non-bonded part. As discussed for the CG models, the bonded part comprises all bond-stretching, bending and dihedral potentials among interconnected atoms; while the non-bonded part includes a term accounting for both *van der Waals* and *Pauli* interactions – i.e. a *Lennard-Jones* (LJ) pairwise additive potential – plus a *Coulomb* potential. Some models may also include atomic polarization potentials additionally. Besides operating on the atomic coordinates, all these potential functions depend on a set of specific parameters, i.e. constant forces, rotation barriers, atomic charges and the LJ  $\epsilon$  and  $\sigma$  parameters. Once again, these parameters may be either target to reproduce well-known desired thermodynamic properties of the system or higher-level calculations. Once again, the interchangeability between these two choices is not

---

<sup>††</sup> In fact, the CG framework has been developed as a “*low-resolution*” version of atomistic simulations, and not the opposite.

<sup>‡‡</sup> A comprehensive discussion on statistical mechanics is out of scope in this text. Interested readers are encouraged to consult the refs. [99] and [100], for example.

<sup>§§</sup> Both methodologies are equivalent according to the so called *Ergodic Hypothesis*.

*a priori* guaranteed. The definition of the suitable parameters for atomistic simulations is always something done on an *ad hoc* basis to some extent.

### 1.3.4 – Quantum Simulations

Despite their peculiarities, all approximation levels described above have at least one similarity: they are all based on classical physics. Nevertheless, there are many materials whose interesting properties are directly determined by their electronic structures. Just to mention some examples; metals, semi-conductors, catalysts, conducting polymers and virtually every single nanostructure belong to this group. So, in order to study such materials it is necessary to go beyond classical approximations and represent them from a quantum mechanical perspective. In fact, the development of quantum simulations has been often considered as one of the pillars of modern nanosciences. Roughly, there are three classes of quantum based computer simulations: *ab initio*, *Density Functional Theory* (DFT) and *Semi-Empirical* methods.

#### 1.3.4.1 – Ab Initio Methods

The term *ab initio*, in Latin, means “from the beginning”. So, the name *ab initio* is given to calculation methods derived directly from theoretical principles, without incorporating any kind experimental data. Historically, the term has been often associated with quantum chemistry methods, especially with those based on the *Hartree-Fock* (HF) theory [103].

Roughly speaking, the main objective of *ab initio* calculations is solving the Schrödinger equation for many-electrons systems, i.e. determining approximate N-electron-wave-functions in order to reasonably describe them. Of course, this task can be accomplished on several levels of accuracy and at different computational costs. Restricted HF method (RHF) – the simplest and least demanding *ab initio level of theory* – is applicable for systems up to few hundreds of heavy atoms if large computational resources are employed [104], but its results do not figure among the most accurate ones<sup>\*\*\*</sup>. Yet the sophisticated *Configuration Interaction* (CI) and *Quantum Monte Carlo* (QMC) methods give the most accurate results within the quantum chemistry framework, but their applicabilities are still restricted to systems with few electrons because of their high computational costs. The choice of a specific *level of theory* always involves a compromise between the accuracy requirements of the study and the computational resources available. Nevertheless, it is important to remark that, even at the RHF level, *ab initio* calculations are generally more – or much more – expensive than their DFT or semi-empirical competitors. Therefore, their application has been more or less restricted to small/middle-size molecules in gas phase.

#### 1.3.4.2 – Density Functional Theory Methods

Traditionally, DFT methods have been widely employed in quantum mechanical simulations of solid-state materials. The heart of the DFT approach is substituting the complex N-electron-wave-functions with a much simpler variable, i.e. the total electronic density. The first attempts to perform this

---

<sup>\*\*\*</sup> The errors in absolute orbital energies may reach ~ 1eV.

paradigm change dates back to 1927, to the pioneer works of *Thomas* and *Fermi*; but the foundations of the modern DFT started to be established almost 40 years later, with the *Hohenberg-Kohn theorems*.

Since their early days, DFT simulations became a fundamental tool in computational materials science. According to *Martin* [105] (pg. 119) DFT “*has provided the key step that has made possible the development of practical, useful independent-particle approaches that incorporate effects of interactions and correlations among particles.*”, and therefore it became the primary theoretical tool for calculating the electronic structure of condensed-phase systems[105]. There is a big controversy on whether DFT methods should be classified as *ab initio* or not. In principle, DFT is a theory formulated from first principles; but in practice exact *Exchange-Correlation* (XC) functionals are unknown except for free-electron gases. Thus, most DFT formulations include XC functionals which are parametrized to reproduce experimental data. Controversies aside, DFT-based simulations usually are the method of choice for studying solid systems with from few dozens to few hundreds of atoms – if enough computing power is available. A detailed discussion on the fundamentals of DFT will be given in Chapter 2.

#### 1.3.4.3 – Semi-Empirical Methods

Semi-empirical methods are almost as old as the Schödinger equation. The first known example of them was the so called *Hückel method* [106] – proposed in 1930 – where a simplified Hamiltonian and minimal set of p-type atomic orbitals have been used to predict the symmetries and energies of  $\pi$ -type molecular orbitals in conjugated hydrocarbons. Since *Hückel's* pioneer work, several other semi-empirical methods have been proposed and extensively used. With a few exceptions, all of them share four basic characteristics [107]:

- i)* The explicit treatment given only for valence electrons.
- ii)* The use of minimal basis sets.
- iii)* Only one- and two-center integrals are computed.
- iv)* The use of parametrized two-center integrals.

Thanks to both its approximated nature and the use of parametrized integrals, semi-empirical methods are extremely efficient in computational terms; being often used in high-throughput applications such as hybrid *Quantum Mechanics/Molecular Mechanics* (QM/MM) simulations<sup>+++</sup>. On the other hand, the transferability of semi-empirical models to problems out of their parametrization scopes is generally problematic and leads to inaccurate results. Nevertheless, semi-empirical methods are still very powerful tools for calculating the electronic

---

<sup>+++</sup> An exciting new research area in computational materials science is the development of the so called *multi-scale hybrid methods*. In such hybrid simulations, two or more approximation levels are hierarchically combined to study problems which cannot be addresses in only one level. A comprehensive text on the subject can be found in ref. [108].

properties of large systems – i.e. from few hundreds to few thousands of atoms. In the context of this work, one important semi-empirical method is the *Self-Consistent Charge Density Functional based Tight-Binding* (SCC-DFTB) approach [108,109], which consists of an approximated form of the *Kohn-Sham* DFT. A detailed introduction to the SCC-DFTB methods will be given in Chapter 2.

## 1.4 – The Aim and Structure of this Work

Across the last sections, the general scientific context of this work has been sketched. In Section 1.1, a brief introduction to hybrid materials was given, emphasizing the class of nano-hybrids and the importance of surface functionalization for the development of such materials. In section 1.2 the most common inorganic building blocks for nanohybrid materials were presented. Finally in section 1.3, a brief outline on computational materials science and its major levels of approximation was offered.

In this work, we are interested in simulating the structural and electronic properties of functionalized ZnO surfaces and nanostructures. As we have seen in section 1.2, these materials have a huge technological potential, while several of their features – especially their surface chemistry – remain not well investigated. So, our basic aim in this work is identifying suitable organic functional groups for ZnO functionalization and understanding the substrate-ligand interactions in each case. As far as the electronic structure information is aimed, quantum simulations are necessary. Additionally, we want to develop a model to allow us simulating large/realistic models for functionalized ZnO nanostructures with reliable accuracy.

We will start our study from DFT simulations of small/medium ZnO solid systems; so Chapter 2 is dedicated to reviewing the fundamentals of DFT and basic solid-state theory – including also an introduction to the Tight Binding model and to the SCC-DFTB method.

Chapter 3 briefly presents our DFT simulations on bulk *w*-ZnO, performed in order to set and test simulation parameters – basis sets, pseudo potentials, etc.

In Chapter 4, the main focus lies on functionalized ZnO non-polar surfaces. We start showing how to set up a surface simulation within the DFT framework, and then use this approach to investigate how different organic functional moieties interact with the ZnO non-polar surfaces<sup>+++</sup>. The aim is identifying suitable functional groups for stable functionalization of ZnO, while gaining some insight into the ZnO surface chemistry.

The simulation of nanostructures poses considerable challenges in computational materials science. Their reduced symmetry make large models – i.e. with several atoms – necessary in order to represent them, and using efficient computational schemes is mandatory for simulating such materials in a realistic way. Therefore, In Chapter 5 we propose/validate a ZnO with organics SCC-DFTB model.

In Chapter 6, we apply our SCC-DFTB model to a real problem – in collaboration with our experimental partners in the University of Bremen:

---

<sup>+++</sup> Non-polar surfaces are the dominant ones in ZnO nanostructures



the characterization of intrinsic defects in ZnO nanowires and the healing of surface defects with organic molecules.

Finally, Chapter 7 brings our concluding remarks and future perspectives.

www.pdftron.com

www.pdftron.com

pdftron

# Chapter 2

---

## Theoretical Background

*"I always thought writing was the foundation and the basis for journalism in the same way being able to draw is the foundation for art."*

*Bob Schieffer – American Journalist.*

In this chapter, we will outline the theoretical background of this work, with special emphasis given on the *Density Functional Theory* (DFT) – the main theoretical framework to be employed in the next Chapters. We will start introducing some basic aspects of *many-body Quantum problems* (Sections 2.1 and 2.2). After that, we will briefly discuss the *Hartree-Fock method* (Section 2.3), from where many important concepts used in DFT come. *Density Functional Theory* is presented in Section 2.4, with its exact formulation (i.e. the *Hohenberg-Kohn Theorems*) introduced in Section 2.4.1, and the *Kohn-Sham* formalism for solving electronic densities self-consistently in Section 2.4.2. *Exchange-correlation* functionals used the *Kohn-Sham* method are discussed in Section 2.4.3; whereas the use of *pseudopotentials* in practical DFT calculations is addressed in Section 2.4.4. Section 2.5 is dedicated to the calculation of atomic forces from electronic structure methods; and Section 2.6 describes the basic theory involved in the simulation of crystalline solids – including a discussion on the *Tight Binding* model and the presentation of the *Self-Consistent-Charge Density Functional based Tight Binding* method (SCC-DFTB). Finally, in Section 2.7 we make some comments on the basis sets used along this work.

### 2.1 – The Time-Independent Schrödinger Equation

Atoms, molecules, crystals and all other forms of matter which are considered in materials science are systems consisting of interacting nuclei and electrons. According to the first postulate of Quantum Mechanics, such systems are fully specified by a wave-function  $\Phi(\{r_i\}; \{R_n\}; t)$  – depending on the coordinates of all  $I$  electrons ( $\{r_i\}$ ), all  $N$  nuclei ( $\{R_n\}$ ) and time ( $t$ ) - which can be determined by solving the *Time-dependent Schrödinger Equation*:

$$i\hbar \frac{d\Phi(\{r_i\}; \{R_n\}; t)}{dt} = \hat{H} \Phi(\{r_i\}; \{R_n\}; t), \quad (2.1)$$

where  $\hat{H}$  corresponds to the system's total Hamilton operator.

Eq. 2.1 represents the fundamental physical law of a many-body quantum problem, but unfortunately its solution is too complicated to be managed in most cases. This point was spotted by *Dirac* early in 1929 [110]: “*The underlying physical laws necessary for the mathematical theory of a large part of physics and the whole of chemistry are thus completely known, and the difficulty is only that the exact application of these laws leads to equations much too complicated to be soluble. It therefore becomes desirable that approximate practical methods of applying quantum mechanics should be developed, which can lead to an explanation of the main features of complex atomic systems without too much computation*”. It is notable that more than 80 years later – after the advent of microelectronics and computer sciences – the words of *Dirac* are in great part still true. Even with the current computer power available, it is still very relevant developing approximate quantum methods and, furthermore, identifying particular cases where the general many-body problem can be simplified.

One important special case of the general quantum many-body problem is that of the conservative systems. In such systems, the  $\hat{H}$  operator can be represented as:

$$\begin{aligned} \hat{H} = & - \sum_{i=1}^I \frac{1}{2} \nabla_i^2 - \sum_{n=1}^N \frac{1}{2M_n} \nabla_n^2 - \sum_{i=1}^I \sum_{n=1}^N \frac{Z_n}{|r_i - R_n|} \\ & + \sum_{i=1}^I \sum_{j>i}^I \frac{1}{|r_i - r_j|} + \sum_{n=1}^N \sum_{l>n}^N \frac{Z_n Z_l}{|R_n - R_l|} \end{aligned} \quad (2.2)$$

where  $M_n$  and  $Z_n$  stand for the mass and charge of the  $n^{\text{th}}$  nucleus respectively.

As long as the  $\hat{H}$  operator does not depend explicitly on time, it is possible to simplify the Eq. 2.1 by assuming the Ansatz:

$$\Phi(\{r_i\}; \{R_n\}; t) = \Psi(\{r_i\}; \{R_n\}) f(t),$$

and proceeding with the following rearrangement:

$$\begin{aligned} \Psi(\{r_i\}; \{R_n\}) i\hbar \frac{df(t)}{dt} &= f(t) \hat{H} \Psi(\{r_i\}; \{R_n\}), \\ \frac{1}{f(t)} i\hbar \frac{df(t)}{dt} &= \frac{1}{\Psi(\{r_i\}; \{R_n\})} \hat{H} \Psi(\{r_i\}; \{R_n\}). \end{aligned} \quad (2.3)$$

Since the left side of Eq. 2.3 is only dependent on the time, and the right side only dependent on the coordinates of electrons and nuclei, both sides must be equal to a constant in order to maintain the equality true.

$$\frac{1}{f(t)} i\hbar \frac{df(t)}{dt} = \frac{1}{\Psi(\{r_i\}; \{R_n\})} \hat{H}\Psi(\{r_i\}; \{R_n\}) = E \quad (2.4)$$

So, each term in Eq. 2.3 can be solved independently with respect to the constant  $E$ . If we concentrate just on the time-independent term, a simple rearrangement of Eq. 2.4 leads us to the so-called *Time-independent Schrödinger Equation*:

$$\hat{H}\Psi(\{r_i\}; \{R_n\}) = E\Psi(\{r_i\}; \{R_n\}) \quad (2.5)$$

Eq. 2.5 has been considered to be the cornerstone of *Quantum Chemistry*. It shows that the problem of determining the wave-function of a given conservative quantum system – like atoms and molecules in their ground state – is reduced to an *eigenvalues* problem. In other words, it shows that stationary states of quantum systems assume discrete energy values. Besides, as  $\hat{H}$  is a *Hermitian* operator, all stationary states which are solutions of Eq. 2.5 must be orthogonal to each other.

Nevertheless, solving the *Time-independent Schrödinger Equation* it still far from being a trivial task; and performing some approximations is still necessary in order to make it tractable.

## 2.2 – The Born-Oppenheimer Approximation

The solution of the *Time-independent Schrödinger Equation* is greatly facilitated by assuming the so called *Born-Oppenheimer approximation*, which consists in factorizing the time-independent wave-function ( $\Psi(\{r_i\}; \{R_n\})$ ) into an electronic and a nuclear component:

$$\Psi(\{r_i\}; \{R_n\}) = \psi(\{r_i\}; \{R_n\})\chi(\{R_n\}).$$

or simply:

$$\Psi = \psi\chi \quad , \quad (2.6)$$

by omitting the spatial variables in order to simplify the notation.

The Ansatz 2.6 is justified by the fact that atomic nuclei are always 3-4 orders of magnitude heavier than electrons. Because of such mass differences, the movements of nuclei are much slower than the movements of electrons, allowing one to assume that the electrons adjust their positions “instantaneously” according to the nuclear positions. Conversely, the atomic nuclei can be considered to move in the average electric field produced by the electrons. Note that the electronic wave-function ( $\psi$ ) in the Ansatz 2.6 depends on both the electronic ( $\{r_i\}$ ) and nuclear ( $\{R_n\}$ ) coordinates. In other words, it means that  $\psi$  can be solved parametrically which respect to a given set of nuclear positions.

Thus, it is possible to separate the system's total energy in an electronic and a nuclear contribution, by substituting the Ansatz 2.6 into Eq. 2.5 and using the identity:

$$\langle \Psi | \hat{H} | \Psi \rangle = E \quad . \quad (2.7)$$

Thereby, Eq. 2.5 becomes:

$$\begin{aligned} \langle \Psi | \hat{H} | \Psi \rangle &= - \left\langle \chi \psi \left| \sum_{i=1}^I \frac{1}{2} \nabla_i^2 \right| \psi \chi \right\rangle - \left\langle \chi \psi \left| \sum_{n=1}^N \frac{1}{2M_n} \nabla_n^2 \right| \psi \chi \right\rangle - \left\langle \chi \psi \left| \sum_{i=1}^I \sum_{n=1}^N \frac{Z_n}{|r_i - R_n|} \right| \psi \chi \right\rangle \\ &\quad + \left\langle \chi \psi \left| \sum_{i=1}^I \sum_{j>i}^I \frac{1}{|r_i - r_j|} \right| \psi \chi \right\rangle + \left\langle \chi \psi \left| \sum_{n=1}^N \sum_{l>n}^N \frac{Z_n Z_l}{|R_n - R_l|} \right| \psi \chi \right\rangle \\ &= - \langle \chi | \chi \rangle \left\langle \psi \left| \sum_{i=1}^I \frac{1}{2} \nabla_i^2 \right| \psi \right\rangle - \langle \psi | \psi \rangle \left\langle \chi \left| \sum_{n=1}^N \frac{1}{2M_n} \nabla_n^2 \right| \chi \right\rangle - \langle \chi | \chi \rangle \left\langle \psi \left| \sum_{i=1}^I \sum_{n=1}^N \frac{Z_n}{|r_i - R_n|} \right| \psi \right\rangle \\ &\quad + \langle \chi | \chi \rangle \left\langle \psi \left| \sum_{i=1}^I \sum_{j>i}^I \frac{1}{|r_i - r_j|} \right| \psi \right\rangle + \langle \psi | \psi \rangle \left\langle \chi \left| \sum_{n=1}^N \sum_{l>n}^N \frac{Z_n Z_l}{|R_n - R_l|} \right| \chi \right\rangle. \end{aligned}$$

So:

$$\begin{aligned} \langle \Psi | \hat{H} | \Psi \rangle &= - \left\langle \psi \left| \sum_{i=1}^I \frac{1}{2} \nabla_i^2 \right| \psi \right\rangle - \left\langle \psi \left| \sum_{i=1}^I \sum_{n=1}^N \frac{Z_n}{|r_i - R_n|} \right| \psi \right\rangle + \left\langle \psi \left| \sum_{i=1}^I \sum_{j>i}^I \frac{1}{|r_i - r_j|} \right| \psi \right\rangle \\ &\quad - \left\langle \chi \left| \sum_{n=1}^N \frac{1}{2M_n} \nabla_n^2 \right| \chi \right\rangle + \left\langle \chi \left| \sum_{n=1}^N \sum_{l>n}^N \frac{Z_n Z_l}{|R_n - R_l|} \right| \chi \right\rangle = E. \quad (2.8) \end{aligned}$$

The first three terms on Eq. 2.8 depend exclusively on the electronic wavefunction ( $\psi$ ), whereas the last two depend exclusively on the nuclear wavefunction ( $\chi$ ). If we are not interested in rotational or vibrational motions, the nuclear kinetic energy operator – i.e. the 4<sup>th</sup> term on Eq. 2.8 – can be neglected, since the nuclear masses are much larger than the electronic ones. Besides, it is convenient solving  $\psi$  parametrically with respect to the nuclear positions; so Eq. 2.8 can be further approximated as:

$$E = \langle \psi | \hat{H}_{Elec} | \psi \rangle + \sum_{n=1}^N \sum_{l>n}^N \frac{Z_n Z_l}{|R_n - R_l|}, \quad (2.9)$$

with:

$$\hat{H}_{Elec} = - \sum_{i=1}^I \frac{1}{2} \nabla_i^2 - \sum_{i=1}^I \sum_{n=1}^N \frac{Z_n}{|r_i - R_n|} + \sum_{i=1}^I \sum_{j>i}^I \frac{1}{|r_i - r_j|}.$$

Hence, for a given geometry, the total energy of a polyatomic system can be calculated simply from its electronic wave-function  $\psi$  plus the classical *Coulomb* repulsion term associated with the atomic nuclei.

## 2.3 – The Hartree-Fock Approximation

As demonstrated in the last section, the *Born-Oppenheimer approximation* allows reducing the problem of calculating the system's *total* stationary wave-function  $\Psi$  into calculating “just” its stationary *electronic* wave-function  $\psi$ . In fact, calculating the electronic wave function of many-electron systems has long been the ultimate aim of *Quantum Chemistry*. Across the years, several methods have been developed for determining  $\psi$  on different *levels of theory* (i.e. levels of accuracy). However, most of these methods are based on the same original foundation: The *Hartree-Fock Theory*.

### 2.3.1 – The Form of the Wave-Function

The first basic approximation in the *Hartree-Fock Theory* – originally proposed by *D. Hartree* – is that the total electronic wave-function  $\psi$  of system with  $I$  electrons can be factorized into a product of  $I$  independent one-electron functions:

$$\psi_{HP}(1,2, \dots, I) = \phi_1(1)\phi_2(2) \dots \phi_I(I).$$

Briefly after its introduction, the so called *Hartree Product* was contested by *V. Fock* and *J.C. Slater*, since it satisfies neither the *Principle of Anti-symmetry* required for multi-fermionic wave-functions nor the *Pauli Exclusion Principle* [103]. *Slater* also demonstrated that both these limitations can be overcome by approximating the total  $I$ -electrons wave functions as an  $I$ -order determinant, whose elements are the  $I$  independent one-electron functions:

$$\psi_{SD}(1,2, \dots, I) = \frac{1}{\sqrt{I!}} \begin{vmatrix} \phi_1(1) & \phi_2(1) & \dots & \phi_I(1) \\ \phi_1(2) & \phi_2(2) & \dots & \phi_I(2) \\ \vdots & \vdots & & \vdots \\ \phi_1(I) & \phi_2(I) & \dots & \phi_I(I) \end{vmatrix} = \frac{1}{\sqrt{I!}} \begin{vmatrix} \phi_{11} & \phi_{21} & \dots & \phi_{I1} \\ \phi_{12} & \phi_{22} & \dots & \phi_{I2} \\ \vdots & \vdots & & \vdots \\ \phi_{1I} & \phi_{2I} & \dots & \phi_{II} \end{vmatrix}$$

$$\psi_{SD}(1,2, \dots, I) = \frac{1}{\sqrt{I!}} \sum_{p=0}^{(I!-1)} (-1)^p P(p) \phi_{11} \phi_{22} \dots \phi_{II}, \quad (2.10)$$

where the factor  $\sqrt{I!}^{-1}$  accounts to the normalization requirement and  $P$  represents a *Permutation operator*. Note that we assumed the 1<sup>st</sup> subscript on the one-electron functions to characterize the function itself, whereas the 2<sup>nd</sup> identifies the electron occupying it. Since its advent, the so-called *Slater*

*Determinant* became the method of choice for constructing anti-symmetric wave functions\*.

### 2.3.2 – The Hartree-Fock Equations

For a given set of atomic positions, the nuclear *Coulomb* repulsion in Eq. 2.8 is always constant and does not interfere with the solution of the electronic wave-function. Thus, we will concentrate just on the electronic Hamiltonian in Eq. 2.9, also dropping the subscript “Elec” from now on. So, the *electronic Schrödinger Equation* can be simply represented as:

$$\hat{H}|\psi\rangle = E|\psi\rangle . \quad (2.11)$$

Before going head, it is also convenient noting that the electronic Hamiltonian can be factorized into one-electron ( $\hat{H}_{1e}$ ) and two-electron ( $\hat{H}_{2e}$ ) operators:

$$\hat{H} = \hat{H}_{1e} + \hat{H}_{2e} = \overbrace{-\sum_{i=1}^I \frac{1}{2} \nabla_i^2 - \sum_{i=1}^I \sum_{n=1}^N \frac{Z_n}{|r_i - R_n|}}^{\hat{H}_{1e}} + \underbrace{\sum_{i=1}^I \sum_{j>i}^I \frac{1}{|r_i - r_j|}}_{\hat{H}_{2e}} .$$

By using the identity in Eq. 2.7 and representing the electronic wave-function as a single *Slater Determinant*, it is possible to rearrange Eq. 2.11 into:

$$E = \langle \psi_{SD} | \hat{H}_{1e} | \psi_{SD} \rangle + \langle \psi_{SD} | \hat{H}_{2e} | \psi_{SD} \rangle . \quad (2.12)$$

Both terms in Eq. 2.12 can be handled separately without prejudice in the final result. So, let’s look at the one-electron term at the first place. The operator  $\hat{H}_{1e}$  contains a summation over all  $I$  electrons in the systems, which means that it can be further factorized into single-electron components ( $\hat{H}_i$ ):

$$\langle \psi_{SD} | \hat{H}_{1e} | \psi_{SD} \rangle = \left\langle \psi_{SD} \left| \sum_{i=1}^I \hat{H}_i \right| \psi_{SD} \right\rangle = \langle \psi_{SD} | \hat{H}_1 + \hat{H}_2 + \dots + \hat{H}_I | \psi_{SD} \rangle$$

By applying the factorized form of  $\psi_{SD}$  (Eq. 2.10) to each single-electron ( $\hat{H}_i$ ) operator, it is not difficult to demonstrate that:

$$\langle \psi_{SD} | \hat{H}_i | \psi_{SD} \rangle = \sum_{j=1}^I \langle \phi_{ji} | \hat{H}_i | \phi_{ji} \rangle = \sum_{j=1}^I \left\langle \phi_{ji} \left| \frac{1}{2} \nabla_i^2 + \sum_{n=1}^N \frac{Z_n}{|r_i - R_n|} \right| \phi_{ji} \right\rangle = \sum_{j=1}^I H_{ij} , \quad (2.13)$$

or, generalizing for all  $I$  electrons, that:

---

\* Note that representing the total electronic wave-function as a single *Slater Determinant* is a strong approximation. In fact, high-level *Multi-configuration Methods* use linear combinations of different *Slater Determinants*.



$$\langle \psi_{SD} | \hat{H}_{1e} | \psi_{SD} \rangle = \sum_{i=1}^I \sum_{j=1}^I H_{ij}. \quad (2.14)$$

It is important to note that, as far as  $\hat{H}_i$  is a linear operator, it is also possible to rearrange Eq. 2.13 into:

$$\langle \psi_{SD} | \hat{H}_i | \psi_{SD} \rangle = \sum_{j=1}^I \langle \phi_{ji} | \hat{H}_i | \phi_{ji} \rangle = \langle \phi_{1i} + \phi_{2i} + \dots + \phi_{Ii} | \hat{H}_i | \phi_{1i} + \phi_{2i} + \dots + \phi_{Ii} \rangle, \quad (2.15)$$

which means that the *Slater Determinant* can be replaced by a simple linear combination of atomic basis as the solution of the single-electron Hamiltonian  $\hat{H}_i$ . In other words, the solution of a one-electron *Molecular Orbital* can be in principle constructed as a linear combination of atomic orbitals.

Now let us turn our attention to the  $\hat{H}_{2e}$  operator. Exactly as for the one-electron term in Eq. 2.12, the *Slater Determinant* (and its complex conjugated) in the two-electrons term can be also expanded to its factorized form. The result is a summation with  $I^2$  two-electrons integral terms for each considered electronic pair – since the *Slater Determinant* is composed of all  $I!$  permutations of the *Hartree Product*. Fortunately, most of these terms vanish, and only two kinds of two-electron integrals remain: The *Coulomb* and the *Exchange Integrals*. Before classifying each of them, it is convenient to introduce a shorter notation for the factorized form of the *Slater Determinant*:

$$\psi_{SD}(1, 2, \dots, I) = \frac{1}{\sqrt{I!}} \sum_{p=0}^{(I!)-1} \zeta_p,$$

where the functions  $\zeta$  represent the  $I!$  permutations of the *Hartree Product* with respect to the electronic occupancy (including their pre-factors  $(-1)^p$ ).

With this notation, the *Coulomb Integrals* ( $J$ ) can be defined as those assuming the form:

$$J_{ij} = \left\langle \zeta_p \left| \frac{1}{|r_i - r_j|} \right| \zeta_p \right\rangle = \left\langle \phi_{ii} \phi_{jj} \left| \frac{1}{|r_i - r_j|} \right| \phi_{ii} \phi_{jj} \right\rangle$$

where the term into the *bra-vector* is identical to that in the *ket-vector*. Note that the *bra* and the *ket* vectors also contain the same permutation pre-factor  $(-1)^p$ , which implies that  $J$  is always positive.

Yet the *Exchange Integrals* ( $K$ ) are those assuming the form:

$$K_{ij} = \left\langle P_{ij} \zeta_p \left| \frac{1}{|r_i - r_j|} \right| \zeta_p \right\rangle = - \left\langle \phi_{ij} \phi_{ji} \left| \frac{1}{|r_i - r_j|} \right| \phi_{ii} \phi_{jj} \right\rangle$$

Where  $P_{ij}$  is pairwise permutation operator, which exchanges the positions of the electrons  $i$  and  $j$  in  $\zeta_p$ . As the term in the *bra-vector* is always a single

permutation of the term in the *ket-vector*,  $K$  always assumes a negative value. With the help of some algebra<sup>†</sup> it is possible to demonstrate that:

$$\langle \psi_{SD} | \hat{H}_{2e} | \psi_{SD} \rangle = \sum_{i=0}^I \sum_{j=0}^I (2J_{ij} - K_{ij}),$$

and, consequently:

$$E = \sum_{i=1}^I \sum_{j=1}^I H_{ij} + \sum_{i=0}^I \sum_{j=0}^I (2J_{ij} - K_{ij}), \quad (2.16)$$

which is the desired form for the electronic energy expression in terms of the *Molecular Orbitals* for a single-determinant, closed shell wave-function.

Finally, from Eq. 2.16 it is possible to define a complete one-electron operator – usually called *Fock Operator*:

$$\hat{F}_i = \hat{H}_i + V_{HF}(i) = \hat{H}_i + \sum_{j=0}^I (2J_j - K_j) \quad (2.17)$$

where  $V_{HF}$  is the *effective Hartree Potential*. Note that the *Coulomb* and *Exchange* integrals contained in  $V_{HF}$  correspond just to an average electrostatic potentials – weighed via the electronic spatial probability distributions  $\phi_i^* \phi_i$  – and do not take any electronic correlation effect into account. For our discussion, the important result is that the *Fock Operator* is purely a one-electron operator; so that it is possible using it to determine the expected value of single electron energies:

$$\langle \psi_{SD} | \hat{F}_i | \psi_{SD} \rangle = \varepsilon_i. \quad (2.18)$$

Eq. 2.18 is useful because, as we have seen in Eq. 2.15, we can expand  $\psi_{SD}$  as a linear combination of atomic orbitals:

$$\varepsilon_i = \langle c_{1i}\phi_1 + c_{2i}\phi_2 + \dots c_{Ii}\phi_I | \hat{F}_i | c_{1i}\phi_1 + c_{2i}\phi_2 + \dots c_{Ii}\phi_I \rangle.$$

Thus, given a suitable set of *atomic basis*, the problem of finding  $\psi_{SD}$  reduces to discovering an appropriate set of linear combination coefficients ( $c_i$ ). It is necessary to remark that for all one-electron wave-functions, the expansion of the  $\psi_{SD}$  uses always the same basis, hence we will drop the index for the electronic occupation in  $\phi$ .

### 2.3.3 – The Variation Theorem and the Roothaan Equations

The *Variation Theorem* [112] of quantum mechanics can be enunciated as:

*Given a system whose the Hamiltonian is  $\hat{H}$ , whose lowest-energy eigenvalue is  $E$ ; and  $\psi$  is any well behaved eigenfunction of  $\hat{H}$  that satisfies the boundary conditions of the problem, then:*

---

<sup>†</sup> See references [103] (Chapter 3) and [111] (Appendix 7) for details.

$$\langle \psi | \hat{H} | \psi \rangle \geq E. \quad (2.19)$$

In other words, the *Variation Theorem* states that the “best”  $\psi$  is that which has the lowest-energy eigenvalue  $E$  as the expectation value.

Now, this result can be used to optimize  $\psi$ . As we have seen in the last section, the single *Slater Determinant wave-function* ( $\psi_{SD}$ ) can be decomposed into a linear combination of atomic orbitals as the input vector for the one-electron *Fock Operator*:

$$\varepsilon_i = \langle \psi_{SD} | \hat{F}_i | \psi_{SD} \rangle = \sum_{j=1}^I \sum_{k=1}^I c_{ji}^* c_{ki} \langle \phi_j | \hat{F}_i | \phi_k \rangle. \quad (2.20)$$

Hence, according to Eq. 2.19, what we need is finding the coefficients ( $c_{ij}$ ) which minimizes the one-electron energy  $\varepsilon_i$ . Additionally,  $\psi_{SD}$  has to be normalized; so the minimization must be subject to the constraint:

$$\langle \psi_{SD} | \psi_{SD} \rangle - 1 = \sum_{j=1}^I \sum_{k=1}^I c_{ji}^* c_{ki} \langle \phi_j | \phi_k \rangle - 1 = 0. \quad (2.21)$$

Fortunately, this problem can be managed via the *Lagrange's Multipliers* method. The method consists in finding the stationary points of a function – i.e. the points where the function is invariant to changes in its variables – which in principle can be minimal or maximal points. In the case of electronic energies, there is no upper limit, and any stationary point of Eq. 2.20 is necessarily a minimum point.

In order to perform the minimization, the first step is defining a functional of both the function to be minimized and the constraint identity. In our case, such functional becomes:

$$L = \sum_{j=1}^I \sum_{k=1}^I c_{ji}^* c_{ki} \langle \phi_j | \hat{F}_i | \phi_k \rangle - \varepsilon_i (\langle \psi_{SD} | \psi_{SD} \rangle - 1)$$

$$L = \sum_{j=1}^I \sum_{k=1}^I c_{ji}^* c_{ki} \langle \phi_j | \hat{F}_i | \phi_k \rangle - \varepsilon_i \left( \sum_{j=1}^I \sum_{k=1}^I c_{ji}^* c_{ki} \langle \phi_j | \phi_k \rangle - 1 \right) \quad (2.22)$$

In the definition of  $L$  we treat the one-electron energy  $\varepsilon_i$  as the *Lagrange's Multiplier* and the linear combination coefficients  $c_{ki}$  as independent variables. It is worthy to stress that, by definition:

$$L = \varepsilon_i = \langle \psi_{SD} | \hat{F}_i | \psi_{SD} \rangle,$$

so any stationary point for  $L$  is also a stationary point for  $\langle \psi_{SD} | \hat{F}_i | \psi_{SD} \rangle$ .

Besides, any stationary point of the functional  $L$  is characterized by the identity:

$$\nabla L = 0, \quad (2.23)$$

where  $\nabla L$  is:

$$\nabla L = \sum_{j=1}^I \frac{\partial}{\partial c_{ji}} \left[ c_{ji}^* \left( \sum_{k=1}^I c_{ki} \langle \phi_j | \hat{F}_i | \phi_k \rangle - \varepsilon_i \sum_{k=1}^I c_{ki} \langle \phi_j | \phi_k \rangle \right) + \text{complex conjugated} \right]. \quad (2.24)$$

As the coefficients  $c_{ji}$  are independent, the identity 2.23 only remains true in two cases: *i*) when all of them are zero (trivial solution) or *ii*) when all terms in round brackets – in Eq. 2.24 – and their conjugated complexes are simultaneously zero:

$$\sum_{k=1}^I c_{ki} \langle \phi_j | \hat{F}_i | \phi_k \rangle - \varepsilon_i \sum_{k=1}^I c_{ki} \langle \phi_j | \phi_k \rangle = 0. \quad (2.25)$$

So, by defining the *Fock Matrix element* ( $F$ ) and the *Overlap Matrix element* ( $S$ ) respectively as:

$$F_{ik} = \langle \phi_i | \hat{F}_i | \phi_k \rangle,$$

and:

$$S_{ik} = \langle \phi_i | \phi_k \rangle,$$

Eq. 2.25 can be rearranged into:

$$\sum_{k=1}^I F_{ik} c_k = \varepsilon_i \sum_{k=1}^I S_{ik} c_k,$$

and finally, by expanding it to all  $I$ -electrons, one finds the so-called *Roothaan Equations*:

$$\mathbf{F}\mathbf{c} = \boldsymbol{\varepsilon}\mathbf{S}\mathbf{c}, \quad (2.26),$$

where  $\mathbf{F}$  and  $\mathbf{S}$  are  $I \times I$  matrices containing all *Fock* and *Overlap Matrix elements* respectively,  $\mathbf{c}$  is the  $I \times I$  *Coefficients Matrix* and  $\boldsymbol{\varepsilon}$  is organized to be a diagonal matrix with all one-electron energies.

Since we have been assuming an *orthonormal basis set*, the *Overlap Matrix* reduces to the *Identity Matrix*, and Eq. 2.26 becomes:

$$\mathbf{F}\mathbf{c} = \boldsymbol{\varepsilon}\mathbf{c}. \quad (2.27)$$

Eq. 2.26 has the form of a generalized eigenvector problem. Thus, from  $\mathbf{F}$  and  $\boldsymbol{\epsilon}$ , it is relatively simple to find the *Coefficients Matrix*  $\mathbf{c}$ . Moreover, as  $\mathbf{F}$  is *Hermitian* and  $\boldsymbol{\epsilon}$  is real and arbitrarily arranged to be diagonal,  $\mathbf{c}$  must be a unitary matrix – i.e.  $\mathbf{c}^\top = \mathbf{c}^{-1}$  (see chapter 8 in [112]) – so the process of solving (2.27) for  $\mathbf{c}$  automatically leads to the diagonalization of  $\mathbf{F}$ .

### 2.3.4 – The Self-Consistent-Field Method

Finally it is necessary to remark that the *Roothaan Equations* are not linear, since the elements in the *Fock Matrix* depend explicitly on the coefficients  $c$  – via the  $J$  and  $K$  integrals (Eq. 2.17). Therefore, it has to be solved iteratively, in a procedure called *Self-Consistent-Field*.

The method consists in using a *trial* set of coefficients as input, in order to estimate the elements in the *Fock* ( $\mathbf{F}$ ) and *One-electron Eigenvalues* ( $\boldsymbol{\epsilon}$ ) matrices, and then solving the *Roothaan's Equation* for a new set of coefficients ( $\mathbf{c}$ ). With this new  $\mathbf{c}$ , it is possible to recalculate  $J$  and  $K$  for every element in  $\mathbf{F}$  and  $\boldsymbol{\epsilon}$ . Then,  $\mathbf{F}$  can be diagonalized again, once more leading to a new set of coefficients  $\mathbf{c}$ . The procedure is repeated until some pre-established convergence condition is satisfied; so ensuring that the final result fulfills the accuracy requirements of the calculation.

## 2.4 – Changing the Paradigm: Density Functional Theory

In the last sections we have seen how one can solve the many-electrons problem within the *Hartree-Fock* approximation. However, despite their obvious importance, all *Hartree-Fock* and *post-Hartree-Fock* methods – i.e. *Møller-Plesset Perturbation Theory*, *Configuration Interaction*, etc. – have one serious inconvenience: The electronic wave-function is a complex entity depending on the position and spin coordinates of all electrons in the system, which is very difficult to translate to a simple and intuitive physical model. Therefore, since the very beginning, there have been attempts of formulating the quantum many-body problem in terms of a simpler and physically meaningful variable: The *electronic density* ( $\rho$ ).

The use of the electronic density as central variable has at least three major advantages: *i)* it depends only on three spatial coordinates, *ii)* its distribution in polyatomic systems is somehow intuitive and *iii)* it can be experimentally measured in X-ray diffraction experiments. As mentioned before, the first endeavor towards an electronic density-based theory was the so called *Thomas-Fermi model* [113,114], where the electronic kinetic energy ( $T$ ) is approximated as a functional of the electronic density – assumed to be locally equal to that in a non-interacting homogeneous electron gas [105]. The original model has been subsequently extended by *Dirac* – the *Thomas-Fermi-Dirac model* – in order to take exchange effects into account<sup>‡</sup> [105]. Nevertheless, at that time there was no formal proof that the electronic density contains enough information to completely characterize a many-electrons quantum system. The proof came almost 40 years later, with the *first Hohenberg-Kohn Theorem*, which is considered today as the foundation of modern *Density Functional Theory*.

---

<sup>‡</sup> Today, the *Thomas-Fermi* and *Thomas-Fermi-Dirac* models have just an historical importance in the context of computational materials simulations. Therefore they will not be addressed in detail here.

## 2.4.1 – The Hohenberg-Kohn Theorems

According to *Koch and Holthausen* [115], the *Hohenberg-Kohn Theorems* represent “the major theoretical pillars on which all modern-day Density Functional Theories are erected”. They establish the basis for an exact many-body theory, which applies to any system of interacting particles under an external potential – inclusive to electrons around static nuclei (*Born-Oppenheimer Approximation*).

### 2.4.1.1 - The First Hohenberg-Kohn Theorem

The *first Hohenberg-Kohn Theorem* can be formulated as:

*The external potential  $V_{ex}(r)$  of a given many-particles system is entirely determined, within a trivial additive constant, by its ground-state particle density  $\rho^0(r)$ .*

Since the Hamiltonian of a many-electrons system is completely determined by its  $V_{ex}(r)$  – except for a rigid energy shift – all its *eigenfunctions*, for both ground and excited states, are fully determined by its  $\rho^0(r)$ . The demonstration of the *first Hohenberg-Kohn Theorem* is straightforward: Let us assume two Hamiltonians,  $\hat{H}^1$  and  $\hat{H}^2$ , which lead to the same ground state  $\rho^0(r)$ , and whose external potentials –  $V_{ex}^1(r)$  and  $V_{ex}^2(r)$  respectively – differ by more than a constant. Let us assume also that  $\psi^1$  and  $\psi^2$  characterize the ground states of  $\hat{H}^1$  and  $\hat{H}^2$  respectively. So, it follows that:

$$\langle \psi^1 | \hat{H}^1 | \psi^1 \rangle = E^1 < \langle \psi^2 | \hat{H}^1 | \psi^2 \rangle,$$

and:

$$\langle \psi^2 | \hat{H}^2 | \psi^2 \rangle = E^2 < \langle \psi^1 | \hat{H}^2 | \psi^1 \rangle.$$

The inequalities can be rewritten as:

$$\begin{aligned} E^1 &< \langle \psi^2 | \hat{H}^2 | \psi^2 \rangle + \langle \psi^2 | \hat{H}^1 - \hat{H}^2 | \psi^2 \rangle, \\ E^1 &< E^2 + \int \rho^0(r) [V_{ex}^1(r) - V_{ex}^2(r)] dr, \end{aligned} \quad (2.28)$$

and:

$$\begin{aligned} E^2 &< \langle \psi^1 | \hat{H}^1 | \psi^1 \rangle + \langle \psi^1 | \hat{H}^2 - \hat{H}^1 | \psi^1 \rangle, \\ E^2 &< E^1 - \int \rho^0(r) [V_{ex}^1(r) - V_{ex}^2(r)] dr, \end{aligned} \quad (2.29)$$

Note that integrals on Eq. 2.28 and 2.29 have the same form because  $\hat{H}^1$  and  $\hat{H}^2$  lead to the same  $\rho^0(r)$ . Finally, by adding Eq. 2.28 and 2.29 we find:

$$E^1 + E^2 < E^1 + E^2 \quad (2.30)$$

Thus, as Eq. 2.30 is absurd,  $\rho^0(r)$  must be a *bijective function*<sup>§</sup> of  $V_{ex}(r)$ .

#### 2.4.1.2 - The Second Hohenberg-Kohn Theorem

One of the consequences of the *first Hohenberg-Kohn Theorem* is that the ground state electronic density  $\rho^0(r)$  contains already the information of all possible wave-functions of a many-electrons system within a particular external potential  $V_{ex}(r)$ . Accordingly, all system's properties – including its total energy – can be represented as functionals of the electronic density; so that the problem now becomes finding the actual form of  $\rho^0(r)$ .

By writing the system's total energy as a functional of a *trial* electronic density  $\rho(r)$ :

$$E = E[\rho(r)],$$

it follows that – according to the *Variation Theorem*(Eq. 2.19):

$$\langle \psi^0 | \hat{H} | \psi^0 \rangle = E^0 \leq E = E[\rho(r)],$$

$$E^0 \leq E[\rho(r)], \quad (2.31)$$

Eq. 2.31 establishes the so called *second Hohenberg-Kohn Theorem*, which states that:

*Given a system with the electronic density  $\rho(r)$ , the ground state energy  $E^0$  corresponds to the global minimum of the total energy functional  $E[\rho(r)]$ , and the density  $\rho^0(r)$  which minimizes  $E[\rho(r)]$  is the exact ground state density.*

Accordingly, finding the ground state energy of a many-electron system corresponds to minimizing the total energy functional  $E[\rho(r)]$  subject to the constraint:

$$\int \rho(r) dr = I.$$

Here we can once more apply the *Lagrange's Multipliers* method by defining:

$$L = E[\rho(r)] - \mu \left( \int \rho(r) dr - I \right),$$

---

<sup>§</sup> If we are working within the Born-Oppenheimer approximation, the system's atomic positions are always given and the electronic density is solved according to it. In this case,  $\{V_{ex}^i(r)\}$  must be considered the functional *Domain* and  $\{\rho^i(r)\}$  the *Image*.

and observing that  $\delta L=0^{**}$  at any stationary point of  $L$ . Thus:

$$\begin{aligned}\delta L &= \delta E[\rho(r)] - \mu \delta \left( \int \rho(r) dr - I \right) = 0, \\ &= \delta E[\rho(r)] - \mu \delta \int \rho(r) dr = 0, \\ \therefore \quad \delta E[\rho(r)] &= \mu \delta I\end{aligned}\tag{2.32}$$

However, the quantity  $\delta I$  is defined as:

$$\delta I = \left( \frac{dI}{d\rho} \right)_{\rho^0} \delta \rho.$$

where :

$$\left( \frac{dI}{d\rho} \right)_{\rho^0} = \tau = \text{constant}.$$

Then, by incorporating  $\tau$  into  $\mu$ , Eq. 2.32 rearranges to its final form:

$$\frac{\delta E[\rho(r)]}{\delta \rho(r)} = \mu.\tag{2.33}$$

The *Lagrange Multiplier*  $\mu$  – usually referred as *Electronic Chemical Potential* – assumes a fundamental physical meaning. According to *Parr and Yang* [118], it “measures the escaping tendency of an electronic cloud. It is constant, through all space, for the ground state of an atom, molecule or solid, and equals to the  $E$  versus  $I$  curve at  $V_{ex}(r)$  constant.”

Note that Eq. 2.33 would be an exact expression for the ground-state electronic density if the form of  $E[\rho(r)]$  were known. Unfortunately, that is still not the case. Despite that, we can extract some valuable information by expanding  $E[\rho(r)]$  in:

$$E[\rho(r)] = T[\rho(r)] + E_{ee}[\rho(r)] + \int \rho(r) V_{ex}(r) dr,$$

where  $T$  is the *kinetic energy* functional and  $E_{ee}$  accounts for all *electron-electron* interactions. Alternatively,  $T$  and  $E_{ee}$  can be grouped into a unique functional:

$$E[\rho^0(r)] = F_{HK}[\rho(r)] + \int \rho(r) V_{ex}(r) dr.\tag{2.34}$$

---

\*\* In most texts, the minimization of the of the functional  $E[\rho(r)]$  is performed via *Calculus of Variations* instead of explicitly deriving the function  $L$ . Here we have preferred this approach in order to keep the coherence with the traditional DFT literature. Although using the *Calculus of Variations* is common in general physics, there might be some readers which are not quite familiar with the technique. For those included in this group, refs. [116] and [117] are suggested.



where  $F_{HK}[\rho(r)]$  is the so-called *Hohenberg-Kohn* Functional. Observe that  $F_{HK}[\rho(r)]$  does not depend on  $V_{ex}(r)$ , which means that it is a *universal functional*. In other words,  $F_{HK}[\rho(r)]$  must have the same form for all imaginable systems, no matter which external potential is experienced by the particles.

Starting from Eq. 2.34, it is also possible to demonstrate that:

$$\frac{\delta F_{HK}[\rho(r)]}{\delta \rho(r)} + V_{ex}(r) = \mu, \quad (2.35)$$

which is equivalent to Eq. 2.33. The demonstration of Eq. 2.35 is essentially the same as that for Eq. 2.33 – except for an intermediate step involving integration by parts – and therefore we will not repeat it here.

## 2.4.2 – The Kohn-Sham Equations

In the last sections, we have seen how the *Hohenberg-Kohn Theorems* allow formulating the quantum many-body theory in terms of functionals of the particles' density. Nevertheless, all the *Hohenberg-Kohn* formalism is based on unknown functionals, and solving Eq. 2.35 for the ground state density  $\rho^0(r)$  is not possible before they are properly defined. Indeed, defining functionals for complex systems – such as many interacting particles – is not a trivial task.

Therefore, in 1965, *Kohn and Sham* [119] have reformulated the DFT problem and created the most popular way to use Eq. 2.35 for realistic electronic structure simulations. The so-called *Kohn-Sham approach* is based on two simple assumptions [105] :

- i) The exact ground state density of an interacting particles system  $\rho^0(r)$  can be represented by the ground state density of an auxiliary system  $\rho_{KS}^0(r)$  composed by many non-interacting particles.
- ii) The auxiliary Hamiltonian is chosen to have the usual kinetic operator and an effective local potential  $V_{KS}$  acting individually on each electron in the system.

According to these statements, the *Kohn-Sham Hamiltonian* assumes the following form (in atomic units):

$$\hat{H}_{KS} = \frac{1}{2} \nabla^2 + V_{KS}. \quad (2.36)$$

By defining  $V_{KS}$  as a one-electron operator,  $\hat{H}_{KS}$  becomes mathematically similar to the *Fock-Operator* (Eq. 2.17). Now, if we assume the Ansatz<sup>††</sup>:

---

<sup>††</sup> The Ansatz 2.37 corresponds to representing the density integral  $\int \rho_{KS}^0(r) dr$  in terms of a single *Slater Determinant*  $\psi^{KS}$  (likewise in section 2.3.1, for the one-electron *Hartree-Fock* Hamiltonian). The functions  $\{\phi^{KS}\}$  corresponds to an appropriate basis set to represent the Kohn-Sham Orbitals.

$$\int \rho_{KS}^0(r) dr = \langle \psi^{KS} | \psi^{KS} \rangle = \sum_{i=1}^I \sum_{j=1}^I c_i^* c_j \langle \phi_i^{KS} | \phi_j^{KS} \rangle = I, \quad (2.37)$$

we can rewrite the *second Hohenberg-Kohn Theorem* as:

$$E^0 \leq \langle \psi^{KS} | \hat{H}_{KS} | \psi^{KS} \rangle = E[\rho^0(r)].$$

Hence, the problem of finding  $\rho_{KS}^0(r)$  - and  $\rho^0(r)$  consequently - reduces to minimizing  $\langle \psi^{KS} | \hat{H}_{KS} | \psi^{KS} \rangle$  subject to:

$$\langle \psi^{KS} | \psi^{KS} \rangle = \sum_{i=1}^I \sum_{j=1}^I c_i^* c_j \langle \phi_i^{KS} | \phi_j^{KS} \rangle = I.$$

Observe that, in the end, we have the same mathematical problem described in section 2.3.3 for the *Hartree-Fock* case; which consequently yields similar set of *Roothaan Equations* after the minimization via *Lagrange Multipliers* - the so-called *Kohn-Sham Equations*:

$$\mathbf{Hc} = \epsilon \mathbf{Sc}, \quad (2.38)$$

where the elements of the *Kohn-Sham Matrix* ( $H_{ij}$ ) are defined as:

$$H_{ij} = c_i^* c_j \langle \phi_i | \hat{H}^{KS} | \phi_j \rangle.$$

Thus, exactly as in the *Hartree-Fock* theory, we can start from a trial set of *Kohn-Sham orbitals* and use the same *Self-Consistent-Field* procedure - as described in section 2.3.4 - in order to obtain  $\rho^0(r)$  and  $E^0$ . In the end of the process, the ground state energy is the sum over the energies of all optimized *Kohn-Sham orbitals*.

It is interesting to remark that there has been much skepticism on using *Kohn-Sham orbitals* in order to interpret chemical processes [119], since they have been long considered as nothing else than an artifice to derive electronic densities in a self-consistent fashion. However, it has been already demonstrated that the form and symmetry of the *Kohn-Sham orbitals* agree very well with those from the *Hartree-Fock theory* or from the *extended Hückel model* [120]. Besides, *Kohn-Sham eigenvalues* have been found to be consistent with the Koopmans theorem after some rescaling [120], confirming that they constitute a reliable basis for qualitative molecular orbital analyses [121,122].

#### 2.4.2.1 - The Kohn-Sham Effective Potential

Although the *Kohn-Sham* equations provide a systematic way to calculate the ground state electronic densities, we still have to define an appropriate  $V_{KS}$  in order to calculate the elements of the *Kohn-Sham Matrix*. Generically,  $V_{KS}$  can be represented as:

$$V_{KS} = V_{ex}[\rho_{KS}(r)] + V_H[\rho_{KS}(r)] + XC[\rho_{KS}(r)]$$

where  $V_{ex}[\rho_{KS}(r)]$  is a functional for the *Coulomb energy* between the electrons and the external potential  $V_{ex}(r)$ :

$$V_{ex}[\rho_{KS}(r)] = \int V_{ex}(r) dr,$$

$V_H[\rho_{KS}(r)]$  is the *Hartree energy functional*:

$$V_H[\rho_{KS}(r)] = \frac{1}{2} \int \frac{\rho_{KS}(r')}{|r - r'|} dr'.$$

accounting to *electron-electron repulsions*, and  $XC[\rho_{KS}(r)]$  is the so-called *Exchange-Correlation Functional*.

The physical meaning of  $V_{ex}[\rho_{KS}(r)]$  needs no further discussion at this point; but there are some important remarks on the  $V_H[\rho_{KS}(r)]$  and  $XC[\rho_{KS}(r)]$ . According to its definition, the functional  $V_H[\rho_{KS}(r)]$  gives the interaction energy of  $\rho_{KS}(r)$  with its own electrostatic field. This *mean-field* approximation is assumed for the sake of computational convenience; but unfortunately it generates a spurious *self-interaction energy* [105, 115]. To check this fact, it is enough to observe that the *Hartree Functional* gives a non-vanishing repulsion energy even for a system with only one electron. In the *Hartree-Fock theory*, this effect is automatically canceled by the *exchange integrals* – which always appear as a stabilizing term in the *Fock Operator* – but the same is not true in the *Kohn-Sham* scheme, where any correction must be incorporated into the *XC* functional – which will be discussed below.

### 2.4.3 – Exchange-Correlation Functionals

As its name already suggests, the *XC* functional must account not only for the *self-interaction* correction but also for the electronic correlation energies. The problem at this point is: the exact form of the *XC* still remains unknown. Several approximated *XC* functionals have been developed during the years. In general, such functionals are parametrized against high-level quantum chemical methods, which is often seen as a weak spot in an otherwise “pure *ab initio*” theory. On the other hand – from a more pragmatic perspective – approximated *XC* functionals give the flexibility necessary to perform small *ad hoc* corrections at a relatively modest computational price. In the words of *Koch and Holthausen* [115], the *XC* functional of DFT became “*a kind of junkyard where everything is stowed away which we do not know how to handle exactly*”. With that said, it is clear that the understanding the approximations included in the existing *XC* functionals is of capital importance. Therefore, we will take a closer look at the most accepted *XC* schemes.

#### 2.4.3.1 – Local Density Approximation

The first successfully *EX* scheme in DFT was the so-called *Local Density Approximation* (LDA), which has been already sketched by *Kohn* and *Sham* early in 1965 [119]. The idea is considering that the electrons of a given system can be treated – in the limit – as *homogeneous electron gas*, where all *XC* effects are strictly local [105,115,118]. The model also assumes that the *XC* functional can

be split in two independent terms, one for the exchange and one for the correlation energies respectively:

$$XC[\rho_{KS}(r)] = V_X[\rho_{KS}(r)] + V_C[\rho_{KS}(r)],$$

so that the XC energy ( $E_{XC}$ ) can be simply computed by:

$$E_{XC} = \int \rho_{KS}(r) V_X[\rho_{KS}(r)] dr + \int \rho_{KS}(r) V_C[\rho_{KS}(r)] dr.$$

The motivation behind these assumptions is that, for a *homogeneous electron gas*, the form of the  $V_X[\rho_{KS}(r)]$  functional is known from the *Thomas-Fermi-Dirac Model* [118]:

$$V_X[\rho_{KS}(r)] = -\frac{3}{4} \left( \frac{3\rho_{KS}(r)}{\pi} \right)^{\frac{1}{3}}. \quad (2.39)$$

which means that – within the LDA – the exchanged energy can be computed exactly.

Concerning on the functional  $V_C[\rho_{KS}(r)]$ , unfortunately there is no such analytical expression defining its form. Nevertheless, an alternative solution arose from the work of *Ceperley and Alder* [123], who have calculated the correlation energy for a *homogeneous electron gas* with great accuracy by using sophisticated *Quantum Monte-Carlo* simulations. Since then, several expressions for  $V_C[\rho_{KS}(r)]$  have been proposed from interpolations of the *Ceperley and Alder's* results. Among them, the most widely used is probably is the one parametrized by *Zunger and Perdew* [124].

For systems like infinite *nearly-free-electron metals* – where the electronic density is essentially uniform – the LDA approach works considerably well in predicting atomistic structures and charge moments. On the other hand, it may dramatically fail for systems such as atoms, molecules and surfaces, where the electronic density decays uniformly outside the system's boundaries. That is because of the form of the LDA  $V_X[\rho_{KS}(r)]$  functional, which always creates a spherical *Fermi hole* centered at the reference electron – no matter where it is. It may be a very a good approximation while considering uniform electron distributions, but indeed does not correspond to the right physical picture if electronic gradients are involved. In non-uniform electronic distributions, *Fermi holes* should vanish in very-low-density regions. Because of this shortcoming, LDA functionals strongly overestimate cohesive properties, thereby reducing its applicability in cases where free-atoms, molecules or surfaces must be taken into account.

### 2.4.3.2 – The Generalized Gradient Approximation

From the discussion above, it is not difficult to intuit that correcting the LDA shortcomings necessarily involves including density gradients in the formulation of XC functionals. However, several attempts to do so have demonstrated that there is no simple and systematic way of accomplishing this task. Instead,

developing improved  $XC$  functionals has been always involving a strong *trial-and-error* character. Currently, there are several different  $XC$  functionals designed to take density gradients into account. Nevertheless, the formulation of a functional is not straightforward, usually involving a considerable amount of algebra and physical intuition. Therefore, here we will refrain from giving details on the derivation of specific functionals, favoring just a brief overview on the general features of gradient corrected functionals.

The first attempt to incorporate gradient effects to  $XC$  functionals was made by interpreting the LDA as the first order term of the Taylor expansion of the exact  $XC[\rho(r)]$  with respect to the electronic density. Consequently, the first logical step towards an improved functional would be incorporating the higher orders of the expansion. Written up to the second order term, the  $XC$  assumes the form of the so-called *Gradient Expansion Approximation* (GEA):

$$E_{XC}[\rho(r)] = E_{XC}^{LDA}[\rho(r)] + \int C_{XC}[\rho(r)] \times \frac{\nabla\rho(r)^2}{\rho(r)^{\frac{4}{3}}} dr , \quad (2.40)$$

where  $C_{XC}$  represents the Taylor expansion coefficient<sup>##</sup>.

However – despite considering the density gradient explicitly – the GEA performs even worse than the LDA. To understand the reason behind such unexpected failure, it is useful to go back to the work of *Gunnarsson and Lundqvist* [126], who interpreted  $E_{XC}[\rho(r)]$  as the electrostatic interaction of each electron of the system with its own  $XC$  hole; so that it can be represented (in atomic units) as:

$$E_{XC}[\rho(r)] = \int \rho(r) dr \int \eta_{XC}(r, r + u) du, \quad (2.41)$$

where  $\eta_{XC}$  is the density of the  $XC$  hole and  $u$  its distance from the reference electron. Still according to *Gunnarsson and Lundqvist*, Eq. 2.41 requires that  $\eta_{XC}$  satisfies the *summing rule*:

$$\int \eta_{XC}(r, r + u) du = -1, \quad (2.42)$$

or in other words, that the  $XC$  hole must contain exactly one *fundamental charge*.

Given that, *Langreth and Perdew* have showed that the GEA hole – which is rather a truncated expansion, instead of an exact formulation for the real hole – violates Eq. 2.42 [127], whereas LDA doesn't [127,128]. Besides, GEA also

---

<sup>##</sup> Note that in most texts, Eq. 2.40 is explicitly expressed in terms of spin dependent densities. However, we have avoided explicitly denoting spin dependencies until now, assuming that different spin orbitals are simply different functions. Therefore – following the example of ref. [125] – we have also preferred skipping the spin notation in Eq. 2.40 in order to keep the consistence with our own notation. Nevertheless, it should be noted that – rigorously – the spins must be taken into account while setting practical applications of Eq. 2.40, since *exchange Integrals* are non-null only if the orbitals involved have the same spin part.

violates other desirable  $XC$  functional boundaries, such as the *negativity condition* and the *Kato's cusp condition* [115], which all together has been often considered the reason why LDA in fact yields better results than GEA.

In part, such failures of the GEA model are related to its spurious behavior for *holes* far from the reference electron (i.e. large  $u$  values) [127-129]. But on the other hand, it has been also demonstrated that the GEA improves the LDA results when the  $XC$  hole is close enough to the reference electron [127-129]. Because of this property, it is possible correcting the GEA functional by simply cutting off its spurious long-range part and fitting its short-range contributions to some arbitrary analytical function ( $F_{XC}$ ), which can be specially chosen in order to satisfy some pre-determined functional boundaries – i.e. the *summing rule* in Eq. 2.41, the *negativity condition*, etc. In the end, the quality of the corrected functional is not evaluated based on its mathematical form, but on how its results compare with either experiments or higher level *ab initio* calculations. This very pragmatic philosophy for constructing  $XC$  functionals is what constitutes the so-called *Generalized Gradient Approximation* (GGA), whose generic functional form is expressed as:

$$E_{XC}^{GGA}[\rho(r)] = \int F_{XC}[\rho(r), \nabla\rho(r)] dr$$

Along the years, several forms have been proposed for  $F_{XC}$ , in general splitting it in an exchange and a correlation parts. Preeminent examples of GGA functionals are the *Becke* [130](exchange) and *Perdew* [131] (correlation) (BP), *Becke* (exchange) and *Lee-Yang-Parr* [132](correlation) (BLYP), *Parr and Wang*[133] (PW91) and the *Parr-Burke-Ernzerhof* [133](PBE) functionals. Despite they have been often classified as “*non-local*” or “*semi-local*” functionals in the literature, it is necessary to emphasize that all GGA functionals have only  $\rho(r)$  and  $\nabla\rho(r)$  as their functional domains, being completely independent of electronic densities and gradients anywhere else than the reference positions  $r$  – i.e. there is no explicit dependence on  $\rho(r')$  and  $\nabla\rho(r')$ . Hence, all GGA functionals are strictly *local*; and classifying them as *non-local* or *semi-local* constitutes a misleading nomenclature [115]. In the conventional DFT calculations along this work we have employed the PBE functional, which is known for describing geometries and cohesive properties of solids and molecules with very good accuracies<sup>§§</sup>.

### 2.4.3.3 – The Band Gap Problem

One serious limitation of the LDA/GGA functionals is their inability of predicting correct *band gap energies*<sup>\*\*\*</sup> ( $E_g$ ) in semiconductors and isolators, which are systematically underestimated in such conventional DFT calculations. This deficiency is particularly important in the context of this work, since ZnO is

---

<sup>§§</sup> Molecular atomization energies can be calculated within mean average errors of 0.3 eV with PBE, whereas LDA and HF calculations give 1.3 eV and 3.1 eV respectively [133].

<sup>\*\*\*</sup> The band gap energy of a given system is formally defined as the difference between the *Ionization Potential* and the *Electron Affinity*. If the system's electrons are approximated as non-interacting particles, the band gap energy reduces to the difference between the highest-occupied and lowest-unoccupied molecular orbitals (HOMO and LUMO respectively).

strongly affected by the so-called *Band Gap Problem* (BGP). Experimentally, the ZnO  $E_g$  is  $\sim 3.3$  eV, whereas PBE predicts  $\sim 0.8$  eV. Also particularly critical is the case of the semiconductor germanium, which is found to be a metal in LDA/GGA calculations.

Historically, several reasons have been appointed to explain the BGP, with some authors – including Sham [134] – even suggesting that it is intrinsic to the DFT formalism itself [134-136]. Despite that, it is consensual that the problem comes from the use of approximated local *XC* functionals. In a recent work [137], Wang *et al* demonstrated that the electronic chemical potentials assume a convex form while using LDA/GGA functionals; resulting in over-delocalized states and consequently to the underestimation of the gap energy. In fact, quasi-particles band structures calculated through the *GW* method – where the many-body problem is handled via the *Green Functions* formalism – are not influenced by the BGP [138], but such calculations are still too demanding to be applied even to modest size models.

One widely used alternative to overcome the DFT gap problem is mixing some *Hartree-Fock Exchange* into the LDA/GGA-*XC* functional; thereby producing a *hybrid functional*. The success of *hybrid functionals* in correcting the BGP is often attributed to the fact that the *HF Exchange* is an exact functional [115]. However, there is some controversy about this statement. As emphasized by Wang *et al* [137], the *HF Exchange* produces a concave behavior on electronic chemical potentials – opposing the LDA/GGA case – thereby inducing over-localized electronic states. So, a suitable balance between LDA/GGA and HF amount in the hybrid *XC* functional may lead to a useful cancelation of errors; and to correct gap energies consequently. Still, hybrid functional-based calculations are also computationally very expensive.

A more computationally efficient alternative to overcome the BGP is correcting the DFT *Coulomb* interactions through the so-called *LDA+U* method [139]. In its most popular implementation – the *Dudarev's rotationally invariant method* [140] – the *LDA+U* approach consists in applying a penalty function to disfavor partial occupations on specific orbitals:

$$E^{LDA+U}[\rho(r)] = E^{LDA}[\rho(r)] + \sum_m \frac{(U_m - J_m)}{2} (n_m - n_m^2),$$

where  $U$  and  $J$  are the orbital dependent *Hubbard* and *exchange parameters* respectively, and  $n_m$  is the occupation number of the orbital  $m$  – note that the penalty function vanishes if  $n_m = 1$ . This method has been often used to calculate ZnO electronic properties, generally reaching improved  $E_g$  values, varying from  $\sim 1.5$  to  $\sim 3.7$  eV depending to the  $U$  and  $J$  parameters employed [141-144].

The *LDA+U* method will be employed in Chapter 4, in order to calculate the electronic properties of functionalized ZnO surfaces.

#### 2.4.4 – The Pseudo Potential Method

Up till now, our discussion on the electronic many-body problem has been made with all electrons in the system being considered explicitly.

However, it is well known that only *valence shell electrons* are active in chemical processes, with *core electrons* being insensitive to the changes in the external environment. Given that, a very reasonable way of speeding up quantum simulations is substituting the inner-shells electrons in the system by effective atomic *pseudopotentials*. By definition, a *pseudopotential* is a function designed to mimic the effect of *core electrons* on the valence shell of a certain atom. So, by using appropriate *pseudopotentials* it is possible to reduce the computational size of electronic structure simulations while keeping the accuracy of all-electrons calculations.

Currently, most *pseudopotentials* used in electronic structure simulations are generated from all-electron atomic calculations. Since such *pseudopotentials* are not fitted according to any kind of experimental data, they are also called *ab initio pseudopotentials*. In order to construct suitable *pseudopotentials*, there are some primary conditions which must be satisfied:

- i) *All-electrons and pseudo-valence eigenvalues must agree for the chosen reference atomic configuration:*

$$\varepsilon_i^{PS} = \varepsilon_i$$

- ii) *All-electrons and pseudo-valence wave-functions agree beyond a chosen cutoff core radius  $R_c$ .*
- iii) *The logarithmic derivative of all-electrons and pseudo-valence wave functions must agree at  $R_c$ .*
- iv) *The integrated charge inside  $R_c$  must be the same for both all-electrons and pseudopotential calculations.*

Conditions *i)* and *ii)* ensures that the pseudopotential reproduces the atomic potential outside the cutoff radius. Condition *iii)* that the pseudo potential is smooth and condition *iv)* that the charge inside  $R_c$  is correct and that the pseudo-orbitals are equal to the true orbitals outside  $R_c$ . Altogether, these four conditions ensure that the pseudopotential is able to reproduce the *core electrons* it is supposed to replace, which is essential for accuracy and transferability purposes. The pseudopotential which satisfies all these four conditions are classified as *norm-conserving*.

In this work, we have used norm-conserving pseudopotentials generated with the Troullier-Martins protocol [145], as implemented in the ATOM program – distributed with the SIESTA package [146]. For the Zn pseudopotential, the *3d* electrons have been included into the valence shell, since it is known such orbitals hybridize with the oxygen *2p* orbitals in ZnO. Table 2.1 brings the reference atomic configuration used for all pseudopotentials in this work.



**Table 2.1** – Reference atomic configurations for the pseudo-atoms used in this work.  $R_c s$ ,  $R_c p$  and  $R_c d$  denote the cutoff radius for the s, p and d pseudopotential components respectively.

Atom	Reference Configuration	$R_c s$ (Å)	$R_c p$ (Å)	$R_c d$ (Å)
H	$1s^1 1p^0$	0.66	0.66	0.66
C	$2s^2 2p^4 3d^0$	0.66	0.66	0.66
N	$2s^2 2p^5 3d^0$	0.66	0.66	0.66
O	$2s^2 2p^4 3d^0$	0.60	0.60	0.60
S	$3s^2 3p^4 3d^0$	0.79	0.89	0.89
Zn	$3d^{10} 4s^2 4p^0$	1.06	1.20	0.91

## 2.5 – Equilibrium Configurations and Atomic Forces

In sections 2.3 and 2.4 we have discussed the two most traditional approaches to the quantum electronic many-body problem: the *Hartree-Fock* model and the *Density Functional Theory*. In both cases, the electronic structure problem is solved within the *Born-Oppenheimer approximation* – i.e. with the nuclear wave-function  $\chi$  decoupled from the electronic wave-function  $\psi$  (Section 2.2). In other words, the electronic many-body problem can, in principle, be solved for any specified atomic geometry, no matter whether it is physically meaningful one or not.

Of course, one of the ultimate aims of Quantum simulations is exactly predicting equilibrium atomic configurations of molecules and solids. So, in practice, what one has to do is sampling the system’s potential energy surface in order to identify its minimum. Roughly speaking, the most efficient way to perform such *geometry optimization* is: *i)* starting from a reasonable trial configuration, *ii)* calculating the forces on each atomic site in the system, *iii)* using these forces to move the atoms accordingly, and finally *iv)* repeating the whole procedure until the all forces in the system become smaller than a given tolerance criteria.

In electronic structure simulations, atomic forces can be calculated via the so called *Hellman-Feynman theorem* [147], which states that the force acting on a nucleus  $n$  is equal to the total energy derivative with respect to the position of  $n$ :

$$F_n = \frac{\partial E}{\partial R_n} = \int \rho(r) \frac{\partial V_{ex}(r)}{\partial R_n} dr + \frac{\partial E_{Nucl.}}{\partial R_n}, \quad (2.43)$$

where,

$$E_{Nucl.} = \sum_{n=1}^N \sum_{l>j}^N \frac{Z_n Z_l}{|R_n - R_l|}$$

It is important to remark that, in calculations using localized basis-sets, the bases are tight to the atomic positions. Consequently, the atomic shifts necessary

to compute the energy gradients in 2.43 induces small changes in the systems wave-function, thereby introducing errors in the forces. Fortunately, Eq. 2.43 can be corrected by the introduction of the so-called *Pulay Forces* [148,149](expressed according to the Kohn-Sham formalism):

$$F_N^{Pulay} = 2 \int \frac{\partial \psi'^{KS*}}{\partial R_N} (\hat{H}'_{KS} - E_{KS}) \psi'^{KS} dr,$$

where  $E_{KS}$  is the Kohn-Sham energy for the unperturbed reference system,  $\psi'^{KS}$  is the *Kohn-Sham wave-function* for the perturbed system and  $\hat{H}'_{KS}$  is *Kohn-Sham Hamiltonian* for the perturbed system. Note that the *Pulay Forces* vanish when the perturbed and unperturbed *Hamiltonians* are equal.

## 2.6 – Modeling Crystalline Solids

Crystals<sup>†††</sup> can simply be defined as periodic arrays of atoms, where the general structure corresponds to the tridimensional repetition of a smaller structural unit – i.e. a *cell* – which is invariant to translational symmetry operations.

Mathematically, a three-dimensional periodic crystal is formed by the combination of two distinct components: *i) a Bravais lattice* and *ii) a basis*.

A *Bravais lattice* is an infinite array of points formed by all possible position vectors ( $\mathbf{R}$ ) with the form:

$$\mathbf{R}(n_a, n_b, n_c) = n_a \mathbf{a} + n_b \mathbf{b} + n_c \mathbf{c} \quad (2.45)$$

where  $\mathbf{a}$ ,  $\mathbf{b}$  and  $\mathbf{c}$  are non-simultaneously coplanar *primitive lattice vectors* and  $n_a$ ,  $n_b$  and  $n_c$  are arbitrary integers. Note that the *Bravais lattice* is only a mathematical abstraction which summarizes the underlying geometry of a periodic structure, regardless what the actual repetition unit is.

Yet the *basis* can be defined as the *minimal set of atoms* that, when replicated along all possible lattice points, gives origin to the actual *crystal structure* (Figure 2.1). Because the lattice points are not physical entities, the basis can be defined at any position within the lattice, without changing the final *crystal structure*.

It is important to remark that in reality there is no infinite crystal. Instead, crystals are always limited in size, being surrounded by real surfaces. Additionally, thermal fluctuations constantly induce changes in the relative atomic positions; and there are always defects to break the crystal's perfect symmetry. Despite of that, the vast majority of the atoms in real crystals are too far away from surfaces and defects to be affected by them, and thermal

---

<sup>†††</sup> According to the *International Union of Crystallography* (IUCr), a crystal is classified as a materials which has an “*essentially sharp diffraction pattern*”[150]. This definition has substituted the classical definition of crystals – i.e. periodic arrays of atoms – in order to incorporate the so-called *quasicrystals* (i.e. structures who have well defined diffraction patterns although they are not strictly periodic in the direct space). Nevertheless, as we will not address any *quasicrystal* in this work, we will keep assuming the old crystal definition for the sake of simplicity.

fluctuations usually have only marginal effects – if any – on the fundamental electronic levels. Therefore, assuming the crystal structure as the infinite repetition of an atomic basis along *Bravais lattices* can be considered a very good approximation to real periodic crystals. In solid-state simulations, this approximation is conventionally referred to the use of *Periodic Boundary Conditions*.

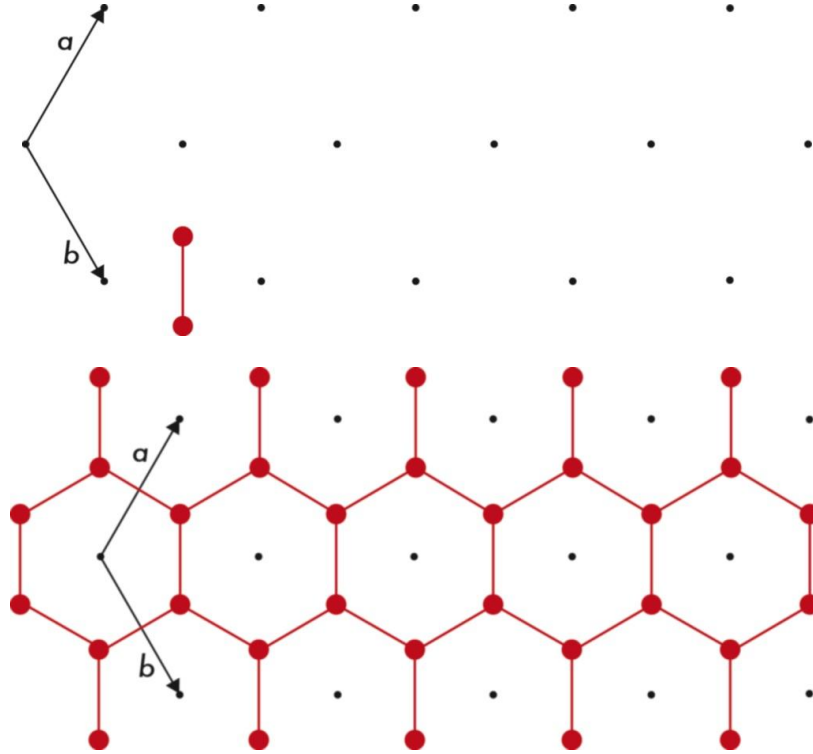


**Figure 2.1** – Representation of the Lattice vectors, lattice points and the atomic basis (top) of a bi-dimensional crystal (bottom).

### 2.6.1 – The Reciprocal Lattice

Fundamental to the analysis of periodical systems, the *reciprocal lattice* can be defined as “the set of all wave-vectors ( $\mathbf{k}$ ) that yields plane-waves with the periodicity of a given Bravais lattice” [151]. Mathematically, this definition can be expressed as:

$$e^{i\mathbf{k}\cdot(\mathbf{r}+\mathbf{R})} = e^{i\mathbf{k}\cdot\mathbf{r}},$$

which must hold true for any reference position  $\mathbf{r}$  and for any *Bravais position vector*  $\mathbf{R}$ . Some more information on  $\mathbf{k}$  can be obtained by simply factoring out the right-hand term above, so that we have:

$$e^{i\mathbf{k}\cdot\mathbf{R}} = 1, \tag{2.46}$$

which implies that:

$$\mathbf{k} \cdot \mathbf{R} = 2\pi \times \text{Integer}. \tag{2.47}$$

Now, if we expand the wave-vector  $\mathbf{k}$  in terms of any three non-simultaneously coplanar vectors:

$$\mathbf{k}(k_j, k_l, k_m) = k_j \mathbf{j} + k_l \mathbf{l} + k_m \mathbf{m}$$

we find that Eq. 2.47 only holds true if the coefficients  $k_j$ ,  $k_l$  and  $k_m$  are integers. In other words, the set of all possible wave vectors  $\mathbf{k}$  which satisfies Eq. 2.46 also corresponds to a *Bravais lattice* itself. Moreover, it can be also demonstrated that there is a mutual correspondence between any *Bravais lattice* and its reciprocal.

## 2.6.2 – The Wigner-Seitz Cell and The First Brillouin Zone

For a given *Bravais lattice*, it is possible to define a *unit cell* as the volume that fills all the *lattice space* – without overlapping with its neighbors or leaving voids – when translated to all possible *lattice points*. According to this definition, there are infinite ways of choosing *unit cells* for a given *Bravais lattice*; with the only constraint being that each *unit cell* must contain only one *lattice point*. Nevertheless, there is one case where all points inside the unit cell are closer to its own lattice point than to any of its translations along the lattice. For a *Bravais lattice* in the *direct space* – i.e. not in the *reciprocal space* – this special *unit cell* construction is called *Wigner-Seitz cell* (WS).

Because of the mutual correspondence between any *Bravais lattice* and its *reciprocal lattice*, there is also a unit cell which corresponds to the WS in the *reciprocal space*, which is called *First Brillouin Zone* (BZ). An important property of WSs and BZs is that they hold exactly the same symmetry properties of their respective *Bravais lattices* – in the direct and reciprocal space respectively.

As we will see in the next sections, important properties of crystals have to be integrated within the BZ – such as the total electronic energy and the density of states (DOS). The graphical representation of the BZ for a hexagonal lattice – the one in the wurtzite ZnO structure – and its high-symmetrical lines is given in Figure 2.3.

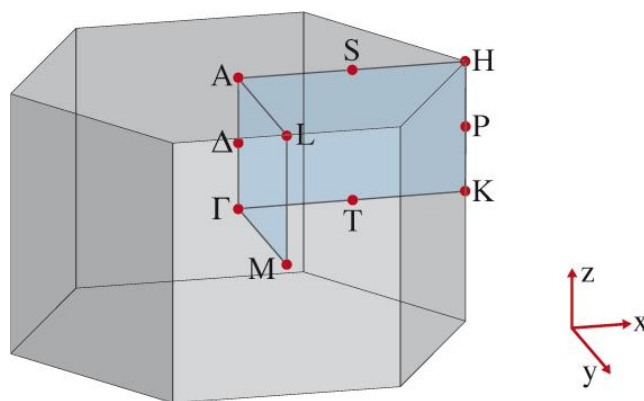


**Figure 2.3** – *First Brillouin Zone* for hexagonal lattices and its highly symmetrical points.

### 2.6.3 – The Bloch Theorem

Given that a crystal is a periodic array of atoms or ions, the external potential experienced by their electrons also must be a periodic function – with the same periodicity of the *Bravais lattice* underlying the system:

$$V_{ex}(r) = V_{ex}(r + \mathbf{R}). \quad (2.48)$$

Consequently, the electronic Hamiltonian of a crystalline solid also becomes periodic – since the Hamiltonian is entirely defined by the form of the external potential. Then, it is convenient to define a *translation operator*  $\hat{T}_R$  with the following properties:

$$\hat{H}\psi(r) = \hat{H}(r + \mathbf{R})\psi(r + \mathbf{R}) = \hat{H}\psi(r + \mathbf{R}) = \hat{H}\hat{T}_R\psi(r) .$$

and :

$$\hat{T}_R\hat{H} = \hat{H}\hat{T}_R \quad (2.49)$$

Additionally, the result of two consecutive translation operations must not be affected by the order in which the translations are performed:

$$\hat{T}_R\hat{T}_{R'}\psi(r) = \hat{T}_R\psi(r + R') = \hat{T}_{R'}\psi(r + R) = \psi(r + R + R') .$$

Consequently, we have that:

$$\hat{T}_R\hat{T}_{R'} = \hat{T}_{R'}\hat{T}_R . \quad (2.50)$$

Eqs. 2.49 and 2.50 establish that the Hamiltonian of a periodic system commutes with the translation operator for any given position vector  $\mathbf{R}$  of the system's *Bravais lattice*.

An important property of commuting operators is that they always share the same set of eigenfunctions [112]. Therefore, for any wave-function  $\psi$  satisfying the time-independent Schrödinger equation, we have:

$$\hat{T}_R|\psi\rangle = u(\mathbf{R})|\psi\rangle , \quad (2.51)$$

where  $u(\mathbf{R})$  is the eigenvalue related to the operator  $\hat{T}_R$ . From Eq. 2.50 and Eq. 2.51, it follows that:

$$\hat{T}_R\hat{T}_{R'}|\psi\rangle = u(\mathbf{R})u(\mathbf{R}')|\psi\rangle .$$

Once  $\mathbf{R}$  is defined in terms of the primitive lattice vectors (Eq. 2.45), we can conclude that:

$$u(\mathbf{R}) = u(\mathbf{a})^{n_a}u(\mathbf{b})^{n_b}u(\mathbf{c})^{n_c} . \quad (2.52)$$

Note that – as a function of the primitive lattice vectors – the eigenvalues  $u$  are also periodic, which allows representing it in the form:

$$u(\mathbf{a}) = e^{i2\pi k_a}$$

Given that, Eq. 2.52 reduces to:

$$u(\mathbf{R}) = e^{i2\pi(n_a k_a + n_b k_b + n_c k_c)},$$

which is equivalent to:

$$u(\mathbf{R}) = e^{i\mathbf{k}\cdot\mathbf{R}}, \quad (2.53)$$

with  $\mathbf{k}$  equal to:

$$\mathbf{k} = 2\pi(k_a \mathbf{j} + k_b \mathbf{l} + k_c \mathbf{m}) .$$

Finally, by substituting Eq. 2.53 into Eq. 2.51, we find that:

$$\psi(r + \mathbf{R}) = e^{i\mathbf{k}\cdot\mathbf{R}}\psi(r). \quad (2.54)$$

Eq. 2.54 is the mathematical expression of the *Bloch Theorem*, which states that:

*To each eigenstate  $\psi(r)$  of a one-electron Hamiltonian  $\hat{H}$  is a wave-vector  $\mathbf{k}$ , so that  $\psi(r + \mathbf{R}) = e^{i\mathbf{k}\cdot\mathbf{R}}\psi(r)$  holds true for every  $\mathbf{R}$  in the lattice.*

Among other consequences to the quantum theory of crystals, the *Bloch theorem* introduces the wave-vector  $\mathbf{k}$ , which can be interpreted as a quantum number for the translational symmetry of a wave-function in a periodic potential [151]. It is interesting to remark that all relevant values of  $\mathbf{k}$  are confined in the *First Brillouin Zone* (BZ) of the system, since any wave-vector  $\mathbf{k}'$  outside the BZ has a corresponding one into it – because of the periodicity of the *reciprocal space* (Section 2.6.1).

### 2.6.3.1 – Energy Bands and Band Structures

Another important consequence of the block theorem is that the eigenvalues of the one-electron Hamiltonian  $\hat{H}$  do not appear as discrete energy levels, but form continuous *energy bands*. Observe that – since  $\hat{H}$  does not operate directly on  $\mathbf{k}$  – there is a *one-electron eigenvalue* ( $\varepsilon_{\mathbf{k}}$ ) for each possible value of  $\mathbf{k}$  in the BZ. Now, if we consider that, in the limit of macroscopic crystal, the *reciprocal lattice* can be approximated as a continuous vectorial space,  $\mathbf{k}$  is allowed to vary continuously within the BZ, and the one-electron eigenvalue becomes a continuous function  $\varepsilon(\mathbf{k})$  – i.e. an *energy band*.

Accordingly for the set  $\{\psi_i\}$  containing all eigenfunctions of  $\hat{H}$ , there will be a corresponding set of energy bands  $\{\varepsilon_i(\mathbf{k})\}$ . This set  $\{\varepsilon_i(\mathbf{k})\}$  is the so-called *band structure* of the system, which contains all the electronic structure information associated with its *unit cell*.

### 2.6.3.2 – Integration over the First Brillouin Zone and $k$ -points Sampling

Considering a semi-conductor/isolator<sup>###</sup> the average electronic energy per unit cell ( $\bar{E}_{elec}$ ) is in principle determined by a sum over all filled one-electron energy bands in the *First Brillouin Zone* (BZ):

$$\bar{E}_{elec} = \frac{1}{\Omega_{BZ}} \sum_i^I \int_{BZ} \varepsilon_i(\mathbf{k}) d\mathbf{k}, \quad (2.55)$$

where  $\Omega_{BZ}$  is the volume of BZ. In practice however, the functional forms of  $\{\varepsilon_i(\mathbf{k})\}$  are not known and the integral in Eq. 2.55 must be substituted by a *reasonable sample* of discrete energy levels in the  $k$ -space:

$$\bar{E}_{elec} = \sum_i^I \sum_{\mathbf{k}} \frac{1}{N_K} \varepsilon_i(\mathbf{k}), \quad (2.56)$$

where  $N_K$  is the total number of  $k$ -points – i.e the number of different wave-vectors  $\mathbf{k}$  – sampled. For a sufficient set of  $k$ -points, Eq. 2.56 gives exactly the expected value of 2.55.

There are several ways to choose an adequate  $k$ -points *sample*. Among them, the most popular is the so-called *Monkhorst-Pack* (MP) grid [152], which is specified by the relation:

$$\mathbf{k} = \sum_{i=1}^3 \sum_{n_i=1}^{N_i} \frac{2n_i - N_i - 1}{2N_i} \mathbf{k}_i$$

where  $\mathbf{k}_i$  represents the primitive vectors of the reciprocal space. The MP grid defines a uniform set of points, which is a scaled version of the system's reciprocal lattice. The *mesh* of the grid is defined by the number of  $k$ -points  $N_i$  taken along each direction. Of course, denser grids lead to more accurate results, but are also computationally more expensive. In practice, performing convergence tests for the system's electronic energy with respect to the mesh of the MP grid is necessary; and then using the sparsest converged grid in all subsequent production calculations. One can also reduce the number of  $k$ -points to be sampled in actual calculations – without losing accuracy – by sampling the  $k$ -space only within the *Irreducible Brillouin Zone* (IBZ), which is the BZ reduced by all symmetry operations of the lattice's point group.

---

<sup>###</sup> The fact that there are no partially filled energy bands in semi-conductors and isolators makes our discussion in this section more straightforward, and therefore we will not comment explicitly on metals here. Nevertheless, the basic principle to be sketched here holds true for semiconductors, isolators and metals.

### 2.6.3.3 – Density of States (DOS)

Usually, the physicochemical information contained in an electronic band structure  $\{\varepsilon_i(\mathbf{k})\}$  is as rich as hard to analyze. Partially, that is because  $\{\varepsilon_i(\mathbf{k})\}$  is a complex energy diagram in the  $k$ -space, whose interpretation is not intuitive at first glance. Although there are important properties which can be directly extracted from  $\{\varepsilon_i(\mathbf{k})\}$  – such as the existence of energy band gaps for example – but rationalizing chemical events based on electronic band structures normally is not straightforward.

However, the information contained in  $\{\varepsilon_i(\mathbf{k})\}$  becomes much more suitable for qualitative chemical analysis if transformed into its *Density of States* (DOS) form:

$$g(E) = \frac{1}{\Omega_{\text{BZ}}} \sum_i \int_{\text{BZ}} \delta(\varepsilon_i(\mathbf{k}) - E) d\mathbf{k}.$$

where  $\delta$  is the Dirac's Delta function, and the sum runs over all electronic states in the *First Brillouin Zone*. Defined in this way, the DOS counts the total number of electronic states with eigenvalue  $\varepsilon_{iK}$  numerically equal to a given reference energy  $E$ . In other words, the DOS represents the energy distribution of all electronic states of a system; showing a clear similarity with traditional molecular energy diagrams used in chemistry.

The information of the DOS can be further refined by separating – or *projecting* – its contributions from individual atoms or orbitals in the system. The so-called *Projected Density of States* (PDOS) is a very useful tool for rationalizing chemical phenomena, since it permits identifying how the electronic states of some particular specie changes when exposed to different environments. PDOS analyses will be extensively employed along Chapter 4 to interpret the interactions of different molecular anchors with ZnO non-polar surfaces.

### 2.6.4 – The Tight Binding Model

The *Tight Binding model* is a very helpful theoretical tool in solid state physics. That is not only because it is the basis for constructing approximated electronic Hamiltonians and computationally efficient methods, but especially because it leads to a very intuitive interpretation for the origin and the physical meaning of electronic bands in the  $k$ -space. Instead of viewing the solid state as an array of positive nuclei immersed into an electron gas – which was implicitly done until now – the *Tight Binding model* assumes that solids are basically formed by a collection of interacting neutral atoms. The difference is that while in the first case each electron is from the very beginning assumed to be delocalized along the system, in the *Tight Binding* approach it is initially considered as bound to a certain atom.

#### 2.6.4.1 – General Tight Binding Formulation

To understand the *Tight Binding model*, let us imagine a crystal where we can change the lattice constants  $\mathbf{R}$  arbitrarily, with all bond lengths varying linearly



with  $\mathbf{R}$ . Additionally, let us assume the independent electron approximation, so that we can represent our system as a sum of one-electron Hamiltonians  $\hat{H}_i$  (see Section 2.3.2). As usual, our problem here becomes finding the set of one-electron wave functions  $\psi_i(r)$  which satisfy the one-electron Schrödinger Equation:

$$\hat{H}_i \psi_i(r) = \varepsilon_i(\mathbf{k}) \psi_i(r). \quad (2.57)$$

At first, let us consider the extreme case where all inter-atomic distances in our crystal are simply very large – i.e.  $\mathbf{R} \rightarrow \infty$  – with the system corresponding to an infinite array of  $M$  isolated atoms. In this case, it follows that the external potential in  $\hat{H}_i$  must reduce to a simple atomic potential. Therefore, it is convenient to define  $\hat{H}_i$  in terms of a simple atomic Hamiltonian ( $\hat{H}_i^{atom}$ )[151]:

$$\hat{H}_i = \hat{H}_i^{atom} + \Delta V(\mathbf{R}), \quad (2.58)$$

where  $\Delta V(\mathbf{R})$  is a correction operator accounting for the external potential differences between the free atom and the crystal cases. Obviously,  $\Delta V(\mathbf{R})$  must vanish for  $\mathbf{R} \rightarrow \infty$ . Note that, according to the ansatz in Eq. 2.58, any atomic orbital  $\phi_i(r)$  will satisfy Eq. 2.57 for  $\mathbf{R} \rightarrow \infty$ . Nevertheless, because of the periodicity of the system, we have to ensure that  $\psi_i(r)$  satisfies not only Eq. 2.57 but also the *Bloch theorem* (Eq. 2.54). Such requirement is fulfilled by expanding  $\psi_i(r)$  as a linear combination of atomic orbitals, localized in all equivalent atomic positions in the lattice:

$$\psi_{ik}(r) = \sum_{\mathbf{R}} c_{\mathbf{R}} e^{i\mathbf{k}\mathbf{R}} \phi_i(r - \mathbf{R}). \quad (2.59)$$

where  $c_{\mathbf{R}}$  are linear combination coefficients – and normalization constants at the same time. Now, let us calculate the expectation value of  $\varepsilon_i(\mathbf{k})$  by using  $\psi_{ik}(r)$  as defined in Eq. 2.59:

$$\langle \psi_{ik}(r) | \hat{H}_i | \psi_{ik}(r) \rangle = \sum_{\mathbf{R}} \sum_{\mathbf{R}'} c_{\mathbf{R}} c_{\mathbf{R}'} \langle e^{i\mathbf{k}\mathbf{R}} \phi_i(r - \mathbf{R}) | \hat{H}_i^{atom} | e^{i\mathbf{k}\mathbf{R}'} \phi_i(r - \mathbf{R}') \rangle. \quad (2.60)$$

Since the atomic functions  $\phi_i(r)$  are eigenfunctions of  $\hat{H}_i^{atom}$ , Eq. 2.60 can be rewritten as:

$$\langle \psi_{ik}(r) | \hat{H}_i | \psi_{ik}(r) \rangle = \varepsilon_i \sum_{\mathbf{R}} \sum_{\mathbf{R}'} c_{\mathbf{R}} c_{\mathbf{R}'} \langle e^{i\mathbf{k}\mathbf{R}} \phi_i(r - \mathbf{R}) | e^{i\mathbf{k}\mathbf{R}'} \phi_i(r - \mathbf{R}') \rangle. \quad (2.61)$$

If  $|\mathbf{R}|$  is larger than the length of  $\phi_i(r)$ 's radial part, the overlap integrals in Eq. 2.61 will vanish unless  $\mathbf{R} = \mathbf{R}'$ . Thus:

$$\langle \psi_{ik}(r) | \hat{H}_i | \psi_{ik}(r) \rangle = \varepsilon_i \sum_{\mathbf{R}} c_{\mathbf{R}}^2 (e^{i\mathbf{k}\mathbf{R}})^* e^{i\mathbf{k}\mathbf{R}} (\langle \phi_i(r - \mathbf{R}) | \phi_i(r - \mathbf{R}) \rangle),$$

$$\langle \psi_{ik}(r) | \hat{H}_i | \psi_{ik}(r) \rangle = \varepsilon_i \sum_{\mathbf{R}} c_{\mathbf{R}}^2 \langle \phi_i(r - \mathbf{R}) | \phi_i(r - \mathbf{R}) \rangle = \varepsilon_i. \quad (2.62)$$

Eq. 2.62 brings two important qualitative results: *i)* the dependency of  $\psi_{i\mathbf{k}}$  on the wave-vector  $\mathbf{k}$  is eliminated if  $\mathbf{R} \rightarrow \infty$ , and *ii)* the eigenvalues associated to  $\psi_{i\mathbf{k}}$  become equal to the eigenvalues  $\varepsilon_i$  of the atomic orbital  $\phi_i(r)$ . Finally, if we recall that for each of the  $M$  atoms in our infinite crystal there must be an electronic level with exactly the same mathematical structure in Eq. 2.59, we arrive at the conclusion that – for the whole crystal – the eigenvalue  $\varepsilon_i$  must be  $M$ -times degenerate. Of course, the degeneracy of  $\varepsilon_i$  will also follow the degeneracy of the atomic orbitals  $\phi_i(r)$  used to expand  $\psi_{i\mathbf{k}}$ . For example, if  $\psi_{i\mathbf{k}}$  is related to atomic  $p$ -levels, then  $\varepsilon_i$  will be  $3M$ -times degenerate.

Now let us consider the case where  $|\mathbf{R}| \ll \infty$  – i.e. a crystal with finite lattice vectors. Remember that – by construction – the potential  $\Delta V(\mathbf{R})$  contains all corrections necessary to turn the one-electron atomic Hamiltonian into the full one-electron crystal Hamiltonian. If that is true, then all we have to do in order to find the band  $\varepsilon_i(\mathbf{k})$  is calculating the expectation value for the  $\Delta V(\mathbf{R})$  operator and adding it to the correspondent atomic eigenvalue  $\varepsilon_i$ :

$$\varepsilon_i(\mathbf{k}) = \varepsilon_i + \langle \psi_{i\mathbf{k}}(r) | \Delta V(\mathbf{R}) | \psi_{i\mathbf{k}}(r) \rangle. \quad (2.63)$$

Here we can once more use the ansatz in Eq. 2.59 in order to expand the one-electron wave function in terms of an atomic basis; thereby rewriting Eq. 2.63 as:

$$\begin{aligned} \varepsilon_i(\mathbf{k}) &= \varepsilon_i + \sum_{\mathbf{R}} \sum_{\mathbf{R}'} c_{\mathbf{R}} c_{\mathbf{R}'} \langle e^{i\mathbf{k}\mathbf{R}} \phi_i(r - \mathbf{R}) | \Delta V(\mathbf{R}) | e^{i\mathbf{k}\mathbf{R}'} \phi_i(r - \mathbf{R}') \rangle, \\ \varepsilon_i(\mathbf{k}) &= \varepsilon_i + \sum_{\mathbf{R}} c_{\mathbf{R}}^2 \langle \phi_i(r - \mathbf{R}) | \Delta V(\mathbf{R}) | \phi_i(r - \mathbf{R}) \rangle \\ &\quad + \sum_{\mathbf{R} \neq \mathbf{R}'} c_{\mathbf{R}} c_{\mathbf{R}'} \langle e^{i\mathbf{k}\mathbf{R}} \phi_i(r - \mathbf{R}) | \Delta V(\mathbf{R}) | e^{i\mathbf{k}\mathbf{R}'} \phi_i(r - \mathbf{R}') \rangle \end{aligned} \quad (2.64)$$

Just like in Eq. 2.61, the dependency on  $\mathbf{k}$  vanishes for  $\mathbf{R} = \mathbf{R}'$  and the first sum in Eq. 2.64 becomes just a rigid one-site energy shift:

$$\beta_i = -\langle \phi_i(r) | \Delta V(\mathbf{R}) | \phi_i(r) \rangle.$$

Furthermore, the second sum in Eq. 2.64 – i.e. the terms where  $\mathbf{R} \neq \mathbf{R}'$  – can be simply rearranged as:

$$\begin{aligned} &\sum_{\mathbf{R} \neq \mathbf{R}'} c_{\mathbf{R}} c_{\mathbf{R}'} \langle e^{i\mathbf{k}\mathbf{R}} \phi_i(r - \mathbf{R}) | \Delta V(\mathbf{R}) | e^{i\mathbf{k}\mathbf{R}'} \phi_i(r - \mathbf{R}') \rangle \\ &= \sum_{\mathbf{R} \neq \mathbf{R}'} c_{\mathbf{R}} c_{\mathbf{R}'} \cdot e^{i\mathbf{k}(\mathbf{R} + \mathbf{R}')} \langle \phi_i(r - \mathbf{R}) | \Delta V(\mathbf{R}) | \phi_i(r - \mathbf{R}') \rangle \\ &= \sum_{\mathbf{R} \neq \mathbf{R}'} c_{\mathbf{R}} c_{\mathbf{R}'} \cdot \cos(\mathbf{k}(\mathbf{R} + \mathbf{R}')) \cdot \langle \phi_i(r - \mathbf{R}) | \Delta V(\mathbf{R}) | \phi_i(r - \mathbf{R}') \rangle, \end{aligned}$$

which leads us to the final *Tight Binding* expression for the energy band  $\varepsilon_i(\mathbf{k})$  in a crystal:

$$\varepsilon_i(\mathbf{k}) = \varepsilon_i - \beta_i + \sum_{\mathbf{R} \neq \mathbf{R}'} c_{\mathbf{R}} c_{\mathbf{R}'} \cdot \cos(\mathbf{k}(\mathbf{R} + \mathbf{R}')) \cdot \Delta V(\mathbf{R}) \langle \phi_i(r - \mathbf{R}) | \phi_i(r - \mathbf{R}') \rangle. \quad (2.65)$$

The first and the second right-hand terms in Eq. 2.65 are rather “rigid” one-site energies, which implies that all the energy dispersion in  $\varepsilon_i(\mathbf{k})$  depends exclusively on the third right-hand term in Eq. 2.65. Hence, it is possible to interpret such energy dispersions as a measure of the overlap between orbitals at different locations in the crystal [151]. In order to confirm that, observe that the dependency of  $\varepsilon_i(\mathbf{k})$  on  $\mathbf{k}$  disappears if the overlap integrals  $\langle \phi_i(r - \mathbf{R}) | \phi_i(r - \mathbf{R}') \rangle$  vanish. So, according to Eq. 2.65, it is possible to draw some important intuitive conclusions on the structure of the energy bands  $\varepsilon_i(\mathbf{k})$ : *i*) energy dispersions are expected to be negligible for core-electron bands, since core-electron orbitals are rather localized and chemically inert; *ii*) the dispersions on  $\varepsilon_i(\mathbf{k})$  are expected to increase with the radial size of the valence orbitals, and *iii*) the dispersions on  $\varepsilon_i(\mathbf{k})$  come mostly from the orbitals’ interactions with their near neighborhood, where the orbital overlaps are more effective. Interactions with the first-neighbors are indeed expected to be dominant, but second and third-neighbors are also often important [105].

Finally, Eq. 2.65 still left the combination coefficients  $c_{\mathbf{R}}$  to be determined. Since we assumed the independent-electrons approximation we can use the variation principle and the *Lagrange multipliers method* (see Section 2.3.3) to minimize the *Tight Binding* total energy expression in its Eq. 2.60 form. In the end – exactly as in Sections 2.3.3 and 2.4.2 – we will find a set of *Roothaan Equations* for the *Tight-Binding* problem – one for each possible point in the *k-space*:

$$\mathbf{H}\mathbf{c}(\mathbf{k}) = \varepsilon(\mathbf{k})\mathbf{S}\mathbf{c}(\mathbf{k}),$$

which can be solved self-consistently in conjunction with Eq. 2.65.

It is important to remark that the *Tight Binding* formalism is not restricted to any type of specific basis-set or further approximation beyond the independent-electrons model. Instead, it is a quite general formulation to solve the electronic structure of periodic systems by employing localized basis sets. In fact, there are several different methods – with different levels of accuracy – constructed on a *Tight Binding* platform, like the DFT implementation in the SIESTA package or the semi-empirical SCC-DFTB method for example – both used in this work. Historically, however, the term “*Tight Binding*” has been often associated with empirical *Tight Binding* models, where the elements of *Hamiltonian matrix* ( $\mathbf{H}$ ) are approximated by empirical analytical functions – fitted against *ab initio* calculations or empirical data.

#### 2.6.4.2 – The SCC-DFTB Method

The SCC-DFTB method is a semi-empirical *Tight Binding* model based on the *Kohn-Sham Density Functional Theory* formalism, which will be detailed in the next two sections. At first we will show how to express the Kohn-Sham total energy formula in terms of density fluctuations in the system – which is a more appropriate form to solve the electronic energy self-consistently with respect to charge distributions. After that we will introduce the set of approximations which characterize the SCC-DFTB method.

### 2.6.4.2.1 – Rearranging the Kohn-Sham Total Energy Formula

Given the *Kohn-Sham* total energy expression:

$$E[\rho(r)] = T[\rho(r)] + V_{KS}[\rho(r)]$$

$$E[\rho(r)] = T[\rho(r)] + V_{ext}[\rho(r)] + V_H[\rho(r)] + E_{XC}[\rho(r)]$$

$$E[\rho(r)] = \sum_{i=1}^I \left\langle \psi_i^{KS} \left| -\frac{1}{2} \nabla_i^2 + V_{ext}[\rho(r)] + \frac{1}{2} \int \frac{\rho(r')}{|r-r'|} dr' \right| \psi_i^{KS} \right\rangle + E_{XC}[\rho(r)], \quad (2.66)$$

the derivation of the SCC-DFTB model starts from separating the electronic density in a reference density ( $\rho^0$ ) and a variation term accounting for density fluctuations in the system ( $\delta\rho$ ):

$$\rho = \rho^0 + \delta\rho,$$

where  $\rho^0$  is chosen to be the superposition of the neutral-atom densities for all species in the system. Given that, we can rewrite Eq. 2.66 as:

$$E[\rho(r)] = \sum_{i=1}^I \left\langle \psi_i^{KS} \left| -\frac{1}{2} \nabla_i^2 + V_{ext}[\rho^0(r)] + \frac{1}{2} \int \frac{(\rho^0(r') + \delta\rho(r'))}{|r-r'|} dr' \right| \psi_i^{KS} \right\rangle + E_{XC}[\rho^0(r) + \delta\rho(r)]. \quad (2.67)$$

Note that Eq. 2.67 already introduces a first approximation into the model, since substituting  $V_{ext}[\rho(r)]$  in Eq. 2.66 simply by  $V_{ext}[\rho^0(r)]$  corresponds to neglecting crystal field effects acting on the system's electrons. Now, Eq. 2.67 can be conveniently rearranged by defining a *zeroth-order Hamiltonian*  $\hat{H}^0$ :

$$\hat{H}^0 = -\frac{1}{2} \nabla_i^2 + V_{ext}[\rho^0(r)] + \int \frac{\rho^0(r')}{|r-r'|} dr' + XC[\rho^0(r)].$$

So:

$$E[\rho(r)] = \sum_{i=1}^I \langle \psi_i^{KS} | \hat{H}^0 | \psi_i^{KS} \rangle - \frac{1}{2} \int \int \frac{\rho^0(r')(\rho^0(r) + \delta\rho(r))}{|r-r'|} dr dr' + \frac{1}{2} \int \int \frac{\delta\rho(r')(\rho^0(r) + \delta\rho(r))}{|r-r'|} dr dr' - \int XC[\rho^0(r)](\rho^0(r) + \delta\rho(r)) dr + E_{XC}[\rho^0(r) + \delta\rho(r)] \quad (2.68)$$

The first double integral in Eq. 2.68 accounts for canceling the *Hartree Integral's double counting* in  $\hat{H}^0$  and the third integral cancels the  $XC[\rho^0(r)]$  term in  $\hat{H}^0$ . Eq. 2.68 can now be simplified by factorizing its double integrals. The terms

depending linearly on  $\delta\rho(r')$  and  $\delta\rho(r)$  will cancel each other for any  $\rho^0(r)$ ; so Eq. 2.68 becomes:

$$E[\rho(r)] = \sum_{i=1}^I \langle \psi_i^{KS} | \hat{H}^0 | \psi_i^{KS} \rangle - \frac{1}{2} \int \int \frac{\rho^0(r')\rho^0(r)}{|r-r'|} drdr' + \frac{1}{2} \int \int \frac{\delta\rho(r')\delta\rho(r)}{|r-r'|} drdr' - \int XC[\rho^0(r)](\rho^0(r) + \delta\rho(r))dr + E_{xc}[\rho^0(r) + \delta\rho(r)]. \quad (2.69)$$

We can also expand the *XC energy*  $E_{xc}[\rho(r)]$  around the reference density  $\rho^0(r)$ :

$$E_{xc}[\rho(r)] = E_{xc}[\rho^0(r)] + \delta\rho(r) \left( \frac{dE_{xc}}{d\rho} \right)_{\rho^0} + \frac{1}{2} (\delta\rho(r))^2 \left( \frac{d^2E_{xc}}{d\rho^2} \right)_{\rho^0} + \mathcal{O}^3. \quad (2.70)$$

Now, if we recall that:

$$\int XC[\rho(r)]\rho(r)dr = E_{xc}[\rho(r)]$$

we have that:

$$E_{xc}[\rho^0(r)] + \delta\rho(r) \left( \frac{dE_{xc}}{d\rho} \right)_{\rho^0} = \int XC[\rho^0(r)](\rho^0(r) + \delta\rho(r))dr. \quad (2.71)$$

Hence, by using Eqs. 2.70 and 2.71 into Eq. 2.69, we get:

$$E[\rho(r)] = \sum_{i=1}^I \langle \psi_i^{KS} | \hat{H}^0 | \psi_i^{KS} \rangle - \frac{1}{2} \int \int \frac{\rho^0(r')\rho^0(r)}{|r-r'|} drdr' + \frac{1}{2} \int \int \frac{\delta\rho(r')\delta\rho(r)}{|r-r'|} drdr' + \frac{1}{2} (\delta\rho(r))^2 \left( \frac{d^2E_{xc}}{d\rho^2} \right)_{\rho^0} + \mathcal{O}^3. \quad (2.72)$$

Finally, if we use the functional derivative identity:

$$(\delta\rho(r))^2 \left( \frac{d^2E_{xc}}{d\rho^2} \right)_{\rho^0} = \frac{d}{d\rho} \left( \frac{dE_{xc}}{d\rho} \right)_{\rho^0} \delta\rho(r)\delta\rho(r) = \frac{d}{d\rho} \delta E_{xc} \delta\rho(r) = \delta(\delta E_{xc}) = \delta^2 E_{xc},$$

we can rewrite Eq. 2.72 in its final functional form:

$$E[\rho(r)] = \sum_{i=1}^I \langle \psi_i^{KS} | \hat{H}^0 | \psi_i^{KS} \rangle - \frac{1}{2} \int \int \frac{\rho^0(r')\rho^0(r)}{|r-r'|} drdr' + \frac{1}{2} \left( \int \int \frac{1}{|r-r'|} drdr' + \frac{\delta^2 E_{xc}}{\delta\rho(r')\delta\rho(r)} \right) \delta\rho(r')\delta\rho(r). \quad (2.73)$$

### 2.6.4.2.2 – The SCC-DFTB Approximations

Except for some minor approximations – i.e. neglecting the crystal field corrections and the truncation error for the expansion of  $E_{xc}[\rho(r)]$  – Eq. 2.73 is just a reformulation of the *Kohn-Sham* total energy expression. Hence, Eq. 2.73 can be solved – at least in theory – with the same accuracy and at similar computational costs as any other Kohn-Sham DFT implementation. In order to turn Eq. 2.73 into a more computationally efficient scheme, we still have to introduce a set of approximations:

- i) The first approximation to be introduced in Eq. 2.73 is assuming that the density fluctuations  $\delta\rho$  can be decomposed as a set of atomic density fluctuations:

$$\int \delta\rho(r)dr = \sum_{\alpha}^M \delta\rho_{\alpha} = 0 .$$

Each atomic density fluctuation can be represented as a multipole expansion. In the SCC-DFTB method, the series is truncated already on the monopole term, so that each  $\delta\rho_{\alpha}$  term is represented as a simple atomic charge fluctuation  $\Delta q_{\alpha}$ :

$$\sum_{\alpha}^M \delta\rho_{\alpha} = \sum_{\alpha}^M \Delta q_{\alpha} = 0 .$$

Observe that the sums above vanish because the system's net charge is constant.

- ii) The second approximation is assuming that, at large distances, the second order exchange-correlation term is negligible; so that last term in Eq. 2.73 can be substituted by a simple pair-wise potential:

$$\frac{1}{2} \left( \iint \frac{1}{|r-r'|} drdr' + \frac{\delta^2 E_{xc}}{\delta\rho(r')\delta\rho(r)} \right) \delta\rho(r')\delta\rho(r) \cong \frac{1}{2} \sum_{\alpha\beta}^M \gamma_{\alpha,\beta} \Delta q_{\alpha} \Delta q_{\beta} .$$

For  $\alpha \neq \beta$ ,  $\gamma_{\alpha,\beta}$  is determined from the Coulomb interaction of two spherical charge distributions centered in the atoms  $\alpha$  and  $\beta$  respectively [109,223]. Yet for  $\alpha = \beta$  – where correlation effects are important and there is no *Coulomb* interaction to take into account –  $\gamma_{\alpha,\alpha}$  is simply approximated as the DFT *chemical hardness* of the atom  $\alpha$ , defined as the second derivative of atomic total energy with respect to the atomic electron occupancy ( $n^{\alpha}$ ):

$$\gamma_{\alpha,\alpha} = U_{\alpha} = \frac{d^2 E^{\alpha}}{d(n^{\alpha})^2} .$$

According to the *Janak's Theorem* [224],  $U_\alpha$  can be also represented as the derivative of the highest occupied atomic orbital (HOAO) with respect to its occupancy:

$$U_\alpha = \frac{d\varepsilon_i^\alpha}{dn_i^\alpha}. \quad i = \text{HOAO}$$

which can be easily obtained from atomic DFT calculations. The *chemical hardness* ( $U_\alpha$ ) is also often called as *Hubbard parameter* in literature.

iii) The third approximation is assuming that the *Kohn-Sham wave-functions* ( $\psi_i^{KS}$ ) can be expanded as linear combinations of non-orthogonal atomic orbitals – Eq. 2.59 – which are individually determined by variationally solving a modified Kohn-Sham equation for the spin-unpolarized free atoms:

$$\left[ \frac{1}{2} \nabla_i^2 + V_{KS} + \left( \frac{r}{r_0} \right)^2 \right] \phi_i^\alpha(r) = \varepsilon_i^\alpha \phi_i^\alpha(r). \quad (2.74)$$

In Eq. 2.74, the additional harmonic potential  $\left( \frac{r}{r_0} \right)^2$  is used in order to enforce the localization of the atomic orbitals and improve the quality of energy bands calculations. In this calculations a minimal *Slater type orbitals* basis is employed.

iv) Once determined the basis set, it is possible to redefine the elements of the *zeroth-order Hamiltonian* according to the *two center approximation*:

$$\langle \phi_i^\alpha | \hat{H}^0 | \phi_j^\beta \rangle \approx \begin{cases} \varepsilon_i^\alpha & \text{if } \alpha = \beta, i = j \\ \langle \phi_i^\alpha | -\frac{1}{2} \nabla^2 + V_{KS}^{\alpha,\beta} | \phi_j^\beta \rangle & \text{otherwise} \end{cases}$$

where  $V_{KS}^{\alpha,\beta}$  stands for a pair effective potential operating only on the electrons in the atoms  $\alpha$  and  $\beta$ . In other words, the diagonal terms of the system's *Hamiltonian* are simply taken as DFT atomic eigenvalues, whereas all non-diagonal terms are obtained via DFT calculations for a  $\alpha$ - $\beta$  dimer. Of course, all non-diagonal elements of the *zeroth-order Hamiltonian* depend on the distances between  $\alpha$  and  $\beta$ . So, in practice, what one has to do is constructing a table – usually called *Slater-Koster table* – for each pair of atoms in the system, containing the values of both the *Hamiltonian* and *Overlap* (to be used below) matrixes' elements in a desired range of interatomic distances. Once constructed, such *Slater-Koster tables* can be accessed for any distance  $\alpha$ - $\beta$  in the range, which avoids the necessity of massive integral calculations during the running-time of a SCC-DFTB simulation.

With the approximation above it is possible to define the *SCC-DFTB electronic energy expression*:

$$E_{Elec}^{DFTB} = \sum_i E_i = \sum_{\alpha,\beta} \left( \frac{1}{2} \gamma_{\alpha,\beta} \Delta q_{\alpha} \Delta q_{\beta} + \sum_{l,j} c_l c_j \langle \phi_l | \hat{H}^0 | \phi_j \rangle \right), \quad \forall l \in \alpha, j \in \beta, \quad (2.75)$$

where  $c_l$  and  $c_j$  are the combination coefficients used to expand the Kohn-Sham wave-function. Observe that, for a given set of atomic positions, a trial set of combination coefficients can be used in order to estimate all one-electron energies of the system via Eq. 2.75 – once all  $\langle \phi_l | \hat{H}^0 | \phi_j \rangle$  elements have been previously stored into the *Slater-Koster tables* and the atomic charge fluctuations can be determined via *Mulliken population analysis*. Moreover, as the Kohn-Sham wave-function has been constructed as a linear combination of atomic orbitals, it is possible to construct a SCC-DFTB secular equation:

$$\sum_i c_{ij} (H_{ij} - E_i S_{ij}) \quad \forall l \in \alpha, j \in \beta, \quad (2.76)$$

where:

$$H_{ij} = H_{ij}^0 + \frac{1}{2} S_{ij} \sum_{\tau}^M (\gamma_{\alpha\tau} + \gamma_{\beta\tau}) \Delta q_{\tau}$$

$$H_{ij}^0 = \langle \phi_l | \hat{H}^0 | \phi_j \rangle \quad \forall l \in \alpha, j \in \beta,$$

$$S_{ij} = \langle \phi_l | \phi_j \rangle \quad \forall l \in \alpha, j \in \beta,$$

Thus, Eq. 2.76 can be solved self-consistently in conjunction with Eq. 2.75 to find the optimal set of linear combination coefficients. Note that the self-consistency is given with respect to the *charge fluctuations*  $\Delta q$ , so inspiring the term “*self-consistent-charge*” in the method’s name.

v) Finally, in order to calculate the *SCC-DFTB total energies*, it is necessary to introduce the nuclear repulsions into the problem – which has not been considered until now. Besides, it is still necessary to reintroduce the double-counting compensation integrals in Eq. 2.73 – which has been also ignored in Eq. 2.75. These both corrections can be performed in a *semi-empirical* fashion, by using a set of distance-dependent pairwise repulsive potentials  $V_{Rep}^{\alpha,\beta}(|R_{\alpha} - R_{\beta}|)$ , modeled as the difference between the *SCC-DFTB electronic energy* ( $E_{Elec}^{DFTB}$ ) and the total *DFT energy* for some reasonably chosen reference system:

$$E_{Rep} = \sum_{\alpha \neq \beta} V_{Rep}^{\alpha,\beta}(|R_{\alpha} - R_{\beta}|),$$

$$V_{Rep}^{\alpha,\beta}(|R_{\alpha} - R_{\beta}|) = E_{Total}^{DFT}(|R_{\alpha} - R_{\beta}|) - E_{Elec}^{DFTB}(|R_{\alpha} - R_{\beta}|).$$



In practice, the repulsive potentials  $V_{Rep}^{\alpha,\beta}$  are constructed by choosing a suitable reference system – where the interatomic distance  $|R_\alpha - R_\beta|$  can be varied arbitrarily – calculating the  $E_{Total}^{DFT}(|R_\alpha - R_\beta|)$  and  $E_{Elec}^{DFTB}(|R_\alpha - R_\beta|)$  energy profiles for this system, and then fitting the difference between them to an adequate polynomial function. Once ready, the potentials  $V_{Rep}^{\alpha,\beta}$  can be also stored in *Slater-Koster tables* for their respective  $\alpha$  and  $\beta$  elements pair.

Finally, the *SCC-DFTB total energy* expression can be written as:

$$E_{Total}^{DFTB} = \sum_i \langle \psi_i^{KS} | \hat{H}^0 | \psi_i^{KS} \rangle + \frac{1}{2} \sum_{\alpha,\beta} \gamma_{\alpha,\beta} \Delta q_\alpha \Delta q_\beta + \sum_{\alpha \neq \beta} V_{Rep}^{\alpha,\beta}(|R_\alpha - R_\beta|) \quad (2.77)$$

Note that all terms in Eq. 2.77 depend explicitly on the atomic positions  $R_\alpha$ . Hence, one can always calculate the gradients of  $E_{Total}^{DFTB}$  with respect to the atomic positions and use the *Hellman-Feynman Theorem* (Section 2.5) in order to derive the atomic forces necessary for geometry optimizations.

## 2.7 – Notes and Remarks on Basis Sets

In quantum simulations, a *basis set* is the finite set of functions used to represent the molecular orbitals.

Given that, it is important to keep in mind that the *exact* representation of molecular orbitals as combinations of basis functions would require an *infinite set* of them [112]. In this sense, the choice of any finite *basis set* to represent orbitals always corresponds to assuming an arbitrary truncation of the complete functional space (*Hilbert space*) where the exact orbitals exist. In general, larger basis sets give better results because they cover a larger region of the *Hilbert space*, but that is not guaranteed in all cases [103, 105, 112]. In practice, the choice of a particular basis set must always be done with a certain pragmatism.

There are several kinds of basis set available for quantum mechanical simulations – most of them based on localized functions [112]. Just to mention some prominent examples: *Slater Type Orbitals* (STO) minimal sets are widely used in semi-empirical calculations (including the SCC-DFTB method, to be employed in Chapters 5 and 6); conventional quantum chemical calculations usually employ *split-valence Pople* (Gaussian) *basis set* and highly-accurate *multi-reference* methods typically employ the so-called *correlation-consistent basis*. In solid state DFT simulations the expansion of the wave-functions in terms of plane waves is also very popular. In periodical calculations, plane-waves basis sets have at least two advantages in comparison to localized basis. First, the integration of plane waves can be performed very efficiently by *Fast Fourier Transform* algorithms, which may result in saving significant amounts of computational time. Second, increasing the size of the basis – i.e. adding more plane waves to it, with shorter wavelengths – always improves its quality. On the other hand, for systems where the electronic densities change very quickly in the direct space – like surfaces, molecules or heavy atoms with explicit core electrons – the use of plane waves might not be the best option for accurate calculations. The reason is that describing fast changing electronic densities requires extending the basis to a large number of plane waves – with very short wavelengths – which might

become computationally too demanding. Besides, the use of localized basis furnishes a much more intuitive interpretation of electronic band structures, as we seen in the description of the *Tight-Binding model*.

In this work, we have preferred the use of localized basis sets. The major part of our *ab initio* DFT calculations (Chapters 3, 4 and 5) have been performed by using *numerical orbitals*<sup>§§§</sup> – as implemented in the SIESTA package [146] – whereas STO-4G orbitals have been employed in all our SCC-DFTB calculations (Chapters 5 and 6). The exceptions have been the calculations dedicated to the qualitative electronic structure analysis of functionalized ZnO surfaces (Chapter 4). In order to overcome the LDA/GGA *band gap problem* (Section 2.2.4), these calculations have been performed by using the LDA+U functional, which is implemented in the VASP code [153,154] – a plane waves based code.

Although it is not a very elegant solution, the use of two different codes was necessary for the work presented in Chapter 4 – since there is no official implementation of the LDA+U method in the SIESTA package\*\*\*\*, and plane waves calculations would be too demanding for all geometry optimizations required. Nevertheless, it is important to emphasize that our choice does not result in any methodological inconsistency, since both VASP and SIESTA codes are just different – but equivalent – implementations of the same Kohn-Sham DFT framework. Moreover, the LDA+U calculations have been performed exclusively for qualitative analysis purposes, with all quantities based on DFT energy differences – i.e. formation energies, cohesive energies, binding energies, etc – being calculated from SIESTA simulations; using the same kind of basis and the same XC functional.

In all our DFT-SIESTA simulations, we have employed a numerical double- $\zeta$  plus polarization function (DZP) basis set. Besides its size – i.e. how many functions are used to represent each orbital – the quality of numerical basis is also controlled by the radial cutoff assumed for each basis function. In the SIESTA implementation, this control can be automatically done via the simulation parameter PAO.EnergyShift, which establishes the tolerance between atomic energies calculated with the confined – i.e. with the cutoff – and unconfined basis. In our case, we have set PAO.EnergyShift to 0.001 Ry (0.0136 eV), which is a rather conservative choice considering the absolute energy errors associated with PBE calculations [133].

For our VASP simulations in Chapter 4 we have assumed a plane-waves energy cutoff of 500 eV, which is also a conservative choice.

In all cases, the Zn-3d electrons have been explicitly included in the atomic valence.

---

<sup>§§§</sup> Numerical orbitals are usually constructed from atom-like calculations where the electrons are subjected to an spherically symmetric confinement potential.

<sup>\*\*\*\*</sup> There is a beta-version implementation of LDA+U in SIESTA, but its use is still discouraged by the developers for production runs.





# Chapter 3

---

## Bulk ZnO

*“Perfection is achieved not when there is nothing more to add, but when there is nothing left to take away.”*

*Antoine de St.-Exupéry – French Writer and Aviator.*

In this chapter we will briefly address the perfect bulk ZnO crystal, which is the reference point for all calculations involving surfaces and nanostructures in the next chapters. We will start by giving a short description of bulk ZnO and its properties. After that we will use the literature available on bulk ZnO to validate our DFT simulation model. We have also extended the validation to the *hcp*-Zn structure, since it will be used in the parametrization of a SCC-DFTB model for ZnO in Chapter 5.

### 3.1 – Bulk ZnO

ZnO is a natural multifunctional material. It is a polar semiconductor, whose the wide band gap (3.3 eV) at the  $\Gamma$ -point and the large excitonic energy (60meV) have been inspiring several applications in electronics and optoelectronics [155-157]. Additionally, its piezoelectric and pyroelectric properties make ZnO a strong candidate for sensing and energy harvesting applications [65]. In its most stable form, ZnO assumes the wurtzite structure (*w*-ZnO) (Figure 3.1), where two distinct *hexagonal closed-packed (hcp)* sub-lattices – comprising the  $\text{Zn}^{2+}$  cations and  $\text{O}^{2-}$  anions respectively – are interconnected, with all ions occupying the center of a tetrahedron with its counter-ions at the corners. Under very special conditions\*, ZnO also can be obtained in the meta-stable *zinc-blend* and *rock-salt* forms [158, 159].

One of the most serious challenges to the development of ZnO-based technologies for electronics is controlling its electric properties. ZnO naturally shows high levels of unintentional *n-type* doping, with carrier concentrations typically varying from  $\sim 10^{16}$  to  $\sim 10^{17}$  electrons  $\text{cm}^{-3}$  [159,160]. Such *n-type* conductivity has been often attributed to intrinsic defects – especially to Zn interstitials and O vacancies – but the subject is still controversially discussed [160]. Furthermore, the natural occurrence of *n-type* conductivity has been hampering the preparation of *p-type* ZnO, since shallow acceptors introduced via

---

\* Zinc Blend ZnO can be obtained by epitaxial growth on ZnS or cubic salts substrates, whereas rock-salt ZnO can be achieved only at very high pressures ( $\sim 10\text{GPa}$ ) and cannot be stabilized in epitaxially grown materials.

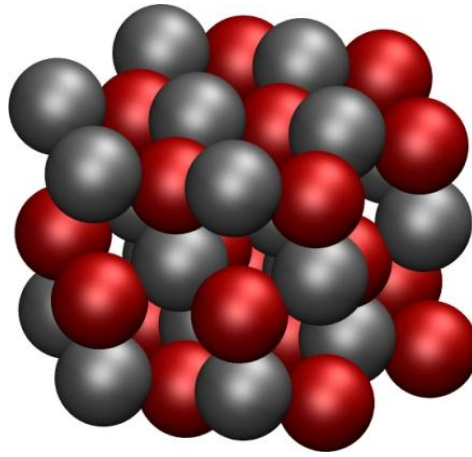


**Figure 3.1** – The *wurtzite Zinc Oxide* (*w-ZnO*) structure, composed of two interconnected hexagonal closed-packed sub-lattices.

doping can be compensated by the intrinsic defect donors. Although p-type doping in ZnO has already been achieved several times in the last few years – with several doping agents and different doping mechanisms being proposed to explain it [160] – the stability and reliability of the resulting materials are also subject of debate [160,161].

Concerning its mechanical properties, ZnO is a relatively soft material; with an average *bulk hardness* of  $\sim 5$  GPa for *c*-axis oriented crystals<sup>†</sup> [156] – compared to  $\sim 12$  and  $\sim 15$  GPa for Si and GaN respectively [162]. Interestingly, ZnO becomes even softer if *a*-oriented crystals are measured ( $\sim 2$  GPa)<sup>‡</sup> [159], with such anisotropy probably related to the orientation of the ZnO basal planes in the wurtzite structure. Despite its relative softness, nano-indentation studies on ZnO have showed that contact-induced defects propagate cracks beyond the experimental contact regions. Moreover, such defects lead to a quenching in the ZnO *near band edge* (NBE) excitonic UV emission [162]; an effect which has been often observed in the *photoluminescence spectra* of ZnO nanostructures.

Another important mechanical property of ZnO is its piezoelectricity. Among the tetrahedrally coordinated semiconductors, ZnO figures among those with the highest piezoelectric constants [161], showing an electromechanical coupling larger than those of GaN and AlN [161]. The origin of the piezoelectricity in ZnO is its wurtzite structure (symmetry space group  $P6_3mc$ ), where the sequence of  $0001(\text{Zn}^{2+})$  and  $000\bar{1}(\text{O}^{2-})$  planes can be viewed as a sequence of parallel capacitors [60]. Additionally, recent theoretical calculations have demonstrated that the piezoelectric properties of ZnO can be strongly enhanced through doping with Hg ions [163]. Because of such outstanding piezoelectric characteristics, ZnO has been attracting much attention as active material in piezotransducers, piezogenerators and self-powered nanodevices [163-165].

---

<sup>†</sup> Value obtained in *plastic penetration* experiments at 300nm depth bellow the contact plane.

<sup>‡</sup> Value obtained in *plastic penetration* experiments at 50nm depth bellow the contact plane.

**Table 3.1** – Selected Properties of ZnO at Room temperature.

<i>Crystal Structure</i>	<i>Wurtzite</i> <sup>a</sup>
<i>Symmetry Space Group</i>	<i>P6<sub>3</sub>mc</i> <sup>a</sup>
<i>Lattice Constants (Å)</i>	<i>a=3.25</i> <sup>a</sup>
	<i>c=5.2</i> <sup>a</sup>
<i>Density (g/cm<sup>3</sup>)</i>	<i>5.6</i> <sup>b</sup>
<i>Bulk Modulus (GPa)</i>	<i>133.7-183</i> <sup>a</sup>
<i>Bulk Hardness (GPa)</i>	<i>5.75</i> <sup>c</sup>
<i>Band Gap Energy (eV)</i>	<i>3.3</i> <sup>a</sup>
<i>Excitonic Binding Energy (meV)</i>	<i>60</i> <sup>a</sup>
<i>Piezoelectric Constant <math>\epsilon_{33}</math> (<math>\mu\text{C m}^{-2}</math>)</i>	<i>0.96</i> <sup>c</sup>
<i>Static Dielectric Constant</i>	<i>8.47</i> <sup>b</sup>
<i>Refraction Index</i>	<i>2.09</i> <sup>b</sup>

a) Ref. [161]

b) Ref. [165]

c) Ref. [159]

### 3.2 – Simulation Details

The DFT-PBE calculations in this chapter have been performed with the SIESTA package [146]. In these calculations, we have used double- $\zeta$  plus polarization function (DZP) basis sets and norm-conserving *Troullier-Martins* pseudo potentials [145] for representing the valence and inner electrons respectively – with *Zn 3d* electrons included in the valence. Converged (8 x 8 x 4) *Monkhorst-Pack* grids [152] have been employed for the *k*-point sampling and all atomic positions have been relaxed with the *conjugated gradient* (CG) algorithm till all forces become smaller than 0.01 eV/Å.

### 3.3 – Structural Properties and Compressibility

The equilibrium structure and the compression susceptibility of a crystalline bulk solid can be determined by using the *Murnaghan equation of state* [166]:

$$E(V) - E(V_0) = \frac{B_0 V}{B'_0} \left[ \frac{V_0/V}{B'_0 - 1} + 1 \right] - \frac{B_0 V_0}{B'_0 - 1}, \quad (3.1)$$

where *V* is volume of the solid's primitive cell, *E* its total energy, *B*<sub>0</sub> is the solid's *bulk modulus* (*B*) – i.e. its resistance to uniform compression – evaluated at the equilibrium unit cell's volume (*V*<sub>0</sub>):

$$B_0 = -V_0 \left( \frac{\partial P}{\partial V} \right)_{T, V=V_0},$$

and *B*'<sub>0</sub> the *bulk modulus derivative* (*B*') with respect to the pressure (*P*), evaluated at *V*<sub>0</sub>:

$$B'_0 = -\frac{\partial}{\partial P} \left( V \frac{\partial P}{\partial V} \right)_{T,P=0}.$$

As  $B_0$  and  $B'_0$  are expected to be well determined values at  $V_0$ , they can be simply treated as parameters in Eq. 3.1. Thus, it is possible to find the *equilibrium volume*  $V_0$  by simply calculating the system's total energy for several different values of  $V$  and fitting the data to Eq. 3.1 using  $B_0$  and  $B'_0$  as fitting parameters.

Given that, we have performed periodic DFT-PBE calculations for the  $w$ -ZnO unit cell (Figure 3.3) assuming different volumes around the experimental value [167] and fitted the data to the *Murnaghan equation of state* (Figure 3.2). In all these calculations, we have used converged (4 x 4 x 8) MP grids for  $k$ -points sampling and the atomic positions have been relaxed till all the forces became smaller than 0.01 eV/Å. The results of the fitting procedure are summarized in Table 3.2, together with experimental and other DFT data found in literature for  $w$ -ZnO. Note that, in hexagonal structures, the volume of the unit cell is related to its lattice parameters through the simple geometric relation:

$$V = \frac{1}{2} \sqrt{3} a^2 c ,$$

so it is easy to extract the system's lattice parameters from the *Murnaghan equation's* fit.

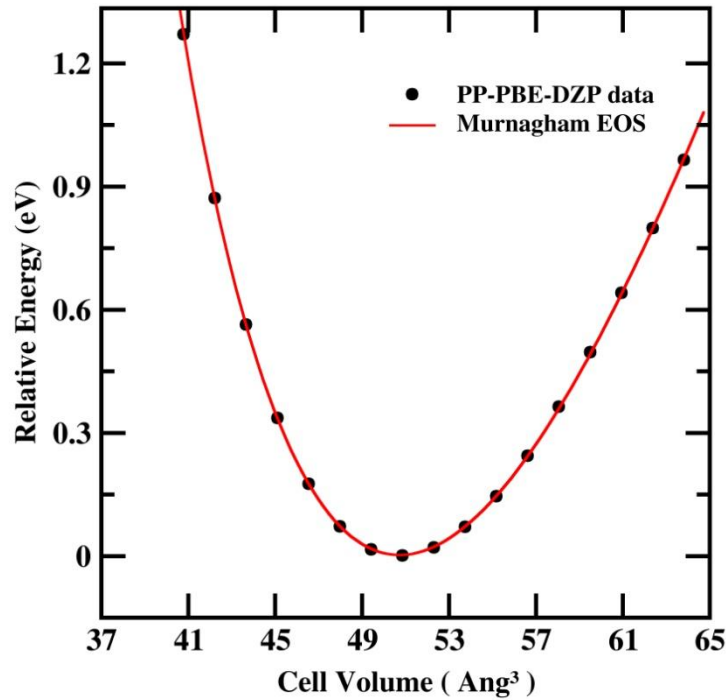


**Figure 3.2** -  $w$ -ZnO lattice parameters optimization. DFT (PP-PBE-DZP) calculations performed for different unit cell volumes (black dots) and their fit to the Murnaghan equation of states (red line).



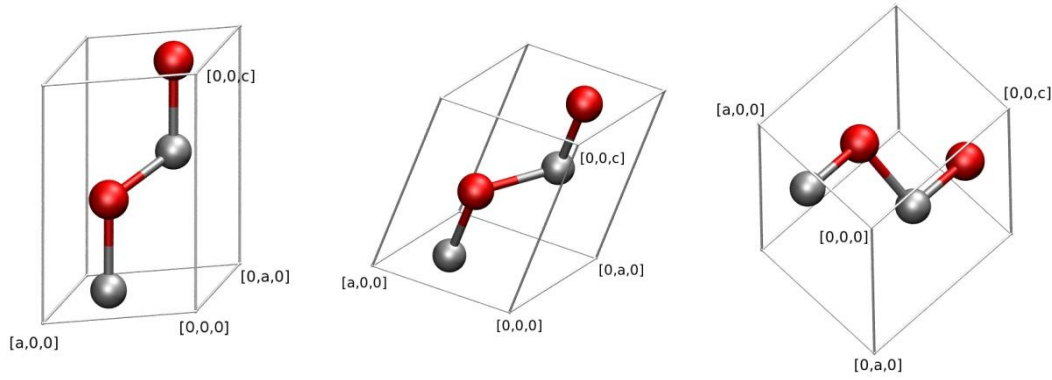


**Figure 3.3** – The *w*-ZnO primitive unit cell from three different perspectives.

**Table 3.2** – Structural and Mechanical Properties of *w*-ZnO calculated with different DFT methods and their comparison with experiments.

<i>Method</i>	$a(\text{\AA})$	$c(\text{\AA})$	$V_0(\text{\AA}^3)$	$B_0(\text{GPa})$	$B'_0$
<i>PP-PBE-DZP</i> <sup>a</sup>	3.30	5.34	51.08	124	4.55
<i>PP-PBE-PW</i> <sup>b</sup>	3.34	5.30	51.40	171	-
<i>PP-LDA-PW</i> <sup>b</sup>	3.23	5.21	47.23	212.5	-
<i>AE-PBE-GTO</i> <sup>c</sup>	3.29	5.29	49.67	133.7	3.83
<i>AE-LDA-GTO</i> <sup>c</sup>	3.20	5.16	45.75	162.3	4.05
<i>Exp.</i> <sup>c</sup>	3.25	5.20	47.62	142.6 - 183	3.6 - 4.0

- a) This work. PP means pseudopotential and DZP double- $\zeta$  plus polarization function numerical basis set.  
b) Ref. [168]. PP means pseudopotential and PW plane waves basis set.  
c) Ref. [167]. AE means all-electrons and GTO Gaussian-type orbitals basis set.

As the table above shows, our results are in good agreement with other PBE calculations in literature. The volume of the unit cell is  $\sim 6,8\%$  overestimated in comparison with experiments – with the lattice vectors  $\mathbf{a}$  and  $\mathbf{c}$  respectively  $\sim 4,5\%$  and  $\sim 2,6\%$  overestimated. Yet the *bulk modulus*  $B_0$  is slightly underestimated in our model – although it agrees within  $\sim 7\%$  with other PBE results calculated by using a localized basis set [167] – whereas the  $B'_0$  is slightly overestimated in comparison with both theoretical and experimental reference data in table 3.2. In general, the size of the deviations is in line with the usual trends observed for GGA calculations, which indicates the reliability of our ZnO model.

Besides *w*-ZnO we have employed the same procedure to simulate metallic Zn in its hexagonal closed-pack (*hcp*) structure – the most stable form of Zn in normal conditions. Such simulations are important not only to further verify our DFT model for Zn, but also because they will be used to validate our SCC-DFTB model for Zn in Chapter 5. The results of our DFT simulations for *hcp*-Zn are summarized in Table 3.3, once more in comparison with experiments and other DFT simulations in literature.

**Table 3.3** – Structural and Mechanical Properties of *hcp*-Zn calculated with different DFT methods and their comparison with experiments.

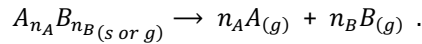
<i>Method</i>	<i>a</i> (Å)	<i>c</i> (Å)	<i>V</i> <sub>0</sub> (Å <sup>3</sup> )	<i>B</i> <sub>0</sub> (GPa)	<i>B</i> ' <sub>0</sub>
<i>PP-PBE-DZP</i> <sup>a</sup>	2.68	5.00	31.24	73	5.93
<i>PP-PW91-PW</i> <sup>b</sup>	2.65	5.10	31.02	60	6.59
<i>PAW-PW91-PW</i> <sup>c</sup>	2.65	4.96	30.79	51.8	7.40
<i>Exp.</i> <sup>b</sup>	2.61	4.91	28.96	60-80	5.2-6.4

- a) This work.  
b) Ref. [169]  
c) Ref. [170]. PAW means Projector-Augmented Wave method.

Once again we find a good agreement between our model and the literature data, with the unit cell volume agreeing within  $\sim 1.5\%$  with other DFT-GGA calculations and  $\sim 7\%$  with experimental results. In this case, both our  $B_0$  and  $B'_0$  estimations are within the experimental variation.

### 3.4 – Cohesive Properties

The *cohesive energy*<sup>§</sup> ( $E_{coh}$ ) of a generic compound  $A_{n_A}B_{n_B}$  is defined as the enthalpy change involved in its atomization:



I.e.:

$$E_{coh}(A_{n_A}B_{n_B}) = n_A \mu_A + n_B \mu_B - E_{A_{n_A}B_{n_B}} , \quad (3.2)$$

where  $\mu_A$  and  $\mu_B$  are the chemical potentials of the atomic species  $A$  and  $B$  respectively, and  $E_{A_{n_A}B_{n_B}}$  is the total energy per formula of  $A_{n_A}B_{n_B}$ . Of course, the definition can be easily extended to compounds with more than two components. Considering  $T = 0K$ ,  $\mu_A$  and  $\mu_B$  reduces to the respective atomic total energies of  $A$  and  $B$  – which can be obtained with reasonable accuracy from DFT calculations.

By starting from the structures optimized in Section 3.2, we have calculated the cohesive energies for both *w*-ZnO and *hcp*-Zn structures – which are given in Table 3.4 in comparison with literature values. In the *w*-ZnO case\*\* our values are in line with other PBE calculations, agreeing with the experimental cohesive energy of ZnO within  $\sim 7\%$ . Recall that, considering the fourth-fold atomic coordination in *w*-ZnO, the absolute error in our model is  $\sim 0.1$  eV per chemical bond with respect to experiments, which can be considered a very good result for PBE calculations employing pseudopotentials. In Table 3.4 it is also possible to

<sup>§</sup> In the chemical literature,  $E_{coh}$  is often called *atomization energy*.

\*\* It is important to remark that the atomic energy of the oxygen atom must be calculated by considering spin polarization effects, since the fundamental states of atomic oxygen is a *triplet state*.

see that the all-electron calculation of *Jaffe et al.* [167] performs slightly better than our pseudopotential-based model, with the  $E_{coh}$  difference below 0.1 eV per chemical bond. It is important to reinforce that the major part of the error in the PBE/LDA cohesive energies are not expected to be related with the errors in the bulk material description itself, but rather with errors while calculating the free-atoms with local XC functionals – as discussed in Section 2.4.3.1. In fact, the ZnO *enthalpy of formation*<sup>††</sup> ( $\Delta H_f$ ) calculated with our model is 3.5 eV per ZnO formula, in excellent agreement with the experimental value of 3.6 eV [174].

**Table 3.4** – Cohesive energies of *w-ZnO* and *hcp-Zn*

	<i>Method</i>	$E_{coh}(eV)$
<i>w-ZnO</i>	<i>PP-PBE-DZP</i> <sup>a</sup>	8.08
	<i>PP-PBE-PW</i> <sup>b</sup>	8.98
	<i>PP-LDA-PW</i> <sup>b</sup>	10.57
	<i>AE-PBE-GTO</i> <sup>c</sup>	7.69
	<i>AE-LDA-GTO</i> <sup>c</sup>	9.77
	<i>Exp.</i> <sup>b</sup>	7.52
<i>hcp-Zn</i>	<i>PP-PBE-DZP</i> <sup>a</sup>	1.92
	<i>PP-PW91-TZP</i> <sup>d</sup>	1.17
	<i>PP-PBE-GTO</i> <sup>e</sup>	0.97
	<i>PP-LDA-TZP</i> <sup>d</sup>	1.91
	<i>PP-LDA-GTO</i> <sup>e</sup>	1.65
	<i>Exp.</i> <sup>f</sup>	1.36

- a) This work.
- b) Ref. [168].
- c) Ref. [167].
- d) Ref. [171]. TZP means Triple- $\zeta$  plus polarization function numerical basis set.
- e) Ref. [172]. Results obtained for experimental lattice constants.
- f) Ref. [173].

In the *hcp-Zn* case the  $E_{coh}$  absolute error per chemical bond in our calculation is  $\sim 0.1$  eV, which is very similar to the PP-LDA-TZP calculation of *Philipsen and Baerends* [171] and slightly worse than their PP-PW91-TZP calculation. The PP-GTO calculations of *Wedig et al.* [172] are also in the same accuracy range. Nevertheless, these last results are probably underestimated in relation to the expected LDA and PBE values for their model, because the experimental *hcp-Zn* structure has been assumed in the calculations – while it is known that LDA/PBE under/overestimate the lattice constants of solids.

<sup>††</sup> I.e. the enthalpy of the reaction  $Zn_{(s)} + \frac{1}{2}O_{2(g)} \rightarrow ZnO_{(s)}$ . In this case, the chemical potential of the  $O_2$  molecule is approximated as its DFT total energy – which also must be performed by considering spin polarization effects, since the ground state of  $O_2$  is a *triplet state*.

### 3.5 – Electronic Properties

As we have seen in Section 2.6.3.1, all the electronic information for a given solid's unit cell is contained in its electronic band structure  $\{\varepsilon_i(\mathbf{k})\}$ , which is usually represented by plotting its energy bands  $\varepsilon_i(\mathbf{k})$  along the highly symmetrical lines of the system's *First Brillouin Zone*. Figures 3.4 and 3.5 show the respective band structures for the *w-ZnO* and *hcp-Zn* solids, obtained from our DFT (PP-PBE-DPZ) simulations. In both cases the calculations have been performed by using the lattice parameters and atomic positions optimized in Section 3.2.

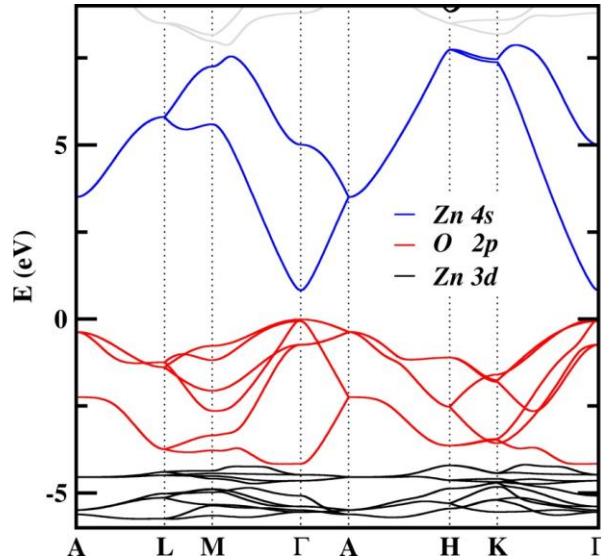


**Figure 3.4** – DFT (PP-PBE-DPZ) *w-ZnO* band structure represented along the highly symmetrical lines of the corresponding *First Brillouin Zone*. The Fermi level – in this case the top of the valence band – corresponds to the origin of the energy axis.

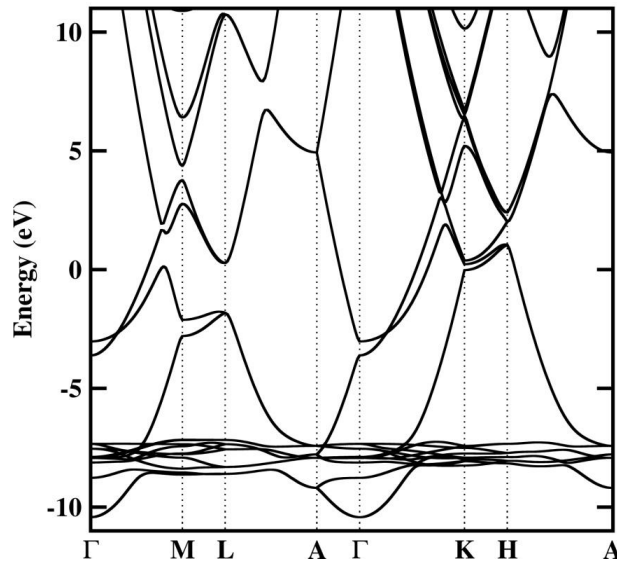


**Figure 3.5** – DFT (PP-PBE-DPZ) *hcp-Zn* band structure represented along the highly symmetrical lines of the corresponding *First Brillouin Zone*. The Fermi level corresponds to the origin of the energy axis.

Our calculations show the *w*-ZnO band structure with a direct  $\Gamma$ -point gap of 0.82 eV, here estimated as the difference between the *Valence Band Maximum* (VBM) and the *Conduction Band Minimum* (CBM). These results are in very good agreement with most theoretical predictions based on conventional DFT calculations, where the size of the *w*-ZnO band gap is strongly underestimated with respect to experimental results because of the *band gap problem* of LDA/GGA functionals (Section 2.4.3.3). By analyzing the composition of the electronic levels  $\varepsilon_i(\mathbf{k})$  – i.e. the contribution of the atomic orbitals in the molecular orbitals – it is possible to see that the bottom of the *Conduction Band* (blue lines in Figure 3.4) basically consists of Zn 4s orbitals, whereas the top of the *Valence Band* (red lines in Figure 3.4) has a strong O 2p orbitals character. Furthermore, the CBM is formed by a single band, whereas the VBM is composed of three non-degenerate bands (Figure 3.6), usually called *A*, *B* and *C* in literature. The energy splitting between the levels *A* and *C* in the  $\Gamma$ -point ( $\sim 50$  meV) is attributed to crystal field effects and is in good agreement with literature results [175]. A small energy splitting between *A* and *B* is also observed in experiments due to spin-orbit coupling effects [175]. Such effects are not included in our calculations and consequently no  $\Gamma$ -point energy splitting between *A* and *B* is evident in our results.

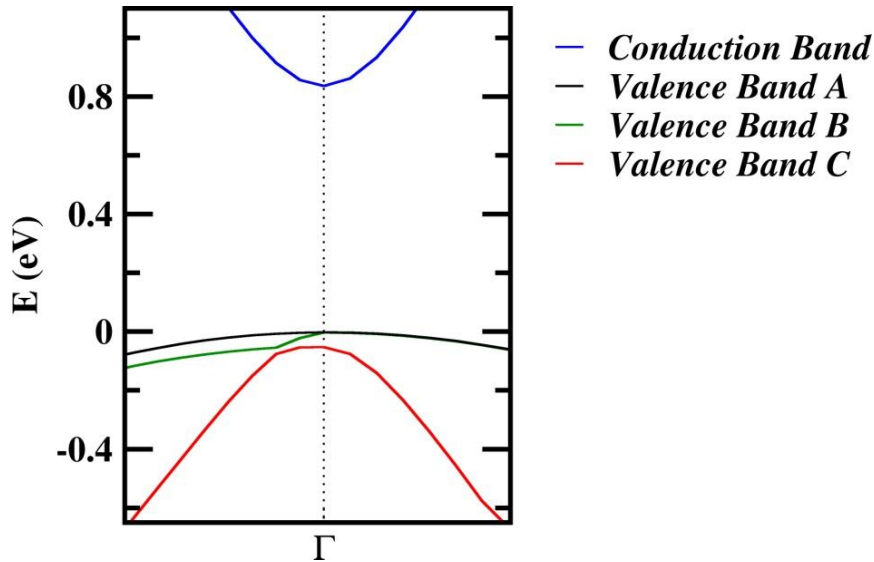


**Figure 3.6** – *w*-ZnO band structure represented around the  $\Gamma$ -point in *First Brillouin Zone*. The Fermi level corresponds to the origin of the energy axis.

The band-structure of *hcp*-Zn is more complex to analyze, because it has important hybridization gaps at the  $\Gamma$ , L and H points. These gaps have been demonstrated to be the origin of the *c/a* distortion observed for the *hcp*-Zn [176]. Nevertheless, a detailed discussion on the *hcp*-Zn band structure is out of scope in this thesis. Here the important result is that our model accurately reproduces other DFT *hcp*-Zn band structures [176], reinforcing the confidence in our calculations.

## Chapter Summary

In this chapter we have performed DFT-PBE simulations on bulk *w*-ZnO and *hcp*-Zn systems in order to test the used simulation parameters to be employed. We have found a good agreement with previous DFT simulations in literature for the electronic, structural and mechanical properties of both systems – which ensures the reliability of our simulations.







# Chapter 4

---

## Functionalized ZnO Non-Polar Surfaces

*"God made the Bulk; but Surfaces were created by the Devil."*

*Wolfgang Pauli – Austrian Physicist.*

In this chapter, we will employ DFT calculations to investigate the interactions of ZnO-(10 $\bar{1}$ 0) surfaces with five different organic functional groups (i.e. –OH, –NH<sub>2</sub>, –SH, –COOH and –CN). Our aim is identifying effective anchoring groups for stable functionalization of ZnO-(10 $\bar{1}$ 0) – the dominant surface in ZnO nanowires – while gaining some insight on its surface chemistry. We will analyze the influence of the surface coverage on adducts' geometries and binding energies, and also compare the relative stability of the surface adducts under different chemical conditions – including humid atmospheres and aqueous media. A special emphasis will be given to the characterization of the ligand-substrate interactions in each case, performed by analyzing the electronic structure of the modified surfaces\*.

### 4.1 – Surface Functionalization and ZnO

Surface functionalization is a critical issue in surface science and nanotechnology. Through functionalization, it is either possible to enhance the intrinsic properties of a material or add new capabilities to them, which is essential to develop high-performance hybrid-materials. In the past few years, several hybrid nanodevices – with specific or multiple functionalities (such as e.g. electric conductivity, molecular recognition properties or light sensing) – have been designed by capping semiconductor surfaces with organic molecules, polymers, biomolecules or inorganic thin films [180-184]. Among the substrates used in such devices, ZnO has been one of the most investigated, once its electric, magnetic and optical properties can be significantly influenced by functionalization [155,157,185,186]. Hybrid ZnO nanostructures are also often suggested for chemical and bio-sensing applications [12,187,188], where the

---

\* The theoretical characterization of clean ZnO surfaces has been addressed several times in literature [177-179]; thus we will not address it specifically in this chapter. The subject will be also extensively discussed in Chapter 5, in the context of the validation of our SCC-DFTB model for ZnO.

functionalization with biomolecules – i.e. enzymes, proteins, nucleic acids, etc. – results in high selective responses against desirable target analytes, such as specific proteins or bio-markers for example.

The functionalization of ZnO surfaces and nanostructures has been attempted with several different molecules – including carboxylic acids, thiols, amines and phosphonic acids [157,185,186,189,190] – but conflicting results have been reported in many cases [157,186,189]. Thiols and benzoic acids, for example, have formed stable monolayer (ML) coverages on ZnO in some experiments [157,190], whereas others have yielded non-uniform coverages or even just weakly physisorbed layers [189,191]. That demonstrates not only that well-controlled experimental conditions are critical while functionalizing ZnO, but also that our understanding of this subject is still rather limited. Fundamental aspects of the ZnO surface chemistry remain either entirely unknown or not well understood. For example, it has been assumed for a long time that Zn sites on ZnO surfaces act as Lewis acids [192-196], although such a hypothesis has never been seriously investigated with theoretical methods. Circumstantial evidences like contact angle measurements[191], cyclic voltammograms [197] or even supposed similarities with other metal oxides [198] have been appointed as signatures of covalent ligand-substrate interactions on ZnO surfaces, even though such evidences can hardly provide any electronic structure information. Hence, the current understanding on the ZnO surface chemistry still has a strong speculative character; and a very limited predictive power consequently.

That is a serious drawback of ZnO compared to other nano-materials, such as carbon or silicon, whose basic functionalization protocols rely on very well-established organic chemistry principles. Besides, the reactivity of carbon and silicon compounds has been for a long time investigated with high-level quantum-chemistry methods and is often rationalized in terms of molecular orbitals – even at introductory textbook level – whereas simulating realistic ZnO models is still challenging in many cases. As a matter of fact, there is a growing activity in simulating the adsorption of small inorganic molecules on ZnO [199-203], but the characterization of the ligand-substrate chemical interactions has been mostly bypassed. In such investigations, the major focus has been dedicated to: *i)* surface adduct geometries [199,201,204], *ii)* adsorption phase-diagrams [199, 200, 204] and *iii)* adsorption-induced changes on energy gaps [205,206] or magnetic properties [207,208], with very little effort done to rationalize the adsorption processes from a chemical perspective. Despite that, understanding the surface chemistry of ZnO at electronic structure level is still a crucial step towards the rational design of functional ZnO hybrid materials.

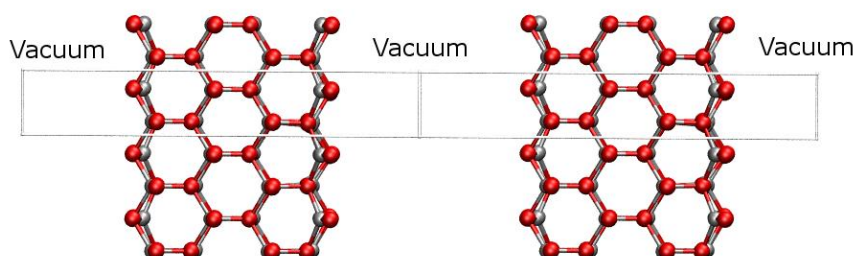


**Figure 4.1** – The slab approach for simulating surfaces with periodic boundary conditions. A suitable vacuum region must be introduced in the system's unit cell – perpendicular to the surface's normal – in order to isolate consecutive surface from each other in the periodic scheme.

## 4.2 – Simulation Details

In this study, we have used substituted methane molecules (Me-X, with X= NH<sub>2</sub>, OH, SH, COOH and CN) as prototype ligands. These molecules have been selected based on two very simple criteria: *i*) the availability of electron lone pairs, necessary for checking the formation of acid-base adducts with the surface Zn sites; and *ii*) the small molecular volume, in order to minimize repulsive steric effects. The surfaces have been modeled within the so-called *slab approach* [179] (Figure 4.1), by using *periodic boundary conditions* (PBC) in all directions and suitably oriented supercells – containing 16-atomic ZnO layers<sup>†</sup> and a 50 Å vacuum region along the [10 $\bar{1}$ 0] direction. We have considered the monolayer (ML) and half-monolayer ( $\frac{1}{2}$  ML) coverages, with one ML corresponding to one ligand molecule for each ZnO surface pair.

The optimized slab geometries and their respective total energies have been obtained from DFT-PBE calculations performed with the SIESTA package [146]. In these calculations, we have used double- $\zeta$  plus polarization function (DZP) basis sets and norm-conserving *Troullier-Martins* pseudopotentials (PP) [145] for representing the valence and inner electrons respectively – with Zn 3d electrons included in the valence. Converged (4 x 3 x 1) *Monkhorst-Pack* grids [152] have been employed for the *k*-points sampling and all atomic positions have been relaxed with the *conjugated gradient* (CG) algorithm till all forces become smaller than 0.01 eV/Å. Along the directions parallel to the surface, the lattice parameters have been derived from the *w*-ZnO structure optimized in Section 3.3.

Although DFT-PBE calculations yield accurate results for the ground-state properties of ZnO, the *band gap problem* (Section 2.4.3.3) may impose serious limitations to the electronic structures analysis of functionalized surfaces if intra-gap states are involved. Therefore, we have performed extra LDA+U calculations in order to get a better qualitative picture of the surfaces' electronic structures, for both bare and functionalized forms. In these calculations we have employed the projected augmented wave method [209] – as implemented in the VASP package [153,154] – using a plane-wave energy cutoff of 500 eV. Single-point calculations have been performed on the geometries previously optimized with the PBE functional, also keeping the same grid for the *k*-points sampling. The LDA+U Hubbard (U) and exchange (J) parameters have been obtained from [142] for the Zn 3d and O 2p orbitals. Test calculations have showed ligands' levels insensitive to the LDA+U corrections applied on their orbitals.

## 4.3 – Thermodynamic Properties of Functionalized Surfaces

### 4.3.1– Ligand-Substrate Bond Strength and Adsorption Regimes

The strength of individual ligand-substrate interactions can be characterized by their binding energies ( $E_B$ ):

$$E_B = \frac{E_T - E_{10\bar{1}0} - n_i \mu_i}{n_i} \quad (4.1)$$

---

<sup>†</sup> Atomic relaxations extend only until the third atomic layer in ZnO-(10 $\bar{1}$ 0) surfaces [177-179], which makes 16-atomic layers a quite conservative choice in order to isolate the two surfaces created in the slab model from each other.

where  $E_T$  is the total energy of the functionalized surface,  $E_{10\bar{1}0}$  is the total energy of the ZnO-(10 $\bar{1}$ 0) bare surface,  $\mu_i$  is the chemical potential of the ligand  $i$  – assumed as the free-ligand total energy – and  $n_i$  is the total number of ligands adsorbed.

Table 4.1 summarizes the binding energies for all the different surface adducts tested. As a general trend, it is possible to identify that the  $\frac{1}{2}$ ML coverages show stronger ligand-substrate interactions than their ML counterparts. Such an effect is partially explained by ligand-ligand repulsions, which are already expected for densely packed coverages. Two different adsorption regimes have been recognized: *i*) the non-dissociative adsorption, favored for the Me–CN, Me–NH<sub>2</sub> and Me–OH ligands and *ii*) the dissociative adsorption, favored for the Me–SH and Me–COOH ones. It is also clear that the ligand-substrate interactions are much weaker for the aprotic Me–CN ligand than for all its protic counterparts.

**Table 4.1.** – Adduct binding energies ( $E_B$ ) for different ligands on the ZnO-(10 $\bar{1}$ 0) surface. All values of  $E_B$  are given in eV.

Me–X	Ligand Form	$\frac{1}{2}$ ML	ML
–CN	<i>Dissociated</i>	-	-
	<i>Non-dissociated</i>	-0.80	-0.48
–NH <sub>2</sub>	<i>Dissociated</i>	-0.94	-0.18
	<i>Non-dissociated</i>	-1.35	-0.88
–OH	<i>Dissociated</i>	-1.06	-0.75
	<i>Non-dissociated</i>	-1.30	-1.02
–SH	<i>Dissociated</i>	-1.79	-1.03
	<i>Non-dissociated</i>	-0.82	-
–COOH	<i>Dissociated</i>	-2.07	-1.39
	<i>Non-dissociated</i>	-	-

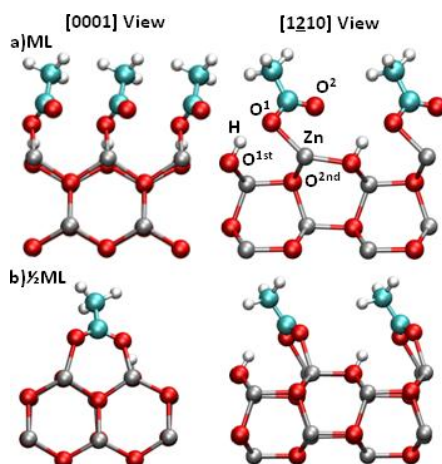


**Figure 4.2** – Optimized geometries for the Me–COOH surface adduct in the ML (a) and  $\frac{1}{2}$ ML (b) coverages.

## 4.3.2 – Coverage Stability

### 4.3.2.1 – Does a Stronger $E_B$ Yield a More Stable Coverage?

Although the  $E_B$  determines how strong individual ligand/substrate interactions are, its definition overlooks how large the area occupied by the surface adducts in each particular case is. However, the thermodynamic stability of a modified surface is always determined by the Gibbs free energy release of the adsorption process – which is an extensive property. Thus, directly comparing  $E_B$  values for analyzing the relative stability of modified surfaces may yield misleading conclusions. Consider the case of the adsorption of Me-COOH (at  $T = 0\text{K}$ ) as example: in the  $\frac{1}{2}\text{ML}$  coverage each Me-COOH molecule adsorbs on two distinct Zn surface sites (Figure 4.2); whereas in ML coverages each Me-COOH molecules docks to only one Zn on the surface. Consider now the Gibbs free energy releases for the adsorption of Me-COOH on a  $2\times 1$  surface unit – i.e. a surface area containing two ZnO pairs: for  $\frac{1}{2}\text{ML}$  case the energy release will be equal to  $E_B^{\frac{1}{2}\text{ML}}$  (i.e.  $-2.07\text{ eV}$ ), since only one molecule occupies the whole  $2\times 1$  surface unit. Yet in the ML case the energy release will be two times  $E_B^{\text{ML}}$  (i.e.  $-2.78\text{ eV}$ ), since there are two molecules occupying the  $2\times 1$  surface unit at the same time. Despite its corresponding surface adduct has a weaker  $E_B$ , the ML coverage is favored because of the larger number of ligand-substrate interactions per unit area. Furthermore, the definition of  $E_B$  also disregards the influence of the experimental conditions on the chemical potential of the ligands, which prohibits estimations of the stability of a particular coverage under reactive conditions.

Thus, the stability of modified substrates can be better estimated by comparing their *surface Gibbs free energy variation* ( $\Delta\gamma$ )[200]:

$$\Delta\gamma_i = \frac{E_T - E_{10\bar{1}0} - n_i(\mu_i + \Delta\mu_i)}{A} \quad (4.2)$$

where  $A$  is an standard area unit, assumed here as the area of a  $2\times 1$  ZnO surface unit, and  $\Delta\mu_i$  is a term introduced to account to the influence of the experimental conditions on  $\mu_i$ .

### 4.3.2.2 – Coverage Stability Under Ligand-rich Conditions.

Under ideal synthetic conditions, a uniform modified surface is formed when the clean substrate is exposed to the ligand, in abundant quantities and without interference of competing adsorbates. Such process can be simply simulated – within the ideal gas approximation – by assuming  $\Delta\mu_i = 0$  in the Eq. 4.2, which corresponds to having a reaction chamber containing only the substrate and a free-ligand gas at standard pressure (i.e.  $1\text{ atm}$ ).

Under such ligand-rich conditions, we have found the ML coverage as the thermodynamically stable phase for the most of the considered ligands (Figure 4.3). The Me-COOH-ML coverage has resulted in the most stable surface, whose  $\Delta\gamma = -2.78\text{ eV}$  indicates the carboxyl group as an effective anchoring agent for ZnO functionalization. The adsorption of Me-SH (ML, dissociative), Me-NH<sub>2</sub> and Me-OH (ML, non-dissociative) also lead to a considerable surface stabilization under ligand-rich conditions, with  $\Delta\gamma = -2.06\text{ eV}$ ,  $-2.02\text{ eV}$  and  $-1.76\text{ eV}$  respectively. This

is in good agreement with recent experiments on ZnO surface modification [185, 186, 189, 190], where these groups have been used to anchor organic molecules on ZnO. The Me-CN-ML coverage has been found less favorable ( $\Delta\gamma = -0,98$  eV), although still fairly spontaneous under the considered conditions.

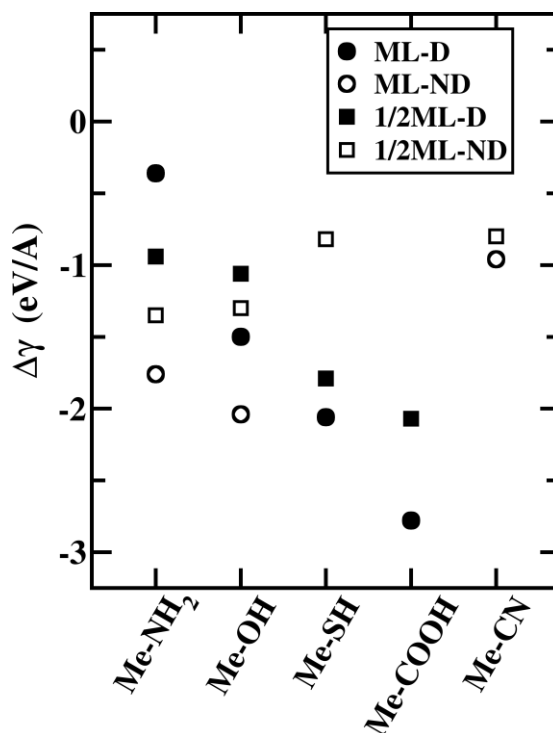


**Figure 4.3** – Surface free-energy variation ( $\Delta\gamma$ ) for ZnO-(10 $\bar{1}$ 0) surfaces functionalized with substitute methane molecules under ligand-rich conditions – calculated with DFT (PP-PBE-DPZ). The abbreviations (D) and (ND) state for the dissociated and non-dissociated ligand forms respectively.

#### 4.3.2.3 – Coverage Stability under Ordinary Laboratory Conditions

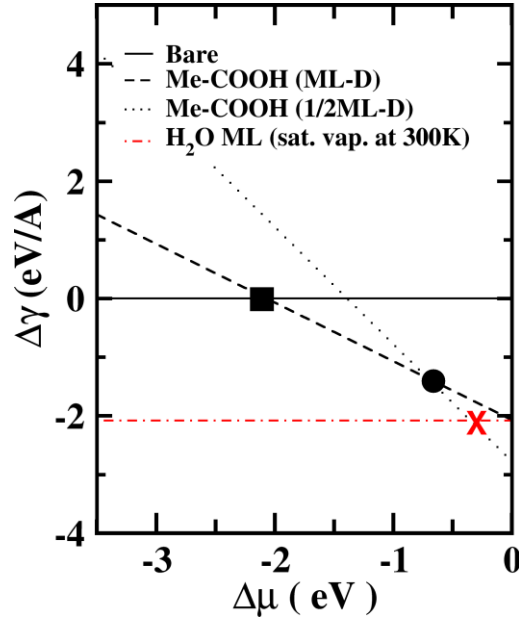
While modified ZnO-(10 $\bar{1}$ 0) surfaces have been shown to form fairly spontaneously under ligand-rich conditions, the technological applicability of such systems depends on their stability under ordinary atmospheric conditions. Therefore, we have estimated the adsorption phase diagrams for all considered ligands by varying their chemical potentials parametrically – via  $\Delta\mu$  in Eq. 4.2.

Figure 4.4 shows the estimated phase diagram for the dissociated Me-COOH case. As discussed in the last section, the ML coverage is favored at ligand-rich conditions (i.e.  $\Delta\mu = 0$ ), with the phase transitions to the  $\frac{1}{2}$ ML and to the bare surface (BS) taking place at  $\Delta\mu \approx -0.7$  eV and  $\Delta\mu \approx -2.1$  eV respectively. These  $\Delta\mu$  values can be better interpreted if translated into macroscopic variables via the thermodynamic relation:

$$\Delta\mu_i = RT\ln(p'_i) \quad (4.3)$$

where  $R$  is the universal gas constant,  $T$  is the absolute temperature and  $p'_i$  is the ligand partial pressure in the gas mixture. Assuming ordinary laboratory

pressure (1atm) and temperature (300K), it follows from Eq. 4.3 that the Me-COOH-ML  $\rightarrow$  Me-COOH- $\frac{1}{2}$ ML transition takes place only under ligand-poor environments, with  $p'_{Me-COOH}$  in order of  $10^{-12}$  atm. Besides, a  $p'_{Me-COOH}$  of  $\approx 10^{-36}$  atm would be necessary in order to completely desorb the Me-COOH- $\frac{1}{2}$ ML. Just to put these values in perspective, the average pressure in outer space is  $\approx 3 \times 10^{-20}$  atm.



**Figure 4.4** – Estimated phase diagram for a ZnO-(10 $\bar{1}$ 0) surface modified with Me-COOH– calculated with DFT (PP-PBE-DPZ). The symbols ● and ■ mark respectively the Me-COOH-ML  $\rightarrow$  Me-COOH- $\frac{1}{2}$ ML and the Me-COOH- $\frac{1}{2}$ ML  $\rightarrow$  Bare Surface phase transitions. The symbol X indicates the Me-COOH-ML  $\rightarrow$  H<sub>2</sub>O-ML transition under an atmosphere saturated with water vapor – at absolute temperature T = 300K and total pressure P = 1atm.

**Table 4.2** – Transition Chemical Potential Shifts ( $\Delta\mu^\ddagger$ ) and Partial Pressures ( $p^\ddagger$ ) calculated for different ZnO-(10 $\bar{1}$ 0) modified surfaces. The abbreviation BS stands for Bare Surface. We have assumed the absolute temperature T = 300K and total pressure P = 1atm.

Me-X	Ligand Form	ML $\rightarrow$ $\frac{1}{2}$ ML		$\frac{1}{2}$ ML $\rightarrow$ BS	
		$\Delta\mu^\ddagger$ (eV)	$p^\ddagger$ (atm)	$\Delta\mu^\ddagger$ (eV)	$p^\ddagger$ (atm)
-COOH	Dissociated	-0.7	$\approx 10^{-12}$	-2.1	$\approx 10^{-36}$
-SH	Dissociated	-0.3	$\approx 10^{-7}$	-1.8	$\approx 10^{-31}$
-NH <sub>2</sub>	Non-dissociated	-0.4	$\approx 10^{-7}$	-1.4	$\approx 10^{-24}$
-OH	Non-dissociated	-0.7	$\approx 10^{-12}$	-1.3	$\approx 10^{-22}$
-CN	Non-dissociated	-0.2	$\approx 10^{-4}$	-0.8	$\approx 10^{-14}$

The phase transition analysis has been extended to the remaining ligands, with their respective *transition chemical potential shifts* ( $\Delta\mu^\ddagger$ ) and *partial pressures* ( $p^\ddagger$ ) summarized in Table 4.2. Besides Me-COOH, Me-OH is the only ligand leading to stable ML coverage at trace ligand amounts (i.e.  $p_i'$  smaller than

$10^{-9}$  atm). Me-SH and Me-NH<sub>2</sub> form stable ML under ligand pressures larger  $10^{-7}$  atm, whereas the ML $\rightarrow\frac{1}{2}$ ML transition is expected at  $p' \sim 10^{-4}$  atm in the Me-CN case. In all cases, the total desorption of the ligand (i.e. the  $\frac{1}{2}$ ML $\rightarrow$  BS transition) is expected only under extreme ligand-poor conditions.

However, the discussion until now has not taken into account possible competing ligands present in the atmosphere. Among potential interfering atmospheric species, water is the most critical for two distinct reasons: *i*) water also strongly binds to ZnO-(10 $\bar{1}$ 0) substrates, with  $E_B = -1.13$  eV for the ML coverage [200]; and *ii*) it is abundant under ordinary laboratory conditions. Thus, in order to consider the influence of water on the stability of the modified substrates, we have calculated  $\Delta\gamma$  for a H<sub>2</sub>O-ML coverage on the ZnO-(10 $\bar{1}$ 0) substrate ( $\Delta\gamma_{H_2O}$ ), under a 1 atm/300K atmosphere saturated with water vapor (i.e.  $p'_{water} = 0.035$  atm). The result has been also included in Figure 4.4 (dotted/dashed red line), where the Me-COOH-ML  $\rightarrow$  H<sub>2</sub>O-ML transition can be identified at  $\Delta\mu \approx -0.35$  eV ( $p'_{Me-COOH} \approx 10^{-6}$  atm). Hence, it is safe to assume that the Me-COOH-ML coverage must be also considerably stable under ordinary room conditions. In contrast, the Me-COOH- $\frac{1}{2}$ ML coverage is not expected to be formed under humid conditions.

For the remaining ligands, thermodynamically stable coverages in humid environments are expected only under ligand-rich conditions – or even extreme ligand-rich conditions for the Me-CN case – as shown in Table 4.3. Nevertheless it is important to keep in mind that the formation of uniformly functionalized ZnO surfaces has been demonstrated to be energetically favorable under controlled atmospheres, while the mechanism of substituting the organic layer by a water layer has never been investigated. In other words, although the most of functionalized surfaces investigated here are expected to be thermodynamically unstable under humid conditions – except for the Me-COOH case – they still may be kinetically stable. Such kinetic stability has been experimentally demonstrated for functionalized TiO<sub>2</sub> nanoparticles, which are able to keep the functionalization even in very aggressive chemical environments after functionalization [210]. However, investigating such kinetic stability hypothesis and its atomistic mechanisms would involve long and demanding molecular dynamics simulations, which are out of our scope.

**Table 4.3** – Thermodynamic critical conditions for *i*-ML  $\rightarrow$  H<sub>2</sub>O-ML surface phase transitions under atmospheres saturated with water vapor – at absolute temperature T = 300K and total pressure P = 1atm.

<i>i</i> -ML $\rightarrow$ H <sub>2</sub> O-ML		
<i>i</i>	$\Delta\mu^{\ddagger}$ (eV)	$p^{\ddagger}$ (atm)
Me-NH <sub>2</sub>	0.16	$\approx 10^2$
Me-SH	0.01	$\approx 1.5$
Me-COOH	-0.35	$\approx 10^{-6}$
Me-OH	0.02	$\approx 2.0$
Me-CN	0.55	$\approx 10^9$



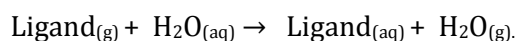
#### 4.3.2.4 – Coverage Stability in Aqueous Media

Since the thermodynamic condition for a gas-liquid equilibrium is the equality of the chemical potentials in both phases, the  $\Delta\gamma_{H_2O}$  value calculated in Section 4.2.2.3 is also valid for the adsorption of liquid water on the ZnO-(1010). Besides, the limiting ligand partial pressures for the ML coverages can be easily converted into molar fractions for an aqueous solution – via the *Raoult's Law*<sup>‡</sup> [211]. Consequently, it is possible to estimate the critical ligand concentrations ( $C^\ddagger$ ) necessary to keep the ML coverages stable in water.

Nevertheless, the *Raoult's Law* does not take solute-solvent interactions into account, and the  $\Delta\mu^\ddagger$  values must be corrected according to the thermodynamic cycle in Figure 4.5. Such correction can be performed by incorporating the ligand/water *relative solvation energies* [212] ( $\Delta\Delta G_{Solv}$ ) into  $\Delta\mu$ :

$$\Delta\mu_i = \Delta\Delta G_{Solv} + RT\ln(p_i) \quad (4.4)$$

where  $\Delta\Delta G_{Solv}$  corresponds exactly to the free energy release of the reaction:



Based on previous molecular dynamics simulations for the considered ligands [213], we have estimated  $\Delta\Delta G_{Solv}$  and  $C^\ddagger$  in water for all cases (Table 4.4). In the Me-COOH case, the low  $C^\ddagger$  (2 mmol·l<sup>-1</sup>) indicates that the stability of the ML coverage must be appreciable in moderate diluted solutions. It is also interesting that, for the Me-SH ligand, the relatively large ligand's  $\Delta\Delta G_{Solv}$  helps in stabilizing the modified surface in the aqueous media, resulting in a  $C^\ddagger$  close to as that for Me-COOH. These results reasonably agree with recent experiments in the literature, which have demonstrated the successful functionalization of ZnO nanotips by immersing them into solutions of carboxylic acids diluted to 2 mmol·l<sup>-1</sup>, although the same procedure has failed for thiols [189]. For the Me-OH and Me-NH<sub>2</sub> cases, the high  $C^\ddagger$  values (~ 30 and 10<sup>4</sup> mol·l<sup>-1</sup> respectively) – although unphysical – clearly indicate that such ligands would be washed out in water.

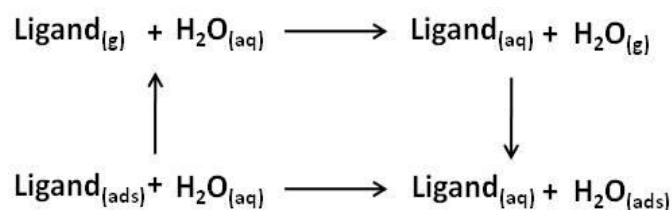


**Figure 4.5** – Thermodynamic cycle for substituting an adsorbed ligand on the substrate for a water molecule in aqueous media.

<sup>‡</sup> Here we have to assume that the solutions density does not change with the solutes concentration.

**Table 4.4** – Solvation Energies ( $\Delta G_{\text{solv}}$ ) and Relative Solvation Energies ( $\Delta\Delta G_{\text{solv}}$ ) for different ligands ( $i$ ) in water, besides the critical chemical potential shifts ( $\Delta\mu^\ddagger$ ), vapor pressure ( $p_{\text{vap}}$ ) and critical ligand concentrations ( $C^\ddagger$ ) for the  $i\text{-ML} \rightarrow \text{H}_2\text{O-ML}$  surface phase transitions in water. We have assumed the absolute temperature  $T = 300\text{K}$  and total pressure  $P = 1\text{atm}$ .

$i\text{-ML} \rightarrow \text{H}_2\text{O-ML}$					
$i$	$\Delta G_{\text{solv}}$ (eV)	$\Delta\Delta G_{\text{solv}}$ (eV)	$\Delta\mu^\ddagger$ (eV)	$p_{\text{vap}}$ (atm)	$C^\ddagger$ ( $\text{mol}\cdot\text{l}^{-1}$ )
<b>Me-NH<sub>2</sub></b>	-0.21 <sup>a</sup>	0.08	0.08	4.189 <sup>b</sup>	$\approx 10^3$
<b>Me-SH</b>	-0.04 <sup>a</sup>	0.25	-0.24	2.061 <sup>c</sup>	$\approx 0.003$
<b>Me-COOH</b>	-0.29 <sup>a</sup>	0.00	-0.35	0.023 <sup>c</sup>	$\approx 0.002$
<b>Me-OH</b>	-0.22 <sup>a</sup>	0.07	-0.06	0.184 <sup>c</sup>	30
<b>H<sub>2</sub>O</b>	-0.29 <sup>a</sup>	-	-	-	-

a) Ref. [213]

b) Ref. [214]

c) Value calculated from the *Antoine Equation* ( $\text{Log}_{10}(p_{\text{vap}}) = A - [B/(C-T)]$ ) for  $T=300\text{K}$  and the parameters  $A$ ,  $B$  and  $C$  obtained from ref. [215].

#### 4.4 – Adduct Geometries and Electronic Structure Analysis

While in the last sections we have identified thermodynamically stable configurations for all considered ligand-substrate pairs under diverse conditions, now we will analyze their electronic structure and discuss the nature of the ligand-substrate interactions in some of these configurations. We will focus on the stable configurations under ligand-rich conditions (i.e.  $\Delta\mu = 0$ ), since they have been determined as the most relevant ones under ordinary laboratory conditions (Section 4.3.2.3).

As mentioned before, the differences in the  $E_B$  values for the different surface adducts are not self-explaining from a chemical point of view. In order to understand them better it is necessary to take a closer look into the electronic structure of each surface adduct. In comparison with the bare ZnO-(1010) surface (Figure 4.6), all ligands induce variations on a broad region of the ZnO Valence Band (VB) – from -2.5 to -6 eV approximately – which is an evidence of delocalized ligand-substrate interactions. Nevertheless, the most noticeable changes take place in the band-gap region, where the surface resonance observed for the clean surface ( $\sim -2.3$  eV) – assigned to electron lone-pairs on oxygen surface sites – is apparently suppressed in the Me-OH and Me-NH<sub>2</sub> cases or substituted by new states in the remaining ones.

In order to gain some chemical insight from these changes, we have analyzed the projected density of states (PDOS) for all ML surface adducts. The results are presented in the next sections, giving a brief discussion on the adsorption geometry in each case.

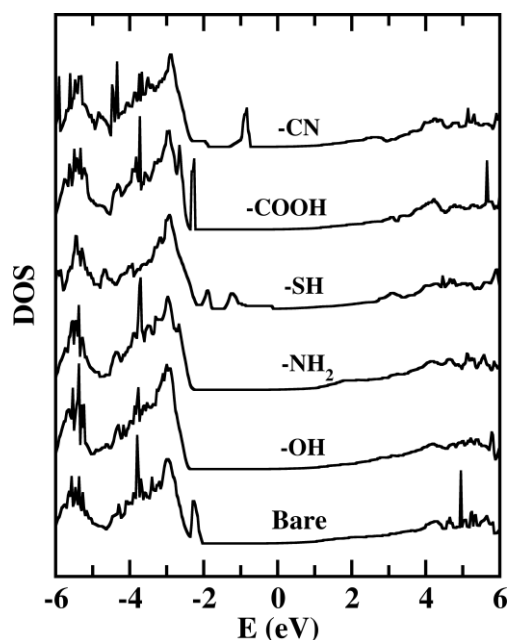


**Figure 4.6** – Density of States (DOS) for the bare and modified ZnO-(1010) surfaces. The origin of the energy axis corresponds to the conduction band minimum in all cases. All levels with negative energies are fully occupied. Calculations within the DFT (PP-LDA+U-PW) level of theory.

#### 4.4.1 – Me-OH and Me-NH<sub>2</sub> on ZnO-(1010)

As mentioned above, both Me-OH and Me-NH<sub>2</sub> ligands favor the non-dissociative adsorptions on the ZnO-(1010) surface, assuming a mono-dentate adduct geometry in both investigated coverages (Figures 4.7 and 4.8). Interatomic distances of 2.09Å and 2.18Å have been respectively determined for the Zn-O<sup>1</sup> and Zn-N pairs in the ML coverage, and 2.09Å and 2.10Å for the ½ML case. Another important similarity is that both adducts show a hydrogen bond with oxygen surface sites (O<sup>1st</sup>) – with bond lengths of 1.40 and 1.71Å for the O<sup>1</sup>H...O<sup>1st</sup> and NH...O<sup>1st</sup> interactions respectively (1.45Å and 1.68Å in the ½ML case). Additionally, the tilting angles of the Methyl group – with respect to the surface plane – have shown the same trend for both ligands, decreasing from ~ 100° in the ML coverage to ~ 30° in the ½ML case.

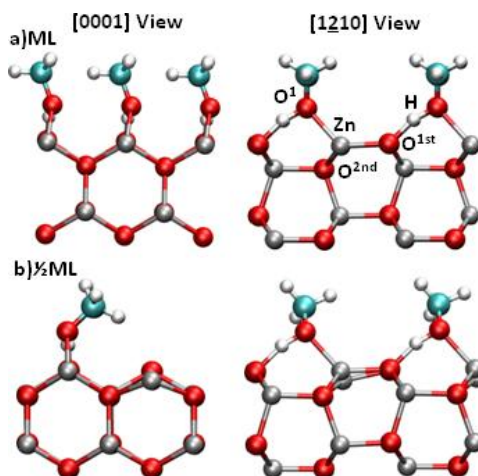


**Figure 4.7** – DFT (PP-PBE-DPZ) optimized geometries for the Me-OH surface adduct in the ML (a) and ½ML (b) coverages.

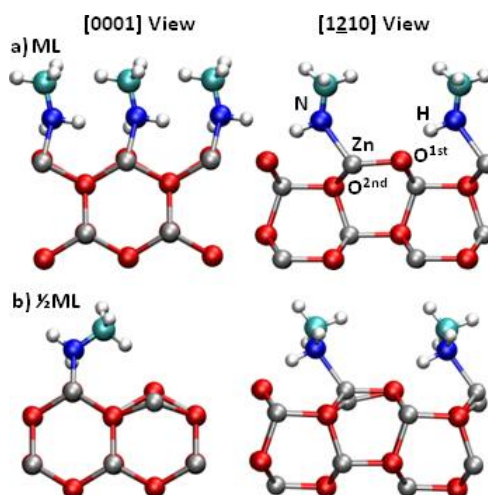


**Figure 4.8** - DFT (PP-PBE-DPZ) optimized geometries for the Me-NH<sub>2</sub> surface adduct in the ML (a) and ½ML (b) coverages.

With comparable adduct geometries, the Me-OH and Me-NH<sub>2</sub> surface adducts lead to very similar changes in the surface's electronic structure. Both ligands appear to suppress the surface resonances observed for the bare surface, resulting in a DOS apparently free of intra-gap levels (see Figure 4.6). This effect is a direct consequence of the hydrogen bonds formed on the surface, as evidenced by the PDOS depicted in the Figure 4.9 for the Me-NH<sub>2</sub> case. The picture shows important contribution from O<sup>1st</sup> to the valence band maximum (VBM), where the PDOS peak at ~ -2.5 eV evidences that localized O states still remain on the surface, although shifted slightly down in energy because of the hydrogen bond with the ligand. The PDOS analysis for the Me-OH case leads to identical qualitative conclusions.

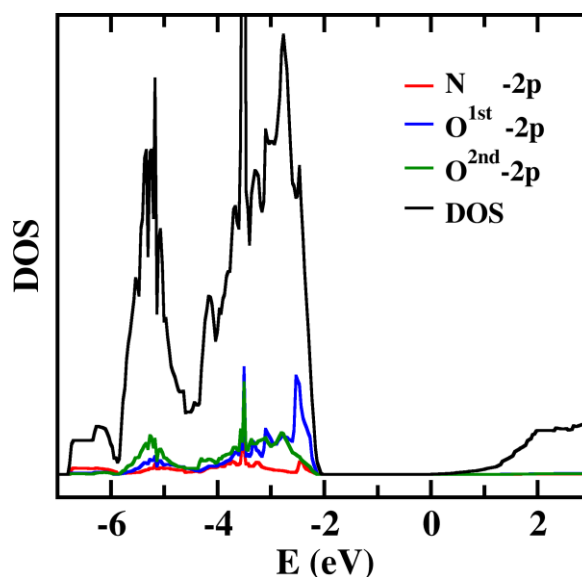


**Figure 4.9** - Projected density of states (PDOS) for the Me-NH<sub>2</sub>-ML surface adduct. The atomic labels convention follows that specified in Figure 4.8.a. The origin of the energy axis corresponds to the conduction band minimum. All levels with negative energies are fully occupied. Calculations within the DFT (PP-LDA+U-PW) level of theory.

Through the PDOS analysis it is also possible to identify the ligand-substrate electronic interaction, with a noticeable component from the N atom spread all along the VB. Nevertheless, the contributions from the Zn 4s orbitals are insignificant along the VB, indicating that the ligand-substrate interaction does not correspond to a Lewis acid-base adduct in this case. Instead, there is a delocalized interaction with the O network in the oxide, with the same pattern also found for the Me-OH case. Note that such delocalized electronic interactions do not necessarily have a bonding character. In fact, every energy band is always bonding in its lower and anti-bonding in its upper half. Hence, the covalent interaction in the Me-NH<sub>2</sub>-ML surface adduct has a slightly anti-bonding character, considering that the PDOS distribution for the N atom – or the O atom in the Me-OH case – is slightly concentrated in the VB's upper-part. In other words, the ligand-substrate covalent interactions are not expected to play any significant role in the stabilization of the surface adduct in these cases.

Despite this fact, the adsorption of Me-NH<sub>2</sub> and Me-OH still results in considerable surface relaxations. Whereas in the bare ZnO-(10 $\bar{1}$ 0) surface the Zn surface sites relax inward to a planar three-fold coordinated structure [178], in the modified case the ligand pulls the Zn atom back – almost to its ideal surface position – reestablishing its tetrahedral fourfold coordinated form. In the absence of remarkable covalent Zn-ligand interactions, such relaxations must be driven by electrostatic forces (ion-dipole interactions), which apparently is the main stabilizing factor in the adsorption process.

#### 4.4.2 – Me-SH and Me-COOH on ZnO-(10 $\bar{1}$ 0)

In contrast to the Me-OH and Me-NH<sub>2</sub> cases, the Me-SH and Me-COOH ligands favor the dissociative adsorption on the ZnO-(10 $\bar{1}$ 0) surface – in both ML and ½ML coverages.

Meta-stable non-dissociated forms have not been observed for the Me-COOH and Me-SH surface adducts in the ML coverage, with the conjugated gradient optimizations always yielding the dissociated forms. The same holds true for the Me-COOH-½ML adduct, whereas a non-dissociated form of the Me-SH-½ ML adduct has been found ~ 0.7 eV less stable than its dissociated counterpart (Table 4.1).

In the ½ML coverage, the Me-SH adduct ( $E_B = -1.79$  eV) relaxes towards a position nearly equidistant from two consecutive Zn sites, assuming a bridging geometry. The interatomic distances Zn<sup>1</sup>-S and Zn<sup>2</sup>-S (Figure 4.10.b) are measured as 2.41 and 2.49Å respectively, showing that the sulfur atom interacts with two distinct Zn sites simultaneously. The adsorption also induces considerable atomic relaxations down to the 3<sup>rd</sup> atomic layer below the surface. The O<sup>2</sup>-Zn<sup>4</sup> bond (Figure 4.10.b) – directly below the S atom – is ~ 5% shorter than its O<sup>1</sup>-Zn<sup>3</sup> and O<sup>3</sup>-Zn<sup>5</sup> analogs. Additionally, the H transfer to the substrate distorts the atomic relaxations, with the distance Zn<sup>2</sup>-O<sup>3</sup> (on the protonated side of the adduct) ~ 3.5% shorter than its Zn<sup>1</sup>-O<sup>1</sup> counterpart.

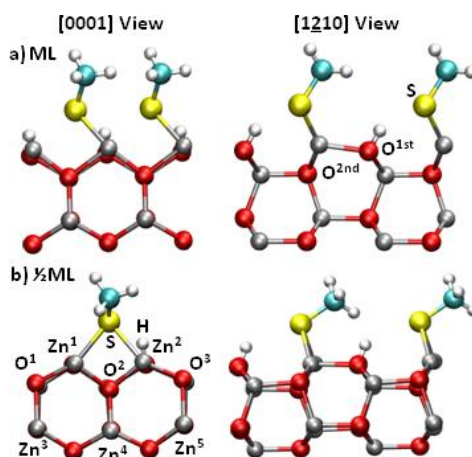


**Figure 4.10** – DFT (PP-PBE-DPZ) optimized geometries for the Me-SH surface adduct in the ML (a) and  $\frac{1}{2}$ ML (b) coverages.

In the ML coverage, the ligand does not assume a bridging geometry, showing the sulfur atom preferentially coordinated with one specific Zn site (Figure 4.10.a). However, different adduct geometries have shown almost isoenergetic behaviors (i.e.  $\Delta E_B \leq 0.01$  eV). For example, for two equally stable competing geometries – including that in Figure 4.10.a – we have found the same Zn<sup>2</sup>-S distance ( $\sim 2.30\text{\AA}$ ), but very different values for Zn<sup>1</sup>-S in each case ( $2.67\text{\AA}$  and  $3.13\text{\AA}$  respectively). This result indicates that the Zn-S interactions are noticeably flexible in such system.

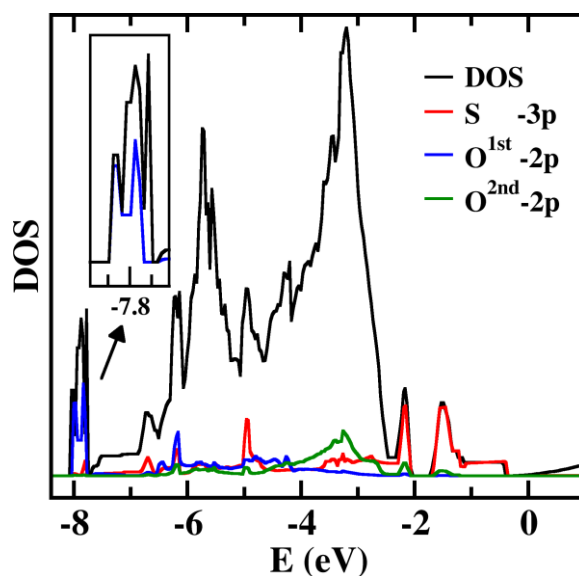


**Figure 4.11** – Projected density of states (PDOS) for the Me-SH-ML surface adduct. The atomic labels convention follows that specified in Figure 4.10.a. The origin of the energy axis corresponds to the conduction band minimum. All levels with negative energies are fully occupied. Calculations within the DFT (PP-LDA+U-PW) level of theory.

Concerning to its electronic structure, the Me-SH-ML adduct introduces two DOS peaks into the ZnO band-gap region, which can be interpreted as electron lone-pairs on the sulfur atom (Figure 4.11). The energy split observed on these levels probably originates on non-uniform electron-electron repulsions

experienced by distinct orbitals from S. Besides, the energy dispersion on the highest intragap level (from  $\sim -1.7$  eV to  $\sim -0.3$  eV) indicates electronic delocalization, which implies some hybridization among S atoms in neighboring ligands in the ML coverage. Note that  $\Delta E_B$  between the Me-SH-ML and Me-SH- $\frac{1}{2}$ ML surface adducts ( $\sim 0.8$  eV) is considerably larger than that between Me-OH-ML and Me-OH- $\frac{1}{2}$ ML cases ( $\sim 0.3$  eV), which is consistent with the larger size of the S atom. The top of the highest sulfur level is close to the conduction band minimum (CBM), but the system still has a small band-gap ( $\sim 0.3$  eV) and keeps its semiconductor character.

As observed for the Me-OH and Me-NH<sub>2</sub> cases, some covalent character is also evident for the Me-SH-ML adduct, with noticeable components from the sulfur orbitals spread all across the VB (see Figure 4.11). Other similarities are the dominance of an anti-bonding character on the sulfur's PDOS distribution and the absence of significant contributions from Zn 4s orbitals in the VB. As an apparent difference, a sharp peak at  $\sim -4.5$ eV occurs, being a signature of the localized S-C bond. In general, the chemical picture drawn for the Me-SH-ML adduct is similar to that in last section. The covalent interaction with the O network is again expected to play just a marginal role in the adduct stabilization, with no significant evidence of a classical Lewis acid-base adduct. This finding is in fact very consistent with the smooth  $E_B$  changes with the adduct's geometry.

Also the electrons on the second ZnO oxygen layer (O<sup>2nd</sup>) become affected by the Me-SH ligand, being shifted to higher energies due to Pauli repulsions with the sulfur electrons. Note that – in comparison with the Me-NH<sub>2</sub> case – the contributions of O<sup>2nd</sup> to the lower part of the VB are completely quenched, whereas their contributions to the VB's upper part are considerably enhanced.

Indeed, neither the dominant anti-bonding character of the covalent ligand-substrate interaction nor the electron-electron repulsion with the O<sup>2nd</sup> electrons are expected to stabilize the surface adduct. Hence, electrostatic interactions must again play a strong role on the stabilization of the surface adduct. In comparison with the Me-OH and Me-NH<sub>2</sub> cases, this mechanism is expected to be even stronger, since the dissociative adsorption – i.e. a proton transfer reaction – results in a positively charged surface plus an anionic ligand atop. In fact the atomic relaxations driven by the Me-SH-ML adduct reflect such enhanced electrostatic interaction, with the positively charged Zn surface sites appearing visibly above the ideal surface plane (see Figure 4.10.a).

Besides, the proton-transfer itself appears as factor to stabilize the Me-SH-ML adduct. The surface resonance otherwise on O<sup>1st</sup> – observed for the clean surface and in the Me-OH/Me-NH<sub>2</sub> cases – is completely quenched with the dissociative adsorption. Instead, a split DOS peak appears below the valence band minimum ( $\sim -7.8$  eV) due to the O-H bond formed on the surface. In other words, the proton-transfer reaction passivates the oxygen lone-pairs on the surface. Indeed, separating this effect from other chemical forces acting on the Me-SH-ML adduct is not trivial, but its importance becomes evident if one notes that  $\Delta E_B$  between the dissociated and no-dissociated Me-SH- $\frac{1}{2}$ ML forms is  $\sim 1$  eV.

For the Me-COOH-ML adduct (Figure 4.2.a), the PDOS analysis shows several similarities with its Me-SH-ML analog. The electronic levels involving O<sup>2nd</sup> are shifted to higher energies, although their contributions to the bottom of the VB are not completely suppressed in this case (Figure 4.12). Furthermore, there is a sharp DOS peak immediately below the valence band minimum ( $\sim 6.5$ eV), whose

the dominant contribution from  $O^{1st}$  indicates the passivation of the surface lone-pair by the proton-transfer reaction (see inset in Figure 4.12). In its place, two sharp DOS peaks appear close to the VBM; both assigned to the carboxylate ion, as evidenced by the strong contributions from the two carboxylic O atoms ( $O^1$  and  $O^2$ ) to these levels (see Figure 4.2.a). Additionally, the carboxylate anion also shows delocalized contributions spread along the VB.

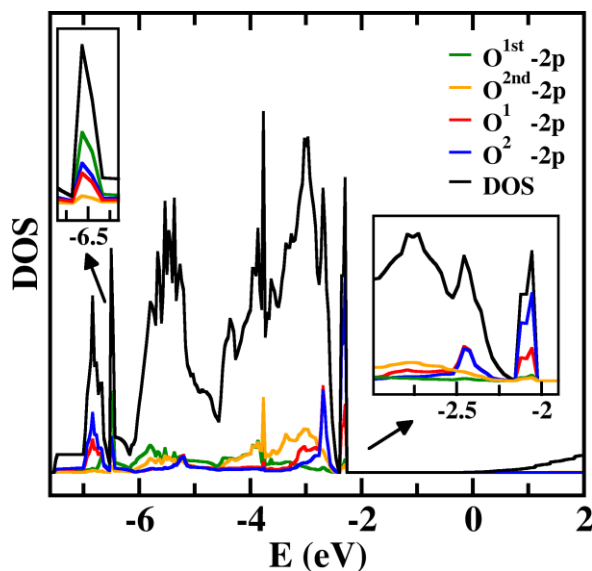


**Figure 4.12** – Projected density of states (PDOS) for the Me-COOH-ML surface adduct. The atomic labels convention follows that specified in Figure 4.2.a. The origin of the energy axis corresponds to the conduction band minimum. All levels with negative energies are fully occupied. Calculations within the DFT (PP-LDA+U-PW) level of theory.

For the surface resonance at  $\sim 2.2$  eV, the signatures of both  $O^1$  and  $O^2$  are quite similar, while a smaller contribution from the carboxylic carbon atom is perceptible in the same region (not shown). All three components show a shoulder in their PDOS distributions – from  $\sim -2.5$  to  $-3$  eV (inset in Figure 4.12), indicating some electronic hybridization with the substrate levels. However, such delocalized contribution decays faster for  $O^2$ , showing that the ligand-substrate electronic interaction is preferentially mediated through  $O^1$ . As discussed for the Me-SH case, such interactions are predominantly anti-bonding and also impose Pauli repulsions to the O network on the substrate. Consequently, electrostatic interactions and the passivation of the surface levels also seem to be the driving forces of the adsorption process in this case.

The ligand-substrate interactions are in fact very similar for the Me-COOH-ML and Me-SH-ML surface adducts. The most remarkable difference is the hydrogen bond verified for the Me-COOH-ML adduct (Figure 4.2.a) – which is completely absent in the Me-SH-ML case. Considering that DFT/PBE hydrogen bonds are estimated as  $\sim 0.23$  eV for  $OH\cdots O$  interactions [216], even their  $E_B$  look extremely similar. Finally, there are no significant contributions from Zn  $4s$  surface orbitals neither along the VB nor in the DOS peaks dominated by  $O^1$  and  $O^2$ . Furthermore, the Mulliken charges on the Zn surface are more positive in the modified surface, by  $\sim 0.2 e^-$ , than in its clean counterpart. These results clearly show that the formation of a classical Lewis acid-based surface adduct is also absent for the Me-COOH adsorption process.



The details on the atomistic structure of the Me-COOH surface adducts, in both ML and  $\frac{1}{2}$ ML coverages, will be given in Chapter 5, in the context of the validation of our SCC-DFTB model for ZnO.

#### 4.4.3 – Me-CN on ZnO-(1010)

Despite the weakest binding energy among all investigated species in this work, the Me-CN surface adducts are the only case where the ligand-substrate interactions are predominantly covalent. Already the adducts' geometries – which are very similar in the ML and  $\frac{1}{2}$ ML coverages (Figure 4.13) – give the first indication of such covalent predominance. Once on the surface, the ligand loses its otherwise linear geometry, with one of its C<sup>1</sup>-N  $\pi$ -bonds broken in favor of forming the O<sup>1st</sup>-C<sup>1</sup> bond with the surface (bond length  $\sim 1.57$  Å). In fact, there are strong contributions from the O<sup>1st</sup> surface site to DOS peaks between -6.5 and -8.6 eV, while the same DOS region is also shared by ligand's levels (see the insets in Figure 4.14). There is a clear hybridization among ligand's and substrate's levels, once more confirming the covalent character of the interaction. Moreover, the intra-gap state observed at  $\sim -1.0$  eV shows a strong component from the N atom, indicating the migration of C<sup>1</sup>-N  $\pi$ -electrons to that site. In fact, the Mulliken charge for the N atom in the adsorbed molecule is about 0.2  $e$  more negative than that for the free molecule.

There are also delocalized ligand levels spread across the VB, indicating the same kind of hybridization with the material's O network discussed in Sections 4.4.1 and 4.4.2. As in the previous cases, the Zn 4s orbital contributes very little to the VB. Despite of that, the Zn-N interatomic distance is measured as 1.94 Å, suggesting a strong electrostatic interaction between these two sites.

While the formation of ligand-substrate covalent bonds is evident for the Me-CN adducts, the interaction with the surface strongly disturbs the ligand's electronic structure. As a consequence, the net energy gain for the global adsorption process is quite small. In other words, the formation of strong ligand-substrate covalent bonds – like the O-C bond formed in this case – does not necessarily mean the formation of stable surface adducts – especially if the adsorption process results also in breaking a strong covalent bond, such as the  $\pi$ -C-N bond in this case.

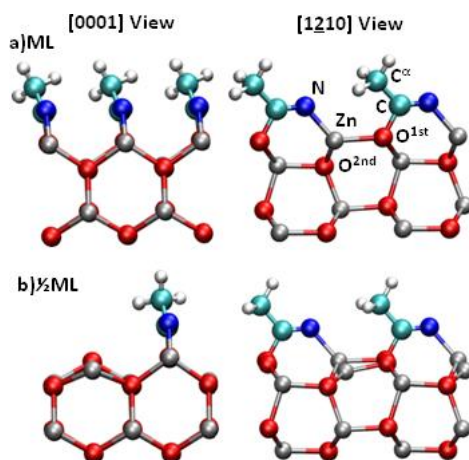


**Figure 4.13** – DFT (PP-PBE-DPZ) optimized geometries for the Me-CN surface adduct in the ML (a) and  $\frac{1}{2}$ ML (b) coverages.

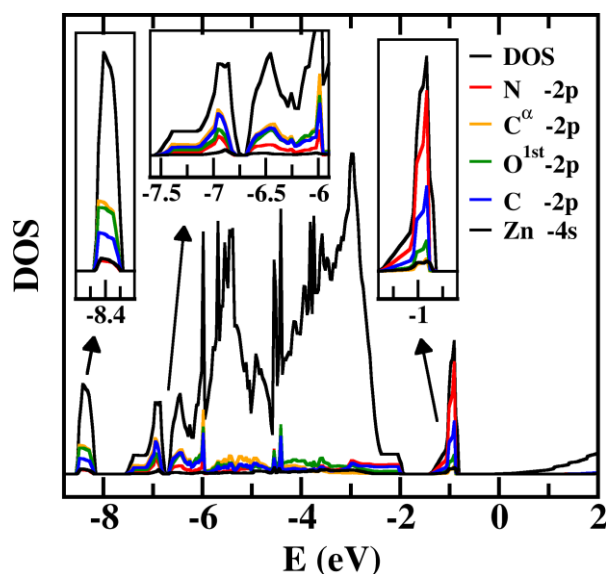


**Figure 4.14** – Projected density of states (PDOS) for the Me-CN-ML surface adduct. The atomic labels convention follows that specified in Figure 4.13.a. The origin of the energy axis corresponds to the conduction band minimum in all cases. All levels with negative energies are occupied. Calculations within the DFT (PP-LDA+U-PW) level of theory.

## Chapter Summary

In this chapter we have employed DFT calculations in order to investigate ZnO-(10 $\bar{1}$ 0) surfaces functionalized with different substituted methane molecules (i.e. Me-X, X = -OH, -NH<sub>2</sub>, -SH, -COOH, and -CN). By analyzing the electronic structure of the surface adducts, we have identified four different chemical forces acting on them: *i*) the covalent interaction between the electron rich-ligands with the ZnO oxygen network, *ii*) the electrostatic attraction between the electron-rich ligands and the positive Zn surface ions, *iii*) surface hydrogen bonds – for the Me-NH<sub>2</sub>, Me-OH and Me-COOH cases – and *iv*) the passivation of surface O levels through proton-transfer reactions – in the Me-COOH and Me-SH cases. Contradicting the usual chemical intuition, the formation of classical Lewis acid-base adducts on Zn surface sites has been not observed. Furthermore covalent ligand-substrate interactions have shown a predominant anti-bonding character for the Me-OH, Me-NH<sub>2</sub>, Me-SH and Me-COOH cases. For the Me-CN case, the formation of a covalent C-O ligand-substrate bond is demonstrated, but it disturbs the ligand's electronic structure, resulting in a small net energy gain for the global adsorption process. Concerning the stability of the modified surfaces, the ML coverage has been found as the favored phase under ligand-rich conditions in all cases. In agreement with experiments, our calculations predict that surfaces modified with Me-COOH are also expected to be stable under ordinary laboratory conditions or even in moderately diluted aqueous solutions.





# Chapter 5

---

## SCC-DFTB Model for ZnO and Organics

*"Simplify, simplify."*

*Henry David Thoreau – American  
Philosopher.*

In this chapter we present our Self-Consistent-Charge Density Functional based Tight-Binding (SCC-DFTB) model for representing zinc and its interactions with hydrogen, carbon, nitrogen, oxygen and sulfur. We will start by commenting on the demand of computationally efficient methods for realistic simulations on ZnO based materials. After that, we will address the parametrization of our ZnO plus organics SCC-DFTB model and its validation, performed by comparing their predictions with DFT reference data for solid-state zinc-containing systems – i.e. *hcp*-Zn, *w*-ZnO and zinc blend ZnS (*zb*-ZnS) structures – ZnO surfaces and nanostructures, adsorption of small molecular species on ZnO, and models for zinc biological complexes.

### 5.1 – Why do we need a SCC-DFTB model?

ZnO and other Zinc-containing systems have been widely investigated by DFT methods along the last years. Nevertheless, although such methods represent the state-of-the-art approach in materials science and solid-state simulations, they become prohibitively expensive at simulating a large number of atoms. In this context, the SCC-DFTB method [217-219] arises as one of the most successful alternatives for large-scale quantum-mechanical simulations in solid-state physics, chemistry, materials science and biophysics [220-222]. The method is an approximation to the *Kohn-Sham* DFT, which combines the accuracy of conventional DFT methods and the computational efficiency characteristic of semi-empirical models. However, the limited set of available parameters is still a drawback of SCC-DFTB, and in some cases the transferability of parameters between solid and molecular environments is still problematic. For example, an earlier SCC-DFTB parametrization for Zn has been successfully applied to investigate zinc-containing biological molecules [222], but it fails in modeling solid-phase zinc systems with acceptable accuracy.

Considering the technological importance that ZnO has achieved along the last decade, it becomes evident that a new SCC-DFTB model, specially designed for ZnO and related materials, would open up several exciting research possibilities – such as simulating realistic models for functionalized ZnO nanostructures.

## 5.2 – The ZnO + Organics SCC-DFTB Parametrization.

With the basis of the SCC-DFTB method already reviewed in Chapter 2, we will directly turn our attention to the construction and validation of a ZnO + Organics SCC-DFTB model. Before starting this discussion however, it is important to keep in mind that the SCC-DFTB parametrization process always has a strong *trial and error* character. To be brief, what one basically has to do is setting some *key input variables* (cf. next section) and extensively testing the resulting model for some well known reference systems – like simple molecules, simple solids, etc. A careful validation is always the most important and most demanding part of the whole parametrization process, since that ensures the reliability of the model. Not avoiding discussing all *input variables* sets we have tried would hardly be more than a presentation of test calculations. Therefore, in Section 5.2.1 we will just present the best set of these *key input variables* among all those we have tried and specify which simulation details we have used while testing them. After that, in Section 5.2.2, we will focus on the validation of our ZnO + Organics SCC-DFTB model, which in fact is the most important part of this chapter.

### 5.2.1 – Parametrization Details

The parameters necessary to represent a given system within DFTB framework include the *Hubbard parameters* for every chemical element, the  $H_{ij}^0$  and  $S_{ij}$  matrix elements and the repulsive pair-wise potentials for all interacting neighbors. Fortunately, all of these parameters are controlled by few main quantities to be determined in the parametrization process, namely: *i*) the reference input density ( $\rho^0(r)$ ); *ii*) the wave-function confinement radius ( $r_0$ ) and *iii*) the repulsive cutoff's, determining the distances where the repulsive pair-wise potentials ( $V_{Rep}^{\alpha,\beta}$ ) vanish.

As the parametrization reported here extends a previous well-established one [109], all parameters not involving zinc atoms are assumed to be the same as in [109], including  $\rho^0(r)$  – i.e. confined atomic densities – and  $r_0$  for the H, C, N, O and S atoms. For zinc,  $\rho^0(r)$  was confined to a 2.69 Å radius while  $r_0$  was chosen to be 1.59 Å – since these values provided a good compromise among the geometries, cohesive properties and electronic band-structures for the *hcp*-Zn and *w*-ZnO structures (Section 5.2.2). The reference systems and cutoff's used to model the Zn-X (X = H, C, N, O, S and Zn) pair-wise repulsive potentials are summarized in Table 5.1.

For the Zn-Zn and Zn-O cases we have opted for using solid state reference systems – namely the *face-centered cubic (fcc)* Zn and the *zinc blend (zb)* ZnO structures – because these structures reproduce the fourfold coordinated local environment of the Zn atoms in our target *w*-ZnO and *hcp*-Zn systems. The choice of cubic lattices is also convenient since all bond lengths in the crystal can be uniformly varied with only one lattice parameter in such systems.

The electronic DFTB parameters – i.e. atomic *Hubbard* parameters,  $H_{ij}^0$  and  $S_{ij}$  matrix elements, were derived directly from DFT calculations, performed with PBE exchange-correlation functional. All parameters derived here are available for the scientific community and can be downloaded from:

[http://www.dftb.org/parameters/download/znorg/znorg\\_0\\_1/](http://www.dftb.org/parameters/download/znorg/znorg_0_1/)

**Table 5.1** – Parametrization details of the pair-wise repulsive potentials for Zn-X interactions ( X = H, C, N, O, S and Zn ).

<i>Interaction</i>	<i>Reference System</i>	<i>Repulsive Cut-off (Å)</i>	<i>Equilibrium Zn-X distance (Å) SCC-DFTB</i>	<i>Equilibrium Zn-X distance (Å) DFT</i>
<b>Zn-H</b>	<i>ZnH<sub>2</sub></i>	1.63	1.63	1.54
<b>Zn-C</b>	<i>Zn(CH<sub>3</sub>)<sub>2</sub></i>	2.01	1.97	1.95
<b>Zn-N</b>	<i>Zn(NH<sub>3</sub>)<sub>2</sub></i>	2.10	1.92	1.95
<b>Zn-O</b>	<i>zb-ZnO</i>	2.23	2.00	1.98
<b>Zn-S</b>	<i>Zn(SH)<sub>2</sub></i>	2.40	2.21	2.17
<b>Zn-Zn</b>	<i>fcc-Zn</i>	2.75	2.79	2.74

### 5.2.1.1 – Reference DFT Calculations: Simulation Details

In the DFT reference calculations for the Zn-X repulsive potentials ( $U_{\alpha\beta}$ ) we have employed the PBE [133] functional (for X = H, C, O and Zn) – as implemented in the SIESTA package[146] – together with a double- $\zeta$  plus polarization function (DZP) basis set and norm-conservative *Troullier-Martins* pseudopotentials [145] (PP) for representing the valence and inner electrons respectively. For X = N, S, the *Becke* three-parameter, *Lee, Yang and Parr* (B3LYP) hybrid functional[130,132] in conjunction with a 6-311G+(d,p) basis set was used – as implemented in the GAUSSIAN03 package [225].

All DFT/PBE calculations in this chapter have been performed by using Periodic Boundary Conditions (PBC). For the *fcc-Zn* and *zb-ZnO* solid state reference systems, the  $k$ -points were sampled with a (8 x 8 x 8) *Monkhorst-Pack* grid [152]. For the molecular reference systems, the calculations have been performed by employing large supercells, including a 25 Å vacuum region in all directions in order to isolate the molecules from their periodic replicas.

### 5.2.2 – Validation of the Parameters

The validation of our SCC-DFTB parameters has been performed by comparing their predictions with standard DFT data taken from literature. In order to do that, the validation set has been separated in five different categories: *i)* Zn-containing bulk solids, *ii)* Zn-containing molecular complexes, *iii)* clean ZnO surfaces, *iv)* ZnO [0001] 1D Nanostructures and *v)* adsorption of small molecules on ZnO non-polar surfaces.

#### 5.2.2.1 – SCC-DFT Calculations: Simulation Details

All our SCC-DFTB calculations have been performed with the DFTB+ code [226]. Solid state *hcp-Zn*, *w-ZnO* and *zb-ZnS* properties were calculated using PBC and converged (8 x 8 x 4), (8 x 8 x 4) and (8 x 8 x 8) MP  $k$ -points, respectively. The calculations for ZnO surfaces (clean and with small adsorbates) have been performed using suitably oriented supercells and PBC within the slab approach [179] (See also Section 4.2). A vacuum region of at least 25 Å along the surface-

normal direction and a (4 x 3 x 1) MP grid for the  $k$ -point sampling has been employed. The ZnO 1D nanostructures' [0001] growth direction has been oriented along the z-axis in the supercell, with vacuum regions of 25 Å along the x and y directions; and a (1 x 1 x 4) MP grid for has been used for the  $k$ -point sampling. The tests for molecular complexes have been performed by geometry optimizations of small zinc-containing complexes, as suggested by *Elstner et al.*[222]. In all SCC-DFTB calculations, the atomic positions were relaxed till the forces in the system become smaller than 0.003 eV/Å.

### 5.2.2.2 – Zn-Containing Bulk Solids

The lattice parameters and elastic properties of bulk *hcp*-Zn, *w*-ZnO and *zb*-ZnS were determined by calculating their energy-volume profiles in a  $\mp$  15% range around the experimental equilibrium volumes; and fitting the results to the *Murnaghan equation of state* (Chapter 3.2). For *hcp*-Zn and *w*-ZnO structures we have fixed the experimental  $c/a$  ratios (1.86 [227] and 1.60 [228] respectively).

As shown in Table 5.2, the DFTB predictions for all considered bulk systems are in a fairly good agreement with DFT and experimental results. The deviations in the cohesive energies are not surprising, since DFTB calculations usually overestimate this property [229], while the error in the Zn bulk modulus is a consequence of strong zinc wave-function compression applied to this element ( $r_0$  only  $\sim$ 1.3 times larger than the Zn covalent radius), which shortens its dissociation bond distances and lowers its electronic energy wells. Nevertheless this strong wave-function compression ensures reasonable band structures for the solid materials, as exemplified in Figure 5.1 for the *hcp*-Zn and *w*-ZnO cases.

**Table 5.2** – Selected *hcp*-Zn, *w*-ZnO and *zb*-ZnS bulk properties calculated with SCC-DFTB, DFT methods and obtained from experiments.

	<i>Method</i>	$E_{coh}$ (eV)	$a$ (Å)	$c$ (Å)	$V$ (Å <sup>3</sup> )	$B_0$ (GPa)	$B_0'$
<i>hcp</i> -Zn	SCC-DFTB <sup>a</sup>	2.45	2.71	5.04	32.20	114	5.67
	PP-DZP/PBE <sup>a</sup>	1.92	2.68	5.00	31.24	73	5.93
	PP-PW/PW91 <sup>b</sup>	-	2.65	5.10	31.02	60	6.59
	Exp.	1.36 <sup>c</sup>	2.61 <sup>b</sup>	4.91 <sup>b</sup>	28.96 <sup>b</sup>	60-80 <sup>b</sup>	5.2-6.4 <sup>b</sup>
<i>w</i> -ZnO	SCC-DFTB <sup>a</sup>	9.77	3.28	5.25	50.04	161	2.49
	PP-DZP/PBE <sup>a</sup>	8.08	3.30	5.34	51.08	124	4.55
	PP-PW/PBE <sup>d</sup>	8.98	3.34	5.30	51.40	171	-
	Exp. <sup>e</sup>	7.52	3.25	5.20	47.62	208	4
<i>zb</i> -ZnS	SCC-DFTB <sup>a</sup>	7.93	5.43	-	160.1	44.2	2.4
	PP-PW/LDA <sup>f</sup>	7.22	5.35	-	153.3	82	4.6
	PP-PW/PW91 <sup>g</sup>	-	5.60	-	175.6	66.7	3.95
	Exp. <sup>f</sup>	6.33	5.40	-	157.5	76.9	4.9

- a) This work.
- b) PW91 calculation in ref. [169]
- c) Ref. [173]
- d) PBE calculation in ref. [168]
- e) Ref. [167]
- f) LDA calculation in ref. [145]
- g) PW91 calculation in ref. [230]



It should be mentioned that due to the minimal basis set employed, the energy band structures calculated with the SCC-DFTB method are not affected by the band-gap problem in the same way as LDA and GGA band structures are. Therefore, with no additional correction scheme being applied, the ZnO band-gap obtained via SCC-DFTB calculations ( $\sim 4.1$  eV) is closer to the experimental value ( $\sim 3.3$  eV) than the LDA/PBE results ( $\sim 0.8$  eV). This fact can be taken as an advantage to study intra-gap electronic states introduced by defects or adsorbed species – and we will use it in Chapter 6 – but it should be clear that the better description of the ZnO band gap is due to a cancelation of errors. It must be also noted that the dispersions at the edge of the conduction-band are considerably smaller than those found in GGA-PBE results and may lead to deviations in calculating transport properties. Despite that, the structures of the SCC-DFTB energy bands are in good qualitative agreement with their DFT counterparts.

Concerning the *hcp*-Zn and *w*-ZnO cohesive energies calculated with SCC-DFTB, the overestimation of  $\sim 0.5$  eV per chemical bond is significant, although in line with the usual DFTB trend. In principle such deviations could be corrected by applying larger cutoff's to repulsive potentials of the Zn-Zn and Zn-O bonds, slightly sacrificing the description of the geometrical parameters. Nevertheless, we have verified that this procedure leads to wrong relaxations for ZnO surfaces and nanostructures, where the outermost atoms move towards the vacuum region in order to avoid the enhanced repulsions.

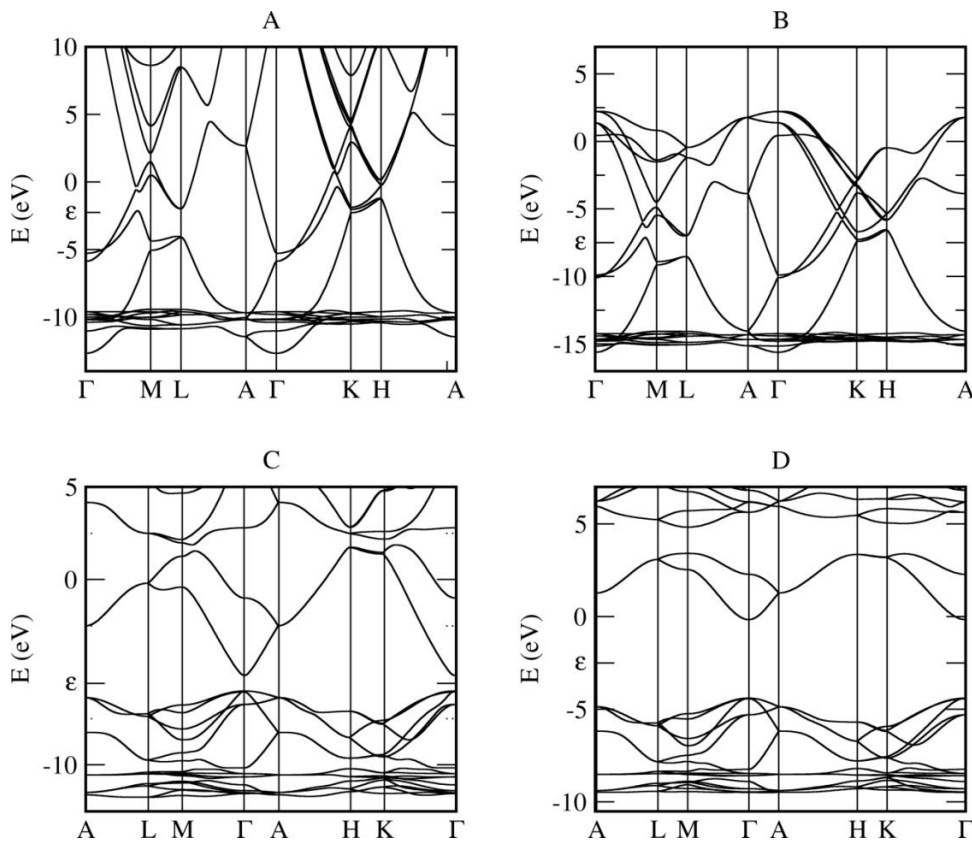


**Figure 5.1** – Comparison between DFT and SCC-DFTB energy band structures for *hcp*-Zn and *w*-ZnO. Panel A: *hcp*-Zn(PBE-PP-DPZ); panel B: *hcp*-Zn(SCC-DFTB); panel C: *w*-ZnO(PBE-PP-DPZ) and panel D: *w*-ZnO(SCC-DFTB). In all panels the Fermi energy is indicated by the symbol “ $\epsilon$ ”.

### 5.2.2.3 – Zn-containing Molecular Complexes

In order to validate our model for Zn in molecular environment, we have simulated small zinc complexes with  $\text{NH}_3$  and  $\text{SH}^-$  ligands, finding a reasonably good agreement with DFT-B3LYP results (see Table 5.3). Besides, we have also reproduced recent B3LYP geometry parameters for cyclic  $\text{ZnC}_n$  ( $n = 2-5$ ) clusters [231] and found the errors in the Zn-C and C-C bonds to be smaller than 0.05 Å.

By applying the procedure suggested by *Elstner et al.*[222], we have calculated three zinc-containing complexes in order to model zinc interactions with specific functional groups in proteins, using  $\text{SH}^-$ ,  $\text{CH}_2=\text{NH}$  and  $\text{HCOO}^-$  ligands for representing the thiol group in cysteine, the imidazole group in histidine and the carboxylate group present in all amino acids, respectively. Figure 5.2 depicts the geometries of the investigated complexes whereas Table 5.4 summarizes their geometrical characteristics calculated with B3LYP and two different SCC-DFTB parametrizations, i.e. our and the work reported in [222]. In comparison with DFT results, both DFTB parametrizations describe the Zn-X ( $X=\text{S},\text{N},\text{O}$ ) reasonably well: Zn-S bond lengths in the Complex 1 were found to be longer by up to 2% compared to DFT ones, whereas the same bonds in the Complex 2 are described

**Table 5.3** – SCC-DFTB and B3LYP/6-311+G(d,p) cohesive energies and equilibrium geometries for zinc-complexes with  $\text{NH}_3$  and  $\text{HS}^-$  ligands.

Species	$E_{\text{coh}}$ (eV)		Bond length (Å) (Zn-X)		Bond Angles (°) (X-Zn-X)	
	SCC-DFTB	B3LYP	SCC-DFTB	B3LYP	SCC-DFTB	B3LYP
<b>Zn-N</b>						
$[\text{ZnNH}_3]^{2+}$	5.98	5.36	1.93	1.97	-	-
$[\text{Zn}(\text{NH}_3)_2]^{2+}$	11.86	10.70	1.92	1.95	180	180
$[\text{Zn}(\text{NH}_3)_3]^{2+}$	13.96	13.34	1.97	2.03	119.9	119.5
$[\text{Zn}(\text{NH}_3)_4]^{2+}$	16.75	15.3	2.02	2.09	109.5	109.4
<b>Zn-S</b>						
$[\text{Zn}(\text{SH})]^+$	18.06	18.35	2.03	2.18	-	-
$\text{Zn}(\text{SH})_2$	27.81	27.56	2.21	2.19	177.5	178.4

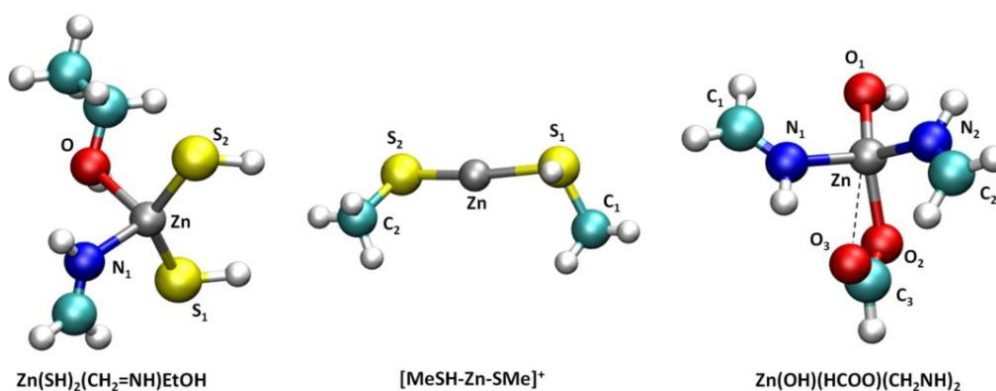


**Figure 5.2** – Optimized geometries of model zinc complexes calculated with SCC-DFTB.

with an accuracy of 0.8% or better with the current parameters. Similar trends have been found in the case of Zn-O bond lengths, with errors around 5% and 2.6% in comparison with DFT values for the complexes 1 and 3 respectively. The non-bonded Zn-O<sub>3</sub> distance in the Complex 3 is also in a good agreement with DFT ones (cf. Table 5.4). The current parametrization leads to an underestimation of the Zn-N bond lengths, as exemplified by both Complex 1 and Complex 3 (within 7% and 5.6 % to DFT, respectively).

Also the bond angles are reasonably described with both DFTB parametrizations. Our S-Zn-S values in Complexes 1 and 2, for instance, agree within 6.6% and 3.3%, respectively, in comparison with DFT results. It should be noted that some bond angles disagree even up to 10 degrees with DFT, which may indicate a relatively floppy bending potential-energy profile.

**Table 5.4** – Geometric parameters of model zinc complexes calculated with B3LYP/6-311+G(d,p) and SCC-DFTB methods.

Complex	Method		
	B3LYP <sup>a</sup>	SCC-DFTB <sup>a</sup>	SCC-DFTB <sup>b</sup>
<b>1: Zn(SH)<sub>2</sub>(CH<sub>2</sub>=NH)·EtOH</b>			
r(Zn-S <sub>1</sub> ) (Å)	2.261	2.258	2.301
r(Zn-S <sub>2</sub> ) (Å)	2.261	2.243	2.290
r(Zn-O) (Å)	2.272	2.288	2.158
r(Zn-N) (Å)	2.155	2.056	2.001
∠(S <sub>1</sub> -Zn-S <sub>2</sub> ) (°)	143.5	140.3	134.0
∠(S <sub>2</sub> -Zn-O) (°)	91.2	102.8	105.4
∠(S <sub>1</sub> -Zn-N) (°)	106.9	104.1	105.4
<b>2: [MeSH-Zn-SMe]<sup>+</sup></b>			
r(Zn-S <sub>1</sub> ) (Å)	2.349	2.293	2.329
r(Zn-S <sub>2</sub> ) (Å)	2.152	2.123	2.169
r(S <sub>1</sub> -C) (Å)	1.853	1.832	1.831
∠(C-S <sub>1</sub> -Zn) (°)	104.9	108.0	104.9
∠(S <sub>1</sub> -Zn-S <sub>2</sub> ) (°)	175.1	169.1	169.9
∠(Zn-S <sub>2</sub> -C) (°)	105.8	110.2	105.5
<b>3: Zn(OH)(HCOO)·(CH<sub>2</sub>=NH)<sub>2</sub></b>			
r(Zn-O <sub>1</sub> ) (Å)	1.876	1.906	1.868
r(Zn-O <sub>2</sub> ) (Å)	1.972	2.080	2.023
r(O <sub>2</sub> -C <sub>3</sub> ) (Å)	1.282	1.301	1.304
r(C <sub>3</sub> -O <sub>3</sub> ) (Å)	1.237	1.241	1.251
r(Zn-O <sub>3</sub> ) (Å)	3.010	2.911	2.931
r(N <sub>1</sub> -C <sub>1</sub> ) (Å)	1.270	1.267	1.262
r(Zn-N <sub>2</sub> ) (Å)	2.129	2.045	2.009
∠(O <sub>1</sub> -Zn-O <sub>2</sub> ) (°)	131.6	109.1	125.8
∠(N <sub>1</sub> -Zn-N <sub>2</sub> ) (°)	103.3	102.7	104.1
∠(N <sub>2</sub> -Zn-O <sub>1</sub> ) (°)	100.3	104.0	109.8

a) Ref. [222]

b) Using current parametrization; this work.

**Table 5.5** – Formation energies (kcal/mol) of model zinc complexes calculated with B3LYP/6-311+G(d,p) and SCC-DFTB methods.

	<i>Method</i>		
	<i>B3LYP</i>	<i>SCC-DFTB<sup>a</sup></i>	<i>SCC-DFTB<sup>b</sup></i>
Reaction 1 <sup>c</sup>	-14.7 <sup>d</sup>	-12.3	-20.1
Reaction 2 <sup>e</sup>	-50.9 <sup>b</sup>	-	-53.2
Reaction 3 <sup>f</sup>	-159.4 <sup>d</sup>	-180.9	-186.9

- a) Ref. [222]  
b) This work.  
c) EtOH + Zn(SH)<sub>2</sub>(CH<sub>2</sub>=NH) → Zn(SH)<sub>2</sub>(CH<sub>2</sub>=NH)·EtOH.  
d) B3LYP/6-311+G(d,p) data from Ref. [222]  
e) CH<sub>3</sub>SH + [Zn(SCH<sub>3</sub>)]<sup>+</sup> → [MeSH-Zn-SMe]<sup>+</sup>.  
f) OH<sup>-</sup> + [Zn(HCOO)(CH<sub>2</sub>=NH)<sub>2</sub>]<sup>+</sup> → Zn(OH)(HCOO)(CH<sub>2</sub>=NH)<sub>2</sub>.

Table 5.5 lists the formation energies of the investigated complexes, calculated as the difference between the total energy of the complex and those of reactants. It can be inferred from this data that the current SCC-DFTB parametrization leads to an overbinding of ligands in zinc complexes with the largest error to DFT of 0.3 eV (37 %) for the first reaction, and 0.1 (4.5%) and 1.2 eV (17.2%) for the second and third reaction, respectively. This finding is however in line with the general overbinding trend of the DFTB method, and one can conclude that the our parametrization is qualitatively applicable to model zinc in molecular/biological environments.

**Table 5.6** – Comparison of geometrical relaxations in ZnO surfaces calculated with DFTB, for selected structural parameters as specified in Figures 2 and 3, with DFT (PP-PW/PW91) results in ref. [177].

Parameter	Surface Layers		Inner Layers	
	SCC-DFTB	DFT-PW91	SCC-DFTB	DFT-PW91
<b>ZnO-(1010)</b>				
$d_{Zn-O}$ (Å)	1.88	1.85	2.01	1.99
$d'_{Zn-O}$ (Å)	2.05	2.06	2.01	1.99
$\alpha$ (°)	117	117	109	-
$\beta$ (°)	108	-	109	-
<b>ZnO- (1210)</b>				
$d_{Zn-O}$ (Å)	1.93	1.87	2.01	1.99
$d'_{O-Zn}$ (Å)	2.00	1.96	2.01	1.99
$d'_{Zn-O}$ (Å)	2.05	2.06	2.01	-
$\alpha$ (°)	118	117	109	-
$\beta$ (°)	97	-	109	-
<b>ZnO-(0001/0001)</b>				
$d_{Zn-O}$ (Å)	1.94	1.92	1.99	1.97
$d'_{Zn-O}$ (Å)	2.08	2.15	2.05	2.08
$\alpha$ (°)	111	113	109	-
$\beta$ (°)	120	120	90	-
<b>ZnO-dep-(0001)</b>				
$d_{Zn-O}$ (Å)	1.90	1.93	1.90	-
$d'_{Zn-O}$ (Å)	2.34	2.4	2.34	-
$\alpha$ (°)	120	120	120	-
$\beta$ (°)	90	-	90	-

#### 5.2.2.4 – Clean ZnO surfaces

Clean ZnO surfaces form a good probe set to test the new parameters, since they have the bulk symmetry broken along one direction. Furthermore, they have been subject to several DFT studies in the recent literature [177-179], which ensures us a reliable comparison basis. The  $(10\bar{1}0)$ ,  $(1\bar{2}10)$ ,  $(0001/000\bar{1})$  and depolarized dep- $(0001)$  ZnO surfaces were constructed starting from the equilibrium SCC-DFTB  $w$ -ZnO structure (Section 5.2.2.2), with the surface unit cells used for these four structures represented in Figure 5.3. In all cases, our results for the surfaces' relaxations are in a good agreement with those reported in [177], as shown in Table 5.6.

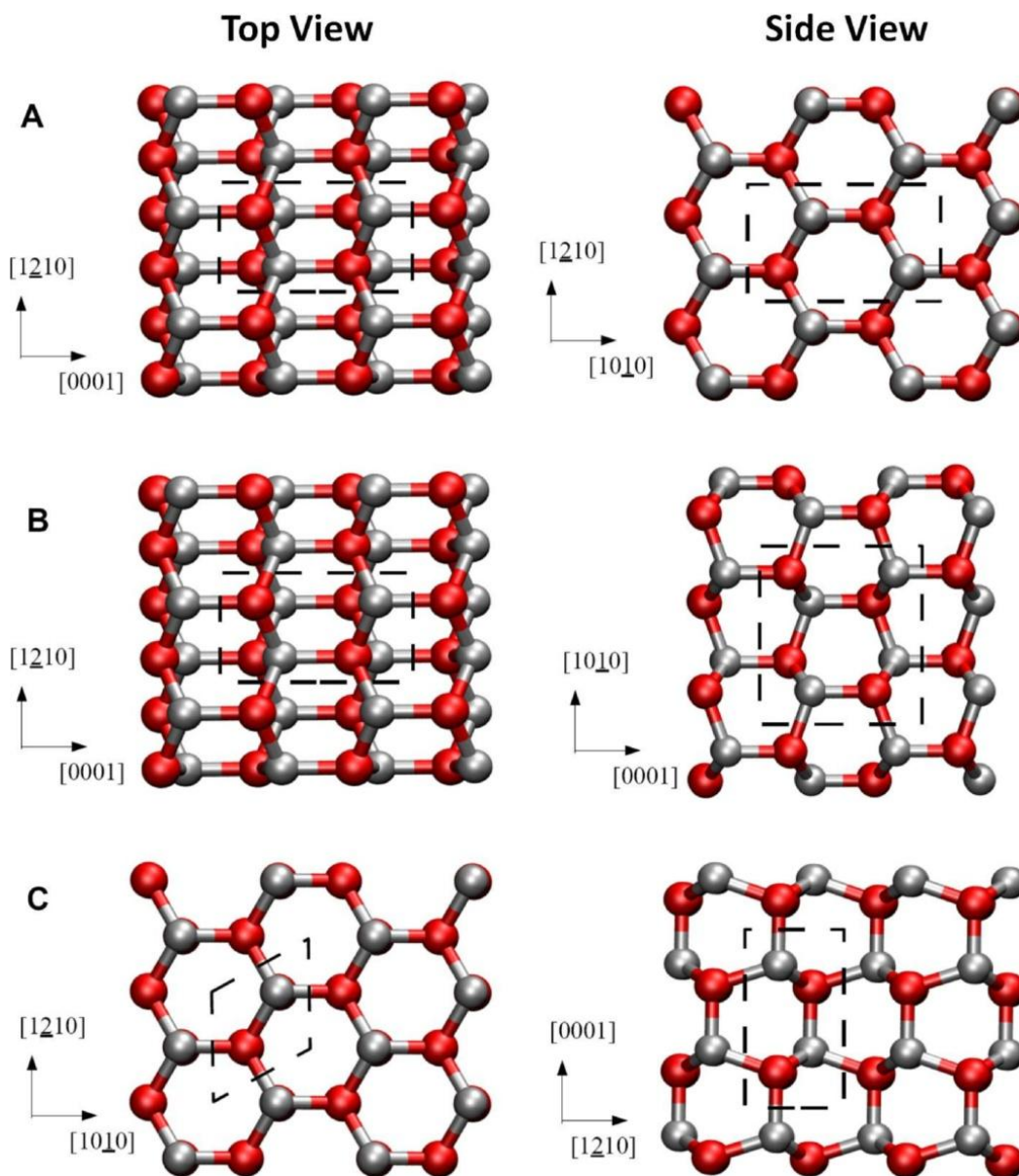


**Figure 5.3** – Top and side views of surface unit cells for  $(10\bar{1}0)$  (A),  $(1\bar{2}10)$  (B) and  $(0001/000\bar{1})$  ZnO surfaces (C). The dep- $(0001)$  surface unit cell is similar to those used for its polar counterpart, but with planar ZnO sheets perpendicular to the  $[0001]$  direction.

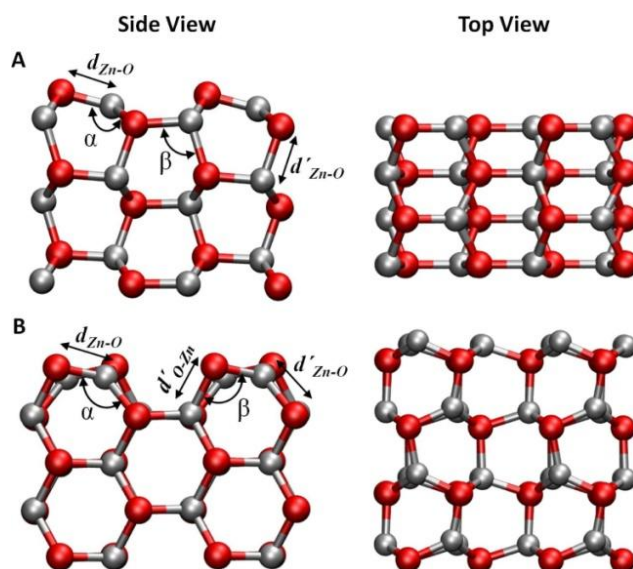


**Figure 5.4** – Side and top views of the relaxed  $(10\bar{1}0)$  (A) and  $(1\bar{2}10)$  (B) ZnO surfaces calculated with the SCC-DFTB method.

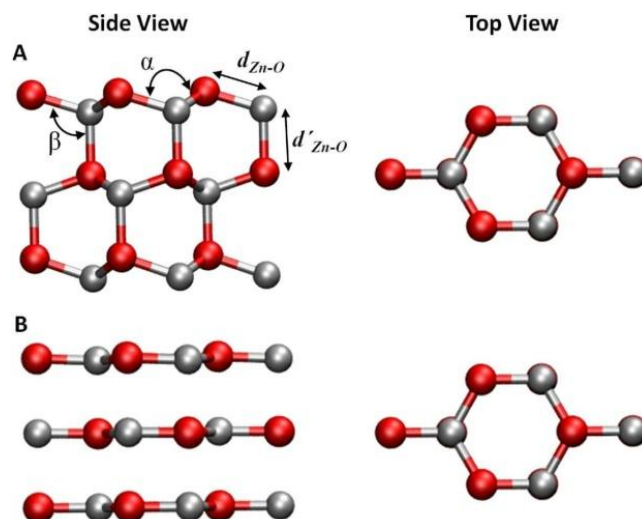


**Figure 5.5** – Side and top views of the relaxed  $(0001/000\bar{1})$  (A) and dep- $(0001)$  (B) ZnO surfaces calculated with the SCC-DFTB method.

The relaxations in the  $(10\bar{1}0)$  terminated slabs (Figure 5.4A) are only significant in the three outermost surface layers. The oxygen atoms remain close to their bulk positions, while the zinc atoms move inward in the top layer and slightly outward in the second layers. In comparison with the bulk values, the bond lengths between the top and the second layer,  $d_{Zn-O}$ , are  $\sim 6\%$  shortened while the bonds between the second and the third layers are  $\sim 3\%$  larger. The O-Zn-O angle ( $\alpha$ ) changes from its  $109^\circ$  bulk value to  $117^\circ$  at the top surface layer, remaining unchanged in the inner layers. The  $(1\bar{2}10)$  terminated slabs follow similar trends, with relaxations observed especially at the outermost Zn atoms, leading to a ZnO bond length  $\sim 4\%$  shorter and strongly distorted bond angles at the surface.

The depolarized (0001) surface relaxation – Figure 5.5.B – agrees well not only with the theoretical prediction derived by *Cleyssens et. al.* [177] but also with recent experimental data confirming such structure in ZnO ultra-thin films [232]. This is a graphite-like structure where both O and Zn atoms assume a planar configuration, with all in-plane bonds  $\sim 3\%$  smaller than those in the *w*-ZnO, and with large interlayer distances ( $\sim 2.34$  Å). In this case, the relaxations do not differ significantly among different layers in the slab and are also not influenced by the slab thickness. For the polar (0001/000 $\bar{1}$ ) surfaces, where the structure resembles the *w*-ZnO (Figure 5.5 A), the relaxations extend through the whole slab and are more sensitive to variations in its thickness as well. Furthermore we also have observed small charge transfers from the oxygen-terminated to the zinc-terminated surface ( $\sim 0.3e$  per slab unit cell), which have usually been considered as a stabilizing mechanism in such surfaces [178,233].

Since the polar (0001) and (000 $\bar{1}$ ) ZnO surfaces are not equivalent, it is not possible to calculate their absolute formation energy separately. Therefore, we have calculated the cleavage energy (the energy required to create two surfaces by cleaving the perfect crystal) for all considered slabs in order to verify their relative stability as a function of the film thickness (Figure 5.6). The results are in excellent agreement with the DFT predictions in [177]. As expected, the slabs with the polar surfaces are less stable than those (10 $\bar{1}$ 0) and (1 $\bar{2}$ 10) terminated. However, the depolarized (0001) structure is the most stable for the thinnest films – in accordance with experiments for ultra-thin ZnO films [232] – but quickly rising in energy with the slab thickness. It is necessary to remark that the phase-transitions from the depolarized 0001- film to the other configurations (in this study found at 5, 6 and 16 layers-thick slabs) take place at points slightly different than those found by *Cleyssens at. al.* (namely at 9, 10 and 18 layers), which does not affect the general conclusions above however.

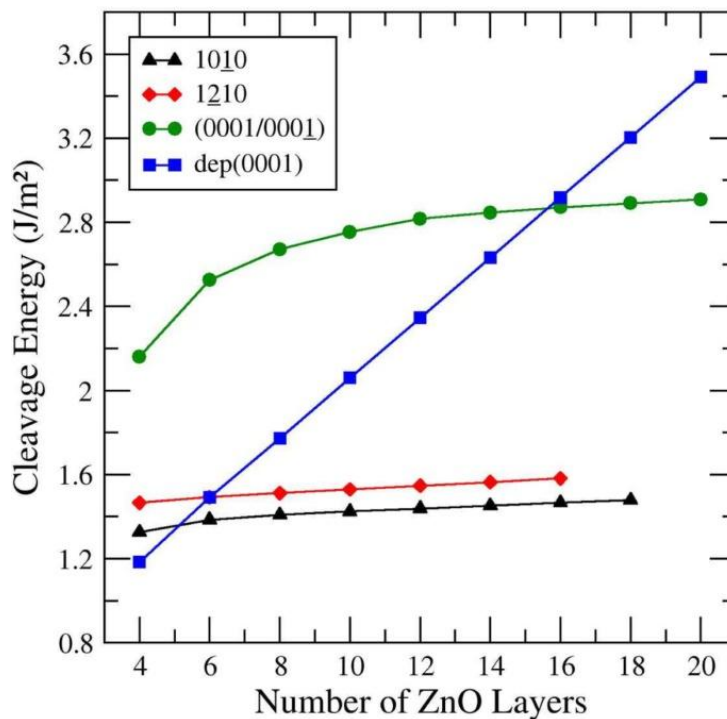


**Figure 5.6** – SCC-DFTB cleavage energy for (10 $\bar{1}$ 0), (1 $\bar{2}$ 10), (0001/000 $\bar{1}$ ) and dep(0001) ZnO surfaces as a function of the slab thickness.

### 5.2.2.5 – ZnO 1D – Nanostructures

In order to extend the validation procedure to ZnO nanostructures, we have investigated (10 $\bar{1}0$ )-faceted hexagonal nanowires with different diameters (3.7, 10, 16 and 23 Å, respectively). Figure 5.7 shows the relaxed cross-sections of the investigated nanowires and their respective band structures, calculated with the SCC-DFTB method. For all nanowires, the relaxations at the outermost layers follow the same general trends observed for the ZnO-(10 $\bar{1}0$ ) surface, being also in very good agreement with previous DFT results [178]. The inner atoms remain close to their positions in the bulk *w*-ZnO, as the O atoms at the surface, whereas the zinc atoms at the surface move inward, shrinking the distance to their nearest inner Zn neighbors to 3.07 Å. The exception is the smallest nanowire – where the relaxations are more pronounced, with 2.86 Å as the minimal distance between Zn atoms. For these wires, the energy band structures along the  $\Gamma$ -Z direction in the *First Brillouin Zone* are in a good agreement with DFT results in [178], with a direct band gap at the  $\Gamma$ -point – shrinking from 4.1 to 3.6 eV with the nanowires' diameter, as a consequence of quantum confinement effects. As expected, the SCC-DFTB band dispersions and band gaps calculated for the nanowires showed the same kind of qualitative deviations – with respect to DFT calculations [178] – as observed for bulk *w*-ZnO.

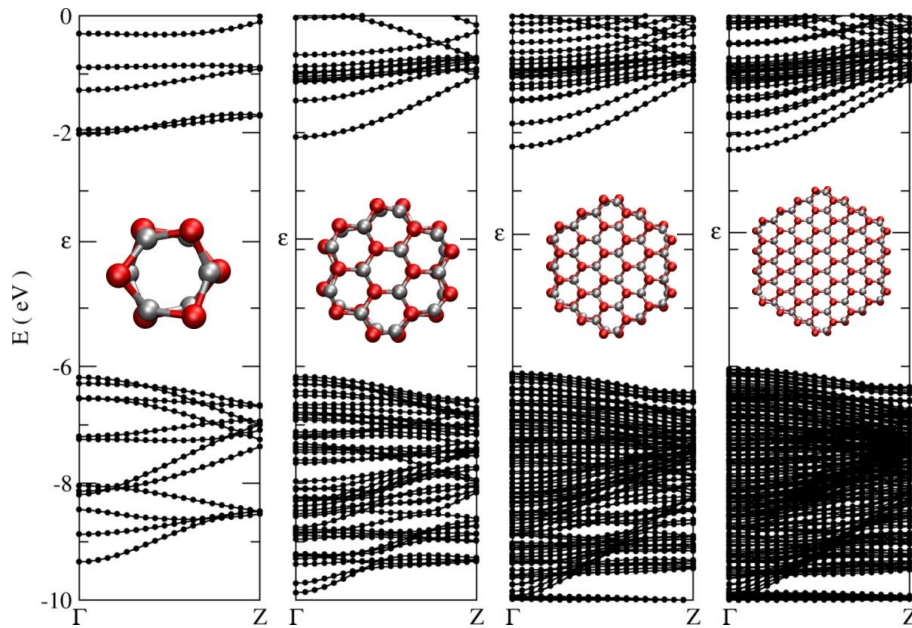


**Figure 5.7** – Relaxed geometries and electronic band structures for hexagonal [0001] ZnO nanowires calculated with the SCC-DFTB method. In all panels the Fermi energy is indicated by the symbol “ $\epsilon$ ”.

The relative stabilities of the nanowires are also in good agreement with plane waves calculations by *Xu et al.* [234], who have also demonstrated that the formation energy ( $E_f = E_T - E_{w-ZnO}$ ) of hexagonal nanowires depends linearly on their ZnO surface pairs ratio. To further validate the parameters, we have calculated [0001]-oriented ZnO nanobelts, finding a similar linear dependence on the surface pair ratio – Figure 5.8. The nanobelts were found to have their relaxations consistent with those observed for their dominant surfaces, with their stabilities lying between that of the corresponding nanowire (diameter of 10 Å) and that of the infinite thin film. As expected, the relative stability of the ZnO nanobelts increases with their width.



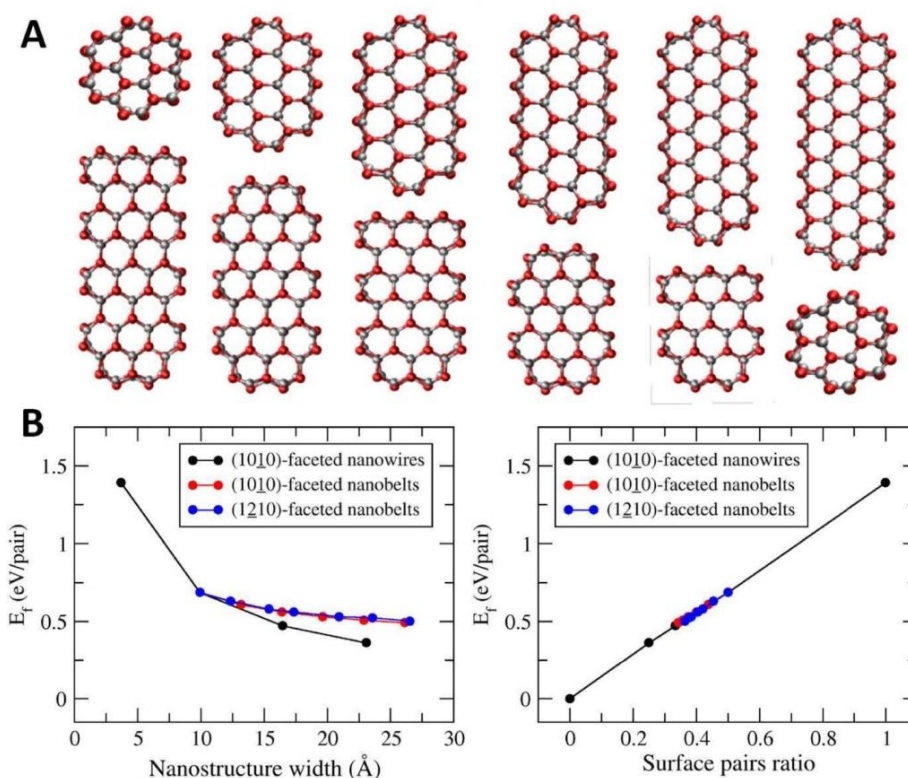


**Figure 5.8** – Panel A: Cross section of (1010)- (top) and (1210)-faceted (bottom) [0001] ZnO nanobelts with different widths along their dominating surface. Panel B: SCC-DFTB formation energies calculated for [0001] ZnO nanostructures, including hexagonal nanowires, (1010)-faceted and (1210)-faceted nanobelts.

### 5.2.2.6 – Small Molecules on ZnO Non-Polar Surfaces.

With the good performance of our ZnO model for bulk materials, surfaces and nanostructures – as demonstrated in the last sections – let us now turn our attention to adsorption processes. At first we will investigate our model's performance in describing the adsorption of two important inorganic species – namely  $\text{NH}_3$  and  $\text{CO}_2$  – on ZnO-(1010). We will analyze their geometrical configurations on the surface and also their *Gibbs free energy variation*  $\Delta G$  (Section 4.3.2.4). After that, we will compare the SCC-DFTB predictions for the functionalized ZnO-(1010) surfaces studied in Chapter 4 – giving a special emphasis to the Me-COOH case.

#### 5.2.2.6.1 – $\text{CO}_2$ and $\text{NH}_3$ on ZnO-(1010)

For the  $\text{CO}_2$ -covered surfaces, the predictions of our SCC-DFTB model are in good qualitative agreement with DFT results of *Wöll et al.* [199]. The surface adduct shows a tridentate carbonate (TC) structure (Figure 5.9) as the most stable adsorbate form, showing bond-lengths and bond-angles in excellent agreement with the DFT predictions. It is interesting to observe that the interaction with the  $\text{CO}_2$  molecule influences the surface geometry in the same way observed for the Me-X series in Chapter 4 – i.e. by pushing the Zn atoms outwards, thereby decreasing the angle  $\alpha$  (Figure 5.4) to  $89^\circ$  and increasing the ZnO dimer distance  $d_{\text{Zn-O}}$  to 2.29 Å.

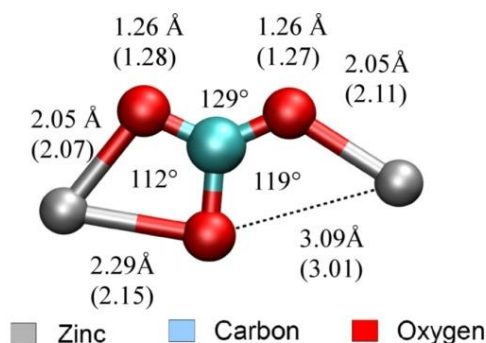


**Figure 5.9** – Geometry of the tridentate surface carbonate structure calculated with SCC-DFTB. The bond length values in round brackets are DFT results taken from [199]. The angles calculated with SCC-DFTB coincide exactly with those reported in [199].

Concerning the adsorption energetics, we have calculated the adsorption's  $\Delta\gamma$  by using the  $\text{CO}_2$  chemical potential as a variational parameter (Section 4.3.2.1), obtaining a phase diagram fairly similar to that in [199] (Figure 5.10). Nevertheless, it should be noted that our  $\Delta\gamma$  values are overestimated by significant  $\sim 0.5$  eV per  $\text{CO}_2$  molecule in comparison with the DFT results. Accordingly, the *Monolayer*  $\rightarrow$  *Half-Monolayer* and *Half-Monolayer*  $\rightarrow$  *Bare Surface* phase-transitions are also shifted towards more negative chemical potentials in comparison with the DFT values. At the first glance such deviation may not be surprising – given the usual overestimation trend of SCC-DFTB calculations in comparison with DFT – but in fact this was the first sign of a more pathological behavior of our parametrization – to be discussed in Section 5.2.2.5.2.

We have also introduced the ammonia molecule in our validation set because ZnO has been considered a promising material for sensing such molecules in a gas phase [234]. Nevertheless, there are only a few theoretical studies on the absorption of  $\text{NH}_3$  on ZnO surfaces, none of them dealing with extended structures. *Taft et al.* [201], for example, have employed cluster models in order to investigate the adsorption of single ammonia molecules on ZnO, finding a binding energy of  $\sim -1.8$  eV for  $\text{NH}_3\text{-ZnO-(10}\bar{1}0)$  surface adduct. Because of such strong binding energy and the small molecular volume of ammonia – in comparison to  $\text{CO}_2$  for example – it is quite probable that adsorption of  $\text{NH}_3$  also lead to the formation of self-assembled monolayers on  $\text{ZnO-(10}\bar{1}0)$ . We have tested this hypothesis with our SCC-DFTB model, finding the monolayer coverage as the stable phase at ligand-rich conditions (Figure 5.11). We have found a binding energy of  $\sim -1.6$  eV for the  $\text{NH}_3\text{-ZnO-(10}\bar{1}0)$  ML and  $\sim -2.2$  eV for the  $\text{NH}_3\text{-ZnO-(10}\bar{1}0)$   $\frac{1}{2}$ ML surface complexes, which indicates a strong overbinding in comparison with the coupled cluster results of *Taft et al.*, which have been calculated for the adsorption of single molecules, where steric repulsion are not involved. Concerning the adduct geometry (Figure 5.12), the adsorption also influences the surface relaxations, reducing the angle  $\alpha$  (Figure 5.4) to  $115^\circ$  and increasing the ZnO dimer distance  $d_{\text{Zn-O}}$  to  $1.96$  Å. No ammonia dissociation was found. Instead, there is a typical hydrogen-bond distance of  $1.68$  Å between ammonia hydrogen and ZnO surface oxygen. The  $\text{NH}_3$  tilting angle with respect to the surface normal of  $41^\circ$  is in fairly good agreement with near-edge X-ray fine-structure spectroscopy reported by *Kamada et al.* [193]. Besides, our surface adduct geometry (cf. Figure 5.12) agrees very well with that from coupled-cluster calculations in [201].

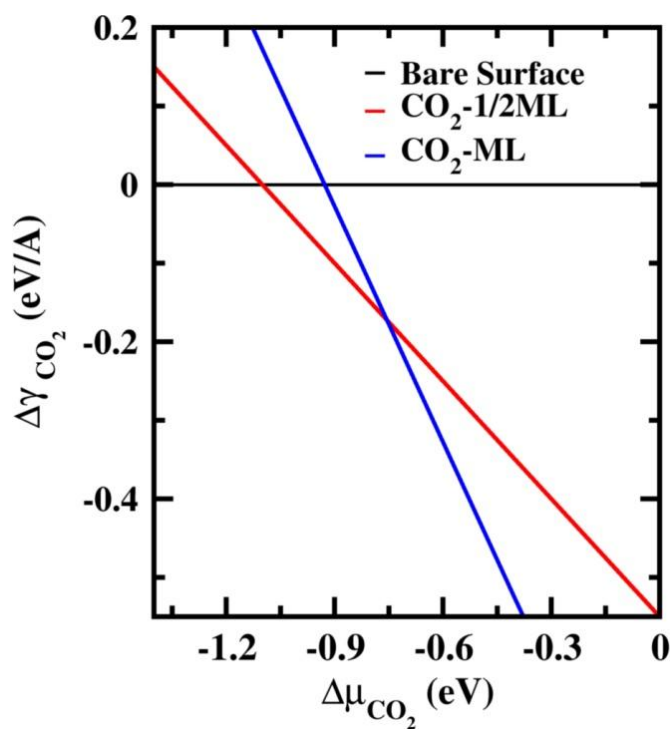


**Figure 5.10** – Phase-stability diagram calculated with SCC-DFTB for different coverages of CO<sub>2</sub> on ZnO-(10 $\bar{1}$ 0) surfaces. The surface free energy variation  $\Delta\gamma$  is given per a standard unit area A corresponding to a 2x1 surface unit.

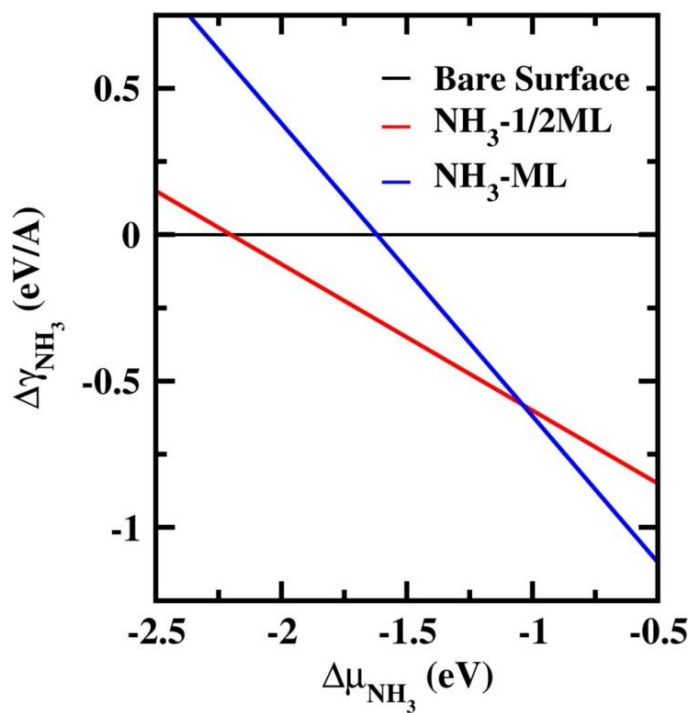


**Figure 5.11** – Phase-stability diagram calculated with SCC-DFTB for different coverages of NH<sub>3</sub> on ZnO-(10 $\bar{1}$ 0) surfaces. The surface free energy variation  $\Delta\gamma$  is given per a standard unit area A corresponding to a 2x1 surface unit.

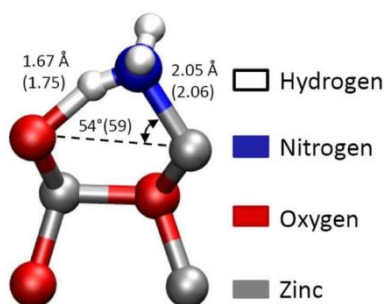


**Figure 5.11** – Geometry of the  $\text{H}_3\text{N-ZnO-(10}\bar{1}0)$  surface complex calculated with SCC-DFTB. The values in round brackets are *ab initio* results taken from [201].

### 5.2.2.6.2 – Organic Ligands on $\text{ZnO-(10}\bar{1}0)$

As last validation step, let us now compare the performance of our SCC-DFTB model with the DFT calculations for substituted methane molecules on  $\text{ZnO-(10}\bar{1}0)$  surfaces (Chapter 4). Figure 5.12 shows the adsorption *free energy variations* ( $\Delta\gamma$ ) for the  $\text{Me-NH}_2$ ,  $\text{Me-OH}$ ,  $\text{Me-SH}$ ,  $\text{Me-COOH}$  and  $\text{Me-CN}$  ligands, obtained with both DFT-PBE and SCC-DFTB calculations.

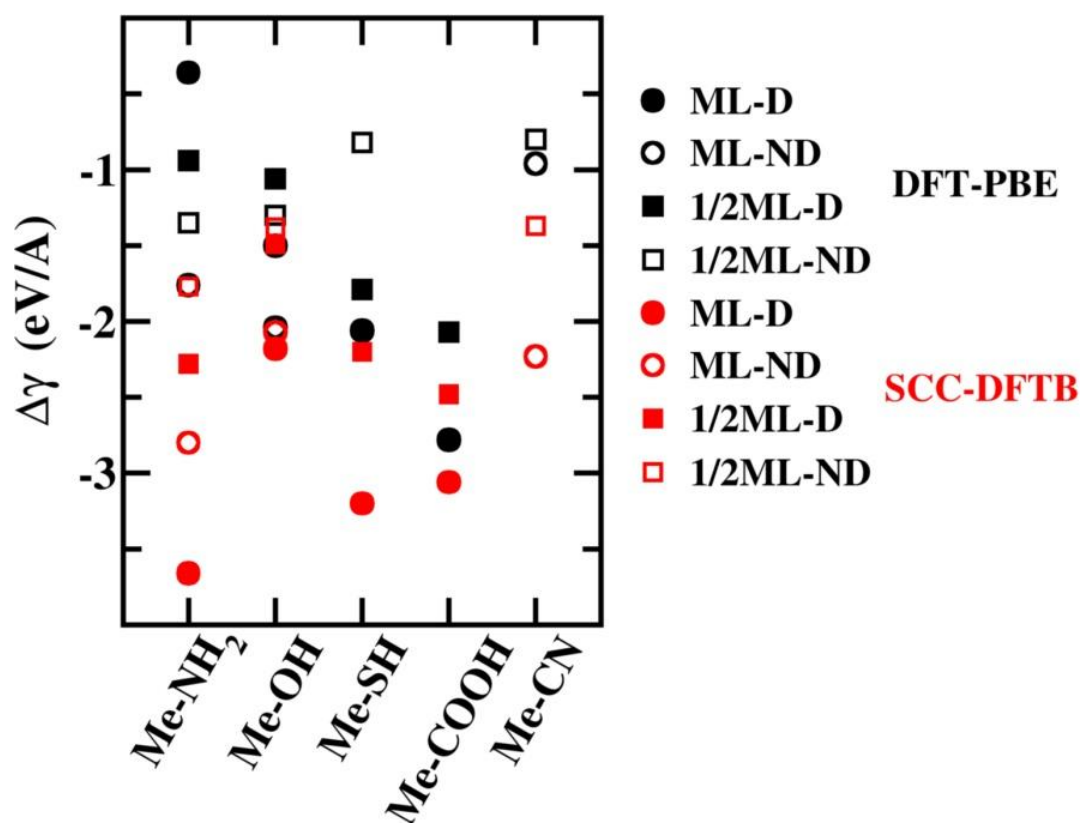


**Figure 5.12** – DFT (PP-PBE-DZP) (black) and SCC-DFTB (red) surface free-energy variations ( $\Delta\gamma$ ), calculated for  $(10\bar{1}0)$ -ZnO surfaces functionalized with substitute methane molecules (ligand-rich conditions). The abbreviations (D) and (ND) state for dissociated and non-dissociated ligand forms respectively. The surface free energy variation  $\Delta\gamma$  is given per standard unit area A corresponding to a  $2\times 1$  surface unit.

As the picture shows, the  $\Delta\gamma$  pattern formed by the SCC-DFTB model is very different from that obtained from DFT calculations. Therefore, it is fair to conclude that our model – in its present form – still does not yield acceptable results for modeling molecular adsorptions on ZnO; clearly requiring corrections before its use can be unrestrictedly recommended for actual simulations. Despite of that, it is interesting to observe that – fortunately – the results for the Me-COOH case are in fact quite reasonable, reproducing very well the qualitative trend verified by the DFT-PBE calculations.

The SCC-DFTB binding energies ( $E_B$ ) for the Me-COOH-ML and Me-COOH- $\frac{1}{2}$ ML adducts – -1.53 and -2.48 eV respectively – are overestimated in relation to their DFT-PBE counterparts, but only up to 0.2 eV per Zn-O bond. Besides, the SCC-DFTB geometries for the Me-COOH surface adducts (Figure 5.13) agree very well with those in our DFT calculations (Table 5.7) – assuming the *bidentate chelating* (BC) and the *bidentate bridging* (BB) configurations for the ML and  $\frac{1}{2}$ ML coverages respectively. In both SCC-DFTB and DFT-PBE simulations, the adsorption of Me-COOH influences the ZnO surface relaxations, by pushing the Zn atoms outwards and increasing the Zn-O surface dimer bond lengths. In the ML-BC configuration, this effect is more pronounced in the SCC-DFTB model, where the surface dimer bond length (Zn-O<sub>3</sub>) is  $\sim 12\%$  larger than that for the clean surface – against  $\sim 9\%$  in the DFT-PBE calculation. For the  $\frac{1}{2}$ ML-BB configuration, SCC-DFTB and DFT-PBE geometries are very alike. Yet for the ML-BC configuration, the only striking difference resides in the Zn-O<sub>1</sub> and Zn-O<sub>2</sub> distances (cf. Figure 5.13), which are almost symmetric in the SCC-DFTB model, but differs by  $\sim 0.3$  Å in the DFT one. Nevertheless, in both calculations, both C-O<sub>1</sub> and C-O<sub>2</sub> bond lengths assume intermediate values between usual single and double C-O bonds (1.4 and 1.2 Å respectively). Additionally, the O<sub>1</sub>-H distance in the ML-BC configuration is compatible with a hydrogen interaction in both SCC-DFTB and DFT-PBE calculations.

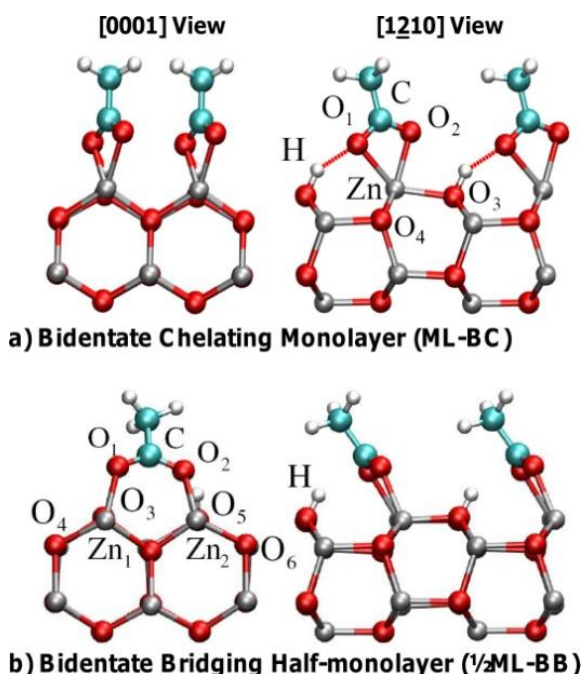


**Figure 5.13** – SCC-DFTB optimized geometries for the stable surface configurations of the ZnO-(1010) functionalized with Me-COOH. The atomic labels introduced here refer to the geometrical parameters in Table 5.7.

In order to further validate our SCC-DFTB model for the adsorption of Me-COOH on ZnO-(10 $\bar{1}$ 0), we have simulated additional surface configurations involving all possible combinations of the three classical adsorption geometries of carboxylic acids on metal oxides with the  $\frac{1}{4}$ ML,  $\frac{1}{2}$ ML and ML coverages (Figure 5.14). As expected, the results are compatible with the DFT-PBE predictions (Section 4.3.2.3), showing only the ML-BC and  $\frac{1}{2}$ ML-BB configurations as stable coverages. Accordingly, no stable coverage has been found with the surface adduct in a mono-dentate ester-type (ME) geometry – which is in good agreement with recent Attenuated Total Reflectance Infrared (ATR-IR) experiments [189]. Besides, meta-stable phases were found neither for the ME nor for BC configurations at partial coverages, with the geometry optimizations always leading to the BB structure.

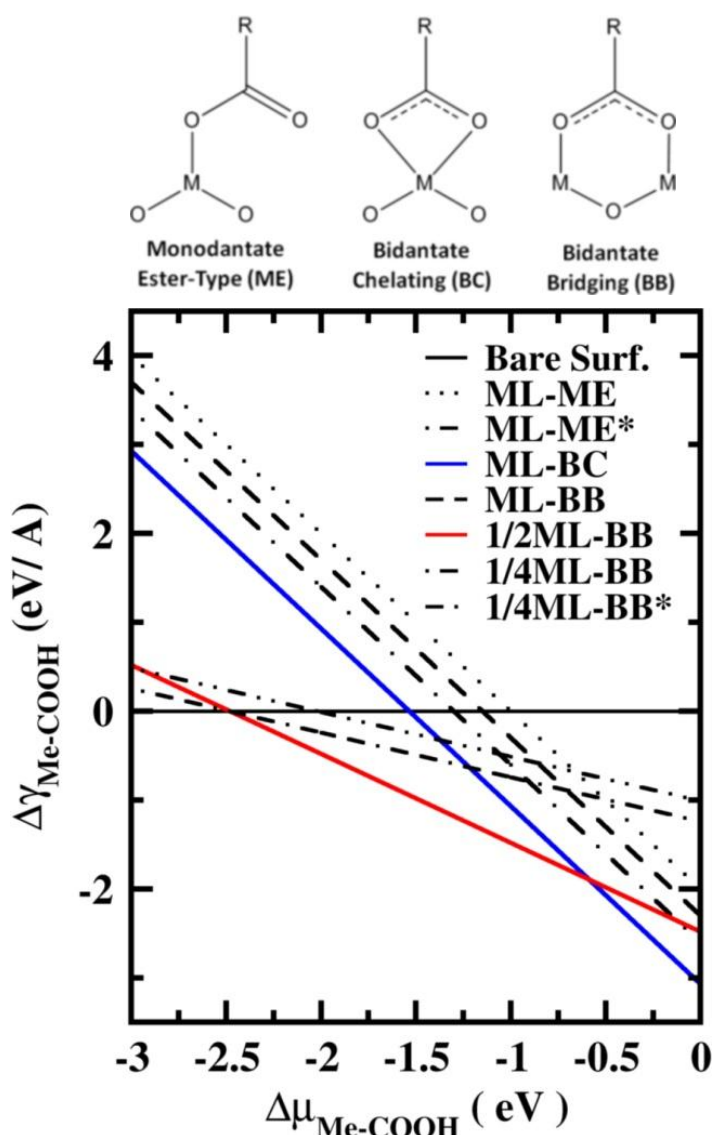


**Figure 5.14** – Classical adsorbate models for carboxylic acids on metal-oxide surfaces; and the SCC-DFTB adsorption phase-diagram for Me-COOH on ZnO-(10 $\bar{1}$ 0). The surface free energy variation  $\Delta\gamma$  is given per standard unit area A corresponding to a 2x1 surface unit. The labels marked with “\*” stand for non-equivalent conformers of the ML-ME and QL-BB configurations.

**Table 5.7** – Geometrical parameters for the Me-COOH-ZnO-(1010) surface adducts – in their ML-BC and ½ML-BB surface configurations – calculated with the SCC-DFTB method and their comparison with the corresponding DFT (PP-PBE-DZP) values (in brackets).

<i>ML-BC</i>		<i>½ML-BB</i>	
<i>Bond Lengths (Å)</i>			
<i>C-O<sub>1</sub></i>	1.28 (1.30)	<i>C-O<sub>1</sub></i>	1.27 (1.27)
<i>C-O<sub>2</sub></i>	1.30 (1.26)	<i>C-O<sub>2</sub></i>	1.30 (1.30)
<i>Zn-O<sub>1</sub></i>	2.16 (2.08)	<i>Zn<sub>1</sub>-O<sub>1</sub></i>	2.05 (2.06)
<i>Zn-O<sub>2</sub></i>	2.15 (2.36)	<i>Zn<sub>2</sub>-O<sub>2</sub></i>	2.04 (2.04)
<i>Zn-O<sub>3</sub></i>	2.10 (2.05)	<i>Zn<sub>1</sub>-O<sub>3</sub></i>	1.95 (1.94)
<i>Zn-O<sub>4</sub></i>	2.07 (2.05)	<i>Zn<sub>1</sub>-O<sub>4</sub></i>	2.04 (2.04)
<i>O<sub>1</sub>-H</i>	1.74 (1.61)	<i>Zn<sub>2</sub>-O<sub>5</sub></i>	2.04 (2.06)
		<i>Zn<sub>2</sub>-O<sub>6</sub></i>	1.99 (2.00)
		<i>O<sub>1</sub>-H</i>	1.99 (2.03)
<i>Angles (°)</i>			
$\angle O_1-H-O_2$	27 (18)	$\angle O_1-H-O_2$	36 (33)
$\angle O_1-C-O_2$	118 (120)	$\angle O_1-C-O_2$	127 (126)
$\angle O_3-Zn-O_4$	101(101)	$\angle O_3-Zn_1-O_4$	109 (112)
		$\angle O_5-Zn_2-O_6$	108 (106)

Finally, we must comment on the failure of our SCC-DFTB model in describing the adsorption of Me-NH<sub>2</sub>, Me-OH, Me-SH and Me-CN on ZnO-(1010). From Figure 5.12 it is possible to observe at least two patent sources of error: *i*) an excessively easy dissociation of the protic ligands and *ii*) the overestimated binding character for the Zn-N interactions. Concerning this last, there is a systematic overbinding of ~ 0.5 eV per Zn-N bond in comparison with DFT calculations – which also appeared in the adsorption of ammonia (Section 5.2.3.5.1) and in the cluster models for zinc complexes with ammonia (5.2.2.3). Note that in the Me-CN case, subtracting 0.5 eV for each Zn-N bond in the surface cell would bring the SCC-DFTB  $\Delta\gamma$  values very close to the DFT-PBE ones, with the same holding true for the non-dissociate surface complexes involving Me-NH<sub>2</sub>.

Regarding the too excessively stable dissociation of Me-NH<sub>2</sub>, Me-OH and Me-SH, the reasons of such behavior is still not fully understood. Within our SCC-DFTB model, these ligands prefer to transfer a proton to the surface and assume a bridging position between two consecutive Zn sites (Figure 5.15). One possible explanation for this spurious behavior is the use the two center approximation itself. Observe that in such bridging geometry, each Zn-site becomes fivefold coordinated. In standard DFT calculations, one of the components expected to counteract such over-coordination is the electronic repulsion between competing ligands *at the coordination site*. Such specific electronic repulsion, however, is given by three center integrals, which are neglected in the SCC-DFTB framework. In theory, such problem can be compensated via the pairwise repulsive potential, but in practice this approach works only if the symmetry of the actual problem is similar to that used to fit the repulsive potential.

Another probable limitation is related to the construction of the *Slater-Koster tables*. Recall that the SCC-DFTB *Hamilton and overlap matrix elements* are obtained from dimer calculations. Once stored in the *Slater-Koster tables*, such values are called during the simulation according only to interatomic distances. In other words, the symmetry of the orbitals are not really taken into account

during the SCC-DFTB calculation, which may lead to such geometry distortions if there are too much degrees of freedom for atomic relaxations. Once again, this effect can be compensated via the repulsive potential, but only if the symmetry of the studied system is similar to that used to construct the repulsion potential. In the Me-COOH case this limitation apparently does not manifest, once it is not possible to translate the carboxylic oxygen atoms independently. In other words, the bidentate structure of the ligand seems to prevent such over-coordination errors.

So far we have shown that the SCC-DFTB performance obtained for the adsorption of Me-COOH molecules on ZnO-(10 $\bar{1}$ 0) is sufficient, but further improvements of our model are subject of future studies.

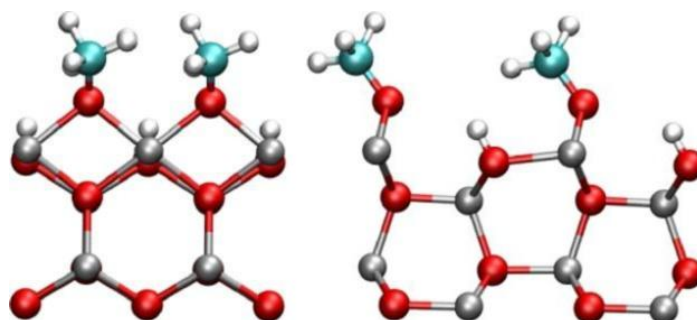


**Figure 5.15** – SCC-DFTB optimized geometry for the dissociated Me-OH surface adduct in the ML coverage.

## Chapter Summary

In this chapter we have presented our SCC-DFTB parametrization for Zn-X interactions ( $X = \text{H, C, N, O, S}$  and Zn). The model has demonstrated a reliable performance in representing different the zinc-containing systems, including bulk phases (*hcp*-Zn, *w*-ZnO and *zb*-ZnS), ZnO surfaces, ZnO nanostructures and model zinc molecular complexes – being transferable among these different chemical environments. Nevertheless, the parameters have not succeeded in accurately describing adsorption processes; making further improvements necessary in the future. An important exception is the adsorption of Me-COOH on the ZnO-(10 $\bar{1}$ 0) surface, whose SCC-DFTB results reproduce their DFT-PBE analogs with adequate accuracy. In order to further validate the Me-COOH adsorption on ZnO-(10 $\bar{1}$ 0), we have tested several different surface configurations involving the classic adsorption modes of carboxylic acids on metal oxides and different surface coverages. The results have confirmed our previous DFT-PBE calculations, being also in line with recent ATR-IR experiments – which confirms its reliability in this case.







# Chapter 6

---

## Native Defects in ZnO Nanowires and Defect Healing with Organic Acids

*"Nature has perfections in order to show us that she is the image of God; and defects to show us that she is only his image."*

*Blaise Pascal – French Physicist.*

In the last chapter we have seen that ZnO surfaces – including the adsorption of organic acids on that – and nanostructures are accurately described by the SCC-DFTB method. In this chapter we will apply SCC-DFTB simulations to a problem we have discussed with our experimental collaborators in the University of Bremen: The characterization of native defects on ZnO nanowires. After that, we will also apply the SCC-DFTB method to study the interaction of surface oxygen vacancies with organic acids, giving a reasonable explanation for the photoluminescence anomalies observed in polymer coated ZnO nanowires.

### 6.1 –Why Characterizing Native Defects on ZnO Nanowires?

As we have discussed during the past chapters, ZnO nanostructures have been often indicated as promising building blocks for electronic and optical nanodevices. However, the development of reliable ZnO-based nanodevices is still hampered by the lack of control on the electric and optical properties of such materials. Controlling the resistivity of ZnO has long been a difficult task because of high levels of unintentional n-type doping and the challenging achievement of p-type doping (as discussed in Section 3.1). The optical properties of ZnO are also not fully understood, since the photoluminescence (PL) spectra of ZnO nanostructures have been often reported to be strongly dependent on synthetic/annealing conditions. In fact, several exciting technological potentialities have been demonstrated for ZnO nanostructures across the last few years, but it is necessary to understand and control their intrinsic properties before they can be applied to new commercial ZnO based technologies.

Both electric and optical properties of ZnO have often been suggested to be dominated by intrinsic defects. Oxygen vacancies and zinc interstitials in ZnO, for example, have been suggested as possible sources of both the n-type conductivity in ZnO [141, 235,236] and the green deep level emissions (DLE) in the PL spectra of ZnO nanowires [237,238]. Several experimental techniques have been employed in order to identify intrinsic defects in ZnO, including photoluminescence spectroscopy, electron spin resonance and positron annihilation spectroscopy [239].

On the theoretical side, first principles density functional theory (DFT) methods have been widely employed for calculating intrinsic defects in bulk ZnO. However, different levels of exchange-correlation treatment and different correction schemes for supercell-size effects have been leading to conflicting results. The most notorious case has been that of oxygen vacancies, whose +2/0 charge state transition has been found in Fermi energies ranging from 1 to 3 eV below the conduction band minimum (CBM)[141, 240-243]. Furthermore, less attention has been given to surface defects, despite there are considerable experimental evidences showing that they are critical for the physical behavior of ZnO films and nanostructures. The differences observed in the photoluminescence spectra of bare and polymer-coated ZnO nanowires [155], for instance, strongly suggest that surface defects dominate the optical properties of such materials. Besides, a recent first-principles DFT study has suggested that neutral oxygen vacancies in ZnO nanowires strongly contributes to their optical absorption in the visible region [142]. Despite of that, most theoretical works on ZnO nanostructures are still limited to the relative stability and size effects in different defect-free systems – such as nanowires [178,203,244-246], thick-/single-walled nanotubes[244,245,247] and nanobelts [248]. Although there are few recent works addressing specific defects in ZnO nanostructures[249,250], a comprehensive characterization of intrinsic defects in these systems is still missing.

In this chapter, we will employ the SCC-DFTB method in order to investigate the relative stability and electronic structure of native point defects in hexagonal [0001] ZnO nanowires. We will investigate the relative stability of four different point defects – *oxygen vacancies* ( $V_o$ ), *zinc vacancies* ( $V_{zn}$ ), *oxygen interstitials* ( $O_i$ ) and *zinc interstitials* ( $Zn_i$ ) – occupying different positions across the wire's cross-section (Figure 6.1). We also will compare the formation energy and the geometries of defects in different charge states, calculated by using a simple potential alignment procedure. Finally, we will demonstrate how neutral oxygen vacancies in non-polar ZnO surfaces can be healed by reacting them with organic acids, constituting a tempting explanation for the suppression of PL-DLE bands observed for polymer-coated ZnO nanowires.

## 6.2 – Simulation Details

The ZnO surfaces and nanowires have been simulated as infinite structures by using Periodic Boundary Conditions and suitably oriented supercells. The calculations have been performed with a suitable vacuum region surrounding the structures – along the directions normal to their surfaces – in order to avoid spurious interactions among consecutive periodic replicas. Geometry optimizations have been performed with the Conjugated Gradient algorithm, until all forces became smaller than 0.005 eV/Å. Convergence tests on the  $k$ -

points sampling showed that a (1 x 1 x 1) Monkhorsh-Pack grid [152] is appropriate for our calculations. As SCC-DFTB is not influenced by the *band gap problem* (Section 2.4.3.3) to the same extent as standard DFT methods, we have applied no post-processing *band gap* correction scheme. All calculations have been performed with the DFTB+ package [226], using the SCC-DFTB model for ZnO reported in Chapter 5.

For the characterization of the point defects, we have performed the simulations by using model-nanowires with 1.6 nm of diameter in supercells ranging from 3 to 9 ZnO bi-layers ( $L$ ) along the wire's growth direction (Figure 6.1.a). The defects have been placed in five different positions across the cross-section of the nanowire (Figure 6.1.b and 6.1.c), and considered in three different charge states in each case – namely 0,1+ and 2+ for  $V_O$  and  $Zn_i$  and 0,1- and 2- for  $V_{Zn}$  and  $O_i$ . Besides, the wires have been simulated into rectangular supercells ( $a \times b \times c$ ,  $a=b$ ) with its lattice vector  $a$  (perpendicular to the growth direction) being empirically determined in order to align the reference potential for calculations involving neutral and charged states (further details will be addressed in Section 6.3). We have not employed any post-processing correction for spurious long-range electrostatic interactions among charged periodic images, once convergence tests have indicated that our alignment potential procedure is enough to eliminate such simulation artifacts (depicted in the Figure 6.5). Besides, the applicability of such correction schemes has been considered controversial for extended structures [141,251,252]. For the reaction between neutral oxygen vacancies and organic acids, the calculations have been performed by using periodic slab models with one single  $V_O^0(S)$  defect for each 4x4 surface unit. Furthermore, we have tested several distinct adsorption geometries as simulation starting points in order to identify different possible meta-stable configurations.

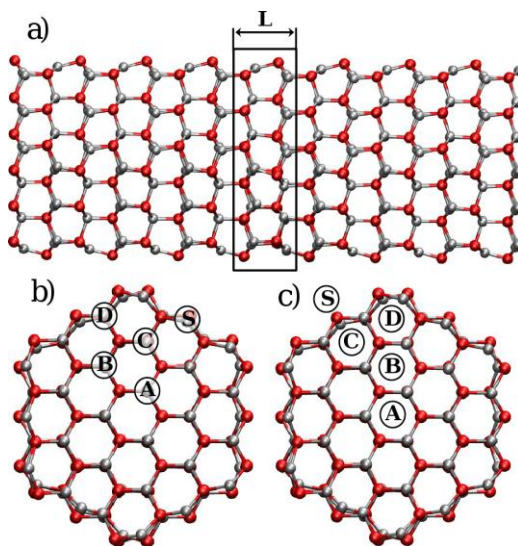


**Figure 6.1** – Side view of a [0001] ZnO nanowire (a), constructed by the periodic repetition of a ZnO bi-layer unit ( $L$ ), and the investigated defect positions – denoted by the symbols A, B, C, D and S – for intrinsic vacancies (b) and interstitials (c) along its cross-section.

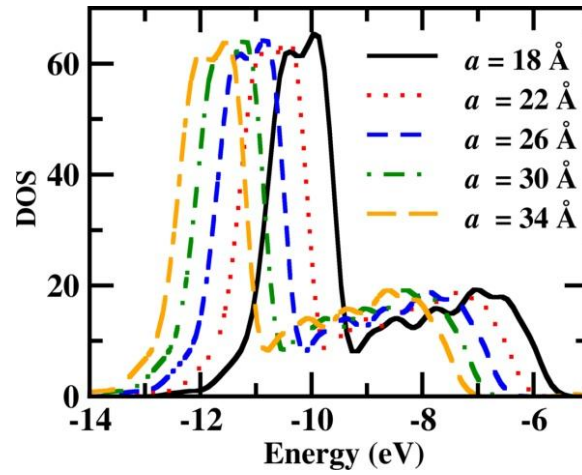


**Figure 6.2** – Influence of the supercell vacuum size on the DOS of a [0001] ZnO nanowire (4xL) with a  $V_O^{2+}(S)$  defect, calculated with the SCC-DFTB method.

### 6.3 – The potential Alignment Procedure

In order to identify and compare different point defects, the pivotal property to be quantified is the defect formation energy ( $E_f$ ):

$$E_f(X^q) = E_t(X^q) - E_t(R^0) - \sum_i n_i \mu_i + qE^F \quad (6.1)$$

where  $E_t(X^q)$  and  $E_t(R^0)$  state for the total energy of the supercell with ( $X^q$ ) and without the defect ( $R^0$ ) respectively;  $n_i$  is number of atoms of type  $i$  removed or added to  $R^0$  in order to create the defect,  $\mu_i$  is the chemical potential of the specie  $i$ ,  $q$  is the defect charge and  $E^F$  is the Fermi energy. The chemical potentials of oxygen and zinc are subject to upper bounds, given by the energy of the O atom in the  $O_2$  molecule (extreme O-rich conditions) and the energy per Zn atom in the hexagonal closed packed structure (Zn-rich conditions). The lower chemical potential bounds are defined by the thermodynamic stability condition for ZnO ( $\mu_O + \mu_{Zn} = \Delta H_f(ZnO)$ ).

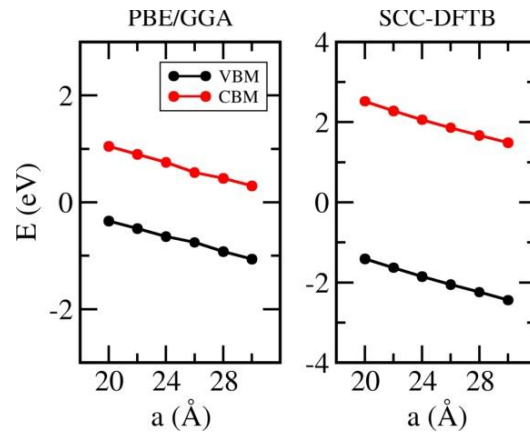


**Figure 6.3** – Influence of the vacuum size on the band edges for a [0001] ZnO nanowire (4xL) with a  $V_O^{2+}(S)$  defect, calculated with the DFT(PP-PBE-DZP) and SCC-DFTB methods.

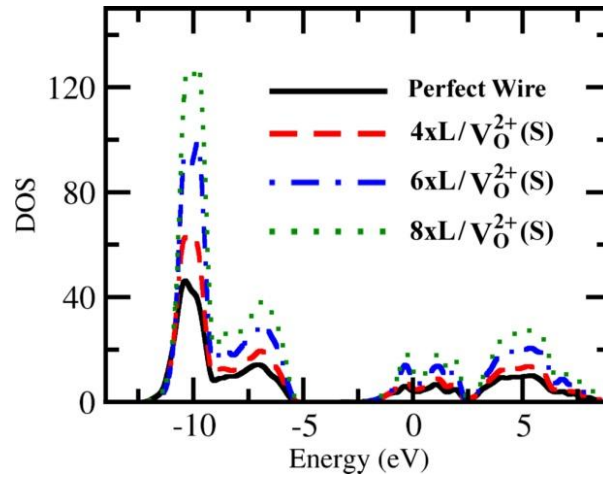


**Figure 6.4** – Optimal DOS alignment for nanowires with  $V_O^{2+}(S)$  defects – calculated with different supercells by using the SCC-DFTB method – obtained with the supercell side length  $a = 26 \text{ \AA}$ .

It is important to note that Eq. 6.1 can only be considered if  $E_t(X^q)$  and  $E_t(R^0)$  are calculated under the same potential reference. However, that is not a trivial task when calculating charged defects in extended structures, since a divergent electrostatic potential arises as a consequence of using periodic boundary conditions. Although this effect is partially compensated by introducing a uniform *jellium* background into the supercell, a finite shift in the electrostatic potential usually remains, which makes a careful potential alignment procedure between  $X^q$  and  $R^0$  generally necessary [253,254].

For charged nanostructures, such potential alignment can be performed through a simple empirical procedure, since the dimensions of the employed supercell influence its own electrostatic potential in two different ways: *i)* by setting the separation among the charged replicas in the periodic superlattice and *ii)* by determining the density of the compensating *jellium background* contained in the supercell. These dependencies appear in the electronic structure of the model, whose density-of-states (DOS) is systematically shifted with the size of the supercell – as shown in Figure 6.2 for a doubly charged oxygen vacancy at the surface of a ZnO nanowire ( $V_O^{2+}(S)$ ). To ensure the reliability of our procedure, we have also reproduced this result with first principles DFT-PBE calculations (Figure 6.3) – using the SIESTA package [146] – and found similar results.

The potential equality between  $X^q$  and  $R^0$  can be achieved by choosing adequate supercell dimensions in order to align their characteristic DOS peaks. This principle is demonstrated in Figure 6.4 for different supercells containing a  $V_O^{2+}(S)$  defect – assuming a perfect/neutral wire as  $R^0$ . In these cases we have found a DOS alignment better than 0.1eV for  $a = 26 \text{ \AA}$ . The alignment of the DOS ensures that the presence of point defects does not influence electronic states far from the defect site, and that all electronic levels are calculated under the same potential reference for both  $R^0$  and  $X^q$ . It is worth to mention that changing the supercell size does not lead to any significant change in the charge distribution across the defective wires, reinforcing that such procedure just influences the external reference potential. We have repeated the procedure for the wires with  $V_O^{1+}(S)$  defects, also achieving a DOS alignment better than 0.1eV with  $a = 26 \text{ \AA}$ .

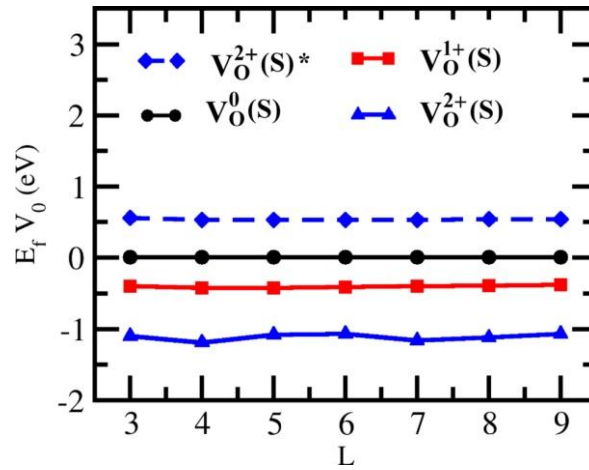


**Figure 6.5** – Formation energies of  $V_O^{2+}(S)$ ,  $V_O^{1+}(S)$  and  $V_O^0(S)$  defects in [0001] ZnO nanowires calculated with different supercell sizes and assuming the Fermi energy as valence band maximum. The dashed line corresponds to the formation energy of non-relaxed  $V_O^{2+}(S)$ .

Our DOS alignment procedure has been further-tested by calculating  $E_f$  for  $V_O^0(S)$ ,  $V_O^{1+}(S)$  and  $V_O^{2+}(S)$  in ZnO nanowires (Figure 6.5) with different supercell sizes (from 3L to 9L). The picture shows converged results for  $V_O^0(S)$  and  $V_O^{1+}(S)$ , with the fluctuations observed for the  $V_O^{2+}(S)$  case identified as minor relaxation effects among the different supercells – since the  $E_f$  for the non-relaxed  $V_O^{2+}(S)$  defects (dashed blue line) have been found to be as convergent as those in the  $V_O^0(S)$ , and  $V_O^{1+}(S)$  cases. These results confirm the reliability of the potential alignment procedure, which has yielded consistent formation energies for charged  $V_O$  defects calculated with different supercell sizes. On the other hand, they also show that supercell-size effects on the atomic relaxations do not vanish. Therefore, for all remaining defects, we have performed the potential alignment for supercells with 8L ( $\sim 864$  atoms), meeting the alignment with  $a = 26\text{\AA}$  for  $V_O$  and  $Zn_i$  and  $a = 27\text{\AA}$  for the  $V_{Zn}$  and  $O_i$  respectively. These values lead to a ratio D/V of  $\approx 1.5$ , where V is the size of the vacuum region into the supercell and D is the diameter of the wire. We have also confirmed this D/V ratio for thinner ZnO nanowires (10  $\text{\AA}$  of diameter) with  $V_O^{2+}(S)$  defects. Similar results have been also reported for the alignment of the Hartree potential in DFT calculations for charged silicon nanowires [255].

## 6.4 – Defect Positions and Atomic Relaxations

After performing the alignment of the DOS, we have calculated  $E_f$  for all defects considered here (Figure 6.6). Both  $V_O$  and  $V_{Zn}$  have shown the surface (S) as preferential site in all charge states, since that position minimizes the number of dangling bonds created by the defects and favors geometry relaxations. The surface has been also the preferential site for the  $Zn_i$  in all charge states and for  $O_i^0$  as well. It is interesting that the formation energy of  $Zn_i^0(S)$ , is 2.7 eV lower in energy than the one for  $Zn_i^0(A)$  whereas the difference between  $O_i^0(S)$  and  $O_i^0(A)$  is only 0.7 eV – which is in line with the atomic size differences between oxygen and zinc.



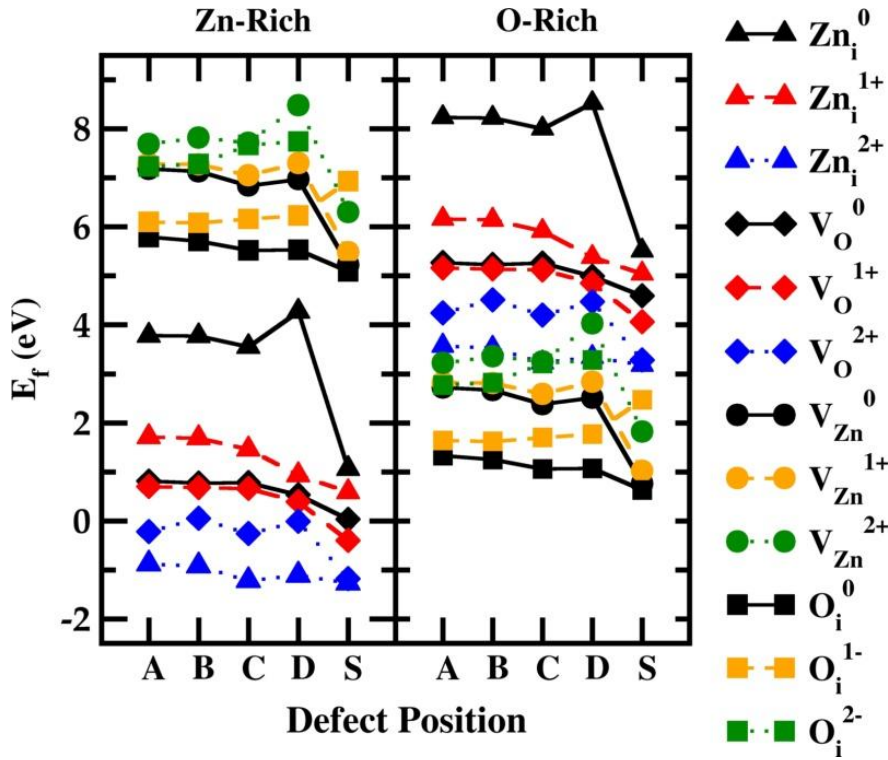


**Figure 6.6** – Relative stability diagram for intrinsic defects in [0001] ZnO nanowires. The defect position labels correspond to those specified in Figure 6.1. In all cases the *Fermi* energy has been assumed to be equal to the valence band maximum.

The states  $O_i^{1-}$  and  $O_i^{2-}$  have been found energetically favorable at the position A (Figure 6.7). Such inner positions favor the electronic hybridizations involving the interstitial atom and the host structure, helping to accommodate the charge excesses in the  $O_i^{1-}$  and  $O_i^{2-}$  states. In fact, compared to  $O_i^0(A)$ , the interstitial atom in  $O_i^{2-}(A)$  shows just a residual increment of  $\sim 0.2 e^-$  in its electronic density, with the most of the charge excess spread among Zn atoms in the host structure. It is interesting to note that polarized PL measurements have recently shown that yellow DLE bands cannot be originated on the surface of ZnO the wires [239], while thermal-annealing/PL experiments have been suggesting oxygen interstitials as sources of such bands. Altogether, our calculations corroborate this picture.

Unlike  $O_i^{1-}$  and  $O_i^{2-}$ , wide charge dispersions have not been verified for  $Zn_i$ . The Mulliken charge on the interstitial atom remains close to zero for  $Zn_i^0(S)$ , but is  $\sim +0.4 e^-$  and  $+0.8 e^-$  for  $Zn_i^{1+}(S)$  and  $Zn_i^{2+}(S)$  respectively. For the  $Zn_i^0(S)$  and  $Zn_i^{1+}(S)$ , the interstitial atom have been found adsorbed on the surface of the nanowire through an oxygen and a zinc sites simultaneously (Figure 6.7.d and 6.7.e), whereas for  $Zn_i^{2+}(S)$  it relaxes towards the surface in order to enhance its interactions with the O surface anions. Moreover, the interstitial atom pushes one Zn surface atom inwards, to the position C approximately, resulting in a split interstitial geometry (Figure 6.7.f). It is interesting to note that the displaced Zn atom also shows a Mulliken charge of  $+0.8 e^-$ , which means that the most of the charge excess in  $Zn_i^{2+}(S)$  is localized on two Zn sites only.

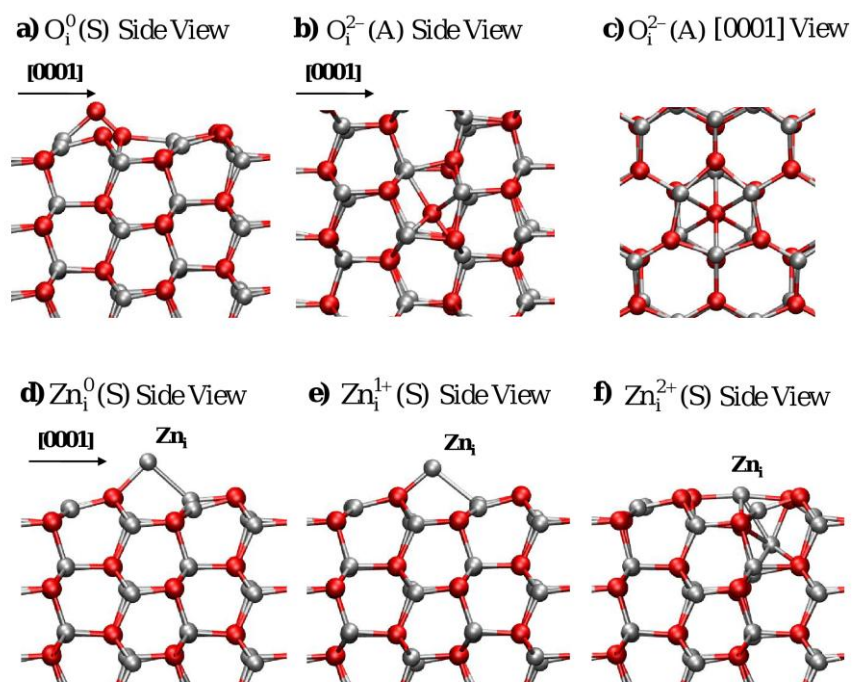


**Figure 6.7** – SCC-DFTB optimized geometries for : a)  $O_i^0(S)$ , b)  $O_i^{2-}(A)$  (Side View), c)  $O_i^{2-}(A)$  (Front View), d)  $Zn_i^0(S)$ , e)  $Zn_i^{1+}(S)$  and f)  $Zn_i^{2+}(S)$  in ZnO [0001] nanowires. The wire growth direction is indicated with the arrow in a), b), d), e) and f); and perpendicular to the paper plane in c).

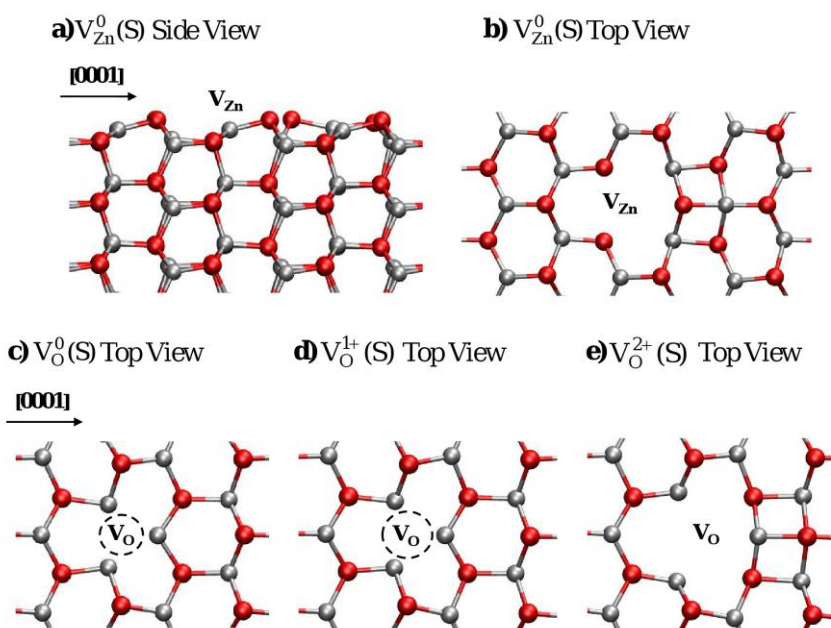


**Figure 6.8** – SCC-DFTB optimized geometries for : a)  $V_{Zn}^0(S)$  (Side View), b)  $V_{Zn}^0(S)$  (Top View), c)  $V_O^0(S)$  (Top View), d)  $V_O^{1+}(S)$  (Top View) and e)  $V_O^{2+}(S)$  (Top View) defects in ZnO [0001] nanowires. The wire growth direction is indicated with the arrows. In b), c), d) and e) the ZnO layers below the surface have been omitted in order to aid the visualization of the defect structure.

The  $V_{Zn}^0(S)$  defect also leads to a noticeable relaxation, with one oxygen surface atom strongly relaxing outwards from the defect site in order to enhance its coordination (Figure 6.8.a and 6.8.b). The relaxations for  $V_{Zn}^{1-}(S)$  and  $V_{Zn}^{2-}(S)$  are very similar to that observed for  $V_{Zn}^0(S)$ , while their respective charge excesses distributed uniformly along the nanowire.

For the surface oxygen vacancies, the atomic relaxations have been found very similar to those in their bulk counterparts [141]. In the neutral case ( $V_O^0(S)$ ), the three Zn sites around the vacancy relax inward to form a sort of small Zn-cluster on the surface of the wire (Figure 6.8.c). The cohesion of this metal cluster is held by a localized defect level – basically composed by the  $4s$  Zn orbitals – which acts like a 3-centers-2-electrons (3c/2e) chemical bond. Thus, the ionization of the defect to its  $V_O^{1+}(S)$  and  $V_O^{2+}(S)$  states corresponds to weakening this bond and leads to the relaxation of the Zn sites around the defect outwards (Figure 6.8.d and 6.8.e). Nevertheless, it is important to remark that oxygen vacancies in ZnO have been a quite controversial issue. Under Zn-rich conditions, formation energies between 0.8 and 5.0 eV have been calculated – with different DFT-based methods – for  $V_O^0$  defects in bulk ZnO. *Janotti and Van de Walle* [141] suggested that oxygen vacancies cannot be the source of n-type conductivity in ZnO because of its high formation energy calculated with LDA+U ( $\sim 3.7$  eV). On the other hand, values around 1.0 eV have been reported for calculations using both GGA and the hybrid *Heyd-Scuseria-Ernzerhof* (HSE) functionals [240, 254], which are consistent with our results for the bulk-like position in the nanowire (position A). Besides, our calculations suggest that the oxygen vacancies are considerably more stable on the surface of the wire, where their formation energies decrease to  $\approx 0.3$  eV, suggesting that such defects are reasonably likely under Zn-rich conditions.

## 6.5 – Healing Surface Oxygen Vacancies with Organic Acids

As mentioned above, recent DFT calculations have demonstrated that neutral oxygen vacancies are the most likely sources of the green DLE PL-bands observed for ZnO nanowires. It has been also demonstrated that such bands are effectively suppressed by capping the wires with polymers and surfactants – most of them containing highly oxidized organic groups – giving a strong evidence that they are originated in the surface of the ZnO nanowires. Altogether, such results suggest that the suppression of the green DLE bands may be related to some chemical reaction involving the  $V_O^0(S)$  defect and the organic matter. In fact, the  $V_O^0(S)$  defect is expected to show an enhanced reactivity under oxidative conditions, since its trigonal planar geometry lets its 3c/2e bond exposed to the environment and susceptible to oxidizing agents consequently. Besides, the reactivity of oxidizing gases (i.e.  $O_2$  and  $NO_2$ ) against neutral oxygen vacancies in single walled ZnO nanotubes has been demonstrated by DFT calculations [250], although the electronic deep-levels observed for their final reaction products strongly suggest that their luminescence spectra would be still dominated by DLE bands. On the other hand, experiments strongly indicate that the organic matter plays a role in such DLE suppression in ZnO nanowires, but such hypothesis has been never addressed theoretically and the atomistic mechanism behind it remains unknown.

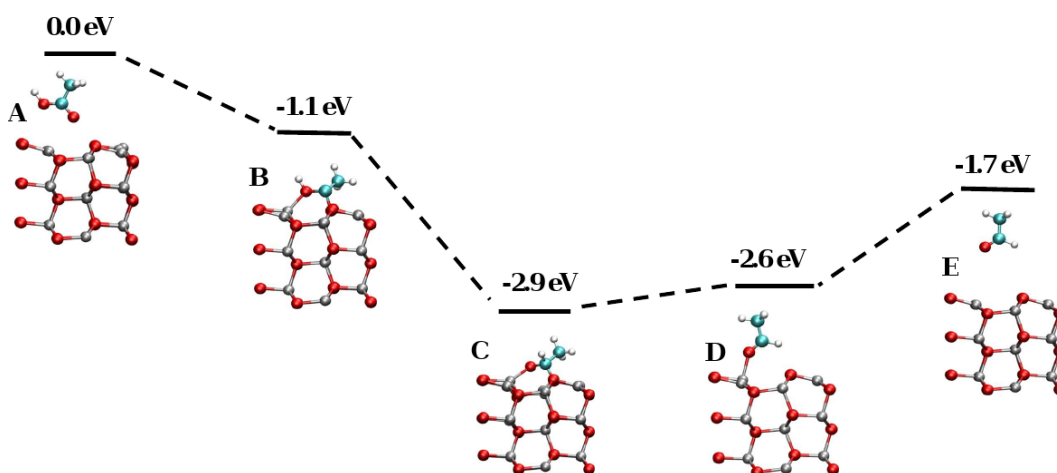


**Figure 6.9** – Virtual reaction pathway for the healing of a  $V_o^0(S)$  with organic acids. The defective surface and a gas-phase Me-COOH molecule (A) have been assumed as starting reactants and the clean surface and a gas-phase formaldehyde molecule (Me-COH) (E) as final products. The surface adducts B, C, and D correspond to intermediate states identified in our calculations.

Therefore, we have investigated the reaction of the  $V_o^0(S)$  defect with small highly oxidized organic groups, using Me-COOH as a prototype molecule. By assuming the defective surface plus the Me-COOH gas phase molecule (A in Figure 6.9) as our energy reference state ( $E=0$ ), we have identified three different adsorbate geometries (B, C and D in Figure 6.9) which can be interpreted as intermediates in a virtual defect healing reaction. In the first case (the adduct B in Figure 6.9) one of the carboxylic oxygen atoms attaches to the surface and fills the vacancy site, with the  $3c/2e$  defect bond being substituted by 3 conventional Zn-O bonds – besides the coordination of the second carboxylic oxygen with an ordinary Zn surface site. So, the carboxyl group receives the electrons coming from the defect state. Since the O atom cannot expand its valence, the carboxylic C=O bond must be broken, and its  $\pi$ -electrons migrate to the carboxylic carbon atom. The carbon atom is then reduced, assuming a  $sp^3$  hybridization in order to accommodate its former  $\pi$ -bond electrons as an lone-pair – identified as a localized deep-level slightly above the former  $V_o^0(S)$  defect level in energy (Figure 6.10). It is worth to mention that the observed  $A \rightarrow B$  adsorption is similar to the dissociative chemisorption of  $O_2$  and  $NO_2$  on  $V_o^0(S)$  defects in single-walled ZnO nanotubes, demonstrated in [250].

Yet the formation of the adduct B leads to a considerable free-energy release of 1.1 eV, it is very unlikely that such specie shows a long life-time under usual temperature conditions. Lone pairs localized on carbon atoms are very reactive and often promote molecular rearrangements, such as hydrogen migrations for example. In fact, we observed that a hydrogen migration in the adsorbed Me-COOH – from the oxygen to the carbon site – results in an additional energy release of 1.8 eV. Besides, the resulting surface adduct (C in Figure 6.9) resembles an aldehyde molecule adsorbed on a perfect ZnO surface, coordinated through both the carbon and oxygen atoms. In other words, the hydrogen migration consolidates the reduction of the Me-COOH molecule by the  $V_o^0(S)$ . It is interesting to notice that no intra-gap state appears in the DOS for the adduct C (Figure 6.10), corroborating the idea that the defect healing through the reaction with the organic molecule may lead to the DLE suppression.

Once the carbonyl group is reduced, the defect healing process can be concluded by cutting the remaining carboxylic C-O  $\sigma$ -bond, yielding a monodentate formaldehyde adsorbate on the defect-free surface (adduct D in Figure 6.9). However, the adduct D has been found 0.3 eV above its bidentate counterpart (adduct C) in energy, being hardly expected to exist in significant amounts under ordinary equilibrium conditions. Regarding to the electronic structure, the DOS calculated for adduct D shows an empty deep-level (Figure 6.10) indentified as the C=O anti-bonding  $\pi^*$ , whose energy is lowered because of the interaction with the surface. Nevertheless, this deep-level is not expected to play any significant role in the ZnO PL spectrum, once the adduct D has been identified just as marginal configuration.

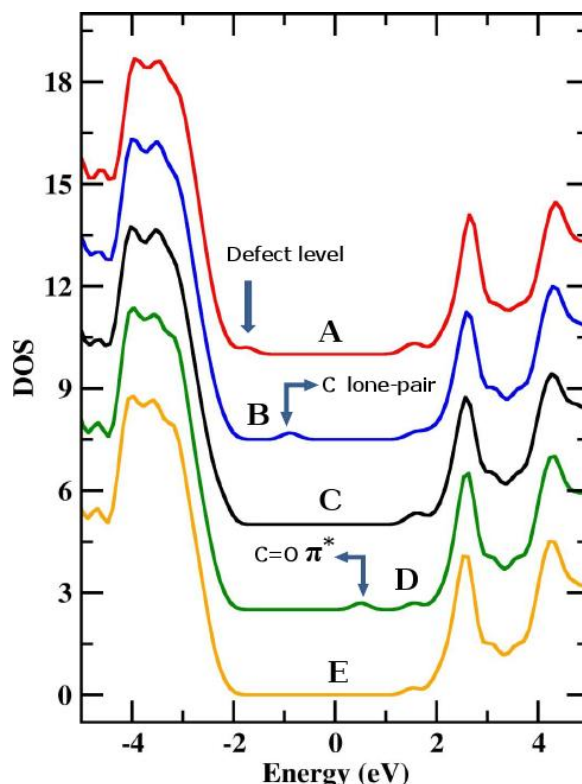


**Figure 6.10** – SCC-DFTB total density of states (DOS) calculated for the reactants, intermediates and products of the reaction between Me-COOH and a  $V_O^0(S)$  defect on the  $10\bar{1}0$ -ZnO surface. The labels A,B,C,D and E refer to the configurations depicted in Figure 6.9.

Finally, we have verified that the dissociation of the adduct D – yielding the clean ZnO surface plus a gas-phase formaldehyde molecule (E in Figure 6.9) – would cost additional 0.9 eV in energy, showing that such process is unlikely to happen under ordinary conditions. On the other hand, the configuration E is still 1.7 eV more stable than the initial configuration A (the gas-phase acetic acid plus the defective surface), which means that E would probably be the favored product on high-vacuum thermal dissociation experiments. It is also interesting to mention that a similar reaction mechanism – also involving neutral oxygen vacancies – has been proposed in order to explain the release of ethylene and  $H_2$  in the *temperature-programed desorption* (TPD) of ethanol on ZnO nanowires [256], which reinforces the confidence in our surface healing model.

In conclusion,  $V_O^0(S)$  defects are hardly expected to survive if exposed to carboxylic acids, which more likely heals the surface by docking one of its oxygen atoms to the defect. In this process, the defect-related electronic deep-level is eliminated; making the surface reaction between the  $V_O^0(S)$  defect and the oxidized organic molecule a tempting explanation for the suppression of DLE bands in polymer/surfactants coated ZnO nanowires.

## Chapter Summary

In this chapter, we have investigated intrinsic point defects in ZnO [0001] hexagonal nanowires by using the SCC-DFTB method. We have demonstrated a consistent empirical potential alignment procedure, which allowed us to calculate and compare formation energies of defects in different charge states in an efficient but accurate manner. We have shown that the defects lie preferentially on the surface of the wire, where their atomic relaxations around the defect are facilitated. The exception has been the  $O_i^{1-}$  and  $O_i^{2-}$  defects, which are stabilized in inner positions due to a better charge accommodation. Finally, we have investigated the surface reaction between neutral oxygen vacancies and carboxylic acids, demonstrating that such molecules can heal the defective surface through an oxidation-reduction reaction, which is a tempting atomistic mechanism to explain the suppression of the anomalous green luminescence bands in organic-coated ZnO nanowires.







# Chapter 7

---

## Concluding Remarks and Future Plans.

*"The future belongs to those who believe in the beauty of their dreams."*

*Eleanor Roosevelt – Former American First Lady and Human Rights Activist.*

In this work, we have employed different *Density Functional Theory* (DFT) based methodologies to investigate functionalized ZnO surfaces and nanostructures.

In order to better understand the surface chemistry of ZnO, we have employed standard *Kohn-Sham* DFT calculations to investigate the interactions of ZnO non-polar surfaces with five different organic functional groups (i.e. -OH, -NH<sub>2</sub>, -SH, -COOH, and -CN). Contradicting the usual chemical intuition, the formation of classical Lewis acid-base adducts has not been confirmed. Instead, we have demonstrated that the major surface stabilization mechanisms in these cases are: *i)* electrostatic interactions involving the ligand and Zn surface sites, *ii)* hydrogen bonds involving O surface sites and *iii)* the passivation of O surface sites through proton-transfer reactions – for the acetic acid and methanethiol cases. We have also discussed the influence of the surface coverages on the adducts' geometries and binding energies, besides quantitatively characterizing their thermodynamic stabilities under different chemical conditions – including humid atmospheres and the aqueous media. Among all the investigated functional groups, -COOH is the most promising one as anchoring agent for ZnO functionalization, being expected to form stable monolayer coverages even in the presence of water.

Aiming to large scale simulations on ZnO hybrid materials, we have also presented an *Self Consistent Charge Density Functional based Tight Binding* (SCC-DFTB) model for ZnO plus organics. The developed parameters comprise all Zn-X

interactions ( $X = \text{H, C, N, O, S}$  and  $\text{Zn}$ ), which have been validated by comparing their predictions with standard DFT results. The parameters have demonstrated a reliable performance in modeling bulk zinc-containing systems – i.e. *hcp*-Zn, *w*-ZnO and *zb*-ZnS – ZnO surfaces, ZnO nanostructures and zinc-containing molecular complexes; showing good transferability among these different chemical environments. Unfortunately, the model was not able to accurately reproduce the interactions of Me–OH, Me–NH<sub>2</sub>, Me–SH and Me–CN with ZnO-(1010) surfaces. The Zn–N interactions showed a systematic overbinding of  $\sim 0.5$  eV per bond. Besides, the dissociation trend of Me–OH, Me–NH<sub>2</sub> and Me–SH was clearly overestimated. Nevertheless, the adsorption of Me–COOH – the most important case among the investigated ligands – has been reproduced with good accuracy; even in quantitative terms.

Finally, we have employed our SCC-DFTB model to investigate the geometry and formation energies of intrinsic defects in ZnO nanowires. We have calculated the atomic relaxations and formation energies for neutral and charged defects, by using an empirical potential alignment procedure developed in this work. Oxygen vacancies and zinc interstitials have been found as the lowest energy defects under Zn-rich conditions, whereas oxygen interstitials and zinc vacancies are favored under O-rich conditions. Most defects have been found to be favored on the surface of the wire; except for charged oxygen interstitials, which prefer inner positions because of a better charge accommodation observed there. Additionally, we have also investigated the interaction between surface oxygen vacancies and carboxylic acids – by using Me–COOH as a prototype molecule – demonstrating that an oxidation-reduction reaction may explain the suppression of green luminescence bands experimentally observed for organic-coated ZnO nanowires.

In conclusion, we have achieved significant progresses at three active topics of the current hybrid-ZnO research: *i*) understanding the surface chemistry of ZnO; *ii*) understanding the defect physics of bare and functionalized ZnO nanostructures and *iii*) developing a computationally efficient method for realistic large scale simulations on ZnO.

Certainly, such advances provide a good starting point for future projects. For example, the stabilization mechanisms identified for organic functional groups on ZnO indicate a clear direction towards more efficient anchoring agents: The electrostatic nature of the ligand-substrate interactions and the role of the proton transfer reaction in the adducts' stabilization suggest that other acid species can be even more effective than the –COOH group. *Phosphonic* and *Sulfonic* groups are the natural candidates to be explored in the near future. Another interesting question is how the strength of ligand-substrate interactions correlates with well known molecular properties of the ligands, such as their acid dissociation constant ( $pK_a$ ). If such correlations exist, how acid can a ligand be before it destroys the ZnO surface in aqueous media? Is it possible to create a stable hydrophobic coat, so that functionalized ZnO nanostructures are kinetically stable in harsh chemical environments? Some of these questions can be addressed directly via standard DFT calculations, but some of them require demanding hybrid *Molecular Dynamics* or QM-MM approaches. Given that, it seems to be urgent improving the SCC-DFTB description of adsorption processes on ZnO.

Another very promising direction is going beyond the standard *Time Independent* DFT in order to investigate photo excitations on functionalized ZnO.

As we have discussed in Chapter 1, ZnO nanowires seem to be the most natural candidates for nano-based *Dye Sensitized Solar Cells* (DSSC); but until now, the reported conversion efficiencies of such devices are rather disappointing – ~ 2 %. Hybrid ZnO nanostructures do have a considerable potential for applications in *photovoltaics*; however, our knowledge on their photo-physics is still too limited, and so our ability of understanding and eliminating the bottlenecks in ZnO-based DSSCs. In this context, we can apply our know-how to characterize the ground state properties of ZnO functionalized with organic dyes, and then use *Time-Dependent Density Functional Theory* (TDDFT) to explore the photo-excitation processes in these systems. Such investigations may have a considerable impact on our understanding of photo-induced electron injections on sensitized ZnO and its use for solar energy generation.

Still related to photo-excitation processes, ZnO is also a prominent material for photo-catalysis – a topic strongly connected with some of the great challenges of our time: energy generation and environmental protection. Exactly as in the DSSC case, we can combine our current know-how on ground state DFT with TDDFT calculations.

It is also important to keep in mind that all these research opportunities above arise as natural extensions of the work developed in this thesis. Nevertheless – as we have mentioned in the Chapter 1 – beyond ZnO there is a large and fascinating variety of metals oxides to be explored: CdO, NbO, CuO, MgO, CeO<sub>2</sub>, PbO<sub>2</sub>, TiO<sub>2</sub>, SnO<sub>2</sub> and many others – In addition to all their possible combinations via doping, surface modification, and so on. ZnO is one prominent example of how our knowledge on metal oxides has changed in the last few years – from an ordinary white pigment to an sophisticated multifunctional nanomaterial – and a good indication on how many possibilities we still have with other less investigated materials. There is still much physics and much chemistry to be unveiled about ZnO and other metal oxides. There is still a long way before these materials can provide more wellness and quality of life for average people, and paving this way is the real challenge to be assumed. Alone, our computer simulations on technical materials possibly cannot be expected to change the world in the next couple of years; but they will certainly help those experimentalists and engineers who will manage that somewhere in the future. That is what thesis is about; that is how this author would like to further contribute, and that is a really very exciting perspective.



# Acknowledgments

There are several people who helped me during the time of this work. I will not mention everyone by name, but I would like to say that I'm extremely grateful for all the energy and friendship I got here in Bremen. Both professionally and personally I had an amazing time here. Bremen is an wonderful city: Friendly people, a rich cultural environment, and everything else that someone needs to be happy. I'm very glad about living here this time.

This work would not be possible if my Professor would not have accepted me in his work group. So I would like to thank my dear Prof. Thomas Frauenheim, for the opportunity and for all the friendship and support during this time. Prof. Frauenheim is also the director of the BCCMS, consequently the main person responsible for the excellent scientific environment there. Besides my scientific supervisor, Prof. Frauenheim has been also a good friend. He takes care of the BCCMS as if it was a big family, to which I'm very proud to belong.

I also would like to express all my gratitude to Dr. Andreia Luisa da Rosa, head of the Semiconductor Nanomaterials Group at the BCCMS. Andreia has been my direct supervisor all this time, guiding my steps in the everyday research life. Andreia is also the one who has selected my application and recruited me to her team here in Bremen, so I'm also thankful for the opportunity. Working with her I've learned how to organize my ideas, how to be more systematic and rigorous. She has an inspiring academic spirit and tremendous disposition to help her students. I would like to thank her for all her efforts on teaching me all this time: about physics, writing, gathering information, and everything else. I also would like to thank her for giving me the space to chase my own ideas, for all the dedication she had in discussing with me along this time and for all the many times she showed me my blind spots. If I may say something about it, I think we have been a very good team under her leadership.

From my other colleagues and collaborators at the BCCMS, I would like to thank especially Dr. Bálint Aradi, Dr. Grygoriy Dolgonos, Dr. Alessio Gagliardi (currently in Rome), Dr. Christof Köhler, Dr. Welch Cavalcanti and Prof. Thomas Niehaus (currently in Regensburg). I've learned a lot with all of them.

I also would like to thank all my fellow students, Professors and other friends at the BCCMS. It has been a pleasure sharing the work place with you.

Still, I would like emphasize my gratitude to Adriel Domingues and Svea Sauer, who have worked together with me in several opportunities, for Zoltan Bodrog and Jianping Xiao, who have been my officemates for quite a long time, and for Markus Rullich for revising this thesis. Thank you all for the collaboration and friendship.

Last but not least among the BCCMS team, I would like to express all my gratitude for Gabriela Berger, Karin Schütte, Marta Holowacz and Christine Frauenheim. These people helped me a lot in overcoming the famous German bureaucracy. Joke aside, without you it would be impossible! You are all great and all very dear friends.

Out of the BCCMS, but still in the Bremen University, I would like to thank my fellow student Jean-Peter Richters and his advisor Prof. Tobias Voss. I've appreciate very much all the discussions we had and I hope we can intensify our partnership in future. It has been very constructive for me.

There is also another reason to thank Prof. Voss : He has agreed to be one of the referees in the defense of this work. At his side in the judging committee, I will have also Prof. Lutz Mädler, from the IWT – University of Bremen and Prof. Robert J. Hammers from the Department of Chemistry - University of Wisconsin. To all of them, I would like to express my deep gratitude for agreeing judging my work. It is an honor to me submitting my work to you.

I'm also extremely grateful for the Deutsche-Israelische Projektkooperation (DIP-40100474) and for the Deutsche Forschungs Gessellschaft (Priority Project SPP-1165) for the financial support of this project. Besides I would like to thank the North Germany Supercomputing Center (HLRN) for the computational resources.

Finally, I would like to thank my former Professors from the Institute of Chemistry – University of Campinas - Brazil: Prof. Luiz Carlos Dias, Prof. Celso Aparecido Bertran, Prof. Roy E. Bruns and Prof. Adalberto B. M. Bassi. Even after all these years, I still hear your voices. Thank you

To my very dear friend Nader: We had to cross the ocean to become good friends. But it paid off! Thank you very much for all the friendship, the hospitality and for your advices.

To my very dear friend Roberto: Thank you for everything you did for me. I hope you know how much I owe you. Not only for believing in me, but also for all the motivation and energy.

To my very dear family: I hope you know I owe all this amazing experience to you. We may have an ocean between us, but I feel you in my heart. Everyday.

Finally, to my very very dear Ann-Kathrin: Thank you for everything. You have done everything someone could possibly do to help me, and I will be forever grateful to you. I'm better when you are around, and I hope I can remember you that for a long long time; everyday.







# References

- [1] Kickelbick, G; *Hybrid Materials: Synthesis, Characterization and Applications*, 1<sup>st</sup> Ed., Wiley-VCH, Weinheim, **2006**.
- [2] Ashby, M.F.; Jones, D. R. H.; *Engineering Materials 2: An introduction to Microstructures, Processing and Design*, 3<sup>rd</sup> Ed., Butterworth-Heinemann, **2006**.
- [3] Hench, L. L.; West, J. K. *Chem. Rev.* **1990**, *90*(1), 33.
- [4] Dorsey, J.G.; Dill, K.A. *Chem. Rev.* **1989**, *89*(2), 331.
- [5] Howard, G. A.; Martin, J. P.; *Biochem J.* **1950**, *46*(5),532.
- [6] Snyder, L.R.; Kirkland, J.J.; Dolan, J.W. *Introduction to Modern Liquid Chromatography*, 3<sup>rd</sup> Ed., Wiley, 2010.
- [7] Toyoshima, Y.; *Bull. Chem. Soc. Jap.* **1961**, *34*(11), 1734.
- [8] Ebbesen, T.W.; Ajayan, P.M. *Nature* **1992**, *358*, 220.
- [9] Murray, C.B.; Kagan, C.R.; Bawendi, M.G. *Annu. Rev. Phys. Chem.* **2000**, *30*, 545.
- [10] Breuer, O.; Sundararaj, U. *Polym.Compos.* **2004**, *25*(6), 630.
- [11] Ekimov, A.I., Onushchenko, A.A. *JETP Lett.* **1981**, *34*(6), 345.
- [12] Taratula, O.; Galoppini, E.; Mendelsohn, R.; Reyes, P. I.; Zhang, Y.; Duan, Z.; Zhong, J.; Lu, Z. *Langmuir* **2009**, *25*(4), 2107.
- [13] Misewich, J.A.; Martel, R.; Avouris, Ph.; Tsang, J.C.; Heinze, S.; Tersoff, J. *Science* **2003**, *300*(5620), 783.
- [14] O'Regan, B.; Grätzel, M. *Nature* **1991**, *353*, 737.
- [15] Law, M.; Greene, L.E.; Radenovic, A.; Kuykendall, T.; Liphardt, J.; Yang, P. *J. Phys. Chem. B* **2006**, *110*(45), 22652.
- [16] Grätzel, M. *Inorg. Chem.* **2005**, *44*(20), 6841.
- [17] Kubo, W.; Kitamura, T.; Hanabusa, K.; Wada, Y.; Yanagida, S. *Chem. Commun.* **2002**, *24*, 374.
- [18] Mazille, F.; Fei, Z.; Kuang, D.; Zhao, D.; Zakeeruddin, S. M.; Grätzel, M.; Dyson, P. J. *Inorg. Chem.* **2006**, *45*(4), 1585.

- [19] Kruger, J.; Plass, R.; Grätzel, M.; Cameron, P. J.; Peter, L. M. *J. Phys. Chem. B* **2003**, *107*(31), 7536.
- [20] Wang, P.; Zakeeruddin, S. M.; Moser, J. E.; Nazeeruddin, M. K.; Sekiguchi, T.; Grätzel, M. *Nature Mater.* **2003**, *2*(6), 402.
- [21] Law, M.; Greene, L.E.; Johnson, J.C.; Saykally, R.; Yang, P. *Nature Mat.* **2005**, *4*(6), 455.
- [22] Burda, C.; Chen, X.; Narayanan, R.; El-Sayed, M.A. *Chem. Rev.* **2005**, *105*(4), 1025.
- [23] Liong, M.; Lu, J.; Kovoichich, M.; Xia, T.; Ruehm, S.G.; Nel, A.E.; Tamanoi, F.; Zink, J.I. *ACS Nano* **2008**, *2*(5), 889.
- [24] Law, M.; Goldberger, J.; Yang, P. *Annu. Rev. Mat. Res.* **2004**, *34*, 83.
- [25] Gudixsen, M.S.; Lieber, C.M. *J. Am. Chem. Soc.* **2000**, *122*(36), 8801.
- [26] Wu, Y.; Yan, H.; Huang, M.; Messer, B.; Song, J.H.; Yang, P. *Chem. Eur. J.*, **2002**, *8*(6), 1260.
- [27] Pan, Z.W.; Dai, Z.R.; Wang, Z.L. *Science* **2001**, *291*(5510), 1947.
- [28] Wang, X.; Li, Y. *Inorg. Chem.* **2006**, *45*(19), 7522.
- [29] Dresselhaus, M.S.; Avouris, P. In *Topics in Applied Physics: Carbon Nanotubes: Synthesis, Structure, Properties and Applications*, Vol. 80, Dresselhaus, M.S.; Dresselhaus, G.; Avouris, P., Eds.; Springer-Verlag: Berlin, **2001**.
- [30] Iijima, S. *Nature*, **1991**, *354*, 56.
- [31] Kasakovskaya, Z.Y.; Chernozatonskii, L.A.; Fedorov, E. A. *JETP Lett.* **1992**, *56*(1), 26.
- [32] Bachtold, A.; Hadley, P.; Nakanishi, T.; Dekker, C. *Science* **2001**, *294*(5545), 1317.
- [33] Klinke, C.; Hannon, J.B.; Afzali, A.; Avouris, P. *Nano Lett.* **2006**, *6*(5), 906.
- [34] White, C.T.; Todorov, T.N. *Nature* **2001**, *411*, 649.
- [35] Endo, M.; Kim, Y.A.; Hayashi, T.; Nishimura, K.; Matsushita, T.; Miyashita, K.; Dresselhaus, M.S. *Carbon* **2001**, *39*(9), 1287.
- [36] Kymakis, E.; Amaratunga, G.A.J. *J. Appl. Phys.* **2006**, *99*(8), 084302.
- [37] Endo, M.; Strano, M.S.; Ajayan, P.M. In *Topics in Applied Physics: Carbon Nanotubes: Advanced Topics in Synthesis, Structure, Properties and Applications*, Vol. 111, Jorio, A.; Dresselhaus, G.; Dresselhaus, M.S., Eds.; Springer-Verlag: Berlin, **2007**.

- [38] Nolan, M.; O'Callaghan, S.; Fagas, G.; Greer, J.; Frauenheim, Th. *Nano Lett.* **2007**, *7*(1), 34.
- [39] Cui, Y.; Zhong, Z.; Wang, D.; Wang, W.U.; Lieber, C.M. *Nano Lett.* **2003**, *3*(1), 14.
- [40] Koo, S.M.; Li, Q.; Edelstein, M.D.; Richter, C.A.; Vogel, E.M. *Nano Lett.* **2005**, *5*(12), 2519.
- [41] Goldberger, J.; Hochbaum, A.I.; Fan, R.; Yang, P. *Nano Lett.* **2006**, *6*(5), 973.
- [42] Zhong, Z.; Fang, Y.; Lu, W.; Lieber, C.M. *Nano Lett.* **2005**, *5*(6), 1143.
- [43] Hahm, J.-I.; Lieber, C.M. *Nano Lett.* **2004**, *4*(1), 51.
- [44] Li, Z.; Chen, Y.; Li, X.; Kamins, T. I.; Nauka, K.; Williams, R.S. *Nano Lett.* **2004**, *4*(2), 245.
- [45] Lew, K.K.; Pan L.; Bogart, T.E.; Dilts, S.M.; Dickey, E.C.; Redwing, J.M.; Wang, Y.; Cabassi, M.; Mayer, T.S. *Appl. Phys. Lett.* **2004**, *85*(15), 3101.
- [46] Cui, Y.; Duan, X.; Hu, J.; Lieber, C.M. *J. Phys. Chem. B* **2000**, *104*(22), 5213.
- [47] Wang, Y.; Lew, K.K.; Ho, T.T.; Pan, L.; Novak, S.W.; Dickey, E.C.; Redwing, J.M.; Mayer, T.S. *Nano Lett.* **2005**, *5*(11), 2139.
- [48] Holmes, J.D.; Johnston, K.P.; Doty, R.C.; Korgel, B.A. *Science* **2000**, *287*(5457), 1471.
- [49] Ma, D.D.D.; Lee, C.S.; Au, F.C.K.; Tong, S.Y.; Lee, S.T. *Science* **2003**, *299*(5614), 1874.
- [50] Wu, Y.; Cui, Y.; Huynh, L.; Barrelet, C.J.; Bell, D.C.; Lieber, C.M. *Nano Lett.* **2004**, *4*(3), 433.
- [51] Hurley, P.T.; Nemanick, E.J.; Brunshwig, B.S.; Lewis, N.S. *J. Amer. Chem. Soc* **2006**, *128*(31), 9990.
- [52] Bansal, A.; Li, X.; Lauer mann, I.; Lewis, N.S.; Yi, S.I.; Weinberg, W.H. *J. Am. Chem. Soc.* **1996**, *118*(30), 7225.
- [53] Bansal, A.; Lewis, N.S. *J. Phys. Chem. B* **1998**, *102*(21), 4058.
- [54] Buriak, J.M.; Allen, M.A. *J. Am. Chem. Soc.* **1998**, *120*(6), 1339.
- [55] Linford, M.R.; Chidsey, C.E.D. *J. Am. Chem. Soc.* **1993**, *115*(26), 12631.
- [56] Sieval, A.B.; Demirel, A.L.; Nissink, J.W.M.; Linford, M.R.; van der Maas, J.H.; de Jeu, W.H.; Zuilhof, H.; Sudholter, E.J.R. *Langmuir* **1998**, *14*(7), 1759.

- [57] Yu, H.; Webb, L.J.; Ries, R.S.; Solares, S.D.; Goddard III, W.A.; Heath, J. R.; Lewis, N.S. *J. Phys. Chem. B* **2005**, *109*(2), 671.
- [58] Buriak, J.M. *Chem. Rev.* **2002**, *102*(5), 1271.
- [59] Patolsky, F.; Zheng, G.; Lieber, C.M. *Anal. Chem.* **2006**, *78*(13), 4260.
- [60] Diebold, U.; Li, S.C.; Schmidt, M. *Annu. Rev. Phys. Chem.* **2010**, *61*, 129.
- [61] Kolmakov, A.; Moskovits, M. *Annu. Rev. Mater. Res.* **2004**, *34*, 151.
- [62] Li, C.; Zhang, D.H.; Liu, X.L.; Han, S.; Tang, T.; Han, J.; Zhou, C. *Appl. Phys. Lett.* **2003**, *82*(10), 1613.
- [63] Xia, Y.; Yang, P.; Sun, Y.; Wu, Y.; Mayers, B.; Gates, B.; Yin, Y.; Kim, F.; Yan, H. *Adv. Mater.* **2003**, *15*(5), 353.
- [64] Wang, Z.L. *Annu. Rev. Phys. Chem.* **2004**, *55*, 159.
- [65] Wang, Z.L. *ACS Nano* **2008**, *2*(10), 1987.
- [66] Wang, Z.L.; Song, J. *Science* **2006**, *312*(5771), 242.
- [67] Wu, X.; Yamilov, A.; Liu, X.; Li, S.; Dravid, V.P.; Chang, R.P.H.; Cao, H.; *Appl. Phys. Lett.* **2004**, *85*(17), 3657.
- [68] Cui, J.; Gibson, U. *Nanotech.* **2007**, *18*(15), 155302.
- [69] Wang, Z.L.; *Mater. Today* **2004**, *7*(6), 26.
- [70] Yang, P.; Yan, H.; Mao, S.; Russo, R.; Johnson, J.; Saykally, R.; Morris, N.; Pham, J.; He R.; Choi, H.J. *Adv. Func. Mater.* **2002**, *12*(5), 323.
- [71] Wang, X.; Wang, X.; Song, J.; Li, P.; Ryou, J.H.; Dupuis, R.D.; Summers, C.J.; Wang, Z.L. *J. Amer. Chem. Soc.* **2005**, *127*(21), 7920.
- [72] Schmidt-Mende, L.; McManus-Driscoll, J.L. *Mater. Today* **2007**, *10*(5), 40.
- [73] Huang, M.H.; Wu, Y.; Feick, H.; Tran, N.; Weber, E.; Yang, P. *Adv. Mater.* **2001**, *13*(2), 113.
- [74] Greyson, E.C.; Babayan, Y.; Odom, T.W. *Adv. Mater.* **2004**, *16*(15), 1348.
- [75] Ramgir, N.S.; Late, D.J.; Bhise, A.B.; More, M.A.; Mulla, I.S.; Joag, D.S.; Vijayamohanan, K. *J. Phys. Chem. B* **2006**, *110*(37), 18236.
- [76] Song, J.; Wang, X.; Wang, X.; Riedo, E.; Wang, Z.L. *J. Phys. Chem. B* **2005**, *109*(20), 9869.
- [77] Solin, S.A. *Annu. Rev. Mater. Sci.* **1997**, *27*, 89.

- [78] Usuki, A.; Kojima, Y.; Kawasumi, M.; Okada, A.; Fukushima, Y.; Kurauchi, T.; Kamigaito, O. *J. Mater. Res.* **1993**, *8*(5), 1179.
- [79] Kojima, Y.; Usuki, A.; Kawasumi, M.; Okada, A.; Kurauchi, T.; Kamigaito, O.; Kaji, K. *J. Polym. Sci. Part B: Polym. Phys.* **1994**, *32*(4), 625.
- [80] Kojima, Y.; Usuki, A.; Kawasumi, M.; Okada, A.; Kurauchi, T.; Kamigaito, O.; Kaji, K. *J. Polym. Sci.: Part B: Polym. Phys.* **1995**, *33*(7), 1039.
- [81] Krishnamoorti, R.; Vaia, R.A.; Giannelis, E.P. *Chem. Mater.* **1996**, *8*(8), 1728.
- [82] Beaudot, P.; De Roy, M.E.; Besse, J.P. *Chem. Mater.* **2004**, *16*(5), 935.
- [83] Gao, Y.; Nagai, M. *Langmuir* **2006**, *22*(8), 3936.
- [84] Torquato, S. *Annu. Rev. Mater. Res.* **2010**, *40*, 101.
- [85] Logan, D.L. *A First Course in the Finite Element Method*, 4<sup>th</sup> Ed., Nelson, Ontario, **2007**.
- [86] Maisuradze, G.G.; Senet, P.; Czaplewski, C.; Liwo, A.; Scheraga, H.A. *J. Phys. Chem. A* **2010**, *114*(13), 4471.
- [87] Reynwar, B.J.; Illya, G.; Harmandaris, V.A.; Müller, M.M.; Kremer, K.; Deserno, M. *Nature*, **2007**, *447*, 461.
- [88] Muller, M.; Katsov, K.; Schick, M. *Phys. Rep.* **2006**, *434*(4-5), 113.
- [89] Meyer, H.; Müller-Plathe, F. *Macromolecules* **2002**, *35*(4), 1241.
- [90] Perter, C.; Kremer, K. *Soft Mater* **2009**, *5*(22), 4357.
- [91] Baron, R.; Trzesniak, D.; de Vries, A.H.; Elsener, A.; Marrink, S.J.; van Gunsteren, W.F. *ChemPhysChem* **2007**, *8*(3), 452.
- [92] Johnson, M.E.; Head-Gordon, T.; Louis, A.A. *J. Chem. Phys.* **2007**, *126*(14), 144509.
- [93] Marrink, S.J.; Periole, X.; Tieleman, D.P.; de Vries, A.H. *ChemPhysChem*. **2010**, *11*(12), 2254.
- [94] Binder, K.; Milchev, A. *J. Comp-Aided. Mater. Design* **2002**, *9*(1), 33.
- [95] Martinez, L.; Nascimento, A. S.; Nunes, F. M.; Phillips, K.; Aparicio, R.; Dias, S. M. G.; Figueira, A. C. M.; Lin, J. H.; Nguyen, P.; Apriletti, J. W.; Neves, F. A. R.; Baxter, J. D.; Webb, P.; Skaf, M. S.; Polikarpov, I. *Proc. Natl. Acad. Sci. U.S.A.* **2009**, *106*, 20717.
- [96] Elson, E.L.; Fried, E.; Dolbow, J.E.; Genin, G.M. *Annu. Rev. Biophys.* **2010**, *39*, 207.

- [97] Martinez, L.; Webb, P.; Polikarpov, I.; Skaf, M. S. *J. Med. Chem.* **2006**, *49*(1), 23.
- [98] Skaf, M.S.; Sonoda, M.T. *Phys. Rev. Lett.* **2005**, *94*(13), 137802.
- [99] Tolman, R.C. *The Principles of Statistical Thermodynamics*, Dover, New York, **1979**.
- [100] McQuarrie, D.A. *Statistical Mechanics*, University Science Books, Sausalito, **2000**.
- [101] Cordier, S.; Pareschi, L.; Piatecki, C. *J. Stat. Phys.* **2009**, *134*(1), 1043.
- [102] Hawkins, R.J.; Aoki, M.; Frieden, B.R. *Physica A* **2010**, *389*(17), 3565.
- [103] Szabo, A.; Ostlund, N.S. *Modern Quantum Chemistry*, Dover, New York, **1989**.
- [104] He, X.; Merz Jr., K.M. *J. Chem. Theory Comput.* **2010**, *6*(2), 405.
- [105] Martin, R.M. *Electronic Structure: Basic Theory and Practical Methods*, Cambridge University Press, Cambridge, **2004**.
- [106] Hückel, E. *Z. Phys.* **1931**, *70*, 204.
- [107] Bredow, T.; Jug, K. *Theor. Chem. Acc.* **2005**, *113*(1), 1.
- [108] Seifert, G. *J. Phys. Chem. A* **2007**, *111*(29), 5609.
- [109] Elstner, M.; Porezag, D.; Jungnickel, G.; Elsner, J.; Haugk, M.; Frauenheim, Th.; Suhai, S.; Seifert, G. *Phys. Rev. B* **1998**, *58*(11), 7260.
- [110] Dirac, P.A.M. *Proc. R. Soc.* **1929**, *123*(792), 714.
- [111] Lowe, J.P.; Peterson K.A. *Quantum Chemistry*, 3<sup>rd</sup> Ed., Elsevier Academic Press, London, **2006**.
- [112] Levine, I.N. *Quantum Chemistry*, 5<sup>th</sup> Ed., Prentice Hall, New Jersey, **1999**.
- [113] Thomas, L.H. *Proc. Cambridge Phil. Soc.* **1927**, *23*(5), 542.
- [114] Fermi, E. *Rend. Accad. Naz. Lincei* **1927**, *6*, 602.
- [115] Koch, W.; Holthausen, M.C. *A Chemist's Guide to Density Functional Theory*, 2<sup>nd</sup> Ed., Wiley-VCH, Weinheim, **2001**.
- [116] Lanczos, C. *The Variational principles of Mechanics*, 4<sup>th</sup> Ed., Dover, New York, **1986**.
- [117] Chow, T.L. *Mathematical Methods for Physicists: A Concise Introduction*, Cambridge University Press, Cambridge, **2000**.

- [118] Parr, R.G., Yang W. *Density Functional Theory of Atoms and Molecules*, Oxford University Press, New York, **1989**.
- [119] Kohn, W., Sham, L.J., *Phys. Rev.* **1965**, *140(4A)*, A1133.
- [120] Stowasser, R.; Hoffman, R. *J. Am. Chem. Soc.* **1999**, *121(14)*, 3414.
- [121] Baerends, E. J.; Gritsenko, O. V. *J. Phys. Chem.* **1997**, *101(30)*, 5383.
- [122] Kohn, W.; Becke, A. D.; Parr, R. G. *J. Phys. Chem.* **1996**, *100(31)*, 12974.
- [123] Ceperley, D.M.; Alder, B.J. *Phys. Rev. Lett.* **1980**, *45(7)*, 566.
- [124] Perdew, J.P.; Zunger, A. *Phys. Rev. B* **1981**, *23(10)*, 5048.
- [125] Mohammed, A.E.; Sahni, V. *Phys. Rev. B* **1984**, *29(6)*, 3687.
- [126] Gunnarsson, O.; Lundqvist, B.I.; *Phys. Rev. B* **1976**, *13(10)*, 4274.
- [127] Langreth, D.C.; Perdew, J.P. *Phys. Rev. B.* **1980**, *21(12)*, 5469.
- [128] Perdew, J.P.; Burke, K.; Wang, Y. *Phys. Rev. B* **1996**, *54(23)*, 16533.
- [129] Wang, Y.; Perdew, J.P.; Chevary, J.A.; MacDonald, L.D.; Vosko, S.H. *Phys. Rev. A* **1990**, *41(1)*, 78.
- [130] Beck, A.D. *Phys. Rev. A* **1988**, *38(6)*, 3098.
- [131] Perdew, J.P. *Phys. Rev. B* **1986**, *33(12)*, 8822.
- [132] Lee, C.; Yang, W.; Parr, R.G. *Phys. Rev. B* **1988**, *37(2)*, 785.
- [133] Perdew, J. P.; Burke, K.; Ernzerhof, M. *Phys Rev. Lett.* **1996**, *77*, 3865.
- [134] Godby, R.W.; Schlüter, M.; Sham, L.J. *Phys. Rev. B* **1988**, *37(17)*, 10159.
- [135] Perdew, J.P.; Levy, M. *Phys. Rev. Lett.* **1983**, *51(20)*, 1884.
- [136] Lany, S. Zunger, A. *Phys. Rev. B*, **2008**, *78(23)*, 235104.
- [137] Mori-Sanchez, P.; Cohen, A.J.; Wang, Y. *Phys. Rev. Lett.* **2008**, *100(14)*, 146401.
- [138] Lany, S. Zunger, A. *Phys. Rev. B*, **2010**, *81(11)*, 113201.
- [139] Anisimov, V. A.; Aryasetiawan, F.; Lichtenstein, A. I. *J. Phys: Cond. Matt.* **1997**, *9(4)*, 767.
- [140] Dudarev. S. L.; Botton, G. A.; Savrasov, S. Y.; Humphreys, C. J.; Sutton, A. P. *Phys. Rev B* **1998**, *57(3)*, 1505.

- [141] Janotti, A.; Van de Walle, C.G. *Phys. Rev. B* **2007**, *76(16)*, 165202.
- [142] Sheetz, R.M.; Ponomareva, I.; Richter, E.; Andriotis, A.N.; Menon, M. *Phys. Rev B* **2009**, *80(19)*, 195314.
- [143] Zhou, X. H.; Hu, Q. H.; Fu, Y. *J. Appl. Phys.* **2008**, *104(6)*, 063702.
- [144] Zhou, C. G.; Sun, L. Z.; Zhong, X. L.; Chen, X.; Wei, L.; Wang, J. B. *Phys. Lett. A* **2007**, *368(1-2)*, 112.
- [145] Troullier, N.; Martins, J. L. *Phys. Rev. B* **1991**, *43(3)*, 1993.
- [146] Soler, J. M.; Artacho, E.; Gale, J. D.; García, A.; Junquera, J.; Ordejón P.; Sánchez-Portal, D. *J. Phys.: Condens. Matter* **2002**, *14(11)*, 2745.
- [147] Feynman, R.P. *Phys. Rev.* **1939**, *56(4)*, 340.
- [148] Pulay, P. *Mol. Phys.* **1969**, *17(2)*, 197.
- [149] Delley, B. *J. Chem. Phys.* **1991**, *94(11)*, 7245.
- [150] International Union of Crystallography: Report of the Executive Committee for 1991 *Acta Cryst.* **1992**, *A48(6)*, 922. See pg. 928.
- [151] Ashcroft, N.W.; Mermin, N.D. *Solid State Physics*, Saunders College Publishing: Florida, **1976**.
- [152] Monkhorst, H. J.; Pack, J. D. *Phys. Rev. B* **1976**, *13(12)*, 5188.
- [153] Kresse, G.; Furthmüller, J. *Phys. Rev. B* **1996**, *54(16)*, 11169.
- [154] Kresse, G.; Furthmüller, J. *Comp. Mat. Sci.* **1996**, *6(1)*, 15.
- [155] Richters, J.P.; Voss, T. ; Wischmeier, L.; Rückmann, I.; Gutowski, J. *Appl. Phys. Lett.* **2008**, *92(1)*, 011103.
- [156] Emanetoglu, N.W.; Zhu, J.; Chen, Y.; Zhong, J.; Chen, Y.; Lu, Y. *Appl. Phys. Lett.* **2004**, *85(15)*, 3702.
- [157] Yip, H.; Hau, S.K.; Baek, N.S.; Ma, H.; Jen, A.K.Y. *Adv. Mater.* **2004**, *20(12)*, 2376.
- [158] Ashrafi, A.; Jagadish, C. *J. Appl. Phys.* **2007**, *102(7)*, 071101.
- [159] Coleman, V.A.; Jagadish, C. In *Zinc Oxide Bulk, Thin-Films and Nanostructures : Processing, Properties and Applications*. Jagadish, C., Pearton, S.J., Eds.; Elsevier: Amsterdam, **2006**.
- [160] Choi, Y.S.; Kang, J.W.; Hwang, D.K.; Parl, S.J. *IEEE Trans. Elec. Dev.* **2010**, *57(1)*, 26.



- [161] Morkoç, H.; Özgür, Ü. *Zinc Oxide: Fundamentals, Materials and Device Technologies*, Wiley-VCH, Weinheim, **2009**.
- [162] Bradby, J.E.; Kucheyev, S.O.; Williams, J.S.; Jagadish, C.; Swain, M.V. *Appl. Phys. Lett.* **2002**, *80*(24), 4537.
- [163] Mitrushchenkov, A.; Linguerri, R.; Chambaud, G. *J. Phys. Chem. C* **2009**, *113*(17), 6883.
- [164] Xu, S.; Qin, Y.; Xu, C.; Wei, Y.; Yang, R.; Wang, Z.L. *Nature Nanotech.* **2010**, *5*, 366.
- [165] Wang, Z.L.; Song, J. *Science* **2006**, *312*(5771), 242.
- [166] Muragham, F.D. *Proc. Natl. Acad. Sci. U.S.A.* **1944**, *30*(9), 244.
- [167] Jaffe, J.E.; Snyder, J.A.; Lin, Z.; Hess, A.C. *Phys. Rev B* **2000**, *62*(3), 1660, and references there.
- [168] Li, C.; Guo, W.; Kong, Y.; Gao, H. *Phys. Rev. B* **2007**, *76*(3), 035322.
- [169] Ghosh, G.; Delsante, S.; Borzone, G.; Asta, M.; Ferro, B. *Act. Mater.* **2006**, *54*(19), 4977.
- [170] Shang, S.L.; Saengdeejing, A.; Mei, Z.G.; Kim, D.E.; Zhang, H.; Ganeshan, S.; Wang, Y.; Liu, Z.K. *Comp. Mater. Sci.* **2010**, *48*(4), 813.
- [171] Philipsen, P.H.T.; Baerends, E.J. *Phys. Rev. B* **1996**, *54*(8), 5326.
- [172] Wedig, U.; Jansen, M.; Paulus, B.; Rosciszewski, K.; Sony, P. *Phys. Rev B* **2007**, *75*(20), 205123.
- [173] Weiss, R.J.; Mazzone, G. *J. Appl. Cryst.* **1981**, *14*, 401.
- [174] Dean, J.A. *Lange's Handbook of Chemistry*, 14<sup>th</sup> Ed., McGraw-Hill, New York, **1992**.
- [175] Fan, J.W.; Xia, J.B.; Agus, P.A.; Tan, S.T.; You, S.F.; Sun, X.W. *J. Appl. Phys.* **2006**, *99*(1), 013702.
- [176] Haussermann, U.; Simak, S.I.; *Phys. Rev. B* **2001**, *64*(24), 245114.
- [177] Claeysens, F.; Freeman, C.L.; Allan, N.L.; Sun, Y.; Ashfold, N.R.; Harding, J.H. *J. Mater. Chem.* **2005**, *15*(1), 139.
- [178] Fan, W.; Xu, H.; Rosa, A. L.; Frauenheim, Th.; Zhang, R. Q. *Phys. Rev. B* **2007**, *76*(7), 073302.
- [179] Meyer, B.; Marx, D. *Phys. Rev. B* **2003**, *67*(3), 035403.

- [180] Soci, C.; Zhang, A.; Xiang, B.; Dayeh, S.A.; Aplin, D.P.R.; Park, J.; Bao, X.Y.; Lo, Y.H.; Wang, Y.H. *Nano Lett.* **2007**, *7*(4), 1003.
- [181] Guo, S.; Dong, S. *Trac-Trends Anal. Chem.* **2009**, *28*(1), 96-109.
- [182] Zhang, J.; Wang, S.; Xu, M.; Wang, Y.; Xia, H.; Zhang, S.; Guo, X.; Wu, S. *J. Phys. Chem. C* **2009**, *113*(5), 1662.
- [183] Patolsky, F.; Lieber, C.M. *Mater. Today* **2005**, *8*(4), 20.
- [184] Huy, K.C.; Ong, H.C.; Lee, P.F.; Dai, J.Y. *Appl. Phys. Lett.* **2005**, *86*(15), 152116.
- [185] Lao, C.; Li, Y.; Wong, C.P.; Wang, Z.L. *Nano Lett.*, **2007** *7*(5), 1323.
- [186] Garcia, M.A.; Merino, J.M.; Fernández-Pinel, E.; Quesada, A.; de la Venta, J.; Ruiz-González, M.L.; Castro, G.R.; Crespo, P.; Llopis, J.; González-Calbet, J.M.; Hernando, A. *Nano Lett.* **2007**, *7*(6), 1489.
- [187] Singh, S.P.; Arya, S.K.; Pandey, P.; Malhotra, B.D.; Saha, S.; Sreenivas, K.; Gupta, V. *Appl. Phys. Lett.* **2007**, *91*(6), 063901.
- [188] Kumar, N.; Dorfman, A.; Hahm, J. *Nanotechnology* **2006**, *17*(12), 2875.
- [189] Taratula, O.; Galoppini, E.; Wang, D.; Chu, D.; Zhang, Z.; Chen, H.G. Saraf, G.; Lu, Y. *J. Phys. Chem. B* **2006**, *110*(13), 6506.
- [190] Perkins, C. L. *J. Phys. Chem. C* **2009**, *113*(42), 18276.
- [191] Allen, C.G.; Baker, D.J.; Albin, J.M.; Oertli, H.E.; Gillaspie, D.T.; Olsson, D.C.; Furtak, T.E.; Collins R.T. *Langmuir* **2008**, *24*(23), 13393.
- [192] Zhang, H.; Wang, J.; Zheng, H.; Zhuo, K.; Zhao, Y. *J. Chem. Phys. B* **2005**, *109*(7), 2610.
- [193] Ozawa, K.; Hasegawa, T.; Edamoto, K.; Takahashi, K.; Kamada, M. *J. Chem. Phys. B* **2002**, *106*(36), 9380.
- [194] Glaspell, G.; Hassan, H. M. A.; Elzatahry, A.; Abdalsayed, V.; El-Shall, M. S.; *Top. Catal.* **2008**, *47*(1), 22.
- [195] Hertl, W. *Langmuir* **1988**, *4*(3), 594.
- [196] Marci, G.; Augugliaro, V.; López-Muñoz, M.J.; Martin, C.; Palmisano, L.; Rives, V.; Schiavello, M.; Tilley, R.J.D.; Venezia, A. M. *J. Chem. Phys. B* **2001**, *105* (5), 1033.
- [197] Marguerettaz, X.; O'Neill, R.; Fitzmaurice, D. *J. Amer. Chem. Soc.*, **1994**, *116*(6), 2629.
- [198] Galoppini, E. *Coord. Chem. Rev.*, **2004**, *248*(13-14), 1283.

- [199] Wang, Y.; Kovacic, R.; Meyer, B.; Kotsis, K.; Stodt, D.; Staemmler, V.; Qiu, H.; Traeger, F.; Langenberg, D.; Muhler, M.; Wöll, C. *Ang. Chem. Int. Ed.* **2007**, *46*(29), 5624.
- [200] Meyer, B.; Rabaa, H.; Marx, D. *Phys. Chem. Chem. Phys.* **2006**, *8*(13), 1513.
- [201] Martins, J. B. L.; Longo, E.; Salmon, O. D. R.; Espinoza, V. A. A.; Taft, C. *Chem. Phys. Lett.* **2004**, *400*(4-6), 481.
- [202] Halevi, B.; Vohs, J. M. *Surf. Science* **2008**, *602*(1), 198.
- [203] Hu, X.; Rosa, A.L.; Frauenheim, Th.; Zhang, R.Q.; Lee, S.T. *Appl. Phys. Lett.* **2007**, *91*(3), 031914.
- [204] Moreira, N.H.; Rosa A.L.; Frauenheim, Th. *Appl. Phys. Lett.* **2009**, *94*(19), 193109.
- [205] Moreira, N.H.; Aradi, B.; Rosa A.L.; Frauenheim, Th. *J. Phys. Chem. C* **2010**, *114*(44), 18860.
- [206] Huang, S. P.; Xu, H.; Bello, I.; Zhang, R.Q. *J. Phys. Chem. C* **2010**, *114*(19), 8861.
- [207] Fang, D. Q.; Rosa, A. L.; Zhang, Q.; Frauenheim, Th. *J. Phys. Chem. C* **2010**, *114*(13), 5760.
- [208] Botello-Méndez, A. R.; López-Urias, F.; Terrones, M.; Terrones, H. *Nano Res.* **2008**, *1*(5), 420.
- [209] Blöchl, P. E. *Phys. Rev. B* **1994**, *50*(24), 17953.
- [210] Bertazzo, S.; Rezwan, K. *Langmuir* **2010**, *26*(5), 3364.
- [211] McQuarrie, D.A.; Simon, J.D. *Physical Chemistry: A Molecular Approach*, 1<sup>st</sup> Ed.; University Science Books; Sausalito, **1997**.
- [212] Morgantini, P.; Kollman, P.A. *J. Am. Chem. Soc.* **1995**, *117*(22), 6057.
- [213] Gonçalves P.F.B.; Stassen, H. *Pure Appl. Chem.* **2004**, *76*(1), 231.
- [214] Felsing, W.A.; Thomas, A.R. *Ind. Eng. Chem.* **1929**, *21*(12), 1269.
- [215] National Institute of Standards and Technology(NIST), chemistry webbook. (<http://webbook.nist.gov/chemistry/>)
- [216] Ireta, J.; Neugebauer, J.; Scheffler, M. *J. Phys. Chem. A* **2004**, *108*(26), 5692.
- [217] Porezag, D.; Frauenheim, Th.; Köhler, Th.; Seifert, G.; Kaschner, R. *Phys. Rev. B* **1995**, *51*(19), 12947.

- [218] Seifert, G.; Porezag, D.; Frauenheim, Th. *Int. J. Quantum Chem.*, **1996**, *58*(2), 185.
- [219] Seifert, G. *J. Phys. Chem. A* **2007**, *111*(26), 5609.
- [220] Niehaus, Th.; Suhai, S.; Della Sala, F.; Lugli, P.; Elstner, M.; Seifert, G.; Frauenheim, Th. *Phys. Rev. B.*, **2001**, *63*(8), 085108.
- [221] di Carlo, A.; Gheorghe, M.; Lugli, P.; Sternberg, M.; Seifert G.; Frauenheim, Th. *Physica B*, **2002**, *314*(1-4), 86-90.
- [222] Elstner, M.; Cui, Q.; Munih, P.; Kaxiras, E.; Frauenheim, T.; Karplus, M. *J. Comput. Chem.* **2003**, *24*, 565.
- [223] Frauenheim, Th.; Seifert, G.; Elstner, M.; Niehaus, Th.; Köhler, C.; Amkreutz, M.; Sternberg, M.; Hajnal, Z.; di Carlo, A.; Suhai, S. *J. Phys: Cond. Matt.* **2002**, *14*(11), 3015.
- [224] Jank, J.F. *Phys. Rev. B* **1978**, *18*(12), 7165.
- [225] M.J. Frisch, G. W. Trucks, H. B. Schlegel, G. E. Scuseria, M. A. Robb, J. R. Cheeseman, J. A. Montgomery, Jr., T. Vreven, K. N. Kudin, J. C. Burant, J. M. Millam, S. S. Iyengar, J. Tomasi, V. Barone, B. Mennucci, M. Cossi, G. Scalmani, N. Rega, G. A. Petersson, H. Nakatsuji, M. Hada, M. Ehara, K. Toyota, R. Fukuda, J. Hasegawa, M. Ishida, T. Nakajima, Y. Honda, O. Kitao, H. Nakai, M. Klene, X. Li, J. E. Knox, H. P. Hratchian, J. B. Cross, V. Bakken, C. Adamo, J. Jaramillo, R. Gomperts, R. E. Stratmann, O. Yazyev, A. J. Austin, R. Cammi, C. Pomelli, J. W. Ochterski, P. Y. Ayala, K. Morokuma, G. A. Voth, P. Salvador, J. J. Dannenberg, V. G. Zakrzewski, S. Dapprich, A. D. Daniels, M. C. Strain, O. Farkas, D. K. Malick, A. D. Rabuck, K. Raghavachari, J. B. Foresman, J. V. Ortiz, Q. Cui, A. G. Baboul, S. Clifford, J. Cioslowski, B. B. Stefanov, G. Liu, A. Liashenko, P. Piskorz, I. Komaromi, R. L. Martin, D. J. Fox, T. Keith, M. A. Al-Laham, C. Y. Peng, A. Nanayakkara, M. Challacombe, P. M. W. Gill, B. Johnson, W. Chen, M. W. Wong, C. Gonzalez, and J. A. Pople, *Gaussian 03*, Revision B.04; Gaussian, Inc: Wallingford CT, **2004**.
- [226] Aradi, B.; Hourahine, B.; Frauenheim, Th. *J. Phys. Chem. A* **2007**, *111*(26), 5678.
- [227] Steinberg, D. J. *J Phys Chem Solids* **1982**, *43*(12), 1173.
- [228] Desgreniers, S. *Phys. Rev. B* **1998**, *58*(21), 14102.
- [229] Koskinen, P.; Häkkinen, H.; Seifert, G.; Sanna, S.; Frauenheim, Th.; Moseler M. *New J. Phys.* **2006**, *8*(1), 9.
- [230] Sahraoui, F.A.; Zerroug, S.; Louail, S.; Maouche, D. *Mater. Lett.* **2007**, *61*(10), 1978.
- [231] Barrientos, C.; Retondo, P.; Largo, A. *J. Chem. Theory Comput.* **2007**, *3*(2), 657.

- [232] Tusche, C.; Meyerheim, H. L.; Kirschner, J. *Phys. Rev. Lett.* **2007**, *99*(2), 026102.
- [233] Wander, A.; Harrison, N. M. *J. Phys. Chem. B* **2001**, *105*(26), 6191.
- [234] Law, J. B. K.; Thong, J. T. L. *Nanotech.* **2008**, *19*(6), 205502.
- [235] Hagemark, K.I. *J. Solid State Chem.* **1976**, *16*(3-4), 293.
- [236] Mohanty, G.P.; Azároff, L.V. *J. Chem. Phys.* **1961**, *35*(4), 1268.
- [237] Monticone, S.; Tufeu, R.; Kanaev, A.V. *J. Phys. Chem. B* **1998**, *102*(16), 2854.
- [238] Özgür, Ü.; Alivov, Y.I.; Liu, C.; Teke, A.; Reshchikov, M.A.; Dogan, S.; Avrutin, V. *J. Appl. Phys.* **2005**, *98*(4), 041301.
- [239] Djurisic, A.B.; Leung, Y.U. *Small* **2006**, *2*(8-9), 944. and references therein.
- [240] Oba, F.; Togo, A.; Tanaka, I.; Peier, J.; Kresse, G. *Phys. Rev B* **2008**, *77*(24), 245202.
- [241] Lany, S.; Zunger, A. *Phys. Rev B* **2008**, *78*(23), 235104.
- [242] Paudel, T.R.; Lambrecht, W.R.L. *Phys. Rev. B* **2008**, *77*(20), 205202.
- [243] Erhart P.; Albe, K. *Phys. Rev B*, **2006**, *73*(11), 115207.
- [244] Shen, X.; Allen, P.B.; Muckerman, J.T.; Davenport, J.W.; Zheng, J.C. *Nanolett.*, **2007**, *7*(8), 2267.
- [245] Zhou, Z.; Li, Y.; Liu, L.; Chen, Y.; Zhang, S.B.; Chen, Z. *J. Phys. Chem. C*, **2008**, *112*(36), 13926.
- [246] Xu, H.; Zhang, R. Q.; Zhang, X.; Rosa, A.L.; Frauenheim, Th. *Nanotech.* **2007**, *18*(48), 485713.
- [247] Xu, H.; Zhan, F.; Rosa, A. L.; Frauenheim, Th.; Zhang, R.Q. *Sol. Stat. Comm.* **2008**, *148*(11-12), 534.
- [248] Moreira, N.H.; Dolgonos, G.; Aradi, B.; Rosa, A.L.; Frauenheim, Th. *J. Chem. Theo. Comput.* **2009**, *5*(3), 605.
- [249] Wang, Q.; Sun, Q.; Chen, G.; Kawazoe, Y.; Jena, P. *Phys. Rev. B* **2008**, *77*(20), 205411.
- [250] An, W.; Wu, X.; Zeng, X.C. *J. Phys. Chem. C*, **2008**, *112*(15), 5747.
- [251] Gerstmann, U.; Deak, P.; Aradi, B.; Frauenheim, Th.; Overhof, H. *Physica B* **2003**, *340-342*, 190.
- [252] Makov, G.; Payne, M.C. *Phys. Rev. B* **1995**, *51*(7), 4014.

- [253] Lany, S.; Zunger, A. *Phys. Rev. B* **2005**, *72(03)*, 035215.
- [254] Lany, S.; Zunger, *Phys. Rev. B*, **2010**, *81(11)*, 113201.
- [255] Leao, C.R.; Fazzio, A.; da Silva, A.J.R. *Nanoletters* **2008**, *8(7)*, 1866.
- [256] Kwak, G.; Yong, K.J. *J. Phys. Chem. C* **2008**, *112(8)*, 3036.







# CURRICULUM VITAE: NEY HENRIQUE MOREIRA

---

## PERSONAL INFORMATION

**Name:** Ney Henrique Moreira  
**Birth date:** 24/09/1976  
**Birthplace:** São Paulo – SP, Brazil  
**Living address:** Berliner Straße 4  
28203 Bremen, Germany



**Phones:** +49(0421) 3098684 Home  
+49(0421) 2187821 Office +49(0176) 20485882 Cell

## EDUCATION

**Bachelor:** State University of Campinas (UNICAMP), Institute of Chemistry  
Campinas-SP, Brazil  
Graduated at 2001 March

**M. Sc. Degree:** State University of Campinas (UNICAMP), Institute of Chemistry  
Campinas-SP, Brazil  
Titled at 2003 February

## TITLES AND DISTINCTIONS

**2001** Bachelor in Chemistry UNICAMP - Brazil

**2003** Master in Physical Chemistry UNICAMP - Brazil

**Lavoisier Medal 2001** Awarded for Academic Merit - Best Student

**Academic Distinction** For accomplishing the first-place at the Ingress Tests for post-graduation Program at the Institute of Chemistry/UNICAMP

## ACADEMIC HISTORY

**Bremen Center for Computational Materials Science – Bremen, Germany**

**Position:** PhD Student

**Project:** Computational Studies of Functionalized Surfaces and Nanostructures

**Supervisor:** Prof. Dr. Thomas Frauenheim

**Cosupervisor:** Dr. Andreia Luisa da Rosa

Since September 2007

**Brazilian Synchrotron Radiation Laboratory – Campinas, Brazil.**

**Position:** Researcher

**Project:** Microfluidical Device's Development by Micro Fabrication Techniques.

**Supervisor:** Dr. Angelo Luiz Gobbi

From July 2006 to August 2007.

**Institute of Chemistry/UNICAMP – Campinas, Brazil.**

**Position:** Trainee Teacher

**Discipline:** Organic Chemistry Laboratory for Chemical Engineers

**Supervisor :** Dr. Lauro Barata.

Summer Semester 2005

**Institute of Chemistry/UNICAMP – Campinas, Brazil.**

**Position:** MS Degree Student

**Project:** Molecular Dynamics Simulation of Liquid/Liquid Interfaces

**Supervisor:** Dr. Munir Skaf.

From 2001 to 2003

**Institute of Chemistry/UNICAMP – Campinas, Brazil.**

**Position:** Undergraduate Student

**Project:** Vibrational Intensities, Core Electron Ionization Energies and Atomic Charges in Fluoroethanes Molecules

**Supervisor:** Dr. Roy Edward Bruns

From 1999 to 2001

**Brazilian Synchrotron Radiation Laboratory – Campinas, Brazil**

**Position:** Summer Fellowships Granted Student

**Project:** Adaptation of *in situ* heating system for the SAXS beam line at LNLS

**Supervisor:** Dr. Iris Torriani

Summer 2000

**Institute of Chemistry/UNICAMP – Campinas, Brazil.**

**Position:** Undergraduate Student

**Project:** Calcium Phosphate Conformable Bioceramics

**Supervisor:** Dr. Celso A. Bertran

From 1997 to 1999

# List of Publications

- Moreira N.H., Garcia A.D., Rosa A.L., Frauenheim Th.  
Stabilization mechanisms of organic functional groups on non-polar ZnO surfaces  
*J. Phys. Chem. C* (Submitted)
- Garcia A.D., Moreira N.H., Dolgonos G., Rosa A.L., Frauenheim Th.  
Glycine Adsorption on (10 $\bar{1}$ 0)-ZnO Surfaces.  
*J. Phys. Chem. C* (Accepted)
- Moreira NH, Aradi B., da Rosa A.L., Frauenheim Th.  
*Native Defects in ZnO Nanowires: Atomic Relaxations, Relative Stability, and Defect Healing with Organic Acids*  
*J. Phys. Chem. C* **2010**, 114(44), 18860.
- Carvalho R.F., Machado D.S., Mendes R.K., Moreira N.H., et al.  
*Development of a disposable amperometric biosensor for salicylate based on a plastic electrochemical microcell.*  
*Biosensors & Bioelec.* **2010**, 25(10), 2200.
- Dolgonos G., Aradi B., Moreira N.H., Frauenheim Th.  
*An Improved Self-Consistent-Charge Density-Functional Tight-Binding (SCC-DFTB) Set of Parameters for Simulation of Bulk and Molecular Systems Involving Titanium.*  
*J. Chem. Theory and Comput.* **2010**, 6(1), 266
- Moreira N.H., da Rosa A.L., Frauenheim Th.  
*Covalent functionalization of ZnO surfaces: A density functional tight binding study*  
*App. Phys. Lett.* **2009**, 94(19), 193109.
- Moreira N.H., Dolgonos G., Aradi B., Rosa A.L., Frauenheim Th.  
*Toward an Accurate Density-Functional Tight-Binding Description of Zinc-Containing Compounds.*  
*J. Chem Theory and Comput.* **2009**, 5(3), 605.
- Moreira N.H., de Almeida A.L.D.J., Piazzeta M.H.D.O, et al.  
*Fabrication of a multichannel PDMS/glass analytical microsystem with integrated electrodes for amperometric detection.*  
*Lab on a Chip* **2009**, 9(1),
- Silvam R.V., Camilli J.A., Moreira N.H., Bertran C.A.  
*The use of hydroxyapatite and autogenous cancellous bone grafts to repair bone defects in rats.*  
*Int. J. Oral Maxillofacial Sur.* **2005**, 34(2), 178.
- Moreira N.H., Skaf M.S.  
*Molecular Dynamics Simulation of H<sub>2</sub>O/CCl<sub>4</sub> Liquid/Liquid Interface.*  
*Prog. in Coll. & Polymer Sci.* **2004**, 128, 203.

Haiduke R.L.A., de Oliveira A.E., Moreira N.H., Bruns R.E.  
*Characteristic substituent-shift models for carbon 1s ionization energies and mean dipole-moment derivatives*  
*J. Phys. Chem. A* **2004**,108(5), 866.

Sonoda M.T., Moreira N.H., Martinez L., et al.  
*A review on the dynamics of water*  
*Braz. J. Phys.* **2004**, 34(1),3.

Moreira, N.H., Bassi, A.B.M.S.  
*On the First Law of Thermodynamics*  
*Química Nova* **2001**, 24(4), 536.